UNIVERSITAT DE VALÈNCIA

Departamento de Física Aplicada y Electromagnetismo

Investigation of the electronic structure of thin films, quantum wells and nanoparticles of $Zn_{1-x}Co_xO$ by optical and transport measurements under high pressures.

Tesis realizada por:

Gloria Almonacid Caballer

Director:
Prof. Alfredo Segura García del Río

Valencia, junio de 2014

Don Alfredo Segura García del Río, catedrático del departamento de Física Aplicada de la Universidad de Valencia.

CERTIFICA:

Que la presente memoria: "Investigation of the electronic structure of thin films, quantum wells and nanoparticles of $Zn_{1-x}Co_xO$ by optical and transport measurements under high pressures", resume el trabajo de investigación realizado, bajo su dirección, por Dña Gloria Almonacid Caballer y constituye su Tesis para optar al grado de Doctor en Física por la Universidad de Valencia.

Y, para que aquí conste, en cumplimiento de la legislación vigente, firma el presente certificado.

Burjassot, a de de 2014

Fdo: Dr. Alfredo Segura García del Río

A mis 7 magníficos (más 2 peludos),
mis 2 angelitos de la guarda (más 2 peludos),
y mi carinyet.

Contents

Agradecimientos

Hay muchas personas a las que me gustaría agradecer personalmente el que hayan hecho posible el desarrollo y término de esta etapa, tanto científica como personalmente.

En primer lugar, quiero darle las gracias a mi director de tesis, Alfredo Segura García del Río. Primero por darme la oportunidad de conocer el mundo del estado sólido y las altas presiones incluso antes de licenciarme. Seguidamente por confiar en mí y aceptarme bajo su tutela para la elaboración de esta tesis. Y sobretodo, por todo lo que he aprendido, el tiempo que me ha dedicado y lo que me ha apoyado a la hora de colaborar con otros grupos y participar en eventos científicos, lo que ha hecho que crezca como científica y como persona.

También quiero dar las gracias a todos los miembros del departamento de Física Aplicada y Semiconductores de la Universidad de Valencia. A los profesores Julio Pellicer y Juan Francisco Sánchez Royo por lo que me han enseñado de sincrotrón y microscopia, respectivamente, y a Said Agouram por la ayuda con el TEM. Pero también a los compañeros, en especial a Juan Ángel y Javi que, tanto en persona como en la distancia me han echado una mano, pues si no estaban no han tardado en responder mis emails de *una preguntita* que, al final, suman muchas. Pero no puedo olvidarme de todos los "compis" con los que tantos ratos de laboratorio (en "la cripta") he compartido (Lorena, Javi-Posy), o de espera mientras se estabiliza el equipo (David, Jorge, Diego); todos los que han ido pasando por el despacho (Vanessa, Salva, Luis, Mauro, Pere, Erica, Braulio, Mauricio); o simplemente nos desahogábamos con un café dentro y fuera de la facultad (Nathalie, Vicent, Rosa, Miguel, Antonio, Lluis, Kumar, Enrico...)

No puedo olvidarme de los otros centros donde he tenido la suerte de trabajar y aprender tanto y, de donde me he llevado tantos amigos. En primer lugar, a todo el grupo de la Universidad de Cantabria, en Santander. Gracias a Fernando Rodríguez por acogerme y junto a Rafael Valiente y Jesús González, gracias por todo lo aprendido y todas las medidas que pude realizar en sus laboratorios. Gracias a Imanol por las medidas de magnetismo. Y, como no, a los compañeros (Cristina, Diego, Álvaro...) pero en especial a Carlos, Rosa y Susana, que además de laboratorio y enriquecedoras charlas de trabajo, hemos disfrutado de congresos y reuniones, creando una muy buena amistad.

I would like to thank the great reception received by the professor Konstantin Kamenev in CSEC (*Centre for Science at Extreme Conditions*), in Edinburgh, and let me access to all laboratories. I also want to thank Anna Kusmartseva all hours dedicated me, day after day, to teach and perfect the art (as it can not be attributed to another name) performing resistivity measurements under high pressure. To Marc and Ángel, for those meals at "Spanish time" and my colleagues and friends, César, Carina and, in particular, Ksenia, with whom I was enchanted with the city and life there.

Igualmente, agradecer la acogida en el *Laboratoire de Physique de la Matière Condensée et Nanostructures* de la Universidad de Lyon por parte del profesor Alfonso San Miguel. Je tiens à remercier mes collègues de bureau Lucas et Abraao, pour les heures qui étaient avec moi et m'a enseignement entraînement d'équipements Raman et des cellules de haute pression.

Y, por último, pero no por ello menos importante, a mi familia. A mis padres por permitirme y apoyarme a continuar en este mundo a pesar de ser tan desconocido para ellos, al igual que mis tíos, y la ayuda que me dedican cuando es posible. A mi hermano por tantos momentos compartidos, de ideas absurdas (o no tan absurdas), de nervios, de apoyo y de comprensión por encontrarse al igual que yo, llegando al final de su doctorado ¡ánimo Jaume!. Y, a Nacho, por su apoyo en todos los sentidos, sobretodo en esta última etapa, donde además de su ayuda científica, me ha hecho ver luz cuando creía que no había y ha respetado tantos días de nervios e incertidumbre, no sin antes sacarme una sonrisa. A todos, millones de gracias.

Chapter 1

Introduction

1.1 Motivation

There are many reasons to justify a thesis on semiconductors. For instance, it is important to know these materials to improve their production as well as to expand the knowledge of its structure and physical properties. The interest in semiconductors is not purely theoretical, indeed, these materials are known for their applications, mainly technological. In this Introduction, I am going to start with some basics statements, defining what is a semiconductor, describing these materials and why they are so useful. In the next section, we will also see immediate applications already studied or implemented for the specific case of ZnO and its derivatives. And finally, I will briefly describe some of the basic structural, electronic and optical properties of the material.

By definition[3], a *semiconductor* is an insulating substance which becomes conductive by the addition of certain impurities. A semiconductor is also described as an element or compound which behaves as a conductor or an insulator depending on various factors such as the electric or magnetic field, pressure, incident radiation or the temperature of the material.

Using the band theory as a starting point, which is the basis for studying the electronic structure of solids, we can define the bandgap as the energy difference between the minimum of conduction band and the maximum of valence band. A semiconductor is defined as a material with a bandgap or nonzero gap with values between a few tens of meV and a few eV. From the viewpoint of electrical properties, and consequently the electronic structure of a semiconductor, it may be defined as a material with an electrical resistivity in the range between 10^{-4} and 10^{9} ohm·cm.

Although some authors consider a material with a gap greater than 3 eV as insulating, the upper limit of the gap in the semiconductor definition

depends on the possibility that a given material can be doped or may be used as the basis for manufacturing semiconductor electronic devices. The family of semiconductor forms one of the most versatile known classes of materials. In fact, they can be found in many different chemical compositions an with a variety of crystal structures.

There is a consensus among the semiconductor community acknowledging that the great advances in solid state electronics have been made possible thanks to building semiconductor crystals in different configurations (single crystals, thin films, nanoparticles...), based on a variety of elements and compounds.

Nowadays, for example, light-emitting diodes with long wave length based on the technology of gallium arsenide (GaAs) are used worldwide. But the development of wide bandgap semiconductors would open the door to progress in optoelectronic devices emitting in the whole range of wavelengths.

For short wavelength optical devices, nitrides are considered, particularly GaN, as the most promising materials. But obtaining GaN layers of good quality is limited by the low availability of substrates[4]. This led to renewed interest in the study of the zinc oxide (ZnO), a wide bandgap semiconductor and its alloys with other divalent metal oxides which give rise to a large family of materials with wurtzite structure. In fact, the nanostructures of zinc oxide are technological materials of great importance due to their applications in solar cells, gas sensors, varistors, paintings, ceramics, cosmetics[5], laser[6], diodes and sensors[7].

ZnO also has a high compatibility when forming ternary compounds. Thus, we arrive to the *diluted magnetic semiconductors* or *DMS*. They are characterized by the replacement of a certain proportion of the cation of the semiconductor by magnetic ions thus changing the properties of the base material.

Summarizing, the physical characteristics of ZnO together with a simple, rapid and economic growth process, which does not require large and complicated infrastructure, propitiate the obtaining of a semiconductor material of good quality at low cost. In addition, its compatibility with other elements allowing the growth of ternary compounds and doping , offer a great variety in the possibilities of this material. That is, the controlled incorporation of ions in ZnO lattice allows the control of physical and electronic parameters and optical properties of the compounds, which benefits the production of specific devices.

When replacing a part of Zn for other divalents ions (alloys) or trivalent ions (doping), new materials are obtained. Their study is required to understand their structures and optical, magnetic and electronic properties.

On doing this, it can be determined the quality of the material and physical characteristics in terms of concentrations of ions incorporated as well as their applications.

Effects of quantum confinement in semiconductor nanoparticles are produced when changing the morphological configuration at nanoscale. These effects are known due to the fact that their electrical and optical properties are significantly different from the massive material, or structured on a micrometric scale. In addition new metastable phases, only observed in nanometric configurations, appear[8]. The semiconductor nanoparticles are interesting because of their basics aspects and their applications in devices. Also, they promise to have a huge and versatile utility as biomarkers[9], applications on health sciences and renewable energy[10][11].

For all the above reasons, this thesis focuses on the study of some DMSs based on ZnO with the aim to contribute to a grater understanding and increase the variety of properties in this vast field with so many applications today. Particularly, in this work we will study thin films of ZnCoO, ZnCoGaO, ZnMgO and ZnMgCoO with different concentrations of ions, and nanoparticles of ZnCoO (for different concentrations of cobalt) and we will begin the characterization of multilayers of ZnMgO/ZnCoO. To conduct our goal, we have carried on measurements with a variety of techniques such as scanning electron microscopy (SEM), Raman and infrared spectroscopy, optical absorption, and transport, resistivity, and magnetic measurements. Several of these experiments have been also performed at low and/or high temperature or high pressure, following the techniques described in the section of experimental methods.

1.2 Applications

As already mentioned, the main application of ZnO-based semiconductors is optoelectronics. This is due to its wide bandgap of 3.3 eV at room temperature and its extraordinary optical properties. For these reasons, ZnO may be an alternative to the GaN, used for the production of emitters of white, green or UV light. ZnO crystals are not only of better quality than GaN but its preparation technique is much simpler and, therefore, much cheaper allowing an easier manufacturing of the ZnO-based devices.

As a wide bandgap semiconductor, there have been promising advances in the engineering of ZnO. The energy gap is adjustable from 2.8 to 3.3 eV by introducing cadmium or from 3.3 to 4 eV by introducing magnesium in the material. This further enhances the performances of UV detectors for controlling the air quality, gas detection, military applications... The

response of these materials depends on various factor such as thickness, grain size, orientation, doping, etc. Mainly controlling the growth, as it can be dome for growing nanowires, other properties are controlled, facilitating the manufacture of micro and nano devices with significant chemical role in the sensors. The work of Kar et al.[12] describes in detail the growth control of ZnO for manufacturing nanowires and UV photodetectors based on them.

The ionization energy of the exciton, 60 meV, allows light generation both at room temperature and at high temperatures, which involves the use of ZnO in lasers in a wide range of temperatures.

Doping ZnO and controlling the doping level, the electrical properties can be changed so that a n-type semiconductor can be transformed into a degenerate semiconductor, preserving its optical transparency. This is very useful for making transparent electrodes for solar cells and panels.

According to Dietl et al.[13], ZnO is also a promising candidate for spintronic applications. These authors predict a Curie temperature < 300 K for Mn-doped ZnO. A ferromagnetic behaviour with stability at high Curie temperature was also predicted for ZnO doped with iron, cobalt and nickel. Although there are publications that confirm these predictions, there is some controversy[7][14].

Investigations are also being conducted about ZnCdO and ZnMgO heterostructures for the fabrication of photoelectrochemical[15] cells in the field of clean energy. ZnMgO is used in quantum well structures in multilayer form of ZnMgO/ZnO/ZnMgO ensuring confinement of carriers of ZnO. Since the production of these materials is easy and affordable, it is logical to incorporate to the new generation of devices for producing clean energy.

Rout et al.[16] have demonstrated that ZnO nanoparticles impregnated with Pt and/or doped with Co show a very good sensitivity for H_2 at relatively low temperature. ZnO nanoparticles sensors are stable for several cycles for long periods of time, thereby demonstrating their practical utility as sensor of H_2. Finally, Y.-z. Lv et al.[17] found that well crystallized ZnO nanorods have a higher sensitivity and selectivity to detect low concentrations of ethanol, benzene, toluene and acetone gases at temperatures of 150°C.

1.3 Material Description

The zinc oxide, ZnO, is an inorganic compound that occurs naturally as the mineral *zincite*, as we can see in figure 1.1. Although most ZnO is produced synthetically for its many applications and uses as an additive in a variety

of materials and products including plastics, lubricants[18], ceramics, glass, pigments, batteries, etc[19].

***Figure 1.1**: ZnO. Picture taken at the Natural History Museum of London.*

ZnO is a semiconductor material of the II-VI family. The electronegativity difference between zinc and oxygen produces a certain ionic character in its bonds. For this reason, ZnO is one of the more ionic compounds of such family[20]. This ionicity causes that its most stable crystalline structure is hexagonal wurtzite type. In this structure the the alternating Zn/O planes and the electrostatic attraction between them maintains the stability of the quasi-tetrahedral coordination.

ZnO has a bandgap of 3.3 eV at room temperature which can be tuned to higher or lower values by appropriate doping. It is an ideal candidate for spintronics applications, because Zn is the last of the first row transition metals, which leads to pretty high solubility of transition metals such as Co or Mn. In a diluted magnetic semiconductor, a fraction of the host atoms are substituted by the transition metal dopant ion.

ZnO has several advantages over the III-V compounds: similar band-gap energy ($\sim$ 3.5 eV); its free excitons is bound with 60 meV, higher than that of GaN ($\sim$ 28 meV); it has a native substrate; wet chemical processing is possible; and, it is more resistant to radiation damage[21].

1.3.1 Crystal structure

At ambient conditions, room temperature and pressure, the ZnO crystallizes in the wurtzite structure. The wurtzite structure has a hexagonal Bravais lattice as shown in Figure 1.2. The primitive lattice vectors ($\vec{A}_1, \vec{A}_2, \vec{A}_3$) are defined in a Euclidean space by the relationships of Equation 1.1.

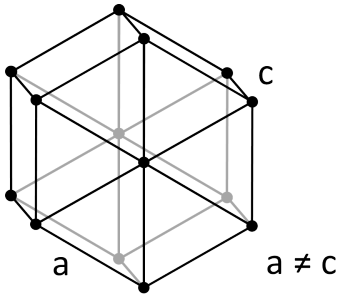

***Figure 1.2**: Hexagonal Bravais lattice.*

$$\begin{aligned} \vec{A_1} &= \frac{1}{2}a\vec{x} - \frac{\sqrt{3}}{2}a\vec{y} \\ \vec{A_2} &= \frac{1}{2}a\vec{x} + \frac{\sqrt{3}}{2}a\vec{y} \\ \vec{A_3} &= c\vec{z} \end{aligned} \tag{1.1}$$

where a and c are the lattice constants. In the case of ZnO at normal conditions, the reported values of the lattice parameters range from 3.2475 to 3.2501 $\mathring{A}$ for the a parameter and from 5.2042 to 5.2075 $\mathring{A}$ for the c parameter according to Ozgur *et al*[22]. The ZnO structure has a motive of 2 atoms of each chemical specie, two zinc and two oxygen atoms, repeating their positions along the reticular points of the Bravais lattice. The resulting structure is shown in Figure 1.3.

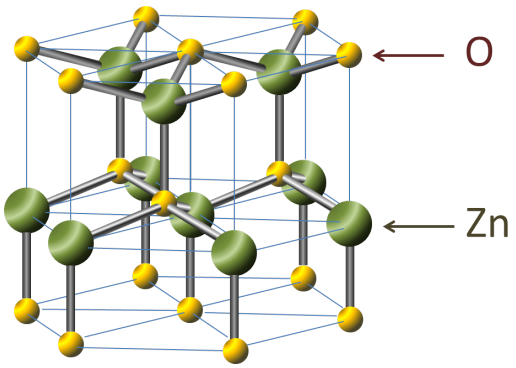

***Figure 1.3**: ZnO wurtzite structure[23].*

The spatial group of this phase is $C_{6v}^4(P6_3mc)$ with a primitive cell formed by 2 unity formulas, in which the atoms occupy the 2b sites of C_{3v} symmetry,

with a hexagonal formation. Therefore, the structure consists of tetrahedrally coordinated zinc and oxygen atoms stacked in an ABAB pattern (Fig. 1.4).

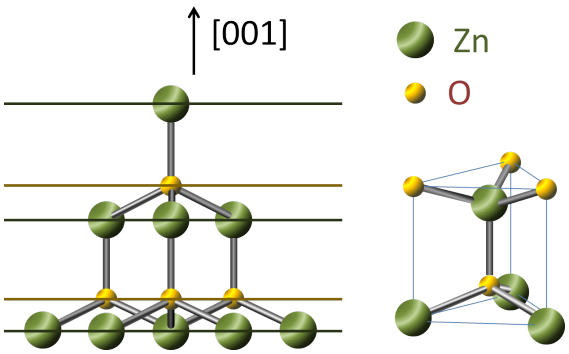

***Figure 1.4**: Pattern and tetrahedral structure of ZnO.*

Each atom is situated at the centre of a tetrahedron formed by atoms of the other element. The position of these atoms may be expressed in terms of the primitive lattice vectors, $\vec{A}_i$, in the way expressed by Equation 1.2. This is typical of sp^3 hybridized covalent bond, though this compound has non negligible ionic character. The C_{6v}^4 symmetry does not require a regular tetrahedron. The primary reason is the difference in the electronegativities between Zn and O. The deformation of this structure may be described by means of an inner parameter called u. This parameter is the ratio between the cation-anion distance along the c-axis and the lattice parameter c.

$$\begin{aligned}
\vec{Z}_1 &= \frac{1}{3}\vec{A}_1 + \frac{2}{3}\vec{A}_2 \\
\vec{Z}_2 &= \frac{2}{3}\vec{A}_1 + \frac{1}{3}\vec{A}_2 + \frac{1}{2}\vec{A}_3 \\
\vec{O}_1 &= \frac{1}{3}\vec{A}_1 + \frac{2}{3}\vec{A}_2 + u\vec{A}_3 \\
\vec{O}_2 &= \frac{2}{3}\vec{A}_1 + \frac{1}{3}\vec{A}_2 + \left(\frac{1}{2}u\right)\vec{A}_3
\end{aligned} \tag{1.2}$$

where $\vec{Z}$ and $\vec{O}$ refer to the respective positions of zinc and oxygen atoms. The u parameter in ZnO at room conditions takes a value of 0.380[24]. Comparing the value of the u for an ideal tetrahedron (u = 0.375), a small uniaxial compression in the c-direction is detected in the wurtzite ZnO. This deformation is due to the attraction between planes of cations and anions, which shows evidence of partially ionic character to its bonds and therefore

the bonding is not entirely sp^3 covalent. However, the principal bonding in wurtzite ZnO remains sp^3 covalent, which is common in tetrahedrally coordinated materials.

On forming a DMS, the lattice parameters change according to the concentration and type of TM (Transition Metal) ion that is substituting zinc. It is important to note that above a certain limit, increasing the TM concentration leads to the formation of secondary phases, at which point the simple description used up to now breaks down. Assuming the absence of secondary phases, the factor that has the greatest influence on the change in lattice constant when forming a DMS is the ionic radius of the TM.

The application of hydrostatic pressure to ZnO causes a decrease in the unit cell volume and an increase of the coulomb repulsion in chemical bonds. The decrease of interatomic distances is confirmed by the high pressure X-ray diffraction experiments performed by Recio *et al*[25]. At a given pressure, the wurtzite structure becomes unstable and it becomes energetically favourable for ZnO to assume the rocksalt structure, with a corresponding decrease in volume of about 17%[26]. In particular, the ZnO transits from wurtzite phase to rock-salt phase on the pressure up-stroke at ∼9 GPa[27]. Relaxing the pressure, ZnO recovers the wurtzite structure at ∼4 GPa[28][29]. The rock-salt structure is formed by a face-centre-cubic (FCC) Bravais lattice (Fig. 1.5) with the following primitive lattice vectors:

$$\begin{aligned} \vec{A_1} &= \frac{a}{2}(\vec{x}+\vec{y}) \\ \vec{A_2} &= \frac{a}{2}(\vec{y}+\vec{z}) \\ \vec{A_3} &= \frac{a}{2}(\vec{z}+\vec{x}) \end{aligned} \tag{1.3}$$

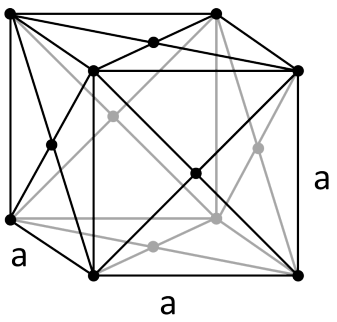

***Figure 1.5**: FCC Bravais lattice.*

The value of lattice constant at room conditions is $4.275 \pm 0.004\mathring{A}$[27]. The motive on the lattice for the ZnO consists of a cation and anion separated $a/2$, where a is the lattice parameter. The coordination of each atom is octahedral and the spatial group of this structure is O_h $(Fm\bar{3}m)$. The resulting structure can be seen in the Figure 1.6.

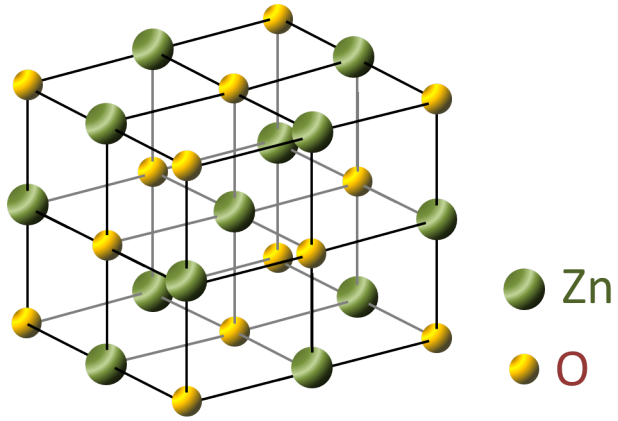

***Figure 1.6**: ZnO rock-salt structure.*

The Wigner-Seitz cell around a point is the set of the lattice points that are closer to this point than to any other. The Wigner-Seitz cell in reciprocal space is called the Brillouin zone, which is very important when the electronic states of a periodic medium are characterized in terms of Bloch wave functions. The high symmetry points in this zone are defined by a system of letters (Γ, X, L, T, etc.) which are used for the description of the band structure. The Brillouin zones corresponding to the hexagonal and FCC Bravais lattices are shown in the Figure 1.7.

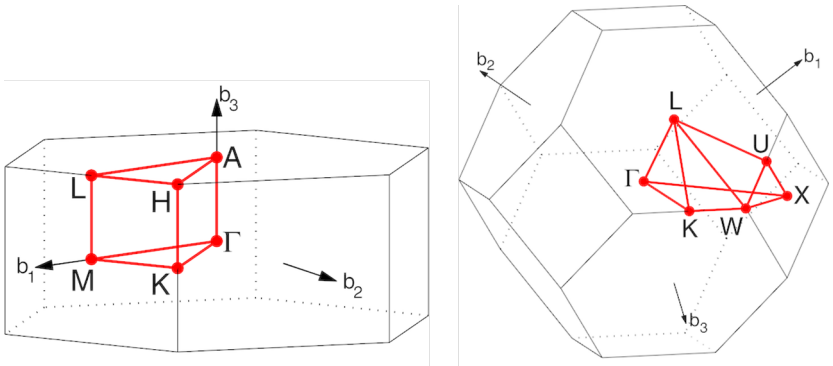

***Figure 1.7**: Brillouin zones for hexagonal Bravais lattice (left) and FCC Bravais lattice (right).*

The wurtzite electronic structure consists of three broad regions with the conduction band comprising of Zn $4s$ levels, the upper valence band of O $2p$ levels and the lower valence band of Zn $3d$ levels. There is significant hybridisation between the O $2p$ and Zn $3d$ levels due to their proximity. The lowest energy transition is located at the center of the zone, i.e. the bandgap occurs at Γ and it is a direct transition because it is produced between the same points of the zone. A typical shortcoming of the LDA (Local Density Approximation) is that it frequently underestimates the energy of the gap, which is clearly seen in this case. This is compounded by the closeness of the Zn $3d$ levels to the gap, making it necessary for these electrons to be included in the valence band[30]. However, the overestimation of their energies, shown in the Fig. 1.8, increases the repulsion from the O $2p$ levels in an effect known as $p-d$ repulsion, which shall be described later (Section 2.2.2). This closes the gap and flattens the band dispersion, distancing the theoretical effective electron and hole masses from the respective experimental values of m_e=*0.19*m_0 and m_h=*1.21*m_0[31].

The $p-d$ repulsion gives rise to a shift to higher energies of the valence band, decreasing the band-gap energy. This decrease is known as a *band-gap anomaly* and is considered as a breakdown of the *common cation rule* in the case of the ZnO.

States at the valence band maximum of semiconductors with wurtzite structure, mainly with anion p orbital character, can be described through the Hopfield quasicubic model[32]. Figure 1.8 shows a diagram of the model. The energies of the three non-degenerate states (Γ_7, Γ_9 and Γ_7)[33] depend on two parameters, the crystal field splitting Δ_C and the spin-orbit-splitting (Δ_{SO}).

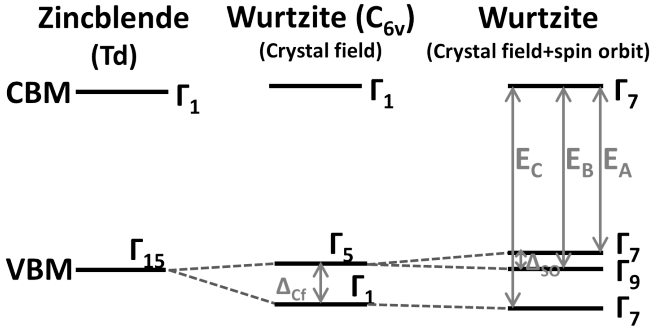

***Figure 1.8**: Diagram of the valence band split.*

In most semiconductors the upper state has Γ_9 symmetry (J=3/2) but

in ZnO, owing to the $p - d$ interaction, the spin-orbit energy is negative, which leads to an inversion of the relative position of Γ_9 and Γ_7 states. The upper state becomes the Γ_7 (J=1/2). This ordering was originally proposed by Thomas, but has been recently the object of some controversy.

Lambrecht et al.[34] published a very complete paper in 2002, in which they present the results of a first-principles band structure calculation using the linear muffin-tin orbital (LMTO) method. They concluded that the valence band ordering is most commonly assumed Γ_7 Γ_9 Γ_7. Their calculations indicate a negative spin-orbit splitting. This may depend on the position of the d bands. The arguments for their reasoning are[35]:

- The mix between p and d orbitals is of antibonding nature, for the valence band maximum, which leads to a negative contribution of the d orbitals to the spin-orbit shift. This implies that the dominant contribution to the net spin-orbit coupling is due to the role of the cation.

- The optical transition energies of the excitonic states follow the same order as that of the band ordering.

- The negative sign of the spin-orbit coupling does not change if we shift the $3d$ orbital energy between the reasonable margins in which it could be found.

1.3.2 Electronic structure

The physical property which distinguishes semiconductors from other materials is the behaviour of their electrons, in particular the existence of gaps in their electronic excitation spectra. The microscopic behaviour of electrons in a solid is most conveniently specified in terms of the *electronic band structure*[36].

Wurtzite electronic structure

Figure 1.9 shows the electronic band structure of ZnO in the wurtzite phase at ambient pressure[37] given by ab-initio pseudopotential calculations with a plane wave basis in the framework of the density functional theory (DFT) in the local-density approximation (LDA). The high symmetry points on the horizontal axis correspond to those shown in the hexagonal Brillouin zone of Figure 1.7 left.

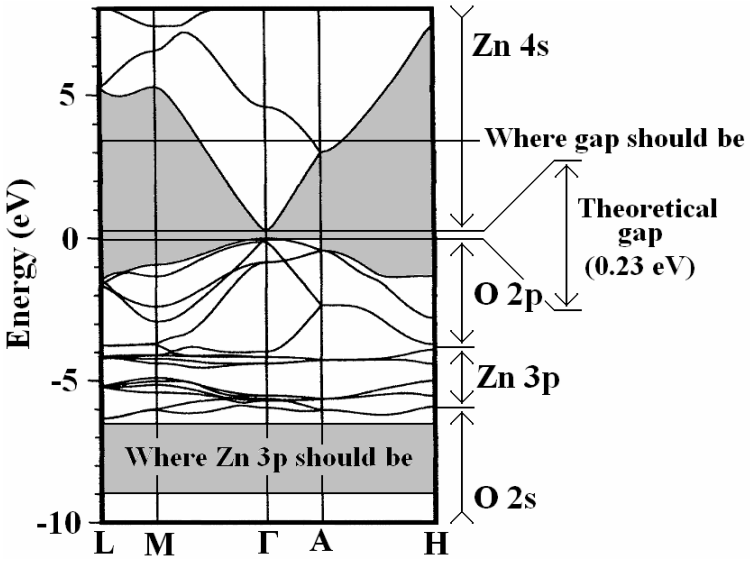

***Figure 1.9**: Electronic band structure of wurtzite ZnO.*

Rock-salt electronic structure

In the rock-salt phase, whose symmetry group includes an inversion center, the p and d orbitals belong to different representations.

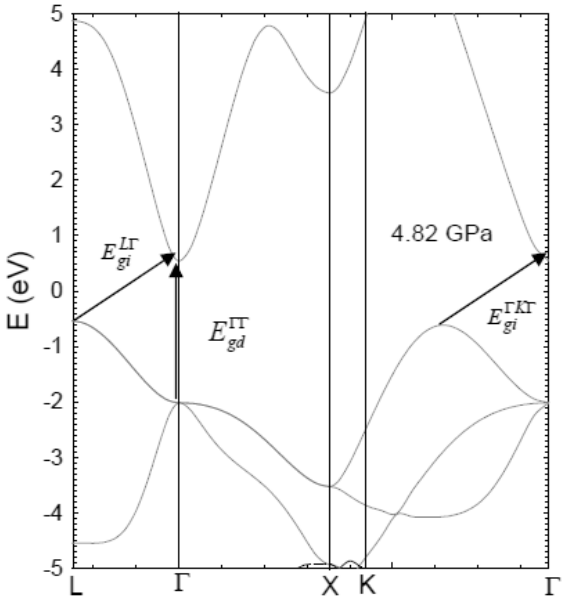

***Figure 1.10**: Band structure for rock-salt-ZnO at 4.82 GPa.*

Therefore, they cannot be mixed in points of the Brillouin zone containing inversion (Γ point). This can be shown in Figure 1.10, where the theoretical calculations carried out by A. Muñoz and M.J. Herrera-Cabrera[38] are represented for rock-salt-ZnO.

Mixing occurs between the orbitals away from the Γ point in the Brillouin zone and the resulting $p - d$ repulsion causes the p bands to shift upward, which forms a new valence band maximum at different points. Hence, the lowest energy transition between the valence band maximum and the conduction band minimum becomes an indirect transition, produced in the directions: Γ-ΓK (Σ) and Γ-L (Λ) of the Brillouin zone. We note that the band-gap energy shown in this figure is underestimated due to the use of the LDA approximation.

Chapter 2

Theory

2.1 Interaction between light and matter

The light interacts with matter in different ways. There are plenty of optical properties observed in solid state materials, which can be classified into three general phenomena: *reflection*, *propagation* and *transmission*.

Suppose that a beam of light incides in a material, some part of this light will be reflected on the first surface (entrance surface) of the material, while the other part descends, spreading through it. When it reaches the near surface surface, part of the light will be reflected and the rest will be transmitted to the outside. A scheme of the above phenomena is shown in Figure 2.1.

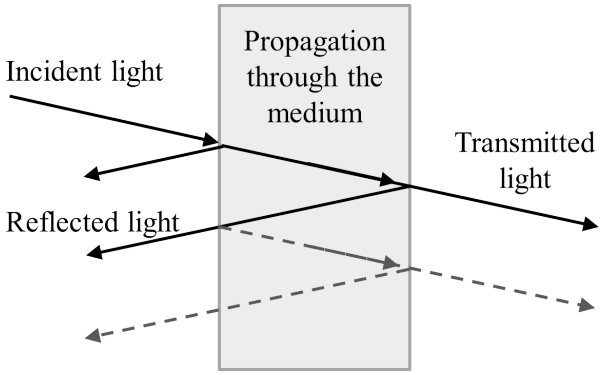

***Figure 2.1**: Scheme of optical processes resulting from the interaction of a beam of light with an optical medium.*

It should be borne in mind also that during the propagation of light through the material, and within the framework of linear optics, *refraction*

phenomena, *absorption*, *luminescence* and *scattering* occur (Fig. 2.2)[39]. *Refraction* is caused by a reduction in the velocity of the wave, while *absorption* causes attenuation. Luminescence can accompany absorption if the excited atoms re-emit by spontaneous emission. *Scattering* causes a redirection of the light. In the Figure 2.2 we can see all these phenomena. The diminishing width of the arrow for the processes of absorption and scattering represents the attenuation of the beam.

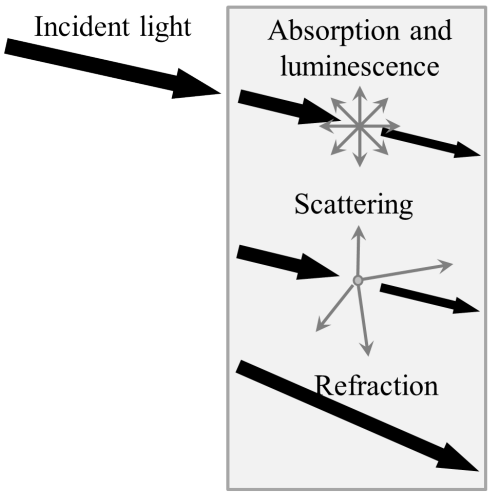

***Figure 2.2**: Scheme of linear optical processes when a light beam propagates through an optical medium.*

The optical phenomena described here can be quantified from a macroscopic viewpoint by certain parameters that determine the properties of the medium. The reflection coefficient or *reflectivity*, **R**, describe the *reflection* that occurs on the surfaces of the medium. Thus, if $\mathbf{\Phi_0}$ is the incident flux and $\mathbf{\Phi_R}$ is the flux reflected, this ratio is defined as:

$$R = \frac{\Phi_R}{\Phi_0} \tag{2.1}$$

In the same way, if $\mathbf{\Phi_T}$ is the transmitted light flux, the transmission coefficient or *transmittance*, **T**, is defined as:

$$T = \frac{\Phi_T}{\Phi_0} \tag{2.2}$$

In addition to the phenomena that occurs on the surfaces of the material, what happens inside it should be considered. The propagation of the beam

through a transparent medium is described using the *refractive index*, **n**, which is defined as:

$$n = \frac{c}{v} \tag{2.3}$$

where **c** is the velocity of light in vacuum, and **v** is the velocity of the light in the medium. The refraction index depends on the frequency of the incident light, a phenomenon known as chromatic dispersion. Along the beam path through the medium, the luminous flux decreases. This phenomenon is called *extinction* due to absorption and scattering. These are defined jointly by the *absorption coefficient*, $\boldsymbol{\alpha}$. It is defined by the Beer's law in Equation 2.4:

$$\begin{gathered} \Phi(z) = \Phi(z=0)e^{-\alpha z} = \Phi_0 e^{-\alpha z} \\ with \qquad \Phi(z=0) = \Phi_0 \end{gathered} \tag{2.4}$$

where $\boldsymbol{\Phi(z=0)}$ is the luminous flux at the entrance of the medium (optical intensity at $z = 0$). The absorption coefficient depends heavily on the frequency, $\boldsymbol{\omega}$, so that the optical material may absorb each colour in a different way. Both, the absorption coefficient and the refractive index can be incorporated into a single optical parameter: the *complex refractive index*, $\tilde{\mathbf{n}}$. This index characterizes the macroscopic optical properties of an isotropic medium and it is defined as:

$$\tilde{n}(\omega) = n(\omega) + i\kappa(\omega) \tag{2.5}$$

where $\mathbf{n}(\boldsymbol{\omega})$ is the refractive index, while $\boldsymbol{\kappa(\omega)}$ is called *extinction coefficient*, which is directly related to the absorption coefficient, $\boldsymbol{\alpha(\omega)}$. These relationships can be easily obtained by the interpretation of light as a plane electromagnetic wave, incident in the z-direction and propagating through a material medium with a complex refractive index. The electric field, $\vec{\mathbf{E}}$, and the magnetic field, $\vec{\mathbf{H}}$ are:

$$\vec{E}(z,t) = \vec{E}_0 e^{i[k(\omega)z - \omega t]} \tag{2.6}$$

$$\vec{H}(z,t) = \vec{H}_0 e^{i[k(\omega)z - \omega t]} \tag{2.7}$$

where **k** is the wave vector of the light and $|\mathbf{E_0}|$ and $|\mathbf{H_0}|$ are the amplitudes at $z = 0$. In the generalized case of an absorbing medium, $\mathbf{k}(\boldsymbol{\omega})$ and $\boldsymbol{\omega}$ are related by the complex refractive index:

$$k(\omega) = \tilde{n}(\omega)\frac{\omega}{c} = \tilde{n}(\omega)k_0 = (n(\omega) + i\kappa(\omega))\,k_0 \tag{2.8}$$

$$with \qquad k_0 = \frac{\omega}{c} \tag{2.9}$$

Combining equations 2.6 and 2.8, we obtain:

$$\vec{E}(z,t) = \vec{E}_0 e^{i[\tilde{n}(\omega)\frac{\omega}{c}z - \omega t]} = \vec{E}_0 e^{-\kappa(\omega)k_0 z} e^{i[n(\omega)k_0 z - \omega t]} \tag{2.10}$$

Clearly this is a damped plane wave which propagates with a phase velocity: $v = c/n$. Given that the luminous flux is proportional to the Poynting vector and, consequently, to the square of the magnitude of the electric field:

$$\Phi(z) = |\vec{E} \times \vec{H}^*| = \Phi_0 e^{-2\kappa(\omega)k_0 z} = \Phi_0 e^{-\frac{2\kappa(\omega)\omega}{c}z} \tag{2.11}$$

Comparing Equations (2.4) and (2.11) we find that the absorption coefficient is:

$$\alpha(\omega) = \frac{2\kappa(\omega)\omega}{c} = \frac{4\pi\kappa(\omega)}{\lambda} \tag{2.12}$$

where $\boldsymbol{\lambda}$ is the wavelength of the light.

From the complex refractive index, according to the Fresnel equations, we can determine the reflectivity of the material. At normal incidence of light on a medium with index $\mathbf{n_0}$, the *reflection coefficient* is given by:

$$R = \left|\frac{\tilde{n} - n_0}{\tilde{n} + n_0}\right|^2 \tag{2.13}$$

If the incident medium is the air, $n_0 = 1$. Then:

$$R = \left|\frac{\tilde{n} - 1}{\tilde{n} + 1}\right|^2 = \frac{(n-1)^2 + \kappa^2}{(n+1)^2 + \kappa^2} \tag{2.14}$$

From the reflectivity and absorption coefficient, the transmissivity of a medium, as shown in the Figure 2.1, is given by:

$$T = (1 - R_1)e^{-\alpha d}(1 - R_2) \tag{2.15}$$

where $\mathbf{R_1}$ and $\mathbf{R_2}$ are the reflectivities of the front and back surfaces respectively, and $\mathbf{d}$ the medium thickness. If both surfaces have equal reflectivities $\mathbf{R}$, and if we neglect multiple reflections, the Equation 2.16 simplifies to:

$$T = (1 - R)^2 e^{-\alpha d} \tag{2.16}$$

In the regime of linear absorption, an exponential decrease in the transmitted flux occurs until it is completely absorbed at distances larger that $1/\alpha$. Hence the reflectivity, $\mathbf{R}$, and the absorption, $\boldsymbol{\alpha}$, are intrinsic parameters of the material, which are related by the *dielectric function*. I.e. the response of a material in the presence of an electromagnetic field can be described by the *complex dielectric function*, $\boldsymbol{\varepsilon}$, expressed as:

$$\varepsilon = \varepsilon_1 + i\varepsilon_2 \tag{2.17}$$

And it is defined in the following way:

$$\varepsilon = \tilde{n}^2 \tag{2.18}$$

In this way, the real and imaginary parts of the dielectric function would be as follows:

$$\begin{aligned} \varepsilon_1 &= n^2 - \kappa \\ \varepsilon_2 &= 2n\kappa \end{aligned} \tag{2.19}$$

2.1.1 Direct absorption

The bandgap of a semiconductor is defined as the energy difference between the maximum of the valence band and the minimum of the conduction band. In a direct semiconductor these two points are at the same value of $\mathbf{k}$. The basic process for an optical transition across the fundamental band gap of a direct gap semiconductor is shown in the Figure 2.3. An electron is excited from the valence band to the conduction band by absorption of a photon ($\hbar\omega$).

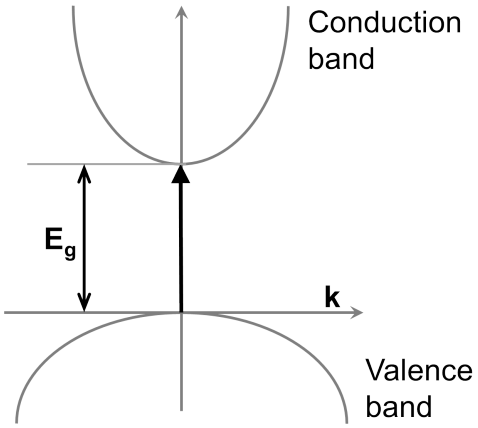

***Figure 2.3**: Direct absorption.*

We may consider the simple case of parabolic form for the bands (figure 2.3). Then, the energy difference $\mathbf{E_{cv}}$ in the vicinity of the energy gap is expressed as:

$$E_{cv} = E_g + \frac{\hbar^2 k^2}{2\mu} \tag{2.20}$$

where $\boldsymbol{\mu}$ is the reduce effective mass of the bands defined by $\mu^{-1} = m_c^{-1} + m_v^{-1}$. It will be assumed that the electric dipole approximation is applicable. By means of the Maxwell theory, the energy loss through the medium may be calculated. This value is obtained using the equation 2.21:

$$\alpha(\hbar\omega) = \frac{\pi e^2}{\varepsilon_0 m^2 c n \hbar\omega} \sum_k |P_{cv}| \delta(E_{cv}(k) - \hbar\omega) \tag{2.21}$$

If we consider that the dipole matrix element is equal to its value at the minimum, the probability density may be removed from the integral:

$$\alpha(\hbar\omega) = \frac{\pi e^2}{\varepsilon_0 m^2 c n \hbar\omega} |P_{cv}| \sum_k \delta(E_{cv}(k) - \hbar\omega) \tag{2.22}$$

Defining the joint density of states as[36]:

$$D_j(E_{cv}) = \frac{1}{4\pi^3} \int \frac{\mathrm{d}S_k}{|\nabla(E_{cv})|} \tag{2.23}$$

In the case of electric dipole direct absorption:

$$D_j(E_{cv}) = \begin{cases} \left[\frac{2^{1/2}\mu^{3/2}}{\pi^2\hbar^3}\right]\sqrt{E_{cv}-E_g} & \text{when} \quad E_{cv} > E_g \\ 0 & \text{when} \quad E_{cv} < E_g \end{cases} \tag{2.24}$$

Then, the absorption coefficient can be written as:

$$\alpha(\hbar\omega) = \begin{cases} A\sqrt{(\hbar\omega - E_g)} & \text{when} \quad \hbar\omega > E_g \\ 0 & \text{when} \quad \hbar\omega < E_g \end{cases} \tag{2.25}$$

where **A** is a constant.

2.1.2 Indirect absorption

When the maximum of the valence band does not coincide in K^3 space with the minimum of the conduction band, a direct transition is not possible. In this case, indirect transition takes place.

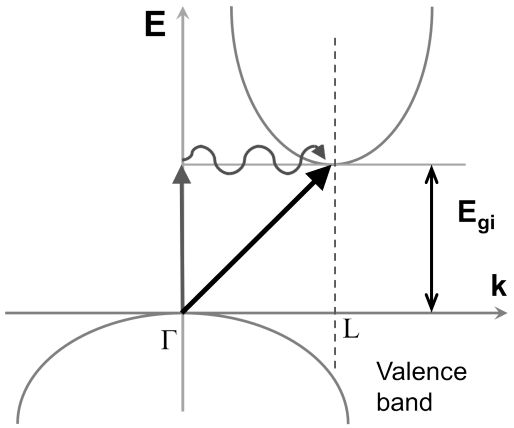

***Figure 2.4**: Indirect absorption.*

If the lowest energy gap is indirect (Figure 2.4), a photon can excite an electron from the valence band to the conduction band with the assistance of a phonon to satisfy momentum conservation. The wavevector difference between the electrons in the two bands is supplied by the phonon. There are two possible ways that this can be done, as the electron can absorb or emit phonons. Therefore, in order to obey the conservation of energy and momentum, the following equations must be satisfied:

$$\hbar\omega = E_{cv} \pm E_{ph} \tag{2.26}$$

$$\vec{k_v} - \vec{k_c} = \pm\vec{q} \tag{2.27}$$

where $\mathbf{E_{ph}}$ is the phonon energy, $\vec{\mathbf{q}}$ is its wave vector and $\vec{\mathbf{k_v}}$ and $\vec{\mathbf{k_c}}$ are the respective wave vectors of the maximum valence band and the minimum conduction band. The "-" and "+" signs correspond to the respective emission and absorption of phonons.

The indirect transition may be considered as a process in two steps. First, the electron is excited by photon absorption to an intemediate state by means of a virtual transition. In a second virtual transition, the electron goes from the intermediate state, $|\boldsymbol{i}\rangle$, to $\mathbf{E_c(L)}$ (according to Figure 2.4) by means of the creation or annihilation of a phonon, leaving a hole in $\mathbf{E_v(\Gamma)}$.

Applying the definition of the joint density of states (eq. 2.23) yields:

$$\alpha(\hbar\omega) = \begin{cases} B\left[n\left(\hbar\omega + E_{ph} - E_{gi}\right)^2 + (n+1)\left(\hbar\omega - E_{ph} - E_{gi}\right)^2\right] \\ \qquad\qquad\qquad\qquad \text{when} \quad \hbar\omega \geq E_{gi} + E_{ph} \\ 0 \qquad\qquad\qquad\qquad \text{when} \quad \hbar\omega < E_{gi} + E_{ph} \end{cases} \tag{2.28}$$

where $\mathbf{B}$ is a constant. All transitions shown in the previous sections are easily identified by inspecting the absorption edge of a semiconductor. However, the obtained expressions are only true if the electrostatic interaction between the hole and electron is neglected. Otherwise, different states, known as excitonic states, must be considered.

2.1.3 Excitonic absorption

An *exciton* is a quasi-particle formed by a free electron and a free hole interacting through the Coulomb force. This electron-hole pair has less energy than the sum of the energies of the two separate particles and it may move through the crystal and transmit energy, while keeping its neutral charge.

To study the behaviour of the exciton, the Wannier description[40] shall be used, which is derived from the Schrödinger equation for two particles (electron and hole).

$$\vec{\Psi}E = \vec{\Psi}\left(\frac{\vec{p_c}^{\,2}}{2m_c} + \frac{\vec{p_v}^{\,2}}{2m_v} - \frac{e^2}{\varepsilon|r_e - r_h|}\right) \tag{2.29}$$

This equation is separable in the following coordinates:

$$\begin{aligned} \vec{r} = & \quad \vec{r_e} - \vec{r_h} \\ \vec{R} = & \quad \frac{m_c\vec{r_e} + m_v\vec{r_h}}{m_c + m_v} \end{aligned} \tag{2.30}$$

Taking the reduced mass $\mathbf{m_r}$, the Schrödinger equation becomes the wave equation for a hydrogenic atom. There are two solutions to this equation at a critical point. On one hand, a solution corresponding to the non-bound states is found and, on the other, we obtain a solution for the set of bound states at each value of $\vec{k} = \vec{k_c} - \vec{k_v}$, with energies of:

$$E_n(\vec{k}) = E_g - \frac{m_r e^4}{2\hbar^2\varepsilon^2 n^2} + \frac{\hbar^2\vec{k}^2}{2(m_c + m_v)} = E_g - \frac{R}{n^2} + \frac{\hbar^2\vec{k}^2}{2(m_c + m_v)} \tag{2.31}$$

For direct transitions ($\vec{k} = \vec{0}$), a quantised set of states is obtained which the exciton can occupy. These bound states form a discrete spectrum which, for low kinetic energy values, are situated in the forbidden band so the absorption peaks are at lower energies than the bandgap.

The solution for non-bound states is:

$$E_n\vec{k} = E_g + \frac{\hbar^2\vec{k}^2}{2(m_c + m_v)} + \frac{\hbar^2(\frac{1}{2}(\vec{k_c} + \vec{k_v}))^2}{2m_r} \tag{2.32}$$

The existence of these states gives rise to considerable changes in the absorption edge, which were calculated by Elliot in 1957[41]. From these states, the continuum spectrum of the Coulomb interaction may be obtained, modifying the shape of the wave functions and producing a change in the matrix elements of the electron-photon interaction. The absorption edge is altered in the following way:

$$\alpha_1 = \alpha_0 \frac{\gamma e^\gamma}{\sinh(\gamma)} \qquad \text{where} \qquad \gamma = \pi\sqrt{\frac{R}{\hbar\omega - E_g}} \tag{2.33}$$

where $\boldsymbol{\alpha_0}$ is the absorption edge without excitonic effects and $\boldsymbol{\alpha_1}$ is the corrected absorption edge.

In a real semiconductor, all states have a finite lifetime, due to the electron-phonon interaction and electronic defects. This interaction produces the broadening of absorption peaks. In the case of weak coupling[41], the

shape of the broadening function is Lorentzian and the expression is given by equation 2.34. In the case of strong coupling, the shape of the broadening function is Gaussian[42].

$$\alpha_d(E) = C\frac{\sqrt{R}}{E}\left[\sum_{i=1}^{\infty}\frac{2R}{i^3}\frac{\Gamma_i/2 + b(E-E_i)}{(\Gamma_i/2)^2 + (E-E_i)^2} + \right.$$
$$\left. + \int_{E_{gd}}^{\infty}\frac{\Gamma_c/2}{(\Gamma_c/2)^2 + (E'-E_i)^2}\frac{\mathrm{d}E'}{\sqrt{1+\exp(-2\pi\gamma)}}\right] \tag{2.34}$$

where $\mathbf{\Gamma_i}$ and $\boldsymbol{E_i}$ are the respective width and energy of the i-indexed exciton, $\mathbf{\Gamma_c}$ is the width of the continuum and $\mathbf{C}$ is the absorption oscillator strength. This integral may be solved in the complex plane, obtaining an analytical expression[43]. Although the binding energy may be weak at room temperature and peaks from the discrete spectrum may not be observed, the effect of the continuum still modifies the absorption edge.

With regards to the electron-phonon interaction, the Lorentzian shape may be substituted by a Gaussian shape, as previously mentioned, in agreement with Toyozawa's prediction[42] for strong exciton-phonon coupling.

2.1.4 Charge Transfer Absorption

Transitions from localized levels (associated to impurities or defects) to extended states in semiconductor bands are in principle possible if the dipolar matrix element between both states is not zero (in which case the transition is forbidden).

Let us remind that in the presence of an electromagnetic wave the time-independent perturbation Hamiltonian is given by:

$$H^l = i\frac{e\hbar}{m}\vec{A}_0 \cdot \nabla \tag{2.35}$$

Where $\mathbf{\vec{A}_0}$ is the amplitude of the vector potential of the electromagnetic wave. In this deduction we will also neglect the spatial dependence as the photon wavevector is much smaller than the one of the electron. The matrix element of the transition is:

$$H_{loc,c} = \int \Phi^*_{loc}(\vec{r}) i\frac{e\hbar}{m}\vec{A}_0 \cdot \nabla \Psi_{c\vec{k}}(\vec{r})\mathrm{d}v \tag{2.36}$$

Where $\mathbf{\Phi_{loc}}$ is the wave function of the electron in the fundamental state of the localized level and $\mathbf{\Psi_{loc}}$ is the wave function of the electron in the conduction band. In the effective mass approximation.

$$\begin{aligned} H_{loc,c} &= \int \Phi^*_{loc}(\vec{r}) i\frac{e\hbar}{m}\vec{A}_0 \cdot \nabla C e^{i\vec{k}\cdot\vec{r}} \mathrm{d}v = iC\frac{e\hbar}{m}\int \Phi^*_{loc}(\vec{r}) i\vec{A}_0 \cdot \vec{K} e^{i\vec{k}\cdot\vec{r}} \mathrm{d}v = \\ &= -C\frac{e\hbar}{m}\vec{A}_0 \cdot \vec{k}\int \Phi^*_{loc}(\vec{r}) e^{i\vec{k}\cdot\vec{r}} \mathrm{d}v \end{aligned} \tag{2.37}$$

The matrix element is then proportional to the Fourier transform of the localized state wavefunction, i.e., its wavefunction in the $\vec{k}$ space.

Hydrogenic-like localized wavefunction

Let us first assume that the localized state has an s-like wavefunction. In this case:

$$\Phi_{loc}(\vec{r}) = \frac{\chi^{3/2}}{\sqrt{\pi}} e^{-\chi r} \tag{2.38}$$

Its Fourier transform can be easily calculated:

$$\Phi_{loc}(\vec{k}) = \frac{\chi^{3/2}}{\sqrt{\pi}} \frac{8\pi\chi}{(\chi^2 + k^2)^2} \tag{2.39}$$

Then the matrix element is:

$$H_{loc,c} = -C\frac{e\hbar}{m}\vec{A}_0 \cdot \vec{k}\frac{\chi^{3/2}}{\sqrt{\pi}} \frac{8\pi\chi}{(\chi^2 + k^2)^2} = -C\frac{8\pi e\hbar}{m}\vec{A}_0 \cdot \vec{k}\frac{\chi^{5/2}}{(\chi^2 + k^2)^2} \tag{2.40}$$

The transition probability by unit time is given by Fermi's golden rule:

$$\begin{aligned} W_{loc,c} &= \frac{2\pi}{\hbar} |H_{loc,c}|^2 \, \delta\left[E_C(\vec{k}) - E_{loc} - \hbar\omega\right] = \\ &= Cte \times A_0^2 \frac{\chi^5 k^2}{(\chi^2 + k^2)^4} \delta\left[E_C(\vec{k}) - E_{loc} - \hbar\omega\right] = \\ &= Cte \times A_0^2 \frac{\chi^5 k^2}{(\chi^2 + k^2)^4} \delta\left[E_C(0) + \frac{\hbar^2 k^2}{2m^*} - E_{loc} - \hbar\omega\right] \end{aligned} \tag{2.41}$$

The number of transitions per unit time and volume can be calculated by integrating over all values of k that fulfil the energy conservation condition:

$$N_{loc,c} = \int_0^\infty Cte \times A_0^2 \frac{\chi^5 k^2}{(\chi^2+k^2)^4} \delta \left[E_C(0) + \frac{\hbar^2 k^2}{2m^*} - E_{loc} - \hbar\omega \right] 4\pi k^2 \mathrm{d}k \quad (2.42)$$

We can change the variable in the Dirac's delta:

$$\begin{aligned} N_{loc,c} &= \int_0^\infty Cte \times A_0^2 \frac{\chi^5 k^2}{(\chi^2+k^2)^4} \delta \frac{[k-k_0]}{\hbar k/m^*}] 4\pi k^2 \mathrm{d}k = \\ &= Cte \times A_0^2 \frac{\chi^5 k_0^3}{(\chi^2+k_0^2)^4} \end{aligned} \quad (2.43)$$

Where k_0 fulfils $E_C(0) + \dfrac{\hbar^2 k^2}{2m^*} = E_{loc} + \hbar\omega$

$$k_0^2 = \frac{2m^*}{\hbar^2}\left[\hbar\omega - (E_C(0) - E_{loc})\right] = \frac{2m^*}{\hbar^2}\left[\hbar\omega - E_i\right] \quad (2.44)$$

where $\mathbf{E_i}$ is the minimum photon energy for the transition (onset of the absorption band).If we put the photon flux as the Poynting vector divided by the photon energy:

$$\Phi_0 = \frac{\left|\vec{S}\right|}{\hbar\omega} = \frac{1}{2\hbar\mu_0} A_0^2 \kappa = \frac{\omega A_0^2}{2cn\hbar\mu_0} \quad \Longrightarrow \quad A_0^2 = \frac{2cn\hbar\mu_0}{\omega}\Phi_0 \quad (2.45)$$

$$N_{loc,c} = Cte \times \frac{2cn\hbar\mu_0}{\omega}\Phi_0 \frac{\chi^5 k_0^3}{\left(\chi^2+k_0^2\right)^4} \quad (2.46)$$

The absorption coefficient is proportional to the quantity multiplying the photon flux:

$$\alpha = Cte \times \frac{\chi^5 \left(\hbar\omega - E_i\right)^{3/2}}{\left(\chi^2 + \dfrac{2m^*}{\hbar^2}\left(\hbar\omega - E_i\right)\right)^4} \quad (2.47)$$

That can be also expressed as:

$$\alpha = Cte \times \frac{(\hbar\omega - E_i)^{3/2}}{\left(\frac{\hbar^2\chi^2}{2m^*} + (\hbar\omega - E_i)\right)^4} = Cte \times \frac{(\hbar\omega - E_i)^{3/2}}{(E_{kin} + (\hbar\omega - E_i))^4} \quad (2.48)$$

The equation has been rewritten by interpreting the first term in the denominator as the confinement kinetic energy of an electron in the localized level. For photon energies close to the threshold energy $\mathbf{E_i}$, $\boldsymbol{\alpha}$ grows as $(\hbar\omega - E_i)^{3/2}$. For larger energies, α tends to zero as $(\hbar\omega - E_i)^{-5/2}$. To calculate the photon energy at which the maximum occurs we calculate the derivative, and impose it to be zero. The numerator must be zero:

$$\frac{3}{2}(\hbar\omega - E_i)^{1/2}(E_{kin} + (\hbar\omega - E_i))^4 - 4(E_{kin} + (\hbar\omega - E_i))^3(\hbar\omega - E_i)^{3/2} = 0$$

Then

$$E_{kin} + (\hbar\omega - E_i) = \frac{8}{3}(\hbar\omega - E_i) \quad \Longrightarrow \quad \hbar\omega_{max} = E_i + \frac{3}{5}E_{kin} \quad (2.49)$$

We can give a more compact expression by introducing a normalized photon energy

$$u = \hbar\omega_{max}/E_i \qquad \text{and} \qquad u_{kin} = E_{max}/E_i \quad (2.50)$$

$$\alpha = Cte \times \frac{(u-1)^{3/2}}{(u_{kin} + u - 1)^4} \quad (2.51)$$

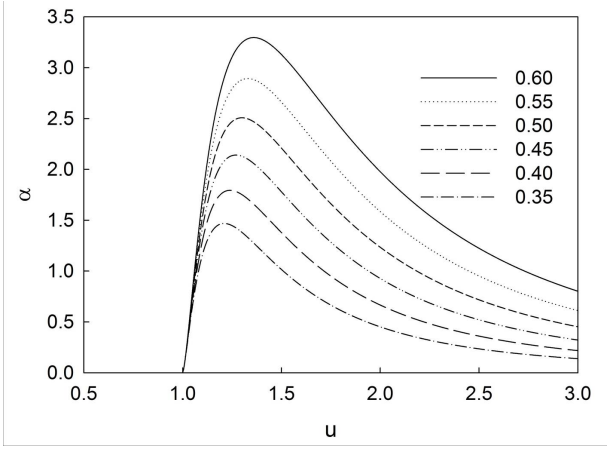

***Figure 2.5**: Absorption spectrum for different values of $\boldsymbol{u_{kin}}$.*

The Figure 2.5 shows the absorption spectrum for different values of u_{kin}. The maximum occurs for $u_{max} = 1 + \frac{3}{5}u_{kin}$. It can be also easily shown that the width at half maximum is of the order of $2u_{kin}$.

Gaussian localized wavefunction

Let us first assume that the localized state has gaussian wavefunction. In this case:

$$\Phi_{loc}(\vec{r}) = C_1 e^{-\chi^2 r^2} \tag{2.52}$$

Its Fourier transform can also be calculated:

$$\begin{aligned}\int \Phi^*_{loc}(\vec{r}) e^{i\vec{k}\cdot\vec{r}} \mathrm{d}v &= C_1 \int e^{-\chi^2 r^2} e^{i\vec{k}\cdot\vec{r}} \mathrm{d}v = C_i \int_0^\infty e^{-\chi^2 r^2} 2\pi r^2 \mathrm{d}r \int_0^\pi e^{ikr\cos\theta} \sin\theta \mathrm{d}\theta = \\ &= C_i \int_0^\infty e^{-\chi^2 r^2} 2\pi r^2 \mathrm{d}r \left[\frac{e^{ikr\cos\theta}}{ikr}\right]_0^\pi = \\ &= \frac{2\pi C_1}{ik} \int_0^\infty r e^{-\chi^2 r^2} \left(e^{ikr} - e^{-ikr}\right) \mathrm{d}r = \frac{4\pi C_1}{i\chi} 2e^{-k^2/\chi^2}\end{aligned} \tag{2.53}$$

Then the matrix element is

$$H_{loc,c} = -C\frac{e\hbar}{m}\vec{A}_0 \cdot \vec{k} \frac{4\pi C_1}{i\chi} 2e^{-k^2/\chi^2} = Cte \times A_0 k e^{-k^2/\chi^2} \tag{2.54}$$

The transition probability by unit time is given by Fermi's golden rule:

$$\begin{aligned}W_{loc,c} &= \frac{2\pi}{\hbar}|H_{loc,c}|^2 \delta\left[E_C(\vec{k}) - E_{loc} - \hbar\omega\right] = \\ &= Cte \times A_0^2 k^2 e^{-2k^2/\chi^2} \delta\left[E_C(\vec{k}) - E_{loc} - \hbar\omega\right] = \\ &= Cte \times A_0^2 k^2 e^{-2k^2/\chi^2} \delta\left[E_C(0) + \frac{\hbar^2 k^2}{2m^*} - E_{loc} - \hbar\omega\right]\end{aligned} \tag{2.55}$$

The number of transitions per unit time and volume can be calculated by integrating over all values of k that fulfil the energy conservation condition:

$$N_{loc,c} = \int_0^\infty Cte \times A_0^2 k^2 e^{-2k^2/\chi^2} \delta \left[E_C(0) + \frac{\hbar^2 k^2}{2m^*} - E_{loc} - \hbar\omega \right] 4\pi k^2 \mathrm{d}k \quad (2.56)$$

We can change the variable in the Dirac's delta:

$$N_{loc,c} = \int_0^\infty Cte \times A_0^2 k^2 e^{-2k^2/\chi^2} \frac{\delta\left[k - k_0\right]}{\hbar k/m^*} 4\pi k^2 \mathrm{d}k = Cte \times A_0^2 k^3 e^{-2k_0^2/\chi^2} \quad (2.57)$$

Where k_0 fulfils $E_C(0) + \dfrac{\hbar^2 k_0^2}{2m^*} = E_{loc} + \hbar\omega$

$$k_0^2 = \frac{2m^*}{\hbar^2}\left[\hbar\omega - (E_C(0) - E_{loc})\right] = \frac{2m^*}{\hbar^2}\left[\hbar\omega - E_i\right] \quad (2.58)$$

where $\mathbf{E_i}$ is the minimum photon energy for the transition (onset of the absorption band). If we put the photon flux as the Poynting vector divided by the photon energy.

$$\Phi_0 = \frac{\left|\vec{S}\right|}{\hbar\omega} = \frac{1}{2\hbar\mu_0} A_0^2 \kappa = \frac{\omega A_0^2}{2cn\hbar\mu_0} \quad \Longrightarrow \quad A_0^2 = \frac{2cn\hbar\mu_0}{\omega}\Phi_0 \quad (2.59)$$

$$N_{loc,c} = Cte \times \frac{2cn\hbar\mu_0}{\omega}\Phi_0 k_0^3 e^{-2k_0^2/\chi^2} \quad (2.60)$$

The absorption coefficient is proportional to the quantity multiplying the photon flux:

$$\begin{aligned} \alpha \; &= Cte \times \left(\frac{2m^*}{\hbar^2}\left[\hbar\omega - E_i\right]\right)^{\frac{3}{2}} e^{-\frac{2\frac{2m^*}{\hbar^2}\left[\hbar\omega - E_i\right]}{\chi^2}} = \\ &= Cte \times \left(\hbar\omega - E_i\right)^{\frac{3}{2}} e^{-\frac{2\left[\hbar\omega - E_i\right]}{E_{kin}}} \end{aligned} \quad (2.61)$$

The equation has been rewritten by interpreting the term in the exponent denominator as the confinement kinetic energy of an electron in the localized level. For photon energies close to the threshold energy $\mathbf{E_i}$, $\boldsymbol{\alpha}$ grows as $(\hbar\omega - E_i)^{3/2}$, as in the previous case. For larger energies, $\boldsymbol{\alpha}$ tends to zero exponentially.

To calculate the photon energy at which the maximum occurs we calculate the derivative, and impose it to be zero.

$$\frac{3}{2}\left(\hbar\omega - E_i\right)^{1/2} e^{-\frac{2[\hbar\omega - E_i]}{E_{kin}}} - \left(\hbar\omega - E_i\right)^{3/2} \frac{2}{E_{kin}} e^{-\frac{2[\hbar\omega - E_i]}{E_{kin}}} = 0$$

Then

$$\hbar\omega_{max} = E_i + \frac{3}{4}E_{kin} \tag{2.62}$$

Again can give a more compact expression by introducing a normalized photon energy, equation 2.50,

$$\alpha = Cte \times (u-1)^{3/2} e^{-\frac{2(u-1)}{u_{kin}}} \tag{2.63}$$

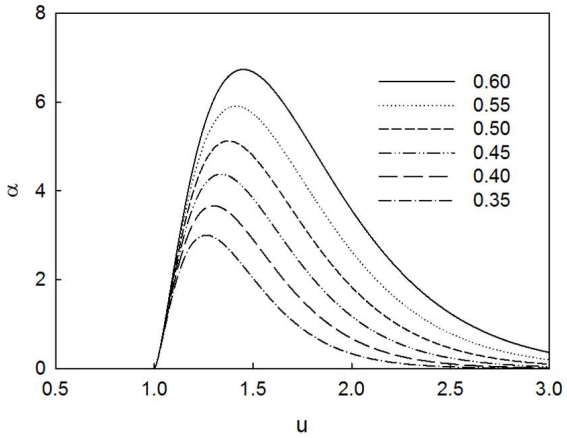

***Figure 2.6**: Absorption spectrum for different values of* $\boldsymbol{u_{kin}}$.

The figure shows the absorption spectrum for different values of u_{kin}. The maximum occurs for $u = 1 + \frac{3}{4}u_{kin}$. It can also be easily shown that the width at half maximum is of below $2u_{kin}$. If we compare the spectra for hydrogenic or Gaussian localization, it is clear that the former are more asymmetric and the maximum occurs at lower energies from the onset. This means that, once the spectra are convoluted with a Gaussian line shape (to take into account scattering processes in the conduction band), Gaussian localization will give better account of the Gaussian shape of the experimental spectra of charge transfer transitions.

The effect of doping

When the semiconductor is degenerate, the states between the CBM and the Fermi level are occupied and then transitions (either from the valence band or the localized states are no longer possible). This can be taken into account simply by making the intensity of the transition proportional to the probability that the final state is empty. The absorption coefficient will be zero for photon energies below $E_0 + E_F$, where $\mathbf{E_F}$ is measured with respect to the CBM. The absorption coefficient will be:

$$\alpha = Cte \times (\hbar\omega - E_i)^{3/2} \, e^{-\frac{2[\hbar\omega - E_i]}{E_{kin}}} \frac{1}{1 + e^{\frac{E_i + E_F - \hbar\omega}{K_B T}}} \tag{2.64}$$

At room temperature, for $E_i = 2.8$ eV and $E_{kin} = 0.25$ eV, when the Fermi level moves from the CBM to 1.2 eV above the CBM the charge transfer band with evolve as shown in Figure 2.7:

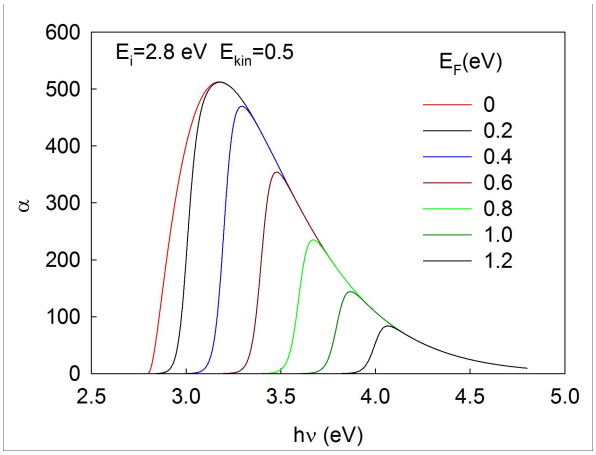

***Figure 2.7**: Absorption spectrum for different values of $\boldsymbol{E_F}$.*

Obviously, the Fermi-Dirac function would introduce an abrupt absorption onset that is not actually observed. In order to obtain a more realistic expression we must use a convolution with a Gaussian giving account of the widening of the final states due to scattering mechanisms.

$$\alpha(\hbar\omega) = Cte \times \int_{E_i}^{\infty} (\hbar\omega' - E_i)^{3/2} \frac{e^{-\frac{2[\hbar\omega' - E_i]}{E_{kin}}}}{1 + e^{\frac{E_i + E_F - \hbar\omega'}{K_B T}}} \frac{e^{-\frac{(\hbar\omega' - \hbar\omega)^2}{2\Gamma^2}}}{\sqrt{2\pi}\Gamma} \hbar d\omega' \tag{2.65}$$

In the same conditions of the previous example, when the widening of the final states is taken into account by Gaussian convolution, with $\Gamma = 0.15$ eV, the evolution of the CTT band as the Fermi level moves is shown in Figure 2.8:

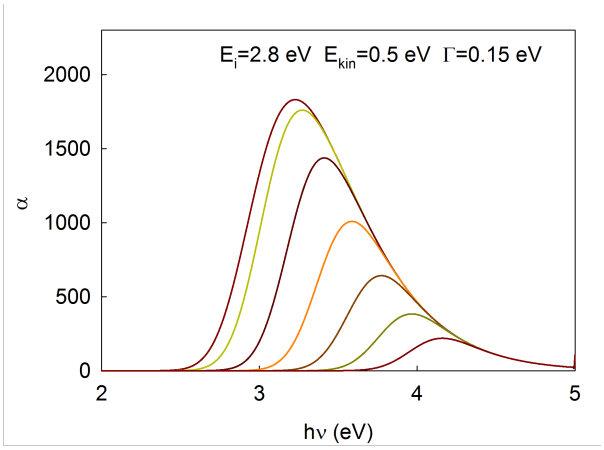

***Figure 2.8**: Absorption spectrum for different values of E_F.*

Gaussian convolution transforms the CTT band shape making it more symmetric but preserves some important features.

In particular, we can plot the photon energy and intensity of the absorption band maximum as a function of the Fermi level. The result is shown in Figures 2.9:

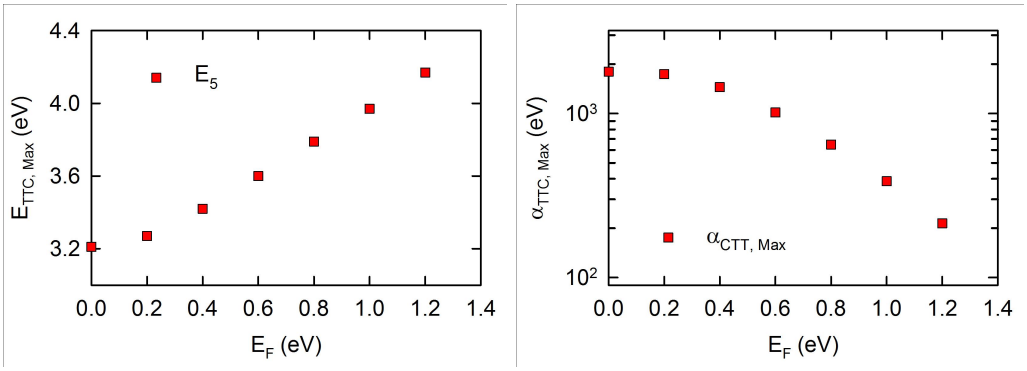

***Figure 2.9**: Photon energy and intensity of the absorption charge transfer transition band maximum.*

These plots indicate that the photon energy at the maximum basically follows the shift of the Fermi level (the shift is slightly sub-linear). The

absorption coefficient at the maximum exhibits an exponential behaviour, as expected from the presence of an exponential in the CTT band spectral shape. Basically, for this value of $\mathbf{E_{kin}}$ (0.25 eV), a shift of 0.2 eV in the Fermi level leads to a 40% reduction of the absorption coefficient at the maximum.

This model is not yet completely realistic, as the width of the final states can increase as the doping level increases. Nevertheless, as we will see in the discussion of the transport properties, the electron mobility (proportional to the lifetime of the final states, in the conduction band) is not catastrophically affected by alloy disorder or Ga doping.

The effect of localization in the final state: charge transfer transition from a Gaussian localized state to a quantum well in the conduction band

Let us assume that the localized state has Gaussian wavefunction:

$$\Phi_{loc}\left(\vec{r}\right) = C_1 e^{-\chi^2 r^2} \tag{2.66}$$

The final state in the conduction and will be a plane wave in the quantum well (QW) plane (xy) and a localized function in the perpendicular direction (z):

$$\Phi_{QW,CB}\left(\vec{r}\right) = C_2 e^{i(k_x x + k_y y)}\Phi(z) \tag{2.67}$$

The dipolar matrix element will be

$$\begin{aligned}
\Phi_{loc,QW,CB} &= \int \Phi^*_{loc}(\vec{r}) i\frac{e\hbar}{m}\vec{A_0}\cdot\bigtriangledown\Phi_{QW,CB}(\vec{r})\mathrm{d}v = \\
&= iC_1C_2\frac{e\hbar}{m}\int \Phi^*_{loc}(\vec{r})\vec{A_0}\cdot\bigtriangledown\left(e^{i(k_x x+k_y y)}\Phi(z)\right)\mathrm{d}v = \\
&= iC_1C_2\frac{e\hbar}{m}\int \Phi^*_{loc}(\vec{r})\vec{A_0}\cdot\Big(i\vec{k_{xy}}e^{i(k_x x+k_y y)}\Phi(z) + \\
&\qquad + e^{i(k_x x+k_y y)}\bigtriangledown_z\Phi(z)\Big)\mathrm{d}v = \\
&= -C_1C_2\frac{e\hbar}{m}\vec{A_0}\cdot\vec{k_{xy}}\int \Phi^*_{loc}(\vec{r})e^{i(k_x x+k_y y)}\Phi(z)\mathrm{d}v + \\
&+ C_1C_2\frac{e\hbar}{m}\vec{A_0}\cdot\vec{k_{xy}}\int e^{i(k_x x+k_y y)}\Phi^*_{loc}(\vec{r})\bigtriangledown_z\Phi(z)\mathrm{d}v = \\
&= -C_1C_2\frac{e\hbar}{m}\vec{A_0}\cdot\vec{k_{xy}}\int C_1 e^{-\chi^2 r^2}e^{i(k_x x+k_y y)}\Phi(z)\mathrm{d}v + \\
&+ C_1C_2\frac{e\hbar}{m}\quad\vec{A_0}\cdot\vec{k_{xy}}\int e^{i(k_x x+k_y y)}C_1 e^{-\chi^2(x^2+y^2)}\mathrm{d}x\mathrm{d}y\int e^{-\chi^2 r^2}\bigtriangledown_z\Phi(z)\mathrm{d}z
\end{aligned} \tag{2.68}$$

The second term includes an integral in **z**, $\int e^{-\chi^2 z^2} \bigtriangledown_z \Phi(z)\mathrm{d}z$ that is the matrix element between two *even* functions (the Gaussian function and the first state of the quantum well) that must be necessarily zero. Then:

$$H_{loc,QW,CB} = -C_1 C_2 \frac{e\hbar}{m} \vec{A_0} \cdot \vec{k_{xy}} \int \Phi^*_{loc}(\vec{r}) e^{i(k_x x + k_y y)} \Phi(z)\mathrm{d}v \tag{2.69}$$

The integral can be calculated:

$$\begin{aligned} &\int \Phi^*_{loc}(\vec{r}) e^{i(k_x x + k_y y)} \Phi(z)\mathrm{d}v = C_1 \int e^{-\chi^2 r^2} \Phi(z)\mathrm{d}v \\ &= C \int_0^\infty e^{-\chi^2(x^2+y^2)} e^{i(k_x x + k_y y)} \mathrm{d}x\mathrm{d}y \int_0^\infty e^{\chi^2 z^2} \Phi(z)\mathrm{d}z \end{aligned} \tag{2.70}$$

The first integral contains the dependence on the k-vector of the electron on the QW plane:

$$\begin{aligned} &\int e^{\chi^2(x^2+y^2)} e^{i(k_x x + k_y y)} \mathrm{d}x\mathrm{d}y = \\ &\int_0^\infty e^{\chi^2 x^2} e^{i(k_x x}\mathrm{d}x \int_0^\infty e^{\chi^2 y^2} e^{i(k_y y}\mathrm{d}y = \quad C e^{(k_x x + k_y y)/\chi^2} \end{aligned} \tag{2.71}$$

The second one is just a numeric parameter depending on **z** localization of the electron in the **z** direction

$$\int e^{\chi^2 z^2} \Phi(z)\mathrm{d}z = C_z \tag{2.72}$$

Then the matrix element is

$$H_{loc,c} = -C \frac{e\hbar}{m} \vec{A_0} \cdot \vec{k_{xy}} \frac{4\pi C_1}{i\chi} 2e^{k^2/\chi^2} = Cte \times C_z A_0 k_{xy} e^{(k_x x + k_y y)/\chi^2} \tag{2.73}$$

The transition probability by unit time is given by Fermi's golden rule:

$$\begin{aligned} W_{loc,c} &= \frac{2\pi}{\hbar} |H_{loc,c}|^2 \delta \left[E_C(\vec{k_{xy}}) + \triangle E_{QW,1} - E_{loc} - \hbar\omega \right] = \\ &= Cte \times C_z^2 A_0^2 k_{xy}^2 e^{-2k_{xy}^2/\chi^2} \delta \left[E_C(\vec{k_{xy}}) + \triangle E_{QW,1} - E_{loc} - \hbar\omega \right] = \\ &= Cte \times C_z^2 A_0^2 k_{xy}^2 e^{-2k_{xy}^2/\chi^2} \delta \left[E_C(0) + \frac{\hbar^2 k_{xy}^2}{2m^*} + \triangle E_{QW,1} - E_{loc} - \hbar\omega \right] \end{aligned} \tag{2.74}$$

The number of transitions per unit time and volume can be calculated by integrating over all values of k_{xy} that fulfill the energy conservation condition:

$$N_{loc,c} = \int_0^\infty Cte \times A_0^2 k_{xy}^2 e^{-2k_{xy}^2/\chi^2} \delta\left[E_C(0) + \frac{\hbar^2 k_{xy}^2}{2m^*} + \triangle E_{QW,1} - E_{loc} - \hbar\omega\right] 2\pi k_{xy} \mathrm{d}k_{xy} \quad (2.75)$$

We can change the variable in the Dirac's delta:

$$N_{loc,c} = \int_0^\infty Cte \times A_0^2 k_{xy}^2 e^{-2k_{xy}^2/\chi^2} \frac{\delta\left[k_{xy} - k_0\right]}{\hbar k_{xy}/m^*} 2\pi k_{xy} \mathrm{d}k_{xy} = = Cte \times A_0^2 k_0^2 e^{-2k_0^2/\chi^2} \quad (2.76)$$

Where k_0 fulfills $E_C(0) + \triangle E_{QW,1} + \frac{\hbar^2 k_0^2}{2m^*} = E_{loc} + \hbar\omega$

$$k_0^2 = \frac{2m^*}{\hbar^2}\left[\hbar\omega - (E_C(0) + \triangle E_{QW,1} - E_{loc})\right] = = \frac{2m^*}{\hbar^2}\left[\hbar\omega - (E_i + \triangle E_{QW,1})\right] \quad (2.77)$$

where $\mathbf{E_i}$ is the minimum photon energy for the bulk CTT transition. The absorption coefficient will be:

$$\alpha = Cte \times \left[\hbar\omega\left(E_i + \triangle E_{QW,1}\right)\right] e^{-2\left[\hbar\omega\left(E_i + \triangle E_{QW,1}\right)\right]/E_{kin}} \quad (2.78)$$

The onset of the CTT transition is shifted to higher energies by the confinement energy of the quantum well. Its intensity is reduced because at the new onset the exponential term is smaller, with respect to its bulk value, by a factor $e^{-2\triangle E_{QW,1}}/E_{kin}$.

2.2 Alloy formation

2.2.1 Common cation-anion rule

In general in materials with a common cation, the direct bandgap at Γ increases as the proton number of the anion decreases. Equally in materials

with a common anion, the direct bandgap at Γ also increases as the cation atomic number decreases[44][45]. This is known as the *common anion-cation rule* and it is supported by experimental data. This rule is based in covalently bonded materials, on the general principle that for stronger covalent bonds (small atomic numbers/smaller bond distances) the energy difference between bonding (valence band) and anti-bonding (conduction band) states is larger than for weaker covalent bonds (larger atomic numbers/larger bond distances). However, there are many exceptions which have been called breakdowns, especially when there is an ionic character to the bonding[46][47]. Some of these trends are shown in Figure 2.10[47].

The main problem with the common anion-cation rule is that it does not consider the specific orbitals involved or the nature of the bonding between those orbitals. Tetrahedrally coordinated materials normally have sp^3 covalent bonding so any rigorous theoretical model would need to take this into account. Hall[48] was the first to do this in 1952 with diamond, using a model based on tight-binding combinations of bonding hybrid orbitals. But this rule was based only on experimental results until the apparition of Harrison's model[49]. The basis of this model is the linear combination of orbitals from a small number of atoms to calculate the band structure. The common cation-anion rule was developed during the following years.

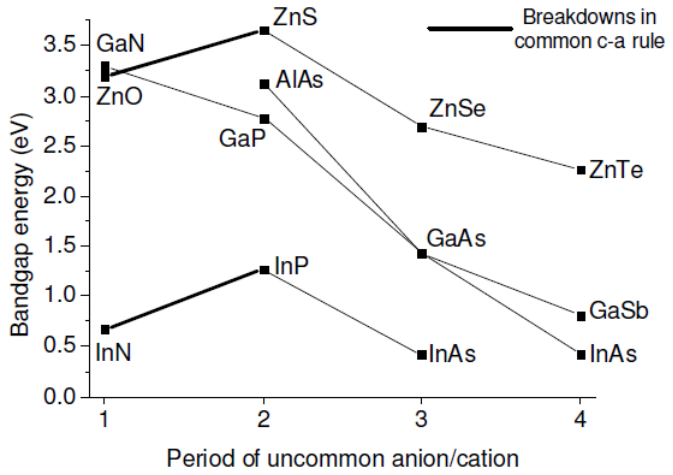

***Figure 2.10**: Successes and failures of the common anion-cation rule.*

After further works, in 1998, Wei *et al.*[50] introduced the effect of d orbitals in the calculation of the different valence band offsets for common cation and common anion compounds from first principles. This explained some cases of breakdown of the common cation or anion rule, due to $p-d$

repulsion. The interaction between the p state of the anion with the d state of the cation results in a bonding state with mainly d character and an anti-bonding state with mainly p character. The $p-d$ interaction energy shifts downwards the bonding state and upwards the anti-bonding state, in such a way that it can be described as an effect of $p-d$ repulsion.

In common cation systems, $p-d$ repulsion decreases as the anion atomic number increases due to increasing p orbital energy. As a result, the valence band offset decreases as the anion atomic number increases. If different series of common-cation system are compared, it may be concluded that when the cation atomic number increases, the $p-d$ repulsion increases, reducing the valence band offset.

Thus, by this rule, the direct bandgap energy of semiconductors in the wurtzite or zinc-blende structure increases as the average atomic number decreases, as in the series ZnTe, ZnSe and ZnS. This rule has some exceptions, like the lower bandgap of ZnO with respect to that os ZnS or the case of copper chalcopyrites, due to $p-d$ hybridization between cation $3d$ levels and anion $2d$ levels[44][45]. Following the general trend, it seems reasonable to expect that the substitution of Zn for lighter transition cations (with lower atomic number) would produce an increase in the bandgap energy of these alloys. Nevertheless, anomalies are to be expected owing to $p-d$ hybridization of O $2p$ levels and M cation $3d$ levels[51].

2.2.2 *p-d* repulsion

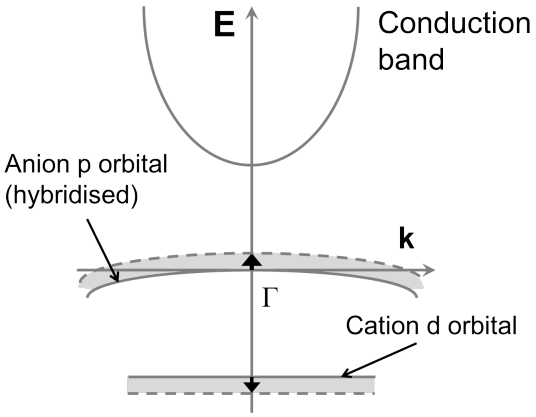

***Figure 2.11**: The effect of p-d repulsion.*

The interaction between p and d orbitals is permitted at Γ when the crystal structure is not centrosymmetric. As this is the case in tetrahedrally coordi-

nated materials, this interaction needs to be taken into account when cation d and anion p orbitals are energetically close enough to overlap. The p and d orbitals hybridise to produce a bonding state with lower energy than the original p orbital. Therefore, the entire effect may be described as an effective repulsion between the p and d orbitals.

If the cation p states can be ignored then this problem simplifies to a two levels system regarding the anion p orbitals $|\boldsymbol{p}\rangle$ and the cation d orbitals $|\boldsymbol{d}\rangle$. The wavefunction for the system is:

$$\Psi = a\,|p\rangle + b\,|d\rangle \tag{2.79}$$

where **a** and **b** are coefficients related to the occupation probabilities of the p and d orbitals, respectively. The total energy of the system (**E**) is determined through the Hamiltonian operator (**H**):

$$H\Psi = E\Psi \tag{2.80}$$

On operating with the Hamiltonian and separating the orthogonal contributions, the following two equations are obtained:

$$\begin{aligned} aE_p + bV_{pd} &= Ea \\ aV_{pd} + bE_d &= Eb \end{aligned} \tag{2.81}$$

where $\mathbf{E_p}$ is the energy of the anion p orbital, $\mathbf{E_d}$ is the energy of the cation d orbital and $\mathbf{V_{pd}}$ is the $p-d$ coupling matrix element. The equations may be solved simultaneously to find the total energy of the system by calculating the determinant of the 2 x 2 matrix:

$$\begin{vmatrix} a(E_p - E) & bV_{pd} \\ aV_{pd} & b(E_d - E) \end{vmatrix} = 0 \tag{2.82}$$

which is solved by a quadratic formula, and after terms corresponding to the second power and greater have been ignored[52]. And by taking the positive and negative roots, two energies of the antibonding $\mathbf{E_{AB}}$ and bonding $\mathbf{E_B}$ orbitals after $p-d$ coupling has taken place.

$$\begin{aligned} E_{AB} &= E_p + \frac{|V_{pd}|^2}{E_p - E_d} \\ E_B &= E_d - \frac{|V_{pd}|^2}{E_p - E_d} \end{aligned} \tag{2.83}$$

The energy difference between the orbitals is:

$$\Delta E = E_{AB} - E_B = E_p - E_d + \frac{2\left|V_{pd}\right|^2}{E_p - E_d} \tag{2.84}$$

In the absence of $p-d$ repulsion, the energy difference is simply $E_p - E_d$, so the effect of $p-d$ repulsion may be found by subtracting this term. It is customary to express this as an energy change per orbital so the result is divided by two:

$$\Delta E_{pd} = \frac{\left|V_{pd}\right|^2}{E_p - E_d} \tag{2.85}$$

Wie and Zunger [44] combined a similar model with numerical data from band structure calculations using all-electron self-consistent electronic-structure techniques to investigate $p-d$ repulsion in II-VI semiconductors. It was found that some physical effects are usually produced: reduction in bandgap and cohesive energy, increase in equilibrium lattice parameters, reduction in spin-orbit splitting, sign change in crystal splitting and modification to charge ditribution.

Moreover, by using this model to calculate the valence band offsets caused by $p-d$ repulsion, the two breakdowns in the common anion-cation rule mentioned may be resolved.

In our case, there are two cations that need to be taken into account: Zn and the dilute TM cation, which substitutes for Zn in a certain fraction, x, of the cation sites. The expression for the energy shift produced by $p-d$ repulsion is:

$$\Delta E_{pd} = x\frac{\left|V_{pd}^{TM}\right|^2}{E_{2p}^{O} - E_{3d}^{TM}} + (1-x)\frac{\left|V_{pd}^{Zn}\right|^2}{E_{2p}^{O} - E_{3d}^{Zn}} \tag{2.86}$$

As the electronic states at the valence band maximum comprise of the hybridised anion $2p$ and cation $3d$, this energy corresponds to the shift in the valence band maximum in function of the dilute cation concentration. Moreover, it also corresponds to the shift in bandgap energy, since the energy of the conduction band minimum is unaffected by $p-d$ repulsion, due to its Zn $4s$ nature. The rate of change of bandgap energy may be determined:

$$\frac{dE_g}{dx} = -\frac{\left|V_{pd}^{TM}\right|^2}{E_{2p}^{O} - E_{3d}^{TM}} + \frac{\left|V_{pd}^{Zn}\right|^2}{E_{2p}^{O} - E_{3d}^{Zn}} \tag{2.87}$$

Hence, there are two factors that affect the bandgap shift as dilute cation concentration increases. The first term corresponds to the effect of the dilute cation. It is interesting to note that this term could be positive or negative, depending on the sign of $E_{2p}^{O} - E_{3d}^{TM}$. If the TM $3d$ levels are more weakly bound than the O $2p$ levels, the sign is negative and vice versa. The Zn $3d$ levels are more strongly bound than the O $2p$ levels, so $E_{2p}^{O} - E_{3d}^{Zn}$ is positive, making the sign of the term positive. Therefore, for the bandgap energy to decrease with x it is not only necessary for the dilute cation $3d$ levels to be more strongly bound than the O $2p$ levels, but the shift they produce must be large enough to compensate for the effect of the reduction in Zn concentration. In all other cases the bandgap energy will increase with x. The effect of the energy of the TM $3d$ orbital is shown diagrammatically in Figure 2.12

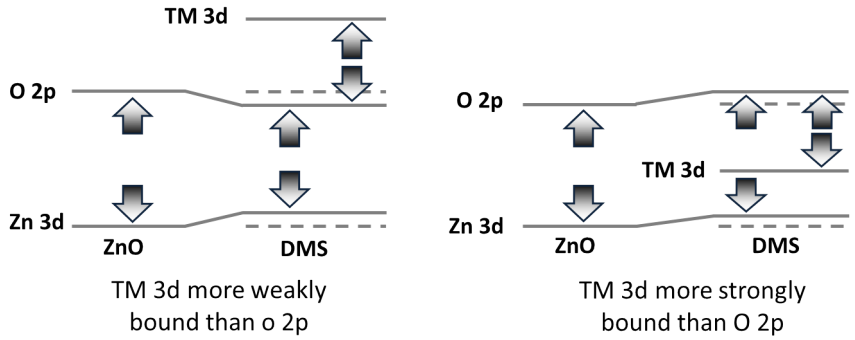

***Figure 2.12**: The effect of TM 3d level energy on p-d repulsion.*

Although theoretical values were not readily available for the bandgap shift in the investigated DMSs, a value of a few meV per percentage increase in x would be expected, by comparison with other common anion series in [44].

2.2.3 Crystal field theory

Crystal field theory is a model that describes the internal electronic transitions in metal complexes. This theory is an ionic theory, which is mainly based on electrostatic theory but ignores all the covalent bonding effects. It has been successfully used it for describing hydration enthalpies[53], magnetic[54] and optical properties[55][56] and spinel structures of transition metal complexes. The combination of this theory with the molecular orbital theory leads to the ligand field theory (LFT)[57], which allows for describing the processes of chemical bonding in transition metal complexes.

The objective of the model is to calculate the change in energy in the five degenerate d orbitals of the TM cation when surrounded by ligands, which are modelled as point charges. There is an attraction between the cation and the unbounded ligand electrons but there is also a repulsion between the cation d orbitals and the ligand electrons, which becomes stronger the closer they are to each other. As not all the d orbitals are the same distance from the ligands, a splitting occurs in the d orbital energies. This splitting depends on various factors, such as the particular cation and ligands in question, the coordination of the cation and its oxidation state.

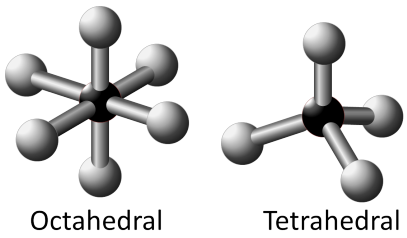

***Figure 2.13**: Arrangement of cation and ligands in different coordination.*

The most common structure of complex is octahedral (Figure 2.13), where six ligands form an octahedron around the metal ion. The shape of the electron density of the 3d orbitals determines the energy position of the orbitals when the TM ion is placed into the octahedron.

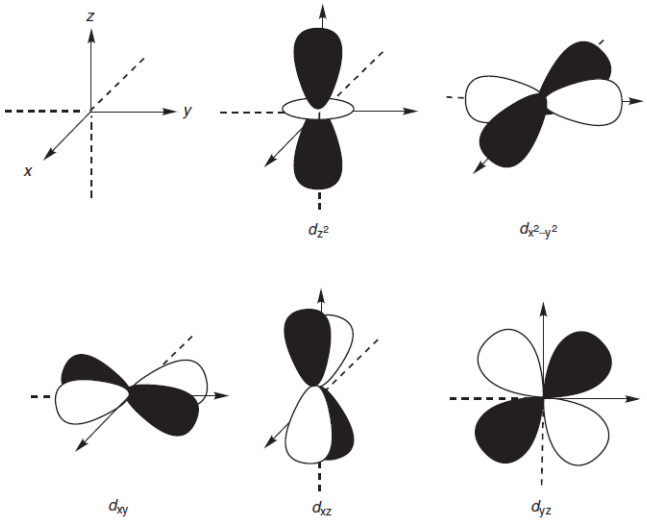

***Figure 2.14**: Representation of the 3d orbitals[58]. The shaded and unshaded areas represent lobes of different signs.*

Figure 2.14 shows the shape of the different $3d$ orbitals[58]. The orbitals which are pointed directly toward the six ions ($3d_{z^2}$ and $3d_{x^2-y^2}$, whose direction is represented by the Cartesian axis, suffer a shift to higher energies due to their closer vicinity to the ligand than the other three ($3d_{xy}$, $3d_{xz}$ and $3d_{yz}$).

For tetrahedral coordination 2.13, four ligands form a tetrahedron around the metal ion. In this case, neither of them is oriented directly towards the $3d$ orbitals producing a reduction on the energy splitting in comparison with the octahedral structure. However we can consider that the tetrahedron is within a cube and then, the orbitals $3d_{z^2}$ and $3d_{x^2-y^2}$ at the centre of the cube lie between the ligands, and the $3d_{xy}$, $3d_{xz}$ and $3d_{yz}$ orbital point toward the ligands.

Figure 2.15 shows how the d orbitals split into two distinct sets. At the left with an energy difference Δ_{Oct} corresponding to the octahedral coordination, and at the right of the figure with an energy difference of Δ_{Tet} corresponding to the tetrahedral coordination.

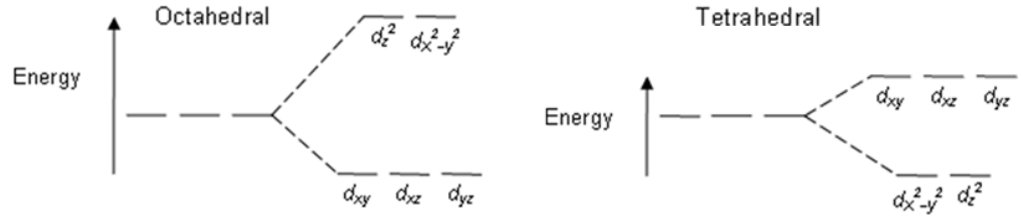

***Figure 2.15**: d orbital crystal field splitting in different coordinations.*

We also note that $\Delta_{Oct} > \Delta_{Tet}$ because the d orbitals are oriented directly towards the ligands in octahedral coordination but this is not the case in tetrahedral coordination.

The oxidation state of the cation affects the size of the crystal field splitting (δ). In general, the higher the oxidation state, the higher the splitting. This is because the change in charge density that occurs when going from, say a TM^{2+} to a TM^{3+} state, allows the ligands to draw closer to the cation, increasing the repulsive potential. Another factor that influences δ is the chemical composition of the ligand. Certain ligands produce a large splitting and are referred to as strong-field ligands. Other ligands produce small splitting and are referred to as weak-field ligands. The reason why ligands produce different field strengths is explained by LFT and is related to the nature of the bonding between the cation and ligands. In complexes with strong-ligands, it is energetically unfavourable to put electrons into the high

energy (e_g) levels produced by the splitting so the lower energy (t_{2g}) levels are filled first, in accordance to the Aufbau principle. Such complexes are referred to as *low spin*, as they tend to have a high proportion of paired d electrons. The reverse is true in the case of weak-field ligands, where it is energetically favourable to place an electron into an unoccupied e_g level rather than overcoming the repulsion caused by pairing it with another electron in a t_{2g} level. Therefore, one electron would be placed in each of the five d orbitals before the occurrence of pairing, in accordance with Hund's rule. The resulting complexes are referred to as *high spin*, as they tend to have a high proportion of unpaired d electrons. In tetrahedral TM complexes, $\delta_{tet} \approx 4/9\delta_{oct}$.

2.3 Size dependent properties

The semiconductor nanoparticles, also called *quantum dots* (QD) when the dimensions of the system approaches the Bohr radius of the exciton[59][60], are nanostructures with properties between the molecular regime and solid state[61]. Their properties can be controlled by their shape and size[9] But the variation is achieved by reducing the size of the crystal, not by altering its chemical composition. The nanocrystals occur in the same crystal structure as the extended solid[62]. There are two major effects which are responsible for these size variations in nanocrystal properties. First, in nanocrystals the number of surface atoms is a large fraction of the total[63]. Second, the intrinsic properties of the interior of nanocrystals are transformed by quantum size effects[64]. And, independent of the large number of surface atoms, semiconductor nanocrystals with the same interior geometry as a known bulk often exhibit strong variations in their optical and electrical properties with size[65]. These changes arise through systematic transformations in the density of electronic energy levels as a function of the size of the interior, known as *quantum size effects*.

In a nanoparticle, charges are confined to a small volume. As the infinite potential well model with a width d. Only the allowed states of the wave function disappear at the edge of the well, as we observe in figure2.16.

Then, we can see how the bandgap energy of a nanoparticle is larger than the bulk. Optical excitations across the gap depend strongly on the size, likewise, the electrical transport properties. Charge transport of electrons and holes are forced to remain confined, so that the electronic levels significantly modify optical and electrical properties.

The electrical characteristics of individual semiconductor nanocrystals, in which Coulomb blockade effects and discrete energy level spacings are both

expected to occur[66].

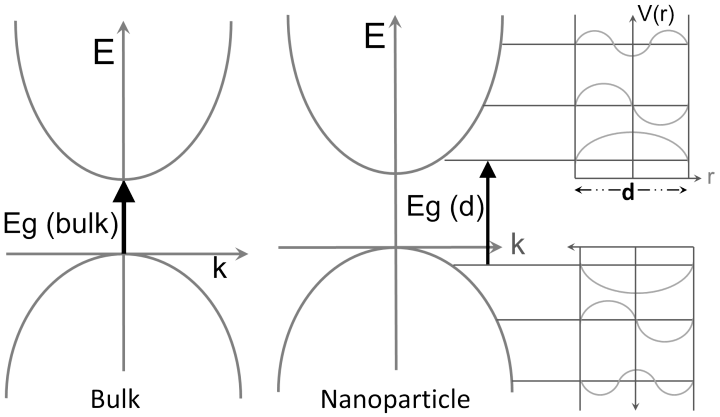

***Figure 2.16**:* Scheme of transition energy for a bulk (left) and a nanoparticle (right).

Different approaches have been proposed to explain the size-dependent development of bulk electronic properties in semiconductor crystallites. The widely accepted model was initially proposed by Efros[67] and further extended by Brus[68][59][69] to include the term of Coulomb interaction of an electron-hole, $e-h$, pair. And, following the work of Brus[68], the confinement effect on the bandgap, $\mathbf{E_g(R)}$, is then expressed as a function of the semiconductor nanoparticle radius, $\mathbf{R}$:

$$E_g(R) = E_g + \frac{\pi^2\hbar^2}{2m_0R^2}\frac{1}{\mu*} - \frac{1.8e^2}{\varepsilon R} + smaller\,terms \tag{2.88}$$

where the first term, $\mathbf{E(_g)}$, represents the bandgap of the bulk semiconductor, and the second term represents the spatial confinement of electrons in the CB and holes in the VB by the potential barrier of the surface or a mono-potential well of the quantum box and has a $1/R^2$ dependence, and the third term represents the Coulomb energy with a $1/R$ dependence. Generally, the second term is more important than the third one. Thus, the apparent band gap will always increase for small enough $\mathbf{R}$.

2.4 High Pressure effects

When a hydrostatic pressure is applied to a material, the interatomic distance is reduced, which usually results in an increased gap, forbidden energy band

between the valence and conduction bands[70]. The physical origin of this increase is in the way that bands are formed from atomic orbitals in forming chemical bonds. While the VB is formed mainly from the bonding molecular orbitals, the CB is essentially formed from the antibonding. The increase in the overlay term reducing the distance between atoms leads to an increase in energy of the separation between bonding and antibonding orbitals and, therefore, an increase of the gap. This is especially true for covalently bound materials. As the main link in the ZnO is covalent, it would be the expected behaviour in pure material and in its DMSs.

In order to know how the hydrostatic pressure affects on the material, we first must define the pressure coefficient, $\mathbf{a_P}$ [52]:

$$a_P = \frac{dE_g}{dP} \tag{2.89}$$

As pressure causes a volume change, the effects of high pressure also often described in terms of volume deformation:

$$a_V = \frac{dE_g}{d\ln V} \tag{2.90}$$

The relationship between these two quantities is written as:

$$a_P = -\frac{a_V}{B} \tag{2.91}$$

Where $\mathbf{B}$ is the *bulk modulus*:

$$B = -\frac{dP}{d\ln V} \tag{2.92}$$

In the calculations, the contributions to the volume deformation potential from the conduction band and valence band are found separately and then combined through the relationship:

$$a_v = \frac{dE^{CBM}}{d\ln V} - \frac{dE^{VBM}}{d\ln V} \tag{2.93}$$

In cubic diamond and zincblende semiconductors, the pressure coefficient of the CBM is always positive for two reasons. Firstly, there is an increase in kinetic energy on applying high pressure, which is inversely proportional to

the square of the anion-cation bond length[46]. Secondly, there is often an accompanying increase in $s-s$ repulsion between the antibondind orbitals at the CBM. The energy of the CBM is described by the following equation, obtainable from the simple tight-binding model[71]:

$$E^{CBM} = \left(\frac{\varepsilon_s^c + \varepsilon_s^a}{2}\right) + \sqrt{\left(\frac{\varepsilon_s^c - \varepsilon_s^a}{2}\right)^2 + V_{ss}^2} \tag{2.94}$$

where $\boldsymbol{\varepsilon_s^c}$ and $\boldsymbol{\varepsilon_s^a}$ are the s orbital energies of the cation and anion, respectively, and $\mathbf{V_{ss}}$ is the coupling potential between the two states.

And, for other part, the pressure coefficient of the VBM is usually also affected by two main factors. Firstly there is the kinetic energy increase on applying high pressure, which increases its energy in a similar way to the CBM. Secondly there is the accompanying increase in $p-p$ coupling between the bonding states at the VBM, which decreases its energy. The energy of the VBM in the simple tight binding model is given by:

$$E^{VBM} = \left(\frac{\varepsilon_p^c + \varepsilon_p^a}{2}\right) + \sqrt{\left(\frac{\varepsilon_p^c - \varepsilon_p^a}{2}\right)^2 + V_{pp}^2} \tag{2.95}$$

where $\boldsymbol{\varepsilon_p^c}$ and $\boldsymbol{\varepsilon_p^a}$ are the p orbital energies of the cation and anion, respectively, and $\mathbf{V_{pp}}$ is the coupling potential between the two states.

Once the combined conduction band and valence band volume deformation potentials are determined, the bulk modulus may be calculated by fitting the total energy, found in the calculations, to Murnaghan's equation of state[72]:

$$B(P) = B(0) + B'P \tag{2.96}$$

where $\mathbf{B'}$ is the pressure derivative of the bulk modulus. Zhang et al. [73] used a different theoretical approach, the *ab-initio* pseudopotential plane-wave method, to calculate the pressure coefficient of wurtzite ZnO directly and a value of 21 meV/GPa was obtained.

This theory could potentially have a significant effect on the pressure coefficient of ZnO based DMSs. This is because substituting Zn for another TM changes the strength of the $s-s$ interaction that determines the pressure dependence of the CBM. This is the principal contribution to the bandgap pressure coefficient because the pressure dependence of the VBM energy is

small. On substituting Zn for any of the investigated dilute cations, the decrease in the TM 4s binding energy is approximately constant with average value of 1.7 eV[74]. Assuming that the anion s orbitals do not alter their energy considerably, it is clear that the value of $(\varepsilon_s^c - \varepsilon_s^a)$ increases, resulting in a decrease in the corresponding volume deformation potential. For this reason, increasing the dilute cation concentration would be expected to cause a decrease in the bandgap pressure coefficient. The physical explanation behind this trend is that as the dilute cation concentration increases, the bandgap increases, showing the material to be more compact and, therefore, more difficult to compress further. As the dilute cation is changed, the pressure dependence of the $p - d$ repulsion can not be ignored. However, it is thought that this factor would be much smaller than the effect of $s - s$ coupling, in agreement with the theory.

2.5 Electric and Transport Properties

When we study electrons and holes located around defect, we consider that these electrons and holes are localized around the defect and they are known as bound electrons and holes, respectively. In contrast, electrons in the conductions band and holes in the valence band of a semiconductor can carry electrical current. Hence they are referred to as free carriers[75]. The response of these carriers to an electric field depends on the field strength. Under high electric fields, carriers in a semiconductor can acquire so much energy that their average kinetic energy becomes higher than that of the lattice.

2.5.1 Resistivity

Electrical resistivity is a key physical property of all materials. It is often necessary to accurately measure the resistivity of a given material. The electrical resistivity of different materials at room temperature can vary by over 20 orders of magnitude. No single technique or instrument can measure resistivities over this wide range[76]

$$\sigma = \frac{1}{\rho} \tag{2.97}$$

The *electrical resistivity* of a material is an intrinsic physical property, independent of the particle size or shape of the sample.

On a microscopic level, electricity is simply the movement of electrons through a material.

The resistivity of a material can vary greatly at different temperatures. The resistivity of metals usually increases as temperature increases, while the resistivity of semiconductors usually decrease as temperature increases. The resistivity can also depend on the applied magnetic field.

The discussion thus far has assumed that the material being measured is homogeneous and isotropic. A more exact definition of resistivity is the proportionality coefficient $\boldsymbol{\rho}$ relating a local applied electric field to the resultant current density, **J**:

$$E = \rho J \tag{2.98}$$

where **E** is the *electric field*. The Equation 2.98 is one form of *Ohm's Law*. The current does not necessarily flow in the direction of the applied electric field.

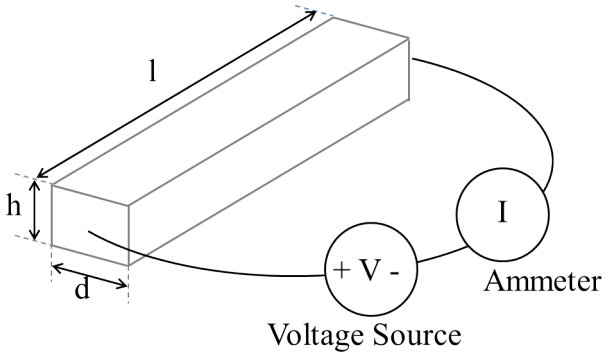

***Figure 2.17**: Two point technique configuration for resistivity measurements.*

$$E = \frac{V}{l} \tag{2.99}$$

$$J = \frac{I}{A} = \frac{I}{hd} \tag{2.100}$$

$$V = \frac{I\rho l}{A} \tag{2.101}$$

Define *resistance*, **R**:

$$R = \frac{\rho l}{A} \tag{2.102}$$

Combining equations

$$I = \frac{V}{R} \tag{2.103}$$

The resistance, **R**, can depend on the size and shape of the sample, while $\boldsymbol{\rho}$ is independent of them.

Relationship between the resistivity $\boldsymbol{\rho}$ and the simple microscopic model is:

$$\rho = \frac{m}{ne^2\tau} \tag{2.104}$$

where **m** is the mass of an electron, **n** is the number of electrons per unit volume carrying current in the material, **e** is the electric charge on an electron, and $\boldsymbol{\tau}$ is the average time between collisions of an electron with the stationary atoms of the materials.

2.5.2 Theory of Measurement Techniques

Two point technique

The resistivity of a material can be obtained by measuring the resistance and physical dimensions of a sample. The material is cut into a shape of length **l**, height **h**, and width **d**. Gold wires are attached to opposite sides of the sample. A voltage source applies a voltage **V** across the sample, causing a current **I** to flow through the material. The amount of current **I** is measured by the ammeter, which is connected in series with the sample and voltage source. The resistance **R** is:

$$R = \frac{V}{I} \tag{2.105}$$

Then, the resistivity is:

$$\rho = R\frac{hd}{l} \tag{2.106}$$

In practice, measuring resistivity with a two-point technique is often not reliable. There is usually some resistance between the contact wires and the material. These additional resistance makes the measurement of the resistivity of the material higher than it really is. A second potential problem is modulation of the sample resistivity due to the applied current. This is often a possibility for semiconducting materials.

Four point technique

In this technique four wires are attached to the sample as shown in the Figure 2.18

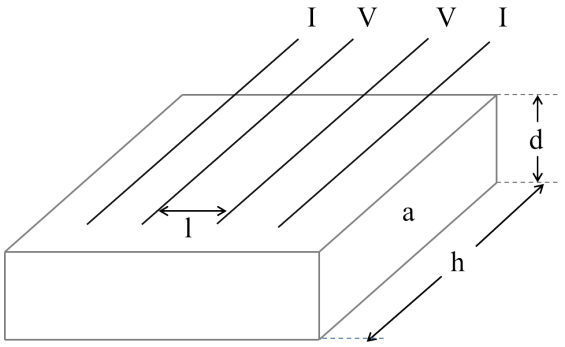

***Figure 2.18**: Four point technique configuration for resistivity measurements.*

The electrical resistivity of a solid can be determined by passing a current **I** through the specimen of cross-section area **a** and measuring the resultant voltage drop **V** over a distance **l** [77]

The electrical resistivity $\boldsymbol{\rho}$ is given by:

$$\rho = \frac{V}{I}\frac{a}{l} = R\frac{a}{l} = R\frac{hd}{l} \tag{2.107}$$

where **R** is the resistance of the sample between the potential contacts.

The most difficult part of making resistivity measurements is often making good electric contacts to the sample. Contacts can be made in many ways using silver-paint, squeezing a wire against the material, soldering wires to the material...

Van der Pauw Technique

The four-point measurement technique described has assumed the material sample has the shape of a rectangular thin film of a bar. There is a more gen-

eral four-point resistivity measurement technique that allows measurements on samples of arbitrary shape, with no need to measure all the physical dimensions of the sample. This is the Van der Pauw technique[78]. There are four conditions that must be satisfied to use this technique:

- The sample must have a flat shape of uniform thickness.
- The sample must not have any isolated holes.
- The sample must be located at the edges of the sample.
- All four contacts must be located at the edges of the sample.

In addition to these four conditions, the area of contact of any individual contact should be at least an order of magnitude smaller than the area of the entire sample. For small samples, this might not be possible or practical. If sufficiently small contacts are not achievable, it is still possible to do accurate Van der Pauw resistivity measurements, using geometric correction factors to account for the finite size of the contacts.

A more common geometry is to attach four contacts to the four corners of a square-shaped sheet of the material.

The equation for calculating the resistivity by Van der Pauw method:

$$\rho = R\frac{\pi d}{\ln 4} \tag{2.108}$$

It is not necessary to measure the width or length of the sample.

Chapter 3

Experimental Methods

3.1 Thin Films Growth Technique: Pulsed laser deposition system (PLD)

The thin film growth process has been conducted by *pulsed laser deposition*. This technique was first used more than 45 years ago by Smith and Turner[79], shortly after the invention of pulsed ruby laser[80].

There are several techniques for growing high-quality ZnO single-crystal films[22] such as *molecular-beam epitaxy* (MBE)[81][82], *pulsed-laser deposition* (PLD)[83][84], *metal-organic chemical-vapor deposition* (MOCVD)[85][86], and *hydride or halide vapor-phase epitaxy* (HVPE)[87][88]. But PLD is a widely used method for the deposition of thin film, particularly films of oxides and other compounds and materials that are difficult to deposit by other means[89]. PLD possesses some attractive qualities that make it potentially useful for the deposition of magnetic multilayer system. It is, in principle at least, capable of a high degree of control in depositing layers of precise thickness.

The advantages of this technique are: the possibility of ejecting compounds of highly complexity retaining the stoichiometry; the ability to control the film thickness with good accuracy, making it possible to work at low dimensional systems which require a few monolayers; cleaning of the process due, firstly, to the energy source is located outside the evaporation chamber and, secondly, the low level of incorporation of impurities due to the short duration of the process, typically in the order of several microseconds; can be combined with other deposition techniques for hybrid configurations to optimize the processes of growth and improved film properties; ability to deposit reactive or inert atmosphere because it does not require electron beams or hot filaments within the deposition chamber (energetic species in the plasma

react readily with the gas molecules to form simpler compounds).

Most important disadvantages are the splashing, which involves the deposition of droplets and the difficulty in obtaining large-area homogeneous layers.

The PLD technique is conceptually simple and can be divided in four steps: ablation, expansion, deposition and nucleation[52].

The PLD system consists of a laser as an excitation source and a vacuum chamber where ejection of material takes place. In the evaporation chamber ultra high vacuum (UHV) is required, alternatively the presence of another gas which is involved in the reservoir can be used to conduct the process in an enriched atmosphere.

We have used a multi-target PLD system. The vacuum chamber is made of stainless steel in a T-shape with different openings for the sample holder, vacuum pumps, sensors, laser radiation and oxygen. To obtain the vacuum, a rotary pump and a turbomolecular pump are used to achieve a pressure 10^{-7} mbar after several hours of operation. The base pressure can be reduced to $6{\cdot}10^{-8}$ mbar. A high vacuum was required to reduce the contamination of the film by unwanted impurities.

The laser used is a quadrupled Nd:YAG pulsed laser with a repetition rate of 10 Hz. The wavelength at which the laser operates is 266 nm, with an energy of 12-15 mJ/pulse. The laser beam is focused on the surface of the target, achieving power densities of up to 10^8 W/cm^2

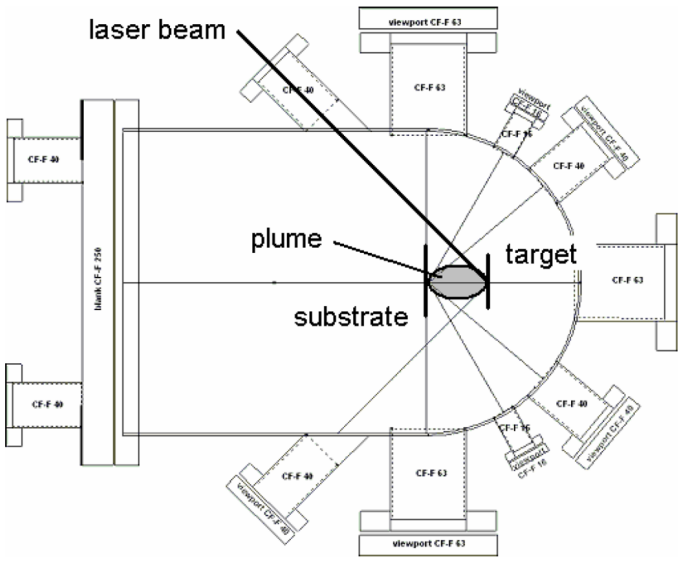

***Figure 3.1**: Horizontal cross-section of the sample deposition chamber.*

The output of a pulsed laser is focused onto a target material, located inside the UHV chamber, typically better than 10^{-6} Torr. The target is usually rotated in order to avoid repeated ablation from the same spot on the target.

Some of the thin films studied in this work were grown by Juan Ángel Sans during his PhD[35]. Moreover, we deposited several ZnCoO:Ga, (Zn,Mg)O, (Zn,Mg,Co)O and (Zn,Co)O-(Zn,Mg)O multilayers to perform some studies. Not being the study of the growth method a goal in this thesis.

3.1.1 The target

Following Kelly[90] the events which occur are generally sub-divided into primary and secondary processes, where the former include thermal, electronic and macroscopic sputtering. Their relative importance depends on the type of material in the target, the laser excitation wavelength and the pulse duration.

Targets were prepared from high purity powders with a stoichiometric mix of the required materials. In order to improve target homogeneity, powders were previously dispersed in pure ethanol before mixing. After drying, the powders were compressed at 8 MPa in a press for some minutes. The resulting pellets were thermally treated in a Nabertherm L3 oven with an air atmosphere at 950 ºC for 12 hours. The profile of the thermal treatment for, for example, ZnCoGaO is shown in Figure 3.2. The aim of the plateau around 100 ºC was to allow any water still in the pellets to evaporate.

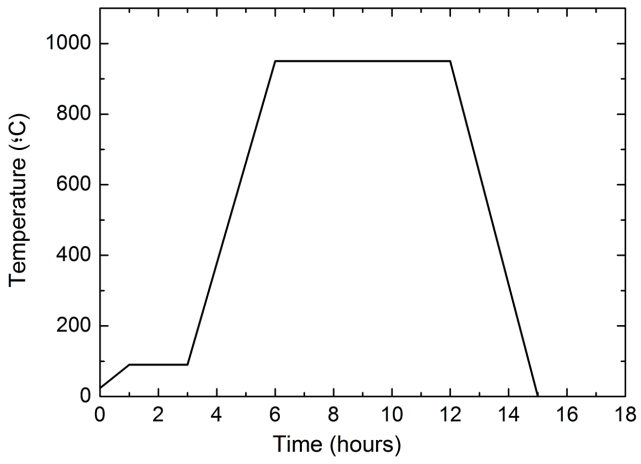

***Figure 3.2**: Profile of the thermal treatment of the pellets.*

3.1.2 Pulsed Laser Deposition

The targets were mounted in a holder, which could be displaced vertically to successive ablation of up to five targets. In this way superlattices could be deposited without breaking the vacuum. To produce the ablation, pulsed radiation from a quadruplet Nd:YAG laser was used. The sample stage is equipped with rotation for greater uniformity and heating. Then to achieve a uniform ablation, the targets were rotated by a magnetic system.

As it has been mentioned before, the PLD technique can be divided in four steps. First, a target is *ablated* by a laser to produce a plasma plume. The incident laser pulse (the radiation has an instantaneous flux of greater than 10^8 W/cm^2) induces extremely rapid heating of a significant mass of target material. It causes evaporation from the surface of target. Material start to boil off and expand into the gas phase[91]. A plasma plume has been produced which *expands* through the chamber toward the substrate positioned parallel to the target at a distance of 4 cm. After cessation of the laser pulse, the target will cool and resolidify. The ejected plume of plasma and neutral material expands away from the interaction volume. The properties and composition of the resulting ablation plume may evolve, both as a result of collisions between particles in the plume and through plume-laser radiation interactions[92]. Its distribution is generally symmetric about the target surface normal. The ejected flux is arranged to impinge on the substrate of interest, and *deposition* occurs. The deposited material then *nucleates* to form the thin film on the surface of the substrate which builds up over time. All of these steps need to be carefully controlled to ensure that the desired composition, uniformity and crystallinity of the film are achieved.

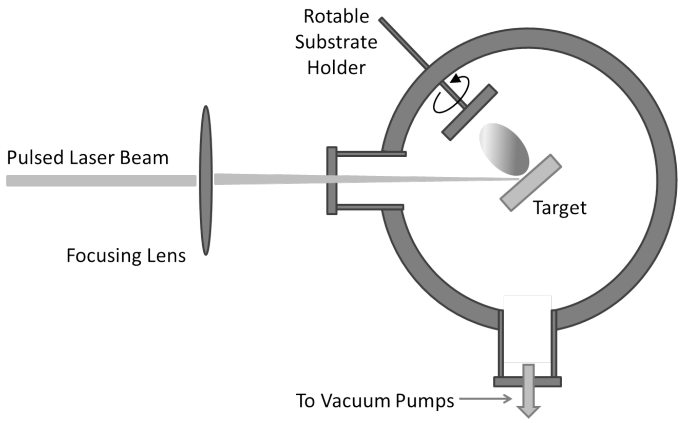

***Figure 3.3**: Schematic diagram of PLD.*

A suitable substrate for PLD must be flat, clean, free from defects and chemically unreactive with the material to be deposited. Mainly, C and R-oriented sapphire (Al_2O_3) and mica ($KMg_3(AlSi_3O_{10})F^2$) substrates were used due to the low mismatch between these substrates and wurtzite ZnO lattice. Furthermore, sapphire has a high transparency in the ultraviolet, the range in which the optical measurements were taken, and mica was used because, being a layered material, surfaces are free of unsaturated bonds and the adherence of the thin film is weak, which, in some cases, allows for the preparation of free standing samples, fully separated from the substrate, that could be used for high pressure measurements in the diamond anvil cell.

3.2 High Pressure Measurements

High pressure measurements are a valuable mechanism to study changes in materials as a function of volume without changing their chemical composition. Hydrostatic pressure is used to modify electronic states energy and transitions probabilities. Sometimes, high pressure can induce structural phase transitions and even stabilize structures not achievable through other means[93]. The application of high pressure as well as being a powerful technique for material preparation is also a very efficient tool for understanding the electronic structure of semiconductors nanostructures and exploring the effect of stress, direct-to-indirect cross-over, etc[94].

3.2.1 Diamon Anvil Cell[1] (DAC)

High pressure measurements were carried out in diamond anvil cells (DACs). The use of diamond has two important advantages over other anvils. First, diamond is the hardest known material and is capable of reaching higher pressures[95]. Second, diamond has a good optical window and it is transparent to photons of energy less than 5.5 eV and X-ray energies above 10 keV.

The diamond anvil cell was developed in the late 1950's in the National Bureau of Standards (NBS) by Weir, Lippincott, Van Valkenburg and Bunting[96]. Charles E. Weir handmade the first cell using only a lathe, drill press, hack saw, soldering iron, threading tools, files and a high speed grinding wheel to polish down the culets of the diamonds. This cell is based on the equation which relates the applied force, **F**, to the pressure, **P**, by means of the area, **A**. That is the principle of any cell: maximum force applied on a minimum surface[97].

$$P = \frac{F}{A} \tag{3.1}$$

Different diamond anvil cells were used for the high pressure experiments in this thesis. But the basic structure and principle are the same and very simple. The diamond cell consists of diamond anvils, mounted on pieces that are integrated separately to a fixed platform already a movable piston respectively[98]. Those diamonds are cut so that they have 16 sides and a regular polygon culet with a circumscribed circumference between 300 and 500 μm diameter. For reaching pressures above 100 GPa (1 Mbar) smaller culets (below 100 microns) are needed and culets must be beveled (using several slopes between the side and the culet. The other side of the diamond, called the table, has a diameter of nearly 4 mm. Then, a metal gasket with a centered hole, with a diameter about 50% of the culet size, containing the sample, the hydrostatic medium and ruby chips is placed between the flat parallel faces of two diamonds (Fig. 3.4). By pushing the two opposed anvils together, the sample pressure increases.

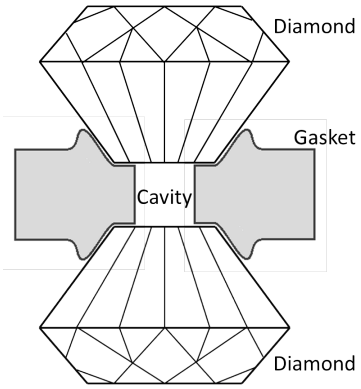

***Figure 3.4**: Diagram of diamonds and metal gasket in a DAC.*

At the University of Valencia we use a type of DAC known as a membrane cell. It was utilized for absorption measurements on nanoparticles and thin films under high pressure. This cell is composed of two steel parts which fit perfectly one into the other and it uses a metallic diaphragm or membrane to generate the pressure. The membrane, a toroidal cavity in which pressurized gas is introduced, is mounted on the upper part of the cell, between the piston and the piece which is joined to the body of the cell. When the membrane is inflated, it pushes the upper cylinder against the other increasing the pressure in the hydrostatic cavity, and transmitting it to the diamonds. This system

allows a fine pressure control and has the advantage that the pressure is controlled from a remote position.

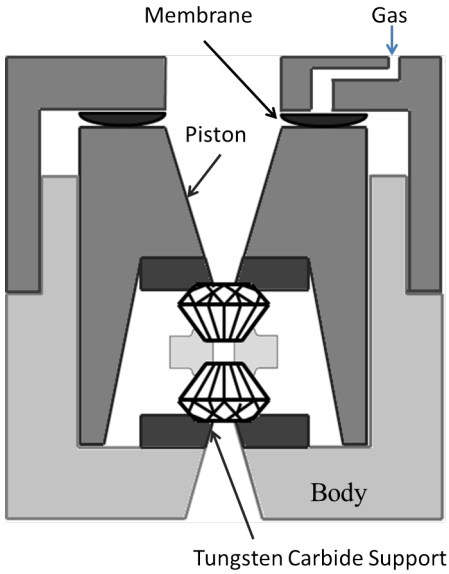

***Figure 3.5**: Vertical cross section of the membrane DAC.*

To carry on resistivity measurements in the Centre for Science at Extreme Conditions at University of Edinburgh we used a diamond anvil cell custom-designed to work at low temperatures into a commercially available physical property measurement system (PPMS) due to severe space limitation. The pressure cell has been built from non-magnetic Cu-Be alloy which is considered to be the best choice in term of magnetic and mechanical properties at room and low temperatures. Pressure between diamonds can be created by means of the driving screw. Using a stainless steel ball bearing in the pressure cell, a radial force generated by the driving screw can be converted into an axial force to the diamond. In order to prevent the rotation of the diamond, a small round-headed screw accessible from the outer wall of the cell body is used. It fits into a rounded groove on the piston along the vertical axis with an extra help from the squared stopper fit into a groove on the main body. Due to the thermal contraction of the cell material at low temperature leading to the unexpected increased of pressure, a Delrin® ring was used to compensate the contraction. The cell has been used for electrical resistivity measurements of ZnCoO:Ga thin films, using standard PPMS data acquisition system.

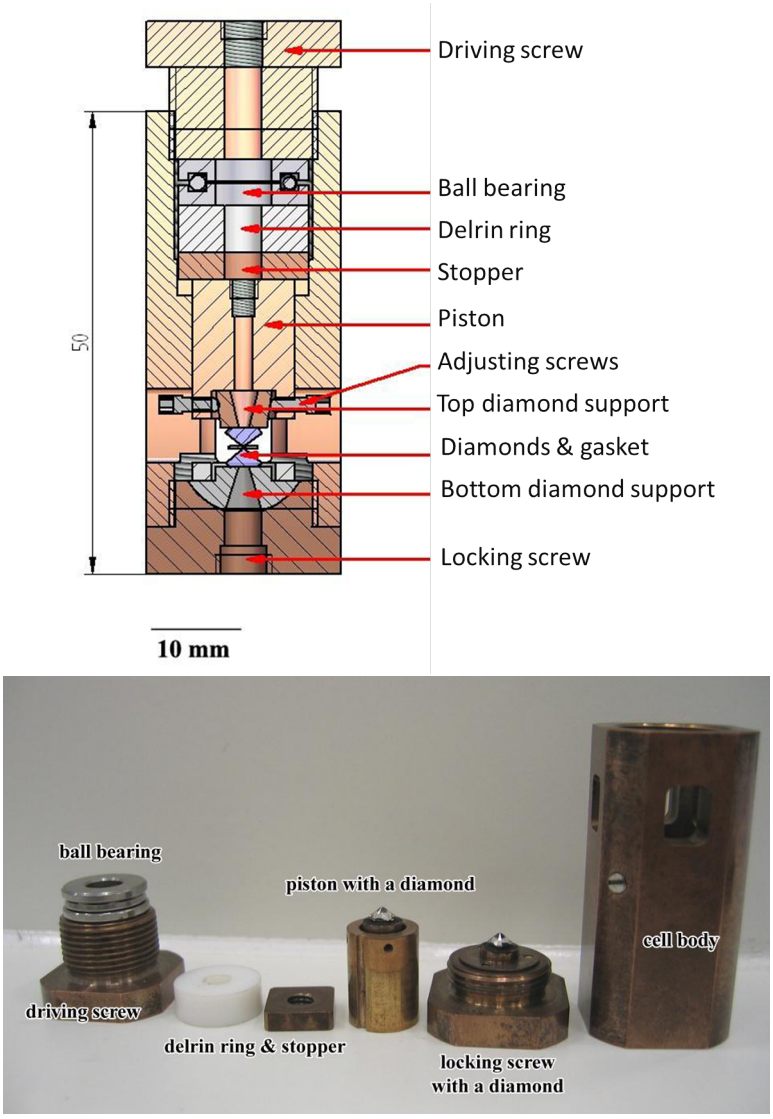

***Figure 3.6**: Up: Vertical cross section of the DAC for PPMS. Down: DAC components.*[99]

Cabin preparation

To form the cabin in which insert the sample, a metal shaped and holey gasket is situated between the small flat faces of the diamonds. By pushing the two parallel opposed anvils together, the sample pressure increases.

Usually the gasket is a steel disk 200 μm thick and 15 mm in diameter and it serves three purposes: it provides the high pressure sample chamber, it avoids directs contact between diamonds, and it gives lateral support to

the conical faces of the anvils. Firstly, the gasket is indented by DAC (until ca. 42 bar of membrane pressure) for compresses and hardens the material. The indented thickness is around 40 μm.

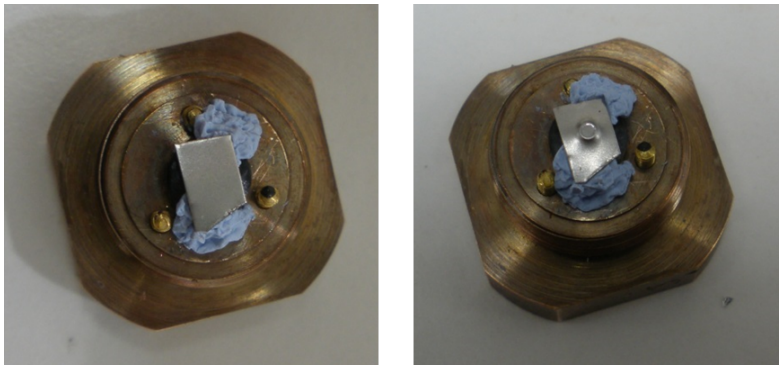

***Figure 3.7**: Gasket before and after indentation.*

Gasket perforation, in the center of the indentation, was performed using a semi-automatic spark erosion machine with tungsten electrodes. The cavity diameter was usually around 200-250 μm. We will see that additional preparation of the gasket is necessary for resistivity measurements.

To complete the preparation of the cell for the experiments, a sample is deposited centred on the small surface of one of the diamonds. Then, the gasket is placed in the same orientation in which the indentation was done by fitting marks and diamonds. With a needle some ruby spheres about 10 μm are added with the sample. They serve to calibrate the pressure inside the cell through of the shift of their luminescence lines that will be described later.

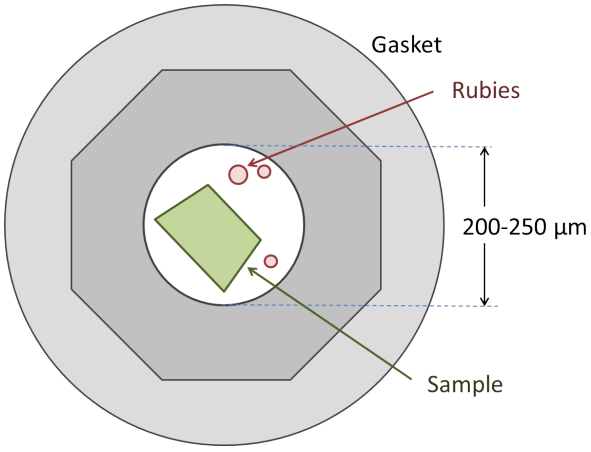

***Figure 3.8**: Look inside the cell when loaded.*

The hole inside the gasket is filled with a pressure transmitting liquid or medium to achieve as close as possible the hydrostatics conditions. A mixture of 16:3:1 methanol-ethanol-water has been used generally in this thesis. Finally, the other part of the cell is placed. The content of the hole is confined between both diamonds and the metal gasket. To prevent the escape of the liquid, we apply as fast as possible pressure (from 0.2 to 0.5 GPa).

3.2.2 Pressure Calibration

The pressure estimation is performed measuring the spectral shift experienced by the **R** lines of the ruby photoluminescence doublet with pressure[100].

The excitation of the ruby was performed using a frequency doubled, laser diode pumped, Nd-YAG solid state laser (532 nm). This laser excites an electron from the fundamental level of the Cr^{3+} ion to the $^4T_{2g}$ level. By emitting a phonon, the electron undergoes a transition from $^2T_{1g}$ or ^2Eg levels and recombines with the $^4A_{2g}$ level emitting a red photon before returning to the original level by the emission of another phonon. Emissions for transitions, from $^2T_{1g}$ or ^2Eg to ground level, are historically called **R1** and **R2** lines respectively[35].

The energy shift of these two peaks with pressure is characterized by the following equation; remain valid up to 23 GPa at room temperature[101]:

$$\frac{\Delta\lambda}{\Delta P} = 0.365 \mathring{A} Kbar^{-1} \qquad \text{with} \quad \lambda(P=0) = 6942 \mathring{A} \tag{3.2}$$

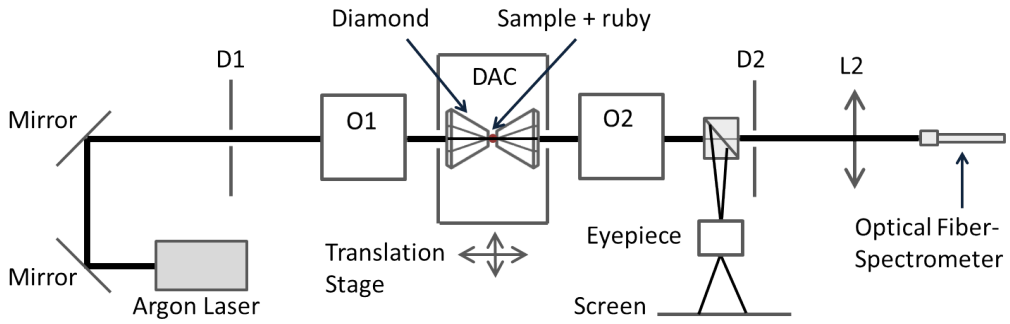

***Figure 3.9**: Optical set-up for measuring the photoluminescence peaks of the ruby.*

The optical set-up for measuring the shift of the mentioned photoluminescence peaks is shown in Figure 3.9.

3.3 Temperature dependence

Many of the spectroscopic characterization and transport measurements, such as optical absorption or resistivity, were accomplished as a function of temperature, both high and low.

***Figure 3.10**: Closed-cycle helium cryostat components (left) and compressor (right) used for low temperature experiments down to 15 K.*

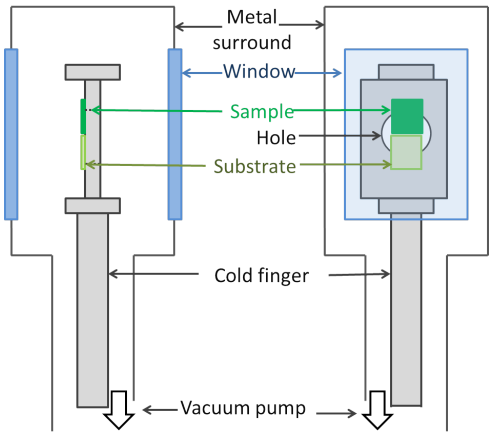

***Figure 3.11**: Cryostat arm scheme for low temperature measurements.*

Low temperature measurements were achieved using a close-cycle helium cryostat (Air Products CS202E). The major components are the expander or cold finger, the compressor, the radiation shield and the vacuum cover.

This system requires a vacuum pump for the sample space. Combination of a diffusion pump (Leybold PD 180 L) with a rotatory pump (Leybold trivac B) as well as a turbomolecular pump (Varian *Turbo Dry 70*) was employed in our experiments. A programmable temperature controller (APD-K cryogenics *HG-2*) together with a Si-diode thermocouple let us modify and stabilize the temperature in the range 15-300 K.

The sample was heated to near 500°C in air conditions using a resistance in thermal contact with the substrate holder. The temperature was calibrated in function of the power supplied to the resistance.

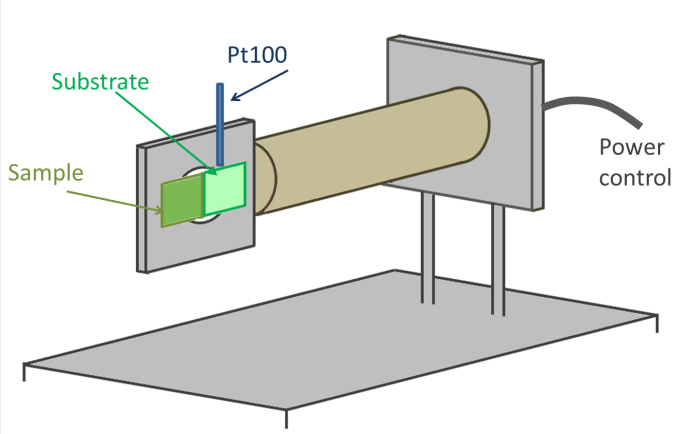

***Figure 3.12**: Heating assembly diagram.*

3.4 Optical Absorption

To characterize the structure, the optical properties of the samples were measured by absorption spectroscopy at room conditions, low and high temperature and high pressure. Low temperature measurements were conducted because the features of the absorption edge are more clearly visible when thermal vibrations are reduced. Moreover, certain vibrational properties of the samples may be determined from the temperature variation of the absorption edge through the Bose model.

To carry on these optical measurements at room temperature and at low temperature, we have used two specific equipments from the University of Cantabria in Santander.

A Cari 6000i (Varian) spectrophotometer was used to register diffuse reflectance spectra in the range 200-1800 nm. It is equipped with two light sources: a quartz halogen lamp for the visible/IR region and a deuterium

lamp for the UV, and two detectors: one photomultiplier (PMT) (Hamamatsu R928) for the visible region and one InGaAs detector for the near IR.

A FT-IR System (2000) (Perkin-Elmer) spectrophotometer was used to obtain the transmission spectra in the IR region. It is made essentially of three components: two radiation sources to cover the 4400-400 cm^{-1} range, one Michelson interferometer and a Mercury-Cadmium-Telluric detector.

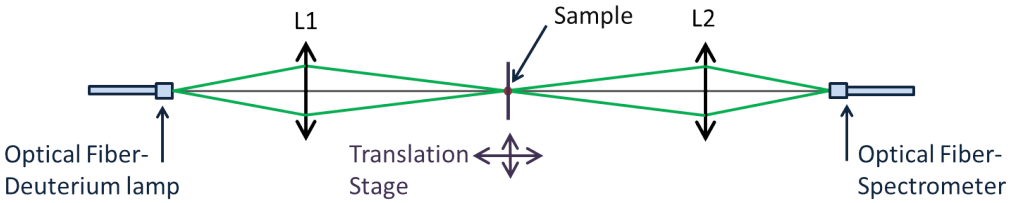

***Figure 3.13**: Optical set-up for measuring absorption spectroscopy at room conditions.*

Also, for this absorption measurements, non-conventional devices have been mounted at University of Valencia. The Figure 3.13 shows the simplest scheme of such assembly. This experimental set-up consists of a continual emission deuterium lamp, as UV light source, connected by an optical fibre focused by a lens (**L1**) in the sample. Light transmitted through the sample was focused (by **L2**) into the fibre optic guide and measured by an Ocean Optics HR2000 spectrometer. This spectrometer is connected to a personal computer for data acquisition and processing. The platform where we placed the sample and the substrate are located on an **xyz** translation stage.

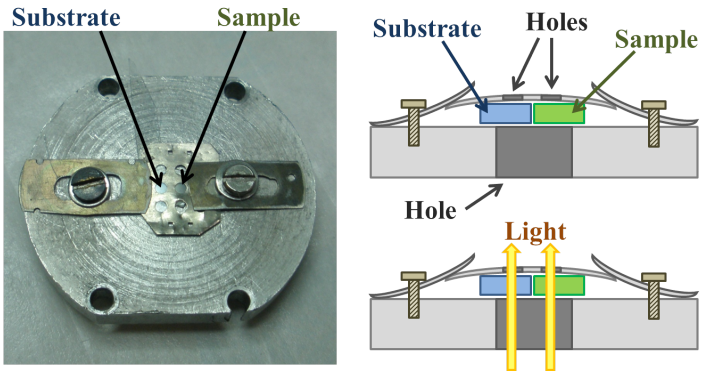

***Figure 3.14**: Left: Picture of the holder for measurements. Right: cross section of the holder.*

The sample and a sapphire substrate were mounted on the holder to enable the respective measurements of the sample spectra and the direct light spectra. This last is required for normalisation purposes. We show a picture of the set-up in Figure 3.14, together with a cross section of the holder and a scheme how the light cross all the system for the measurement. And **xyz** system was used to change the position of the focus between the sample and the substrate.

Also, measurements have been performed with polarized light. For this, a polarizer is positioned between lens **L1** and the sample. On what follows, we describe in more detail some aspects or changes that were conducted to carry on specific measures on temperature or pressure.

3.4.1 Temperatures

To execute measurements at high and low temperature, it is only necessary to replace the sample by the corresponding device in which the sample will be: either the cryostat or the heating system. Both devices are located on a **xyz** platform in order to position the sample (and the substrate) at the point where the beam is focused.

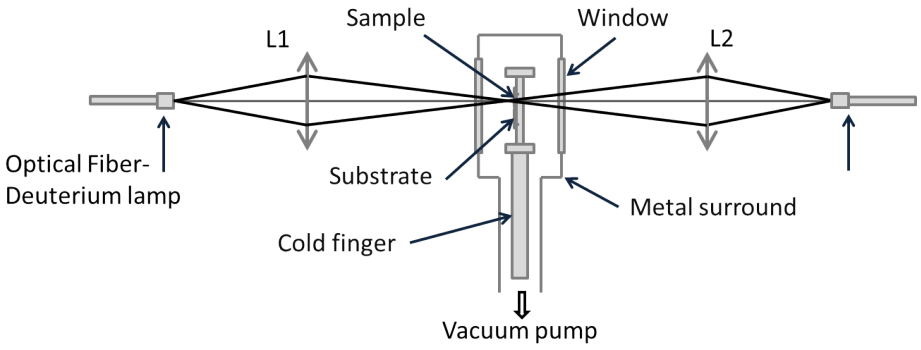

***Figure 3.15**: Optical set-up for measuring absorption spectroscopy at low temperature.*

3.4.2 High pressure

To carry on measurements under pressure, more elements are required to focus the beam inside the cell. After the deuterium lamp and the collimating lens holder (**L1** and **L2**), the collimated beam passes through a calibrated hole (**D1**) and enters a confocal optical system which consists on two reflection Cassegrain objectives 15x (**O1** and **O2** in the figure). The diamond

cell is loaded with the sample, rubies and the transmitting medium between O1 and O2. The reflecting objectives were incorporated in order to avoid chromatic aberration.

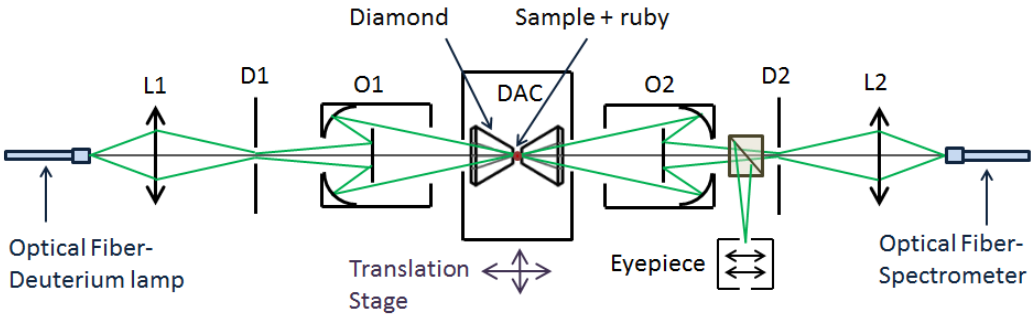

***Figure 3.16**: Experimental set-up for the optical absorption measurements at high pressure.*

The cell is placed on a **xyz** positioner, which, by manual manipulation, allows the beam focusing both on a plane of the sample and outside it (Fig. 3.17). This targeting process is done visually. For this end, at the confocal system output, there is a prism with a perpendicular displacement to the optical bench in order to direct the beam path to an eyepiece. This allows direct visualization of the interior of cell where the sample is. The final signal arrives by an optical fibre to the detector.

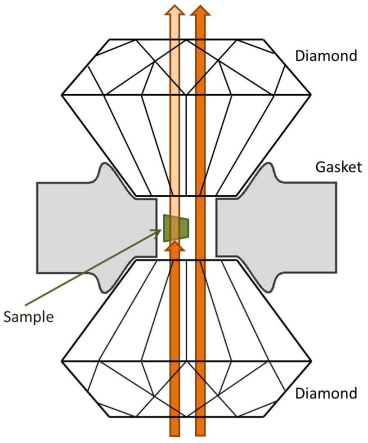

***Figure 3.17**: Light beam through the cavity inside and outside the sample.*

3.5 Raman Spectroscopy

Raman spectroscopy deals with the study of the fraction of incident light scattered by a sample. Rayleigh scattering is an elastic photon process in which the scattered photon energy is equal to the incident photon energy. However, in Raman spectroscopy the light is inelastically scattered by a substance. The Stokes and anti-Stokes Raman scattering involve virtual levels which do not correspond to real states, as a result, Raman spectra are much weaker than fluorescence spectra by a factor of about 10^6-10^8. Raman experiments are usually carried out under non-resonant illumination so that the Raman spectrum is not masked by the more efficient emission spectrum[102][103]. A typical Raman spectrum shows an intense band at the incident frequency, $\boldsymbol{\omega}$, resulting from Rayleigh scattering, and fainter Raman band on both sides of $\boldsymbol{\omega}$ at distances corresponding to vibrational frequencies, $\boldsymbol{\omega_k}$. In practice, the Stokes Raman scattering, proportional to $n+1$ (n = number of excited phonons), is more intense than the anti-Stokes, proportional to n, and the lower spectral region is used[104].

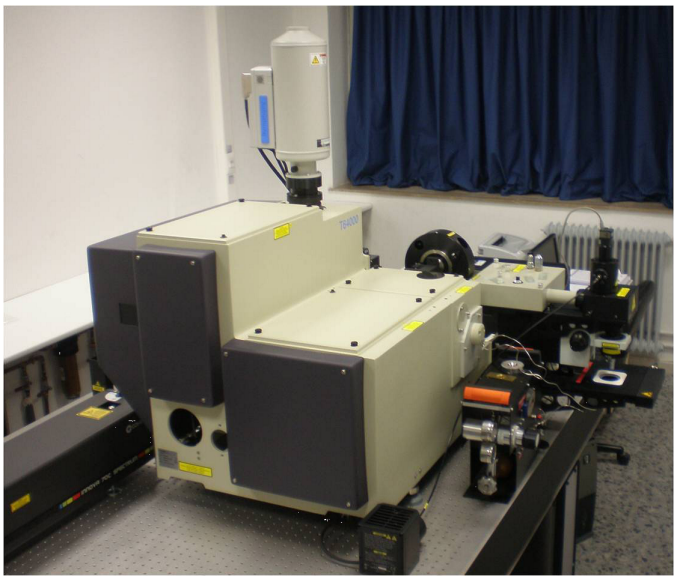

***Figure 3.18**: Equipment used for Raman measurements at the High Pressure an Spectroscopy group laboratories at University of Cantabria.*

The T64000 Raman spectrometer system (Horiba), together with a Kripton-Argon laser (Coherent Innova Spectrum 70C) (the 514.5nm green line used), and a Nitrogen cooled CCD (Jobin-Yvon *Symphony*) with a confocal microscopy for the detection, were employed for Raman experiments. The

T64000 system is composed of three monochromators (640 nm focal length) with two basic configurations; triple additive mode, with the three monochromators operating in series (3x640 focal length), and subtractive mode, in which the two first monochromators filter the laser, and the analysis is done with the third one. LabSpec software permits data acquisition and treatment.

The samples grown on sapphire substrate were measured at the University of Cantabria. During the stay at the University of Lyon, some of these measurements were repeated for subsequent pressure dependent experiments. But, unfortunately, we did not get a sufficiently clear and defined signal inside the anvil cell with any of the equipment available there.

Samples with 10 and 20% of cobalt were measured in Lyon with a blue laser of 473 nm and the sample of 2% of Co in Santander with a green laser of 514.5 nm. Possibly, due to a different calibration between equipments, the entire spectrum of the sample of 2% is displaced to less wavenumber. Lyon spectra are closer to the literature[105][106][107]. The difference was of 5 nm that has been corrected for understanding better the results.

3.6 Fourier-Transform Infrared Spectroscopy

Fourier-transform infrared (FTIR) spectroscopy is an excellent spectroscopic technique with which to investigate the lattice dynamics and electronic excitations in solids[108].

For the FTIR studies, we used an experimental set-up constructed at the University of Valencia.[109]. It consists in a compact TEO-400FTIR interferometer module and an external microscopic optical bench with cassegrain focusing objectives. This set-up is capable of recording transmission and reflection infrared spectra at high pressure.

The equipment arrangement for the reflection measurements is shown in Figure 3.19.To implement this configuration we have introduced a right angle mirror (RAM) with a 45º reflecting surface prior to the first Cassegrain objective (CG1). This mirror cuts a half portion of the incident IR beam and allows the other half to pass through the Cassegrain objective (CG1). The back-reflected IR beam from the sample in the DAC is again reflected by the 45º mirror (RAM) and focused at micro-iris (S2); it also acts as a spatial filter, stopping most of the IR light reflected from the diamond surface. The back-reflected IR beam is then focused on the mercury cadmium telluride (MCT) detector by means of the parabolic mirror PM2[109].

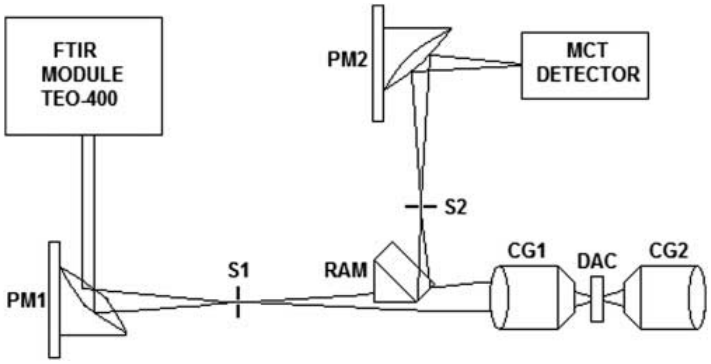

***Figure 3.19**: The optical layout of the FTIR set-up in the reflection configuration (PM1, parabolic mirror; S1, micro-iris; RAM, right angle mirror; CG1, Cassegrain objective; DAC, diamond anvil cell; CG2, Cassegrain objective; S2, micro-iris; PM2, parabolic mirror).*

3.7 Microscopy

3.7.1 Transmission Electron Microscope

Measurements with high resolution analytical transmission electron microscopy (TEM and HRTEM), selected area electron diffraction (SAED), and energy-dispersive X-Ray Spectroscopy (EDX) were conducted in microscopy services at University of Valencia. The system used is the Tecnai G^2 F20 S-TWIN. It is a true multi-purpose, multi-user 200 kV instrument. It is possible combining high performance in all TEM, EFTEM, Lorentz, STEM and EDX/EELS spectrum imaging modes.

TEM is the most effective and direct technique available to fully characterize a material in the atomic scale. A TEM is an instrument that relies on the fact that we can probe the atomic nature of a material because the resolution obtainable is comparable to the wavelength of the probing beam.

In TEM measurements, electrons are generated from an electron gun and accelerated by a high voltage and focused on the specimen (sample) using multiple electromagnetic lenses. After passing through the sample, electrons are collected and the resulting image and diffraction pattern can be captured on film or a CCD camera. The main parts or the microscope are: electron source, sample holder, light and electron optics, electron detection and display. The TEM resolution, the smallest distance that can be resolved $\boldsymbol{\delta}$, is given by $\delta = 0.61\lambda/\beta$, where $\boldsymbol{\lambda}$ is the wavelength of the radiation and depends on the electrons energy, and $\boldsymbol{\beta}$ is the semi-angle of collection of the

magnifying lenses. Some disadvantages of the TEM are that it is a destructive technique, some materials are sensitive to electron beam radiation and the data obtained is from a very small region. Moreover, TEM presents 2D images of 3D specimens, so the information is average through its thickness. To perform TEM imaging, samples were prepared by suspending solid samples in ethanol solvent in a small glass vial followed by a sonication treatment in an ultrasonic water bath[110]. One drop of the prepared suspension was applied to carbon films on copper grids. The thickness of a TEM specimen must be very small: usually in the range 10 nm to 1μm [111]

3.8 Electric Measurements

The resistivity measurements have been done using of the four points method at ambient pressure and by the Van der Pauw and two points method for measurements under high pressure. All these methods are explained in the theory chapter.

3.8.1 The Setup At Ambient Pressure

To conduct ambient pressure measurements of electrical resistivity, the sample has to be large enough to measure the distance between the connections. For that reason, we have used the four point technique.

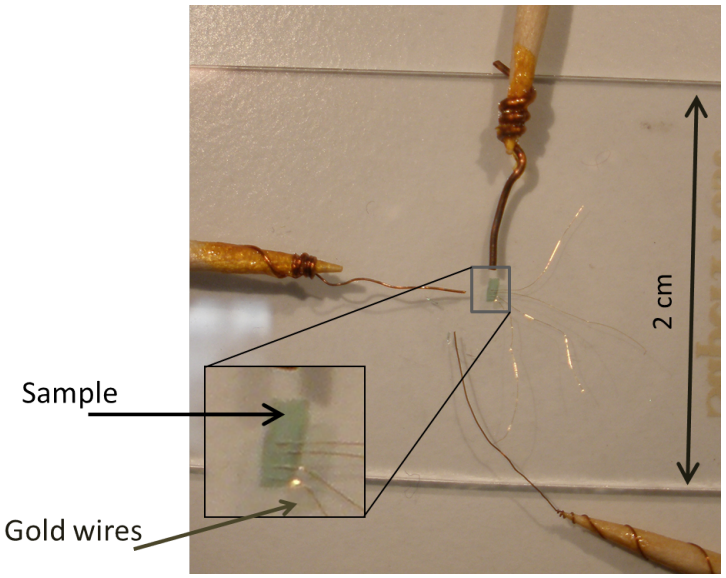

***Figure 3.20**: Wire connections done on the sample for electrical resistivity measurements at ambient pressure.*

The geometry of the sample and the electric contacts can be important. The contacts are often made by painting silver-paint or applying metal electrodes to the sample. If these contact areas are large or close to each other, this could reduce the accuracy of the resistivity measurement. It is better to make the two voltage contacts in a four-point measurement as small or thin as possible, and make the distance between the inner electrodes much larger than the sample thickness. This also allows a more accurate estimate of the effective volume of the sample being probed. It is critical that the four contacts to the sample in a four-point measurement being completely independent; there should be nothing other than the material of the sample connected to each of the four wires.

Next, on a sample holder, the sample is cut to an approximate size of 0.7 x 1.5 mm. On the sample there are 4 gold wires, whose ends have dipped in silver paint. The distance between these wires is about 300 μm.

For silver paint dries, the specimen is placed on a heating stage and held at 200 °C during two hours. Once the sample is cooled, it is placed on the proper platform to cryostat and to solder the gold wires to connections that later link to the circuit prepared in PPMS.

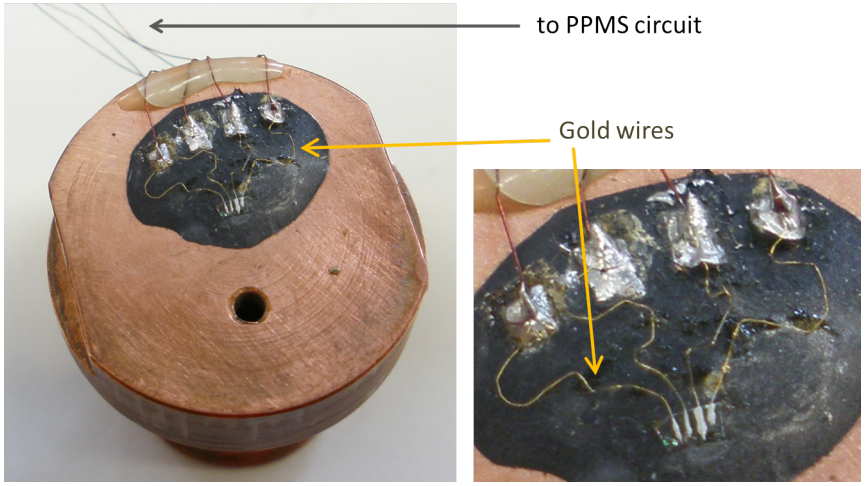

***Figure 3.21**: Left: the sample prepared on the platform of PPMS. Right: zoom on the sample and the gold wires.*

3.8.2 The Setup At High Pressure in DAC

To conduct the measurements at high pressure into the diamond anvil cell, due to the small sample size, the two point and Van der Pauw technique have been used. As mentioned above, for carry on the electrical measurements,

additional preparation is required for the cell, to prevent the contact between the wires and the gasket.

After performing the indentation and the hole in the gasket, it is placed on the bottom diamond and fixed to it. Separately, resin is prepared coming into two liquid phases over alumina (STYCAST 1266) mixing in proportions determined by the manufacturer. This mixture is kneaded until it is compact but workable. Then, the gasket is covered from the top of the crater to the outer edges (with a not very thin layer). The mass is saturated with alumina and covered with it inside the crater and the hole. After that the system dries at least two hours at ambient conditions (or three minutes on a platform heating). Then a hole is made by melting the resin with a laser, or eroding it with a needle. The hole in the resin should be centred on the gasket and be smaller. For example, if the gasket is 200 microns, the final hole should be about 150 microns.

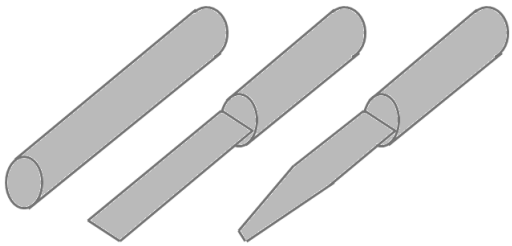

***Figure 3.22**: Preparation process of the gold wire.*

In our case the sample should be about 100 x 100 μm. Due to this very small size, the gold wires are heated during 5 min at 600 °C. In this way, they are more malleable, and thus the tip is flattened and cut (as shown in Fig. 3.22) to obtain a much thinner contact.

Once prepared, the gold wires are fixed to the sample in the same way as it was done in the measurements at ambient pressure. We impregnate the wire tip in silver paint, placing it on the sample and heating it to dry. Next, the sample has to be placed into the hole, leaving the wires above the Stycast. After the sample is stabilized inside the hole and secured the gold wires, they are soldered to copper wires that are attached with epoxy. That leaves the cell prepared for connections.

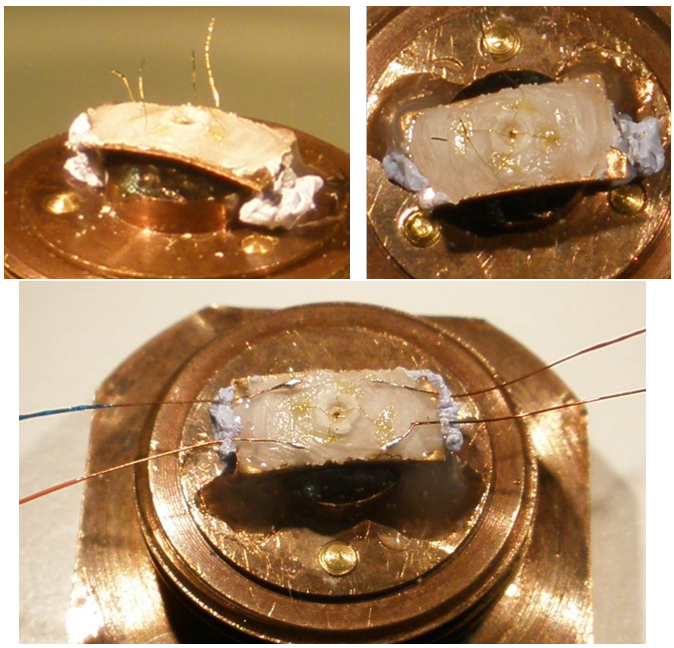

***Figure 3.23**: Up: the sample with the gold wires on the gasket. Down: the sample, the gold and the Cu wires.*

It remains adding a ruby with the sample, close the bottom of the cell, extract the wires, add the PTM (pressure transmitting medium), close the top and solder the wires to the side of the cell in the areas ready for this purpose.

3.9 Magnetic Measurements

For the magnetic characterisation, a Semiconductor Quantum Interference Device, SQUID, were used during the stay at University of Cantabria, in Santander. The SQUID magnetometers are the most sensitive of all magnetic field measuring instruments[112]. In particular, we have used a QD-MPMS XL 5T (Figure 3.24). It is composed by a superconducting ring with one or two Josephson junctions. In standard measurements, when a magnetic dipole moves perpendicular to the SQUID surface, a tunneling current through the Josephson barrier is produced. The generated current is proportional to the dipole size[113][114].

SQUIDs measure the change in the magnetic field from some arbitrary field level; they do not intrinsically measure the absolute value of the field. The SQUID is also capable of measuring AC susceptibility $\boldsymbol{\chi_{AC}}$. This is

achieved by applying a small oscillating magnetic field with a determined frequency $\boldsymbol{\omega}$, and measuring the time response. Then the AC susceptibility $\chi(\omega) = \chi' + i\chi''$ can be obtained. The critical (maximum) field of the superconducting coil is $H = 50$ kOe, and includes a system to quench the coil above its critical temperature, in order to remove any remanent magnetisation.

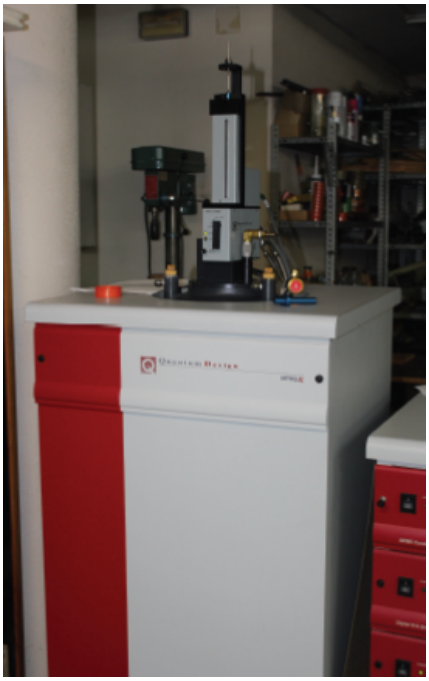

***Figure 3.24**: SQUID magnetometer. The Dewar is here enclosed within a wooden cabinet. The most salient apparatus is the arm (top of the image) guiding the sample in the SQUID and allowing up/down movement, for the extraction measurement.*

Chapter 4

Results: ZnO and (Zn,Co)O Thin Films

For a coherent development and presentation of the results, we will progressively show the different studies we have done of diluted magnetic semiconductors based on zinc oxide. Therefore, to follow a certain order, we begin by thin films of zinc-cobalt oxide alloy semiconductor..

As we shall see in what follows, we start from the basis on other previous studies on this material[35][52]. But, for example, if in previous works the optical properties were studied at room temperature, here we also see what happens if we take these spectra at low temperature, or if we use polarized light on oriented samples.

Likewise, we show some SEM images made on this material and the results of Raman spectroscopy for ZnO thin films with different concentrations of cobalt and grown on different substrates (mica and sapphire).

4.1 Scanning Electron Microscope

Figures 4.1, 4.2 and 4.3 show the images obtained by the electron microscope for samples of pure ZnO and ZnCoO with 20 and 30% of cobalt, respectively. The image corresponding to pure ZnO (Fig. 4.1) shows a fairly compact and regular homogeneous surface, but they show some small cracks or craters and some droplets or aggregates. Figure 4.2, corresponding to 20% Co thin film, although it shows a compact and homogeneous surface, it shows granular aggregates. Figure 4.3, corresponding to a sample with 30% of Co, shows a very homogeneous and smooth surface (similar to the ZnO), but with small crystals embedded. This would be similar to other previous work in which the films show uniform and smooth surface with granular microstructure due

to the columnar growth mode.

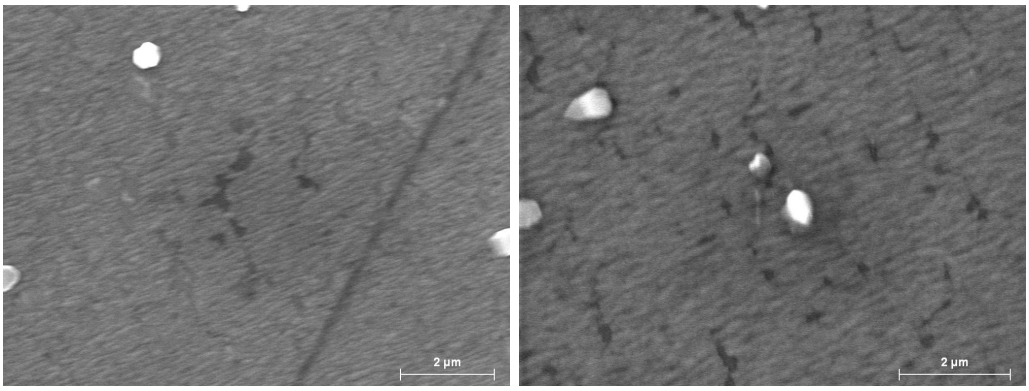

***Figure 4.1**: SEM image of a pure ZnO sample grown in a R-sapphire.*

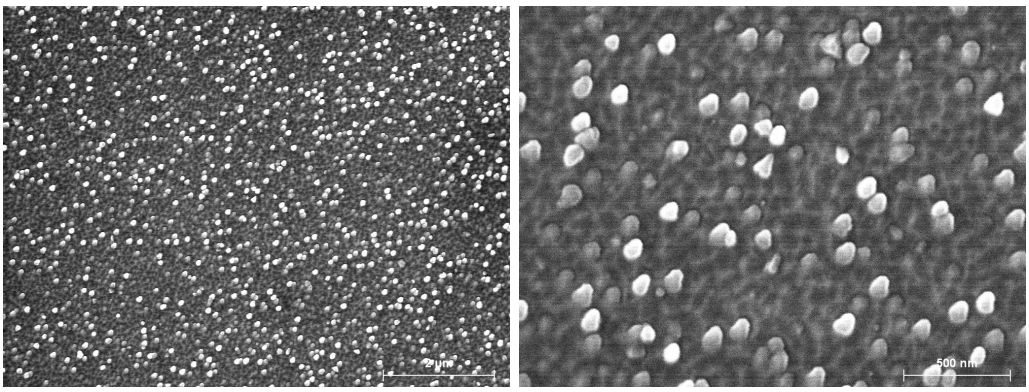

***Figure 4.2**: SEM image of a $Zn_{1-x}Co_xO$ with 20% of Co.*

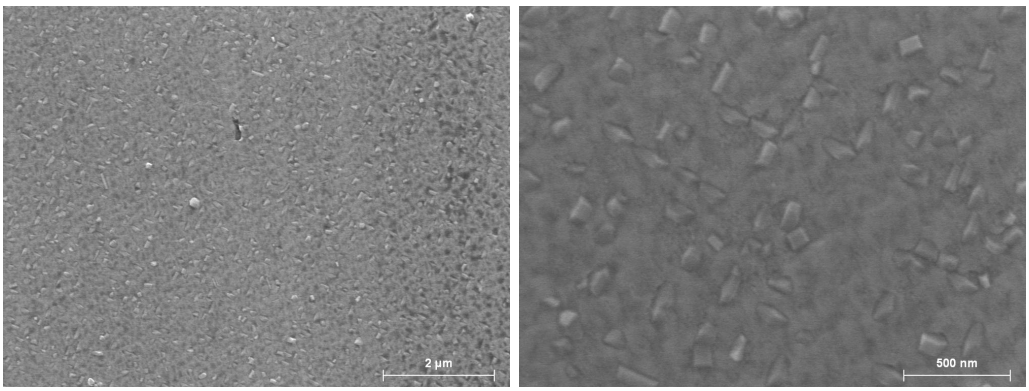

***Figure 4.3**: SEM image of a $Zn_{1-x}Co_xO$ with 30% of Co grown in a R-sapphire.*

4.2 Optical Properties

In this section we are going to focus on the study of the optical properties of thin films of $Zn_{1-x}Co_xO$ with different content of cobalt, and the evolution of this optical spectra as a function of temperature.

4.2.1 Optical Properties at Room Conditions

In the PhD thesis of J.A. Sans[35] and many other works[115][116][117][118][119], we can find the study on (Zn,Co)O thin films with wurtzite structure alloys as a function of the amount of alloyed cation. This previous research shows several effects on the optical properties due to the presence of substitutional Co in Zn site. We have performed new optical absorption measurement at room conditions and we have done a more comprehensive study. These spectra will serve us as a guide for the development of the rest of this work.

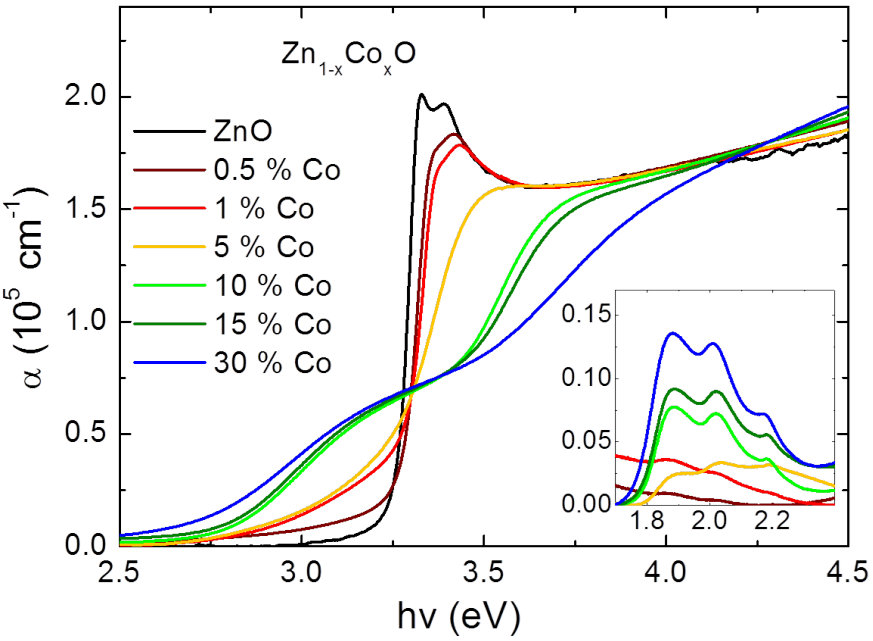

***Figure 4.4**: Optical absorption of $Zn_{1-x}Co_xO$ thin films with different cobalt content.*

Figure 4.4 shows the absorption spectra for thin films of $Zn_{1-x}Co_xO$ grown on c-oriented sapphires with different concentrations of cobalt. A pure ZnO absorption spectrum is included as reference. These results reproduce what was obtained in other works earlier. Then I make a brief explanation of what can be observed.

As pointed out in several references[35][52], absorption spectra show three main differences with respect to pure w-ZnO:

1. It is obvious that the addition of cobalt produces an increase in the energy of of the absorption edge which corresponds to *band to band transition*. This is due to the $p-d$ repulsion between the $3d$ levels of the transition element and the $2p$ of the oxygen. The $p-d$ repulsion causes that the valence band moves to lower energies. Also, as Zn is replaced by Co, the $p-d$ "up-repulsion" due to Zn $3d$ electrons also decreases which contributes to the shift of the VBM to lower energies. The effect is larger when the $3d$ level is closer to the $2d$ O. As a consequence, the fundamental absorption edge shifts to higher energies.

2. We also observe that an absorption band develops below (and overlapping) the fundamental absorption edge, at 2.5-3 eV approximately. This band is the *charge transfer transition* (CTT) band, and by their behaviour under pressure, it was assigned to a transition from the ground state of $3d$ Co level to the conduction band of the alloy. Its intensity increases with increasing the cobalt content.

3. The *exciton peak* is clearly visible in the pure ZnO thin film indicating good quality. But it reduces its intensity and shift to higher energies as the Co proportion increases.

4. Between 1.7 and 2.3 eV three bands increase their intensity in proportion with the increase of cobalt[115]. These bands are due to electronic transitions in the tetrahedral crystal-field split $3d^7$ Co^{+2} levels, from the d ground level to the third excited one. The presence of these peaks indicate that cobalt is substituting as Co^{+2} on Zn lattice sites in the films. In particular, the peaks situated at energies of 1.9 eV, 2.0 eV and 2.2 eV correspond to the $^4A_2(F) \rightarrow {}^2E(G)$, $^4A_2(F) \rightarrow {}^4T_1(P)$ and $^4A_2(F) \rightarrow {}^4A_1(G)$, respectively[120].

In order to get as much information as possible from experimental spectra, we have calculated their numerical derivatives, that are shown in Figure 4.5. For low Co concentration (1 to 5%), features associated to AB exciton peaks are observed (the derivative becomes negative for a small interval. For the larger Co concentrations (10 to 30%) the derivative spectrum mainly exhibits two peaks. The low energy one is associated to the charge transfer transition and the high energy one is associated to the onset of band-to-band transition.

This shape allow for the determination of several spectroscopic features. Three of them are quite immediate as they derive from two maxima and a minimum.

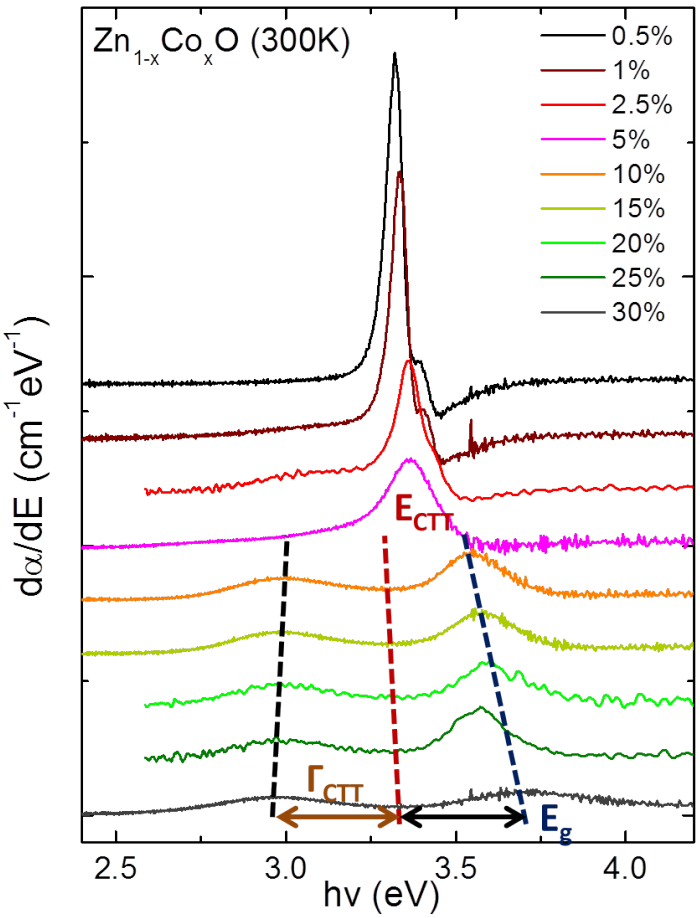

***Figure 4.5**: Numerical derivatives of the experimental spectra of (Zn,Co)O thin films.*

If we associate the minimum to the maximum absorption of the CTT band, assumed to have Gaussian shape, the energy interval between this minimum and the low energy maximum can be associated to the full-widht-at-half-maximum (FWHM) of the charge transfer transition band. The fact that the minimum and the high energy maximum shift to higher energies at a close rate (as a function of the Co content) is consistent with the interpretation of the CTT as a transition from the ground state of Co $3d$ states to the alloy conduction band. The fact that the low energy maximum shifts to lower energies indicates that the width of the charge transfer transition increases

with the Co concentration. This is confirmed by the behaviour of a less well-defined feature, shifting also to lower energies as the Co concentration increases (the onset of the low energy maximum).

In order to have a more quantitative description we proceed to the interpretation of the absorption spectra by means of a modified version of the Elliot-Toyozawa equation including (besides the discrete exciton and continuous absorption) a Gaussian to give account of the exciton-LO resonance and another one giving account of the charge transfer transition band.

Let's stress that describing the CTT by a symmetric Gaussian band (and not a more realistic equation like those described in the theory introduction) is a simplification, but it is justified both from experimental and interpretation reasons:

- Experimentally, because the derivative spectra shown in Figure 4.5 exhibit a clear Gaussian shape (this is expected because scattering mechanisms give rise to a widening of the electronic states in the conduction band and then they smear out of the well-defined onset of the CTT). The asymmetry would quickly be compensated by Gaussian convolution.

- From an interpretation point of view, the use of an asymmetric function getting deep into the band-to-band part of the spectrum would introduce an artificial increase of the intensity in a part of the spectrum where there are no spectral features allowing for a separation of the charge transfer transition and band-to-band contribution. The fact that no discernible increase of the continuum intensity is observed also indicates that the CTT is actually contributing mainly near or below the band to band onset.

- The fact that a Gaussian band gives account of the CTT also indicates that the localization wave function must be Gaussian: as we saw in the theory section, hydrogenic functions give rise to very asymmetric absorption bands with a slowly decreasing tail extending to quite high energies.

For 1 to 5% Co, the discrete exciton contribution must be taken into account (the temperature evolution of the spectrum confirms this, as the exciton peaks become more defined).

For 10 to 30% of cobalt content, the alloy disorder makes the exciton lifetime too short to give rise to defined discrete states. Only the CTT and continuous band-to-band are needed to get a food fit. Figure 4.6 shows the fits.

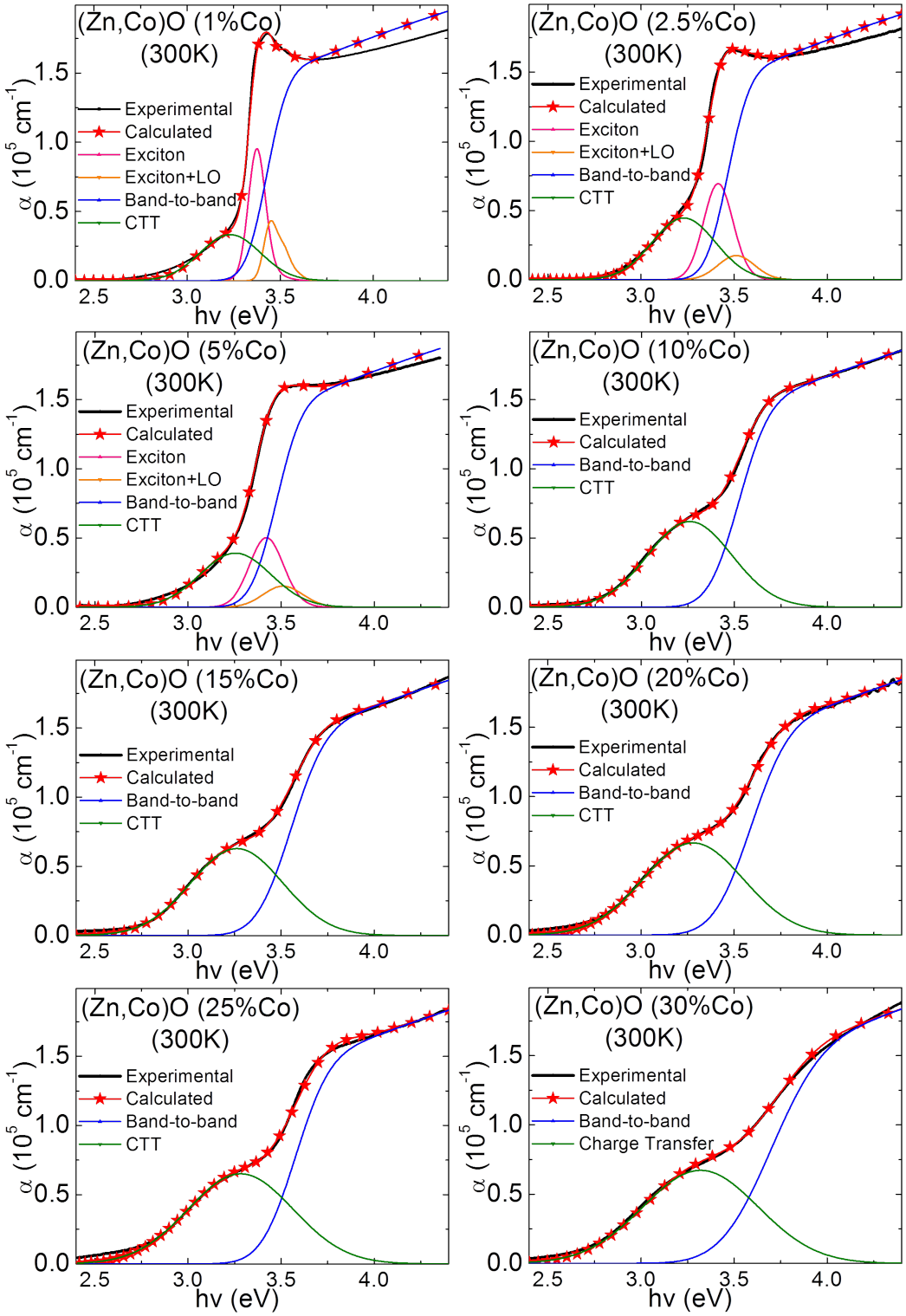

***Figure 4.6**: Fitting of absorption spectra of $Zn_{1-x}Co_xO$ thin films.*

In order to show the good correlation between the derivatives spectral features and the fitting parameters, both spectra are shown together for some concentrations.

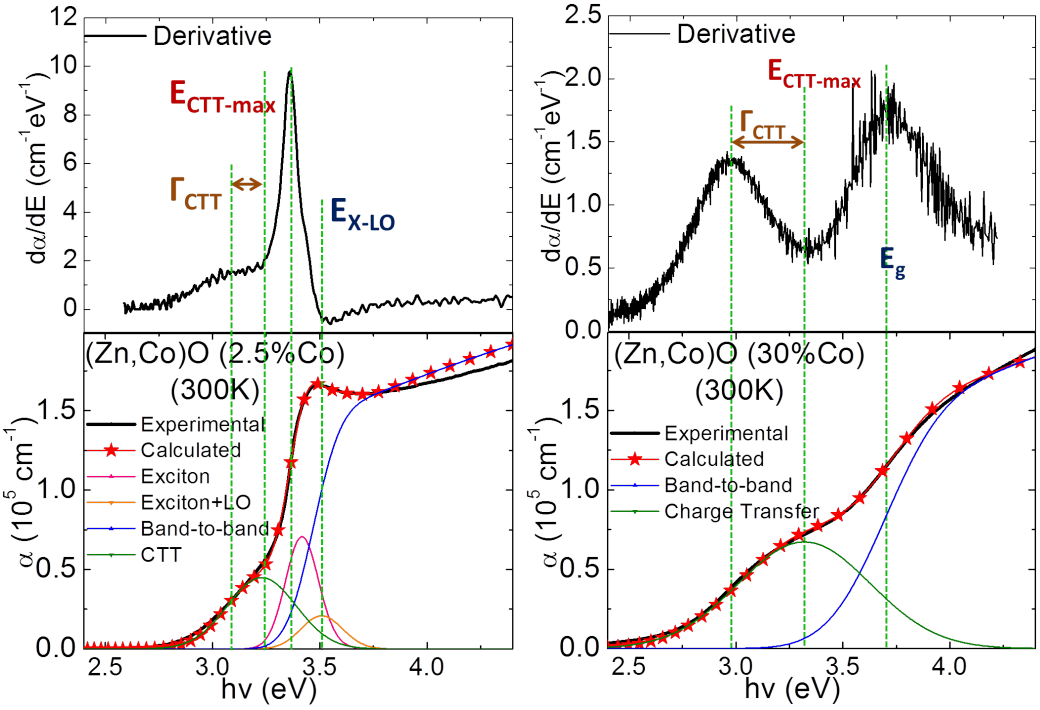

***Figure 4.7**: Correlation between the derivative of the spectra and the fitting parameters.*

For the 30% Co film spectrum the coincidence is perfect: the above mentioned spectroscopic features of the derivative appear nearly exactly at the energies where the fitting procedure places the bandgap, CTT maximum and low energy half-intensity of the CTT maximum.

For the 2.5% Co thin film spectrum features are more complicated as the exciton contributions are more mixed near to the band-to-band onset. The zero derivative energy (maximum of the spectrum) turns out to be very close to the exciton-LO contribution. The derivative maximum does not correspond to a well-defined energy (it occurs just below the exciton peak. For the CTT band spectral interval (even if the derivative minimum is not well defined) the agreement is better.

Once the consistence of the results is shown, we present the parameters obtained in the fitting, that are given in Table 4.1 and shown in Figure 4.8.

***Table 4.1**: Fitting parameters for the absorption spectra at room conditions.*

Nominal Co Content	E_{gap} **(eV)**	Γ_{gap} **(eV)**	E_{CTT} **(eV)**	Γ_{CTT} **(eV)**	I_{CTT} **(cm^{-1})**
30	3.674	0.210	3.305	0.300	67175.9
25	3.570	0.145	3.278	0.285	65075.6
20	3.586	0.160	3.278	0.270	66489.9
15	3.550	0.150	3.260	0.245	63152.3
10	3.528	0.132	3.260	0.230	61862.3
5	3.478	0.110	3.255	0.200	39054.0
2.5	3.470	0.100	3.230	0.160	44586.7
1	3.430	0.063	3.200	0.150	33244.0

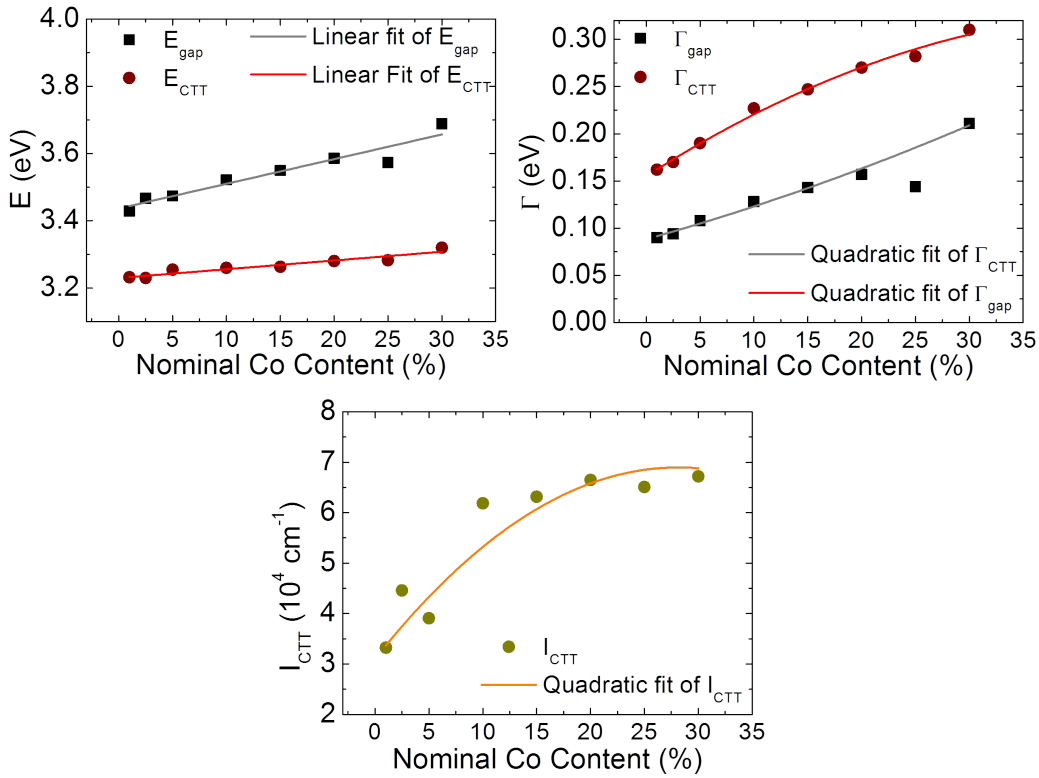

***Figure 4.8**: Dependence of the fitting parameters with the content of cobalt.*

Let us first notice that both the band-to-band and CTT maximum energies increase nearly linearly with the Co concentration, as observed previously.

The transition width (Γ parameter) of both transitions increases as the alloy disorder increases but, while the temperature dependence indicates that for the exciton discrete states there is some phonon scattering contribution (as their width further decrease as temperature is lowered), this is not the case of the CTT band that is much less independent of temperature, which indicates that it has an intrinsic width related to its discrete to continuous character). The CTT intensity is obviously directly correlated to the Co content, but, contrary to the $d - d^*$ bands, it exhibits a clearly nonlinear behaviour.

Let us now discuss if we can extract a reliable value of the localization parameter of the Co 3*d* ground state from the above described results. Let us first remember that the charge transfer transition energy (theoretically the difference between the conduction band and the ground level of tetrahedral Co 3*d* states) does not correspond to the maximum of the CTT absorption band. It correspond to the onset of the charge transfer transition band.

The nonlinear behaviour of both the width and intensity of the CTT indicates that there must be effects associated to the interaction between Co atoms at high Co concentration. It is well-known that the amount of second neighbour Co-atoms, at a distance basically equal to the *a* lattice parameter, increases quickly with cobalt concentration. Even if the energy of the crystal-field states is not very much affected, the width of photoluminescence and absorption peaks becomes larger, indicating some interaction.

In this way, the best estimation should be given by the spectra of low Co concentration thin films. For the 1 and 2.5% thin films the Gaussian width turns out to be 0.16 eV, and the maximum occurs at 3.2 eV. The onset is smeared as a consequence of relaxation and scattering processes, that introduces some uncertainty in its determination. In order to have a better estimation let us recall that, independently of the localization function, the dependence of the *absorption coefficient* on the photon energy, near to the onset energy, is given by:

$$\begin{aligned} \alpha_{CTT}(\hbar\omega) &= Cte \times (\hbar\omega - E_{CTT})^{3/2} \\ [\alpha_{CTT}(\hbar\omega)]^{2/3} &= Cte^{3/2} \times (\hbar\omega - E_{CTT}) \end{aligned} \tag{4.1}$$

Then, $\boldsymbol{\alpha^{2/3}}$ should depend linearly on the photon energy and the extrapolation of a linear fit would give a good estimation of the $\mathbf{E_{CTT}}$. The test is shown in Figure 4.9

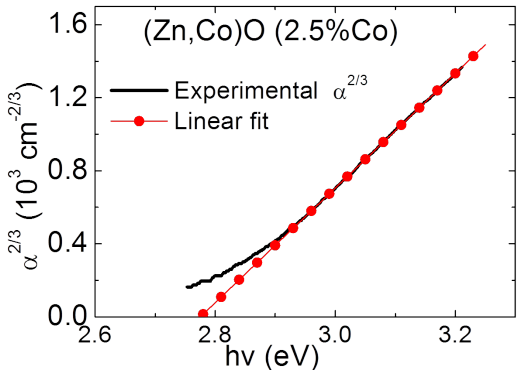

***Figure 4.9**: Dependence of $\alpha^{2/3}$ on the photon energy*

from which a value $E_{CTT} = 2.78$ eV is obtained.

The maximum of the CTT band occurs at a photon energy depending on the localization energy:

$$\hbar\omega_{max} = E_{CTT} + \frac{3}{4}E_{kin} \tag{4.2}$$

Given that the maximum of the CTT band for the 2.5% Co thin film occurs at 3.23 eV (fitting procedure, table 4.1), the localization *kinetic energy*, $\mathbf{E_{kin}}$, would be:

$$E_{kin} = \frac{4}{3}\left(\hbar\omega_{max} - E_{CTT}\right) = 0.60eV \tag{4.3}$$

Which, for an *electron effective mass* of $0.27m_0$ [121] would yield a localization parameter about 0.50 nm.

Later in this thesis we will test the reliability of this result by two independent physical effects affecting both the energy and intensity of the CTT band: doping with Ga and quantum confinement. Both effects change the energy and occupation of the charge transfer transition final states.

To finish this discussion, let us remind that, in spite of the fact that the CTT band maximum shifts to higher photon energies (as expected from the increase of (Zn,Co)O alloy bandgap), the absorption onset shifts to lower photon energies, which would correspond to an increase of the localization energy. This is unexpected as the estimated value of the *localization parameter* (0.5 nm) indicates that firsts neighbours Co atoms (at a distance basically equal to the a lattice parameter, 0.328 nm) strongly interact, which should lead to more delocalized states. Then, the observed CTT band broadening would be the consequence of the existence of several configurations of

Co sites, along with the large increase of the alloy disorder scattering (that would be maximum for $x = 0.5$).

Discussion about the Charge Transfer Transition

If our conclusions about the charge transfer transition are compared with other works, several issues about the nature of this CTT arise. We think that the work of Gamelin et al.[122][123] gives reliable results in which concerns the energy of the excited state of the Co $3d$ shell (let us call it Co $3d^*$) with respect to the conduction band minimum. They show that the energy difference between the conduction band minimum and the Co $3d^*$ ($^4T_1$) state increases proportionally to the concentration of cobalt. For small concentrations of cobalt, photoconductivity measurements clearly place the excited Co $3d^*$ $^4T_1$ level on the edge of the conduction band, since only in this situation photoconductivity can be observed at very low temperature.

Moreover, evidences on the nature of the CTT are also quite clear (photoconductivity, positive pressure coefficient, sensitivity to Burstein-Moss shift by filling the conduction band, the quantum confinement sensitivity) and establish that it is a transition from the Co $3d$ ground state to the conduction band.

The disparity between the energies of both transitions (about 2 eV for the transition to the $^4T_1$ state and around 3 eV for CTT) rises a problem:

- If we place the ground state Co $3d$ guided by the CTT, the excited state $^4T_1$ would be well below the band, in contradiction with Gamelin's group photoconductivity results.
- If we place the fundamental Co $3d$ state guided by photoconductivity, about 2 eV below the conduction band, final CTT states would be at least 1 eV above the minimum of the band. Given the dependence of the matrix element with energy, at these kinetic energies the intensity of the transition would be negligible. Moreover, its intensity and energy would only be sensitive to Burstein-Moss effect (filled band) when the Fermi level were at least 1 eV above the bottom of the band, i.e., at electron concentrations much higher of 10^{21} cm^{-3}, unobtainable by doping the ZnCoO alloy with Ga.

This apparent contradiction may be due to the use of a very simple model for both the meaning of the optical transition energies and the CTT.

Figure 4.10 shows an absorption spectrum of a ZnCoO (13% Co) sample with the three optical transitions observed in this range. In the scheme of

the bands, final states are represented and an approximate assignment of the relative positions of these initials and final states on the valence and conduction band is done.

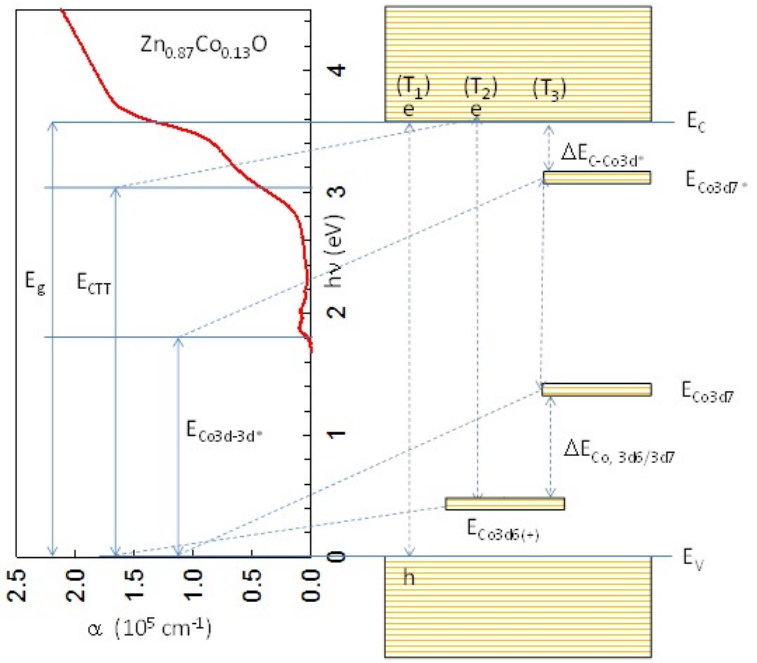

***Figure 4.10**: Comparison of an absorption spectrum of $Zn_{1-x}Co_xO$ (13% Co) with the optical transitions.*

The first problem that arises is the different meaning of the energies of optical transitions as they occur either in electronic structures that can be described by one-electron states (bands of a semiconductor) or in strongly correlated electronic structures whose states are always multielectron ($3d$ states of the transition elements).

In this regard, we observed three different transitions:

1. In T_1 (band to band)the final state is an electron in the conduction band and a hole in the valence band: this is the only optical transitions in which, due to the large width of the bands, the transition energy can be assimilated to an energy difference between one-electron states (because we can use the concept of free hole).

2. For T_2 the initial state is the ground state of Co $3d^7$, and the final state (indicated in the bands scheme) includes an electron in the conduction band and a multielectron state (Co $3d^6)^{+1}$. The exponent +1 means

that, beyond the environment of first neighbours of cobalt, this would be a ionized centre that generates an attractive Coulomb potential for electrons. Locally, at the scale of covalent bond, it is a Co^{3+} ion in tetrahedral coordination with four oxygen atoms.

3. In T_3, both the initial state (ground state of Co $3d^7$) and the final (excited state Co $3d^7$ $^4T_1$) are multielectron states and it is not correct to assimilate them as one-electron states. That means that, by itself, this energy transition gives us no track to locate the fundamental or excited states of tetrahedral Co 3d with respect to the semiconductor bands.

In the final states of the transitions T_1 and T_2 there is an electron in the conduction band. The energy of the electron is clearly attached to the band scheme. Since both transitions are measured by the same method, it seems reasonable to use them to locate the ground state Co $3d$ with respect to the valence and conduction bands. But we have seen that this would lead to an inconsistency with the results of photoconductivity which does clearly place the $^4T_1$ excited level relative to the conduction band.

This may be because we have not considered that the transition T_2 is actually an internal ionization (ionization inside a solid) of Co $3d^7$. In the final state, in addition to the electron in the conduction band there is a Co atom in a state $(Co\ 3d^6)^{+1}$. There is a remarkable change in the configuration of Co $3d$ multielectronic system, which goes from 7 to 6 electrons. In the calculations of the spectrum of CTT that was made at J.A. Sans PhD[35] and the APL[124], the initial (localized, with a Gaussian wavefunction) and final (conduction band, plane wave) states are described as one-electron states, which leads to the absorption spectrum:

$$\alpha = Cte \times (\hbar\omega - E_0)^{3/2}\, e^{-2[\hbar\omega - E_0]/E_{kin}} \tag{4.4}$$

$\mathbf{E_{kin}}$ is the *kinetic energy* of localization in the initial state, that is inversely proportional to the square of the localization radius. Absorption threshold would be:

$$\hbar\omega = E_0 = E_C - E_{Co3d} \tag{4.5}$$

If we face the problem considering that in the final state there is also a Co $3d^6$, the matrix element would be much more complex. In the *effective mass approximation* (considering a plane wave for the electron in the conduction band) dipole matrix element would be:

$$H_{i,f} = \left\langle \Psi_{3d7}\left(\vec{r_1},...,\vec{r_7}\right) \left| \sum_1^7 \left(-ie\hbar\vec{A}\cdot\nabla_i\right) \right| \Psi_{3d6}\left(\vec{r_2},...,\vec{r_6}\right) e^{i\vec{k}\cdot\vec{r_1}} \right\rangle \quad (4.6)$$

$$\begin{aligned} H_{i,f} &= \left\langle \Psi_{3d7}\left(\vec{r_1},...,\vec{r_7}\right) \left| e^{i\vec{k}\cdot\vec{r_1}} \sum_1^6 \left(-ie\hbar\vec{A}\cdot\nabla_i\right) \right| \Psi_{3d6}\left(\vec{r_2},...,\vec{r_6}\right) \right\rangle + \\ &+ \left\langle \Psi_{3d7}\left(\vec{r_1},...,\vec{r_7}\right) \left| \Psi_{3d6}\left(\vec{r_2},...,\vec{r_6}\right) \left(-ie\hbar\vec{A}\cdot\nabla_{\vec{r_i}}\right) \right| e^{i\vec{k}\cdot\vec{r_1}} \right\rangle \end{aligned} \quad (4.7)$$

$$\begin{aligned} H_{i,f} &= \left\langle \Psi_{3d7}\left(\vec{r_1},...,\vec{r_7}\right) \left| e^{i\vec{k}\cdot\vec{r_1}} \sum_1^6 \left(-ie\hbar\vec{A}\cdot\nabla_i\right) \right| \Psi_{3d6}\left(\vec{r_2},...,\vec{r_6}\right) \right\rangle + \\ &+ e\hbar\vec{A}\cdot\vec{k} \left\langle \Psi_{3d7}\left(\vec{r_1},...,\vec{r_7}\right) \mid \Psi_{3d6}\left(\vec{r_2},...,\vec{r_6}\right) e^{i\vec{k}\cdot\vec{r_1}} \right\rangle \end{aligned} \quad (4.8)$$

The second term is the dominant one, because in the first matrix element is only different to zero if the electron-phonon interaction is introduced, while the second includes a Fourier transform and overlap integral of the wavefunctions with the same parity. To calculate the absorption coefficient from these matrix elements, we use the Fermi golden rule:

$$W_{i,f} = \frac{2\pi}{\hbar} \left|H_{i,f}\right|^2 \delta \left[E_C + \frac{\hbar^2 k^2}{2m^*} + \triangle E_{3d6/3d7} - E_{3d7} - \hbar\omega\right] \quad (4.9)$$

To avoid counting of the ionization energy twice, the term $E_C - E_{3d7}$ corresponds to the energy difference between the ground level and the conduction band and the term $\triangle E_{3d6/3d7}$ corresponds to the internal energy difference between the two configurations. Due to the condition of energy conservation represented by the Dirac delta, whatever the localization function we choose, the integral over **k** would lead to a threshold absorption:

$$\hbar\omega_{th} = E_C - E_{3d7} + \triangle E_{3d6/3d7} \quad (4.10)$$

I.e., by conservation of energy, the energy of charge transfer transition, besides the energy difference between the conduction band and the ground state Co $3d^7$, should also include a contribution due to the difference of energy between configurations Co $3d^7$ and (Co $3d^6$)$^{+1}$. This result is in agreement with Joergensen rule according to which the crystal field of trivalent Co is much higher than the divalent Co. Consequently, the above described interpretation solves the problem of the apparent incompatibility between the observation photoconductivity in the Co $d - d^*$ absorption band and the onset of the CTT.

4.2.2 Optical Properties in Temperature

Now we will study the evolution of the absorption spectra at low temperature. The measurement of the absorption spectra at low temperature is a powerful tool in semiconductor physics[35]. It is considered as a quality test of the sample. If there are any growth defects on the thin films, the width and the intensity of the exciton peak is determined by intrinsic mechanisms (phonon dispersion) and the observed absorption peaks are better defined (stronger and narrower) at low temperature.

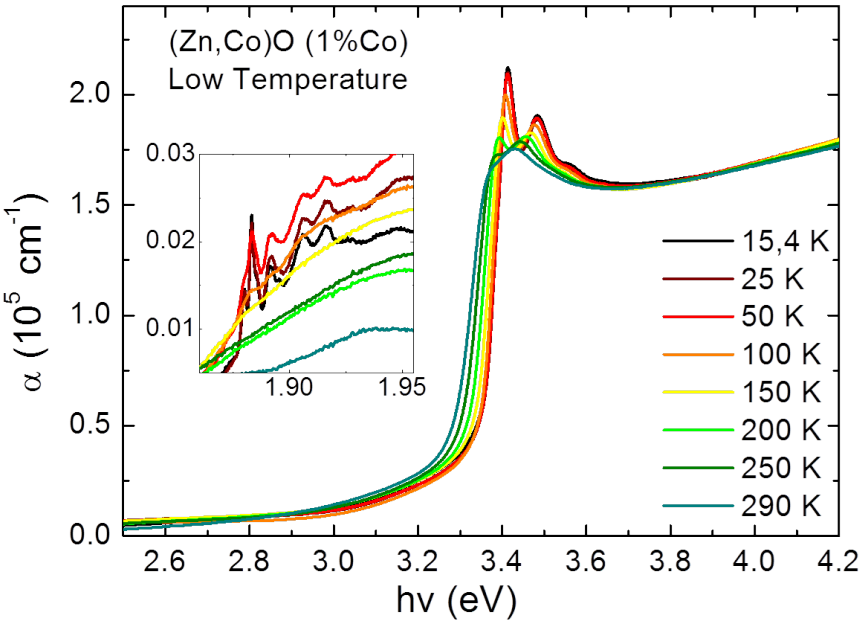

***Figure 4.11**: Evolution with temperature of the optical absorption of (Zn,Co)O thin film with 1% of Co.*

Figure 4.11 shows the evolution of the optical spectrum with temperature for (Zn,Co)O with 1% of Co. At low temperature, the excitonic peak experiences a decrease in the width and an increase in the intensity due to the decrease of the phonon population. Thus, at low temperature we can clearly distinguish three peaks which are at 3.41, 3.48 and 3.55 eV. For previous works[35][52] and the same distance between them (72 meV corresponding to the longitudinal optical, LO, phonon energy), we know that they correspond to the excitonic peak and their LO phonon resonances. The inset shows the evolution under temperature of the internal transitions in the tetrahedrally split Co 3*d* shell: it is interesting to see that, even if they are not very well defined at room temperature, they are clearly observed as

their width becomes smaller at low temperature).

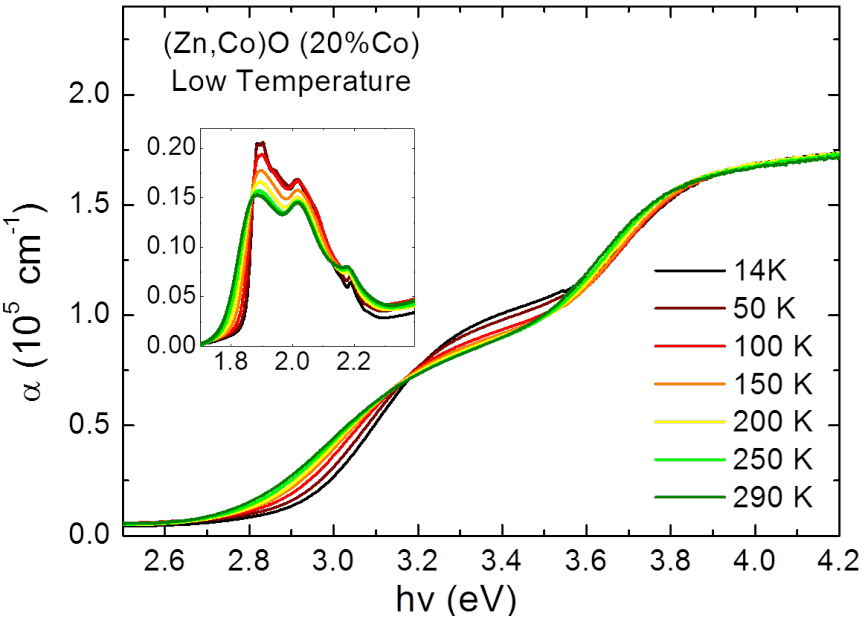

***Figure 4.12**: Evolution with temperature of the optical absorption of (Zn,Co)O thin film with 20% of Co.*

Figure 4.12 show the evolution of the optical absorption for a sample of (Zn,Co)O with 20% of cobalt. For this sample, the Co concentration is large enough for alloy scattering to prevent the observation of the exciton peaks. Nevertheless, phonon scattering seems also to be acting, as the width of the CTT seems to decrease with temperature.

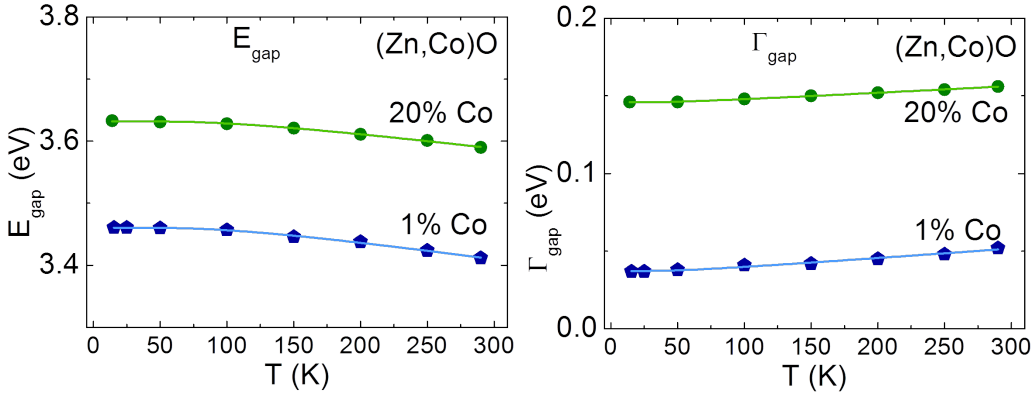

***Figure 4.13**: Temperature dependence of energy and width of the absorption edge for samples of (Zn,Co)O of 1% (blue) and 20% (green) of cobalt.*

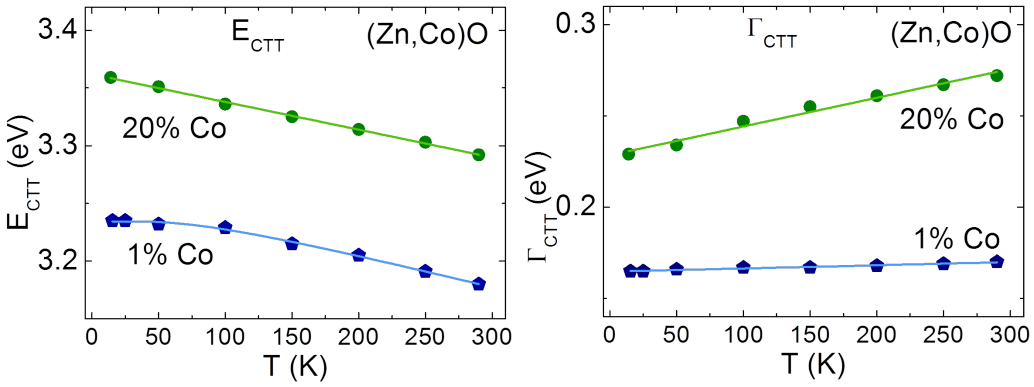

***Figure 4.14**: Temperature dependence of energy and width of the charge transfer transition band for samples of (Zn,Co)O of 1% (blue) and 20% (green) of cobalt.*

As in the previous section, we use the Elliot-Toyozawa model to determine the parameters that describe the optical properties of the films in function of the temperature. Figures 4.13 and 4.14 shows the variation of both samples of the energies and width of the absorption edge and CTT band, respectively. The results show a decrease for the energy and an increase for the width with increasing temperature. We have fitted according to the Bose-Einstein model, shown by the line in the same figures of the parameters (Figures 4.13 and 4.14).

The Bose-Einstein expression relates the optical phonon population to the variation of the band-gap energy with temperature. The equation is expressed as a function of the *phonon "temperature"*, $\mathbf{\Theta_B}$, that is defined as its energy divided by the Boltzmann constant:

$$E_g(T) = E_g(0) - \frac{\alpha_B \Theta_B}{e^{\Theta_B/T} - 1} \tag{4.11}$$

For fitting the width of the optical transitions, we use:

$$\Gamma_g(T) = \Gamma_g(0) + \frac{\Gamma}{e^{\Theta_B/T} - 1} \tag{4.12}$$

The results of the fits of the behaviour of the band-gap energy and width with the temperature are shown in Table 4.2.

***Table 4.2**: Results of the dependence with temperature of the spectra parameters.*

Nominal Co Content	**1%**	**20%**
$\boldsymbol{E_{gap}(0)}$ **(eV)**	3.4610 ± 0.0007	3.6320 ± 0.0006
$\boldsymbol{\alpha_B}$ **(meV/K)**	0.30 ± 0.02	0.364 ± 0.019
$\boldsymbol{\Theta_B}$ **(K)**	320 ± 30	330 ± 30
$\boldsymbol{\Gamma_{gap}(0)}$ **(meV)**	37.2 ± 0.6	145.9 ± 0.2
$\boldsymbol{\Gamma}$ **(meV)**	0.93 ± 0.20	6.3 ± 1.3
$\boldsymbol{\Theta_B}$ **(K)**	150 ± 60	140 ± 20

The effective phonon temperature remains the same, within experimental errors, for both Co proportions. This is consistent with the fact that Zn and Co have very close atomic mass and phonon energies are expected to be very close for both compositions.

As regards the transition widths for the fundamental gap, the 20% thin film exhibits a much larger width due to alloy disorder scattering that increases the width of initial (valence band) and final (conduction band) states.

The temperature dependence of the CTT energy basically follows the one of the bandgap. As discussed previously, its transition width has an intrinsic (temperature independent) contribution, due to its localized-to-extended character, and also a temperature dependence coming from the temperature dependent width of the final state.

4.2.3 Anisotropy

On *C*-sapphire, mica and $ScAlMgO_4$ substrates, thin films grow in the direction of the axis *c*. On *R*-sapphire, thin films of ZnO and alloys derived with wurtzite structure grow with the *c*-axis parallel to the surface of the substrate[125][126]. So it is possible to study the anisotropy of optical properties when the polarization of light is parallel or perpendicular to that axis.

In this section we will present the optical absorption measurements that we have done by inserting a polariser between the light source and the sample. As the axis orientation of the *R*-sapphire substrates is not known, in order to find the *c*-axis orientation of the ZnCoO thin films we have rotated the polariser with respect to the thin film in order to find the polariser orientations for which there is a maximum shift of the absorption edge to higher photon energies (corresponding to the ZnO C absorption onset) or maximum

shift of the absorption edge to lower photon energies (corresponding to the ZnO A-B absorption onset) and verified that, once these orientations are found, the light polarization is preserved as it crosses the sample. In the case of ZnO or ZnO with low Co concentration the difference is most appreciated in the excitonic peaks.

To show an example, in the first graph (4.15) we have represented the energy range where we find the excitonic peaks, the absorption spectra corresponding to different polarizations. For each spectrum we have been rotated the polariser 5 degrees. The entire cycle has been measured at low temperature (13 K). And figure 4.16 shows the evolution of the absorption spectra with the temperature for the both opposite polarizations. Both figures correspond to the pure ZnO sample. It was found that the films deposited onto *R*-sapphire show a clear anisotropy with a displacement of the absorption edge of 40.6 meV toward higher energies for given polarization angle.

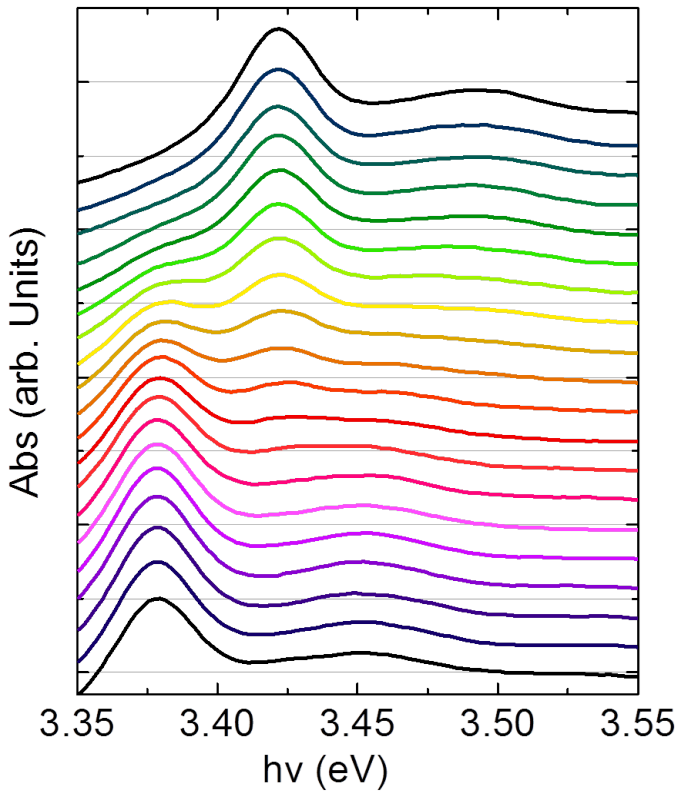

***Figure 4.15**: Displaced spectra of ZnO corresponding to a cycle of polariser at 13K.*

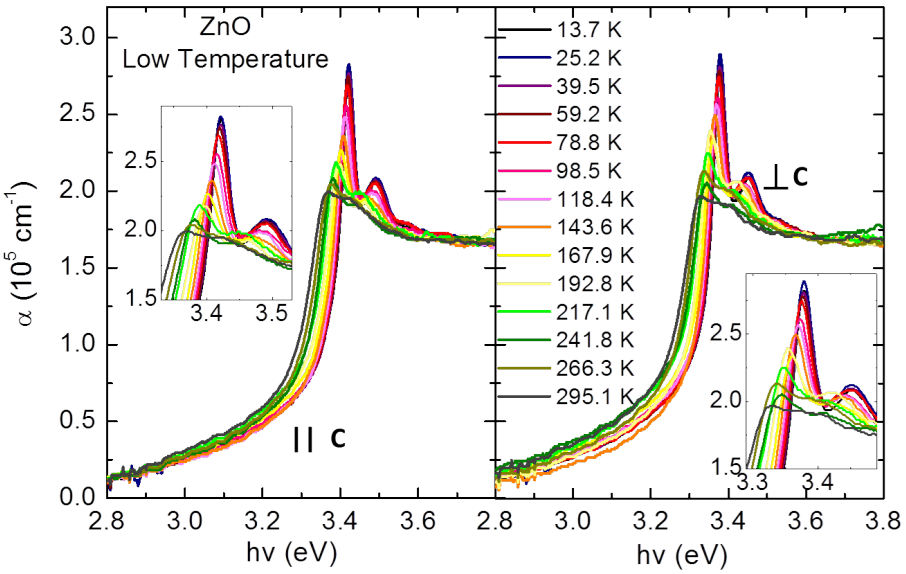

***Figure 4.16**: Evolution in temperature of the absorption spectra of ZnO thin film for both polarizations.*

Table 4.3 compares the energy of the exciton peaks in both polarization to those given in the literature[127] one of the reference papers on the optical properties of ZnO:

***Table 4.3**: Energies of exciton peaks in both polarization.*

Ref	A-exciton (eV)	B-exciton (eV)	C-exciton (eV)	$E_C - E_B$ (meV)
Liang et al[127]	3.3781	3.3856	3.4264	40.8
This work	–	3.3835	3.4241	40.6

Apart from the shift of about 2 meV in the absolute position of peaks B and C, we can see that the difference between the exciton peaks observed in our samples corresponds to the difference observed by Liang et al.[127]. Consequently we identify this direction as corresponding to ZnO *c*-axis, as for light polarized parallel to the *c*-axis only transitions from the C-valence band to the conduction band are allowed. For the perpendicular orientation, only transitions from A-B valence band to the conduction band are allowed. So the exciton peak for this orientation, that is at the same energy we observe for samples grown on *c*-sapphire substrates, corresponds to the A-B exciton.

We should recall that the A-exciton is resolved from the B-exciton in very high quality thin films[128].

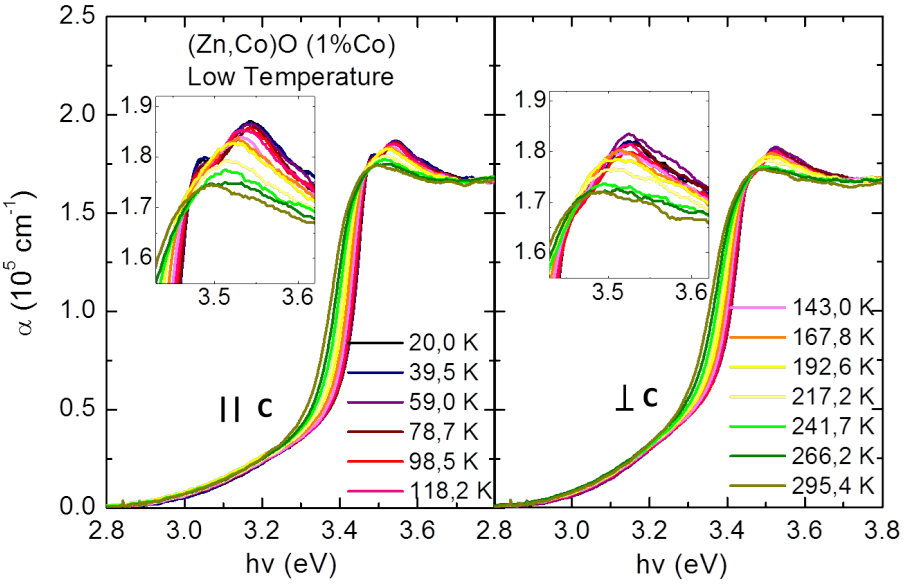

***Figure 4.17**: Evolution in temperature of the absorption spectra of $Zn_{1-x}Co_xO$ with 1%Co thin film for both polarizations.*

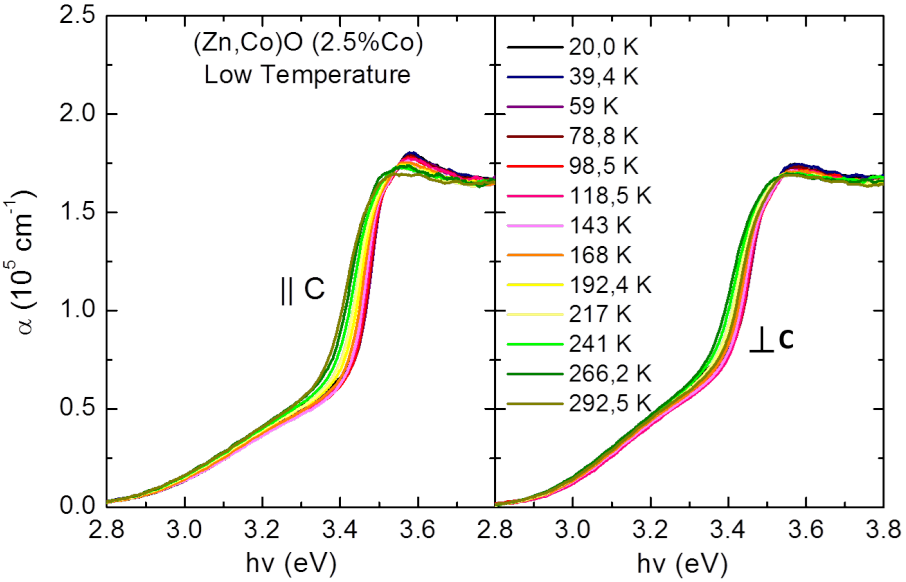

***Figure 4.18**: Evolution in temperature of the absorption spectra of $Zn_{1-x}Co_xO$ with 2.5%Co thin film for both polarizations.*

Fig. 4.17 and 4.18 show the temperature dependence of the absorption edge for both light polarizations in ZnCoO (1% Co and 2.5% Co respectively). Unfortunately, in the case of the 1% Co thin film the exciton peak is well defined only for polarization parallel to the c-axis and, for the 2.5% Co thin film, only the exciton+LO maximum is observed, which prevent an accurate determination of the energy difference between both polarizations.

From the derivative spectrum the difference E_C-E_B can be determined to be of the order of 21 meV for the 1% thin film and some 15-18 meV for the 2.5% thin film. There are no reliable studies about the evolution of the A-B-C valence bands splitting as a function of the Co content. Pacuski et al.[129] could resolve the A and B excitons only for Co proportions below 0.4% and the C exciton only for Co proportions below 0.2%. The crystal field splitting is expected to increase slightly with the Co content (as a consequence of the a/c ratio increase). The effective spin-orbit splitting should also change a little, but the Co concentration is far too low to produce such large change in the B-C splitting.

The most likely origin of the observed decrease in the difference E_C-E_B is some degree of disorder in the orientation of the c-axis. The fact that the exciton+LO resonance are much larger in ZnCoO films (Figs. 4.17 and 4.18) than in ZnO films (Fig. 4.16). In the presence of such orientation disorder, spectra with the largest shift to lower or higher photon energies always contain a proportion of the other polarization.

Obviously, disorder is expected to be larger for larger concentrations and, as shown in Figs. 4.19 and 4.20, for 15 and 25% of Co the energy shift for different polarizations becomes smaller.

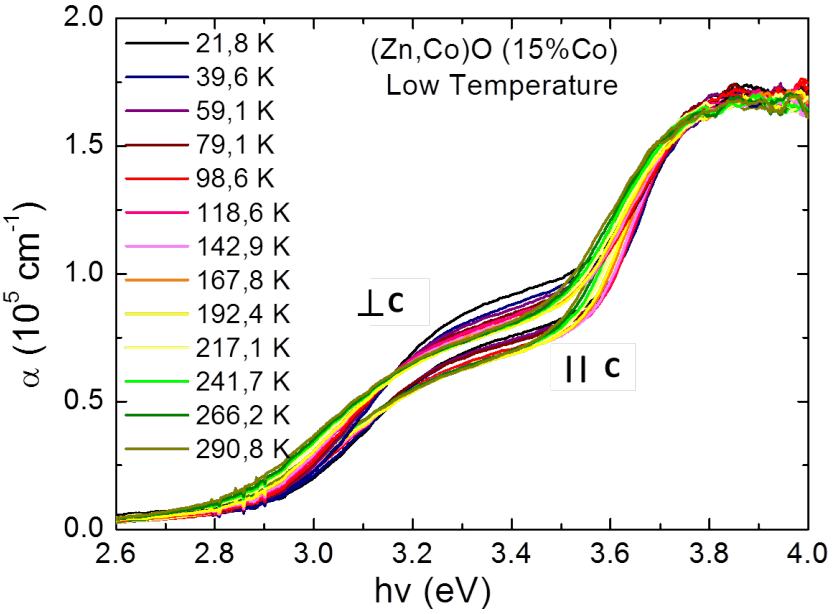

***Figure 4.19**: Evolution in temperature of the absorption spectra of $Zn_{1-x}Co_xO$ with 15%Co thin film for both polarizations.*

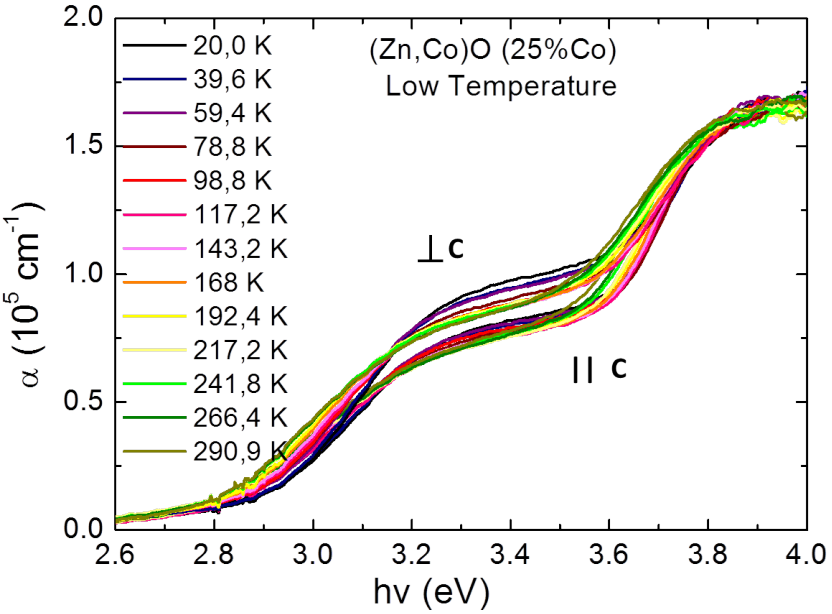

***Figure 4.20**: Evolution in temperature of the absorption spectra of $Zn_{1-x}Co_xO$ with 25%Co thin film for both polarizations.*

What is common to all spectra is the fact that there is no observable

shift of the CTT band, as expected from a transition in which the initial and final states do not change when changing polarizarion, but there is a clear anisotropy in the intensity. As Fig. 4.21 shows the CTT is about 25% more intense for polarization perpendicular to the *c*-axis. As the transition is allowed for both polarization, the anisotropy could simply reflect a small anisotropy in the localization parameter of the ground state of the Co 3*d* state, that is expected in an uniaxial crystal like ZnO.

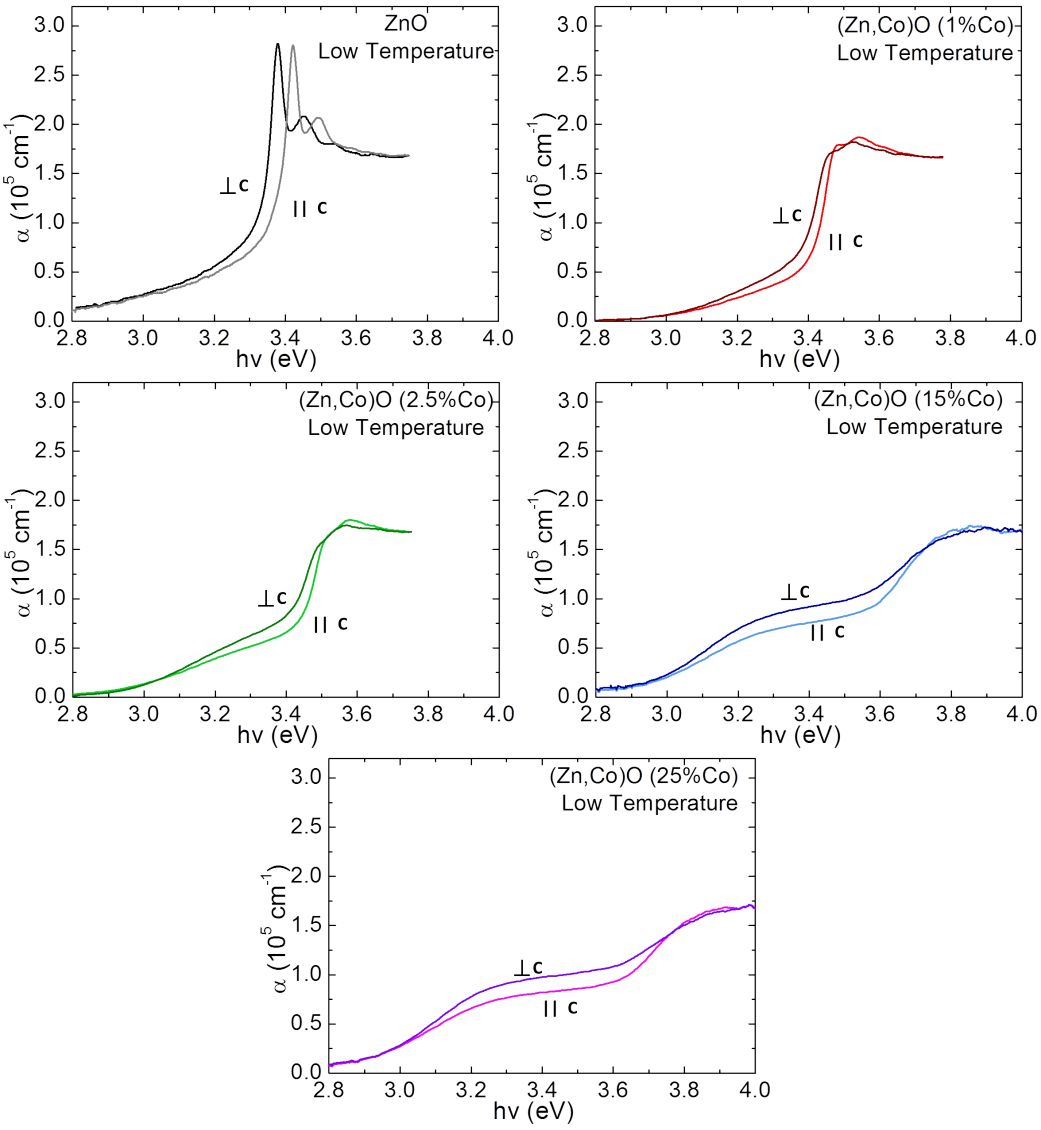

***Figure 4.21**: Absorption spectra for both polarizations of samples of $Zn_{1-x}Co_xO$ with different Co content. At low temperature.*

4.3 Raman Spectroscopy

Raman spectroscopy, which we have described in the theory chapter, is a widely used technique in characterization of semiconductors materials[36]. All spectra shown here are made at environmental conditions.

Figure 4.22 shows the spectra of $Zn_{1-x}Co_xO$ thin film grown on mica with concentrations of 2, 10 and 20% of cobalt.

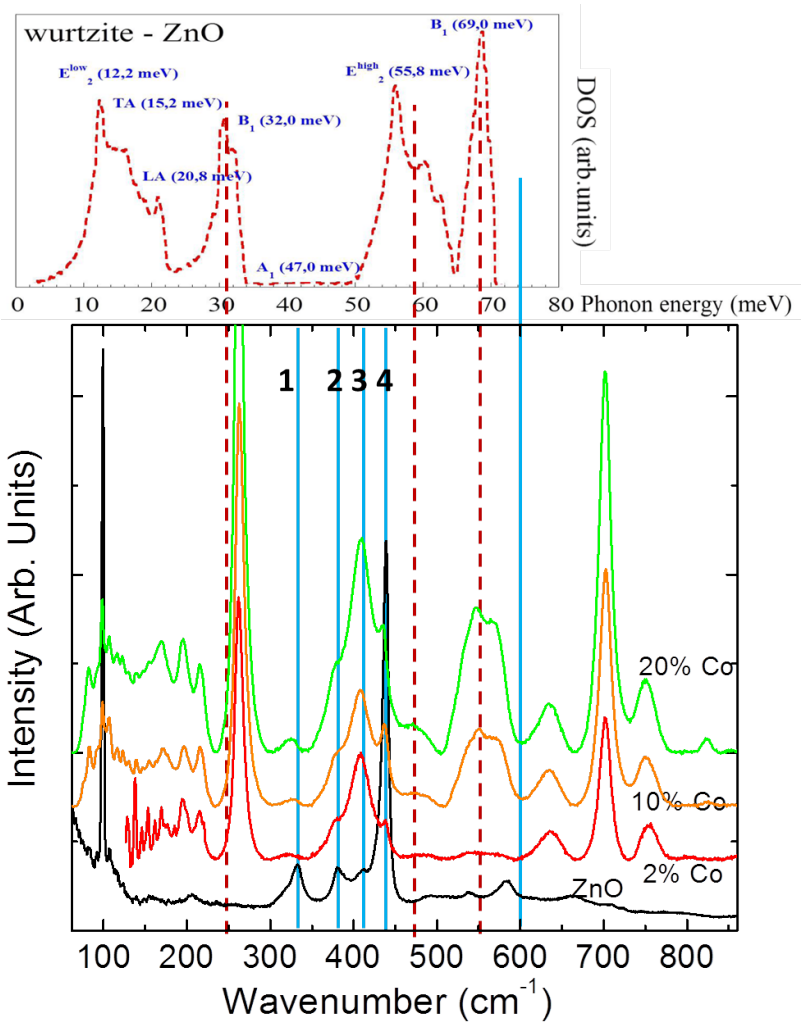

***Figure 4.22**: Raman spectra of (Zn,Co)O thin films growth in mica substrate.*

In these spectra corresponding to samples grown on mica, it is clearly distinguishable the peak that corresponds to the E_2^{low} mode. The structure

that we can see from 100 cm^{-1} to 300 cm^{-1} correspond to the mica substrate. Peaks numbered 1 to 4 seem to correspond to ZnO. But, peaks 2 and 3 are both in position and intensity that correspond with peaks of mica. Therefore, we can not ensure identification. Instead, it is clearly seen that peak 4 corresponds to E_2^{high}. Between 450 cm^{-1} and 600 cm^{-1}, the substrate has not any signal, but we can not make a clear correspondence with the sample of ZnO. In the ZnO reference spectrum, the only peak that appears in this range is the E_1(LO), at 584 cm^{-1}, that does not appear even for the ZnCoO film with 1% Co. Instead, in this area, we observe a broad band centred at 540 cm^{-1} and an additional mode at 475 cm^{-1}[105]. The intensity of both structures is correlated with the Co content in the sample[130].

The three peaks that appear to wavenumbers grater than 600 cm^{-1} are from the substrate. The Raman features observed are listed in Table 4.4, where they were compared with previous results obtained in the literature.

The three peaks that appear to wavenumbers grater than 600 cm^{-1} are from the substrate. Table 4.4 compares the peak frequencies of the reference ZnO and thin films with those of Cuscó et al. [107].

***Table 4.4**: Experimental Raman phonon frequencies (in cm^{-1}) at ambient conditions for samples grown on mica.*

Mode	**ZnO**	**ZnO:2%Co**	**ZnO:10%Co**	**ZnO:20%Co**	ref. [107]
E_2^{low}	99.0		98.7	98.5	99
		261.9 (mica)	262.8 (mica)	262.1 (mica)	
E_2^{high}-E_2^{low}	332.4	324.0	328.2	325.6	333
A_1(TO)	381.0	379.3 (mica)	379.3 (mica)	379.8 (mica)	378
E_1(TO)	412.1	408.5 (mica)	408.7 (mica)	409.5 (mica)	410
E_2^{high}	438.9	438.2	437.3	435.4	438
		477.4	475.3	472.1	
	538.8	543.9	546.5	544.0	
E_1(LO)	584.2				590

In order to find an explanation for the most prominent structure of the ZnCoO Raman spectrum, we compare with ZnO phonon mode density shown on top of Fig. 4.22. It seems clear than the band centered at 540 cm^{-1} correspond to the mode density peak of the upper optical branch. Alloy disorder break the wurtzite symmetry and relaxes the Raman effect selection rules, inducing the appearance of the mode density peak.

In fact, once this peak is interpreted as a mode density peak, it seems

clear that the peak at 475 also corresponds to the upper frequency part of the mode density peak extending from 400 to 520 cm^{-1}. The maximum of this band overlaps with intense peaks from the substrate, making its identification in the film less obvious, but the coincidence in the frequency range where no substrate peaks are observed confirms the assignment.

Below (Fig. 4.23) we show the measurements of the samples grown on sapphire. We have compiled the peak values in Table 4.5.

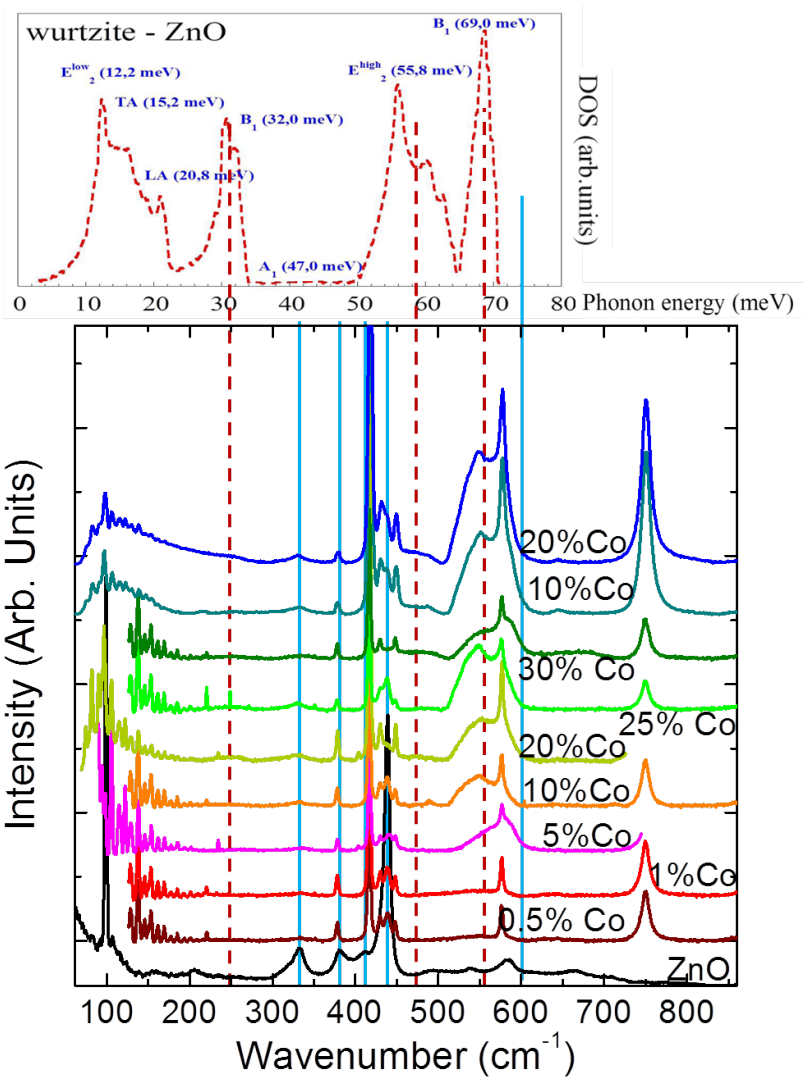

***Figure 4.23**: Raman spectra of (Zn,Co)O thin films grown in sapphire substrate.*

The structure observed up to 300 cm^{-1} corresponds to the substrate. In

some samples, there is a quite prominent peak around 99 cm^{-1}. We have noted it in the table, although we can not be absolutely certain that it is the E_2^{low} mode. The peaks located at about 417.8 cm^{-1}, 430 cm^{-1} and 449 cm^{-1} correspond to the substrate. But among them, it is possible to identify the E_2^{high}. As for thin films deposited on mica, but here with all the Co concentration series, in the range from 500 to 600 cm^{-1} we can clearly follow the emergence of a band clearly correlated with the Co content and tentatively assigned to a mode density peak. The high frequency tail of this band overlaps the $E_1(LO)$ peak. Unfortunately, a substrate peak is also observed at 577 cm^{-1}, which makes difficult to identify this mode even for low Co concentration thin films, for which the mode density peak is not observed.

***Table 4.5**: Experimental Raman phonon frequencies (in cm^{-1}) at ambient conditions for samples grown on sapphire.*

Mode	**ZnO pure**	**ZnCoO 0.5%Co**	**ZnCoO 1%Co**	**ZnCoO 5%Co**	**ZnCoO 10%Co**
E_2^{low}	99.0				
E_2^{high}-E_2^{low}	332.4	332.8	332.6	333.6	331.7
A_1(TO)	381.0	378.2	378.2	378.5	378.1
Substrate		416.7	416.7	417.1	416.7
Substrate		430.8	430.7	430.5	429.8
E_2^{high}	438.9	439.0	438.7	440.6	438.4
Substrate		448.2	448.2	448.4	448.2
		548.2	549.8	554.8	548.7
Substrate		576.4	576.4	576.8	576.4
E_1(LO)	584.2			583.3	590.7
	ZnCoO 20%Co	**ZnCoO 25%Co**	**ZnCoO 30%Co**	**ZnCoO 10%Co**	**ZnCoO 20%Co**
E_2^{low}	96.8			97.0	98.2
E_2^{high}-E_2^{low}	331.6	328.3	334.6	330.9	329.6
A_1(TO)	378.5	378.0	378.1	378.3	379.1
Substrate	417.2	416.7	416.7	417.9	417.9
Substrate	430.2	430.3	429.7	430.7	431.2
E_2^{high}	437.1	438.5	435.9	438.4	437.4
Substrate	448.7	448.7	448.1	449.4	449.6
	550.5	547.6	548.6	548.9	545.2
Substrate	576.8	576.1	576.5	577.4	577.7
E_1(LO)			582.2	579.3	

4.4 Conclusions

In this first chapter of results we have focused on the study of thin films of ZnO and $Zn_{1-x}Co_xO$ with different concentrations of cobalt, grown on different types of substrates.

First, we have shown some images of microscopy, which shows that the samples have homogeneous and compact surfaces, but with small crystals (granular aggregates in the case of 20% of Co and crystals embedded for 30% of Co). These results are similar to previous works using the same thin film preparation technique.

Secondly, we studied the optical properties of the material, both at room temperature to different Co concentrations (between 0% and 30%), and also at low temperature for two samples, one with low concentrations and another one with high Co content.

We were able to confirm the three main effects of introducing cobalt in ZnO structure:

1. The fundamental absorption band (band-to-band transition) shifts to higher energies. The consequent shift of the exciton peak is associated to a quick increase of its width, due to alloy disorder, in such a way that the exciton/exciton+LO resonances are not observable for Co concentretions larger than 5%.

2. An intense absorption band appears below the bandgap, whose intensity increases with increasing the cobalt content, corresponding to the charge transfer transition (CTT) from the fundamental state of $3d$ Co shell in tetrahedral site to the conduction band. The maximum of the CTT transitions shifts to higher energies as the Co content increases, but its width also increases.

3. A complex structure of bands is observed between 1.7 and 2.3 eV whose intensity is also proportional to the Co content. These bands are associated to transitions from the fundamental state to excited states in the tetrahedral crystal-field split $3d^7$ Co shell.

This work has focused on a detailed investigation of the CTT, by studying its onset energy, intensity and width as a function of the Co content, temperature and polarization. This study has yielded the following conclusions:

- The CTT is a transition from a localized to an extended state. The initial state is the fundamental state of the crystal-field split Co $3d$ shell in tetrahedral site. The final state is the ZnCoO alloy conduction band.

- The shape and width of the CTT absorption band corresponds better to an initial state with a Gaussian shaped wavefunction rather than a hydrogenic one.

- The edge of the CTT band exhibits a $(\hbar\omega\text{-}E_i)^{3/2}$ dependence on the photon energy, from which it is possible to determine the onset energy E_i, by extrapolation of the $\alpha^{2/3}$ plot. This procedure yields E_i=2.8 eV for low Co concentrations (about 2.5%).

- From the onset and the maximum of the CTT it is possible to obtain the localization energy of the fundamental state, defined as the kinetic energy corresponding to the inverse Gaussian localization parameter. The localization energy is of the order of 0.6 eV, corresponding to a localization parameter of some 0.5 nm.

- For higher Co proportions, even if the CTT maximum shifts to higher energies, along with the alloy bandgap, a nonlinear behaviour is observed for both its width and intensity. This indicates that there must be effects associated to the interaction between Co atoms in second neighbour position. This is to be expected as the localization distance of the fundamental state of the Co 3*d* shell is slightly larger than the a parameter (typical second neighbour distance). This second neighbour interaction in isolated pairs or larger clusters should affect the energy and localization of the isolated Co 3*d* fundamental state giving rise to a distribution of onset energies and widths.

- Experiments at low temperature indicate a decrease for the energy and an increase for the width both for gap and for CTT with increasing temperature.

- We have discussed and explained the apparent contradiction between our results and photoconductivity results, that place the excited state of the Co 3*d* shell in resonance with the conduction band minimum for low Co concentrations. This would place the fundamental state of the Co 3*d* shell 1.8 eV below the conduction band minimum, indicating that the onset of the CTT should be at 1.8 eV, nearly 1 eV below the previously obtained value E_i=2.8 eV. The apparent discrepancy is solved by taking into account that the CTT involves an internal ionization of the Co 3*d* shell, from the doubly ionized stoichiometric configuration (Co $3d^7)^{+2}$ state to the triply ionized configuration (Co $3d^6)^{+3}$. The 1 eV difference would correspond to the configuration energy difference between both ionization states.

- Thin films grown on R-sapphire have allowed for an investigation of the CTT anisotropy. No energy shift has been detected between polarization parallel and perpendicular to the wurtzite *c*-axis. Nevertheless we observe systematically and independently of the Co proportion a larger absorption intensity for polarization perpendicular to the *c*-axis.

- Concerning the exciton absorption peaks at the fundamental absorption of the alloy, we observe a decrease of the energy difference between the C-exciton (polarization parallel to the *c*-axis) and the A-B exciton (polarization perpendicular to the *c*-axis) as the Co concentration increases. Given that the anisotropy crystal field is expected to increase as the Co proportion increases, the observed decrease is most probably due to some disorder in the orientation of the *c*-axis in the thin film crystallites.

- Finally, we have carried out Raman scattering measurements of Co doped ZnO thin film grown on mica and sapphire substrates. Even if the most characteristic phonon of ZnO (E_2 high and low) are observed alloy disorder partially breaks the wurtzite symmetry and gives rise to the appearance of Raman peaks associated to the maxima of the total phonon density of states.

Chapter 5

Results: ZnCoGaO Thin Films

This chapter will be focused on a systematic study of Ga-doped (Zn,Co)O thin films. We will discuss their morphological, transport, optical (infrared and UV-visible), lattice-dynamic and magnetic properties. Some of them will be studied as a function of pressure or temperature and some other as a function of both parameters simultaneously. In particular, optical studies under pressure will allow for an investigation of the properties of the high pressure phase (NaCl) of these doped alloys.

As we see throughout the chapter, the measurements on ZnCoO thin films doped with Ga and annealed at different temperatures, and especially the correlation between transport and optical properties, will illustrate several effects of the conduction band filling on the optical properties of (ZnCo)O films.

On one hand, we will see the effect of continuous variation of the carrier concentration on the absorption edge. And secondly, we will be able to confirm the continuous decrease in intensity of the charge transfer transition band by increasing the concentration, an effect that leads directly to the determination of the localization parameters of the electrons in the ground state of $3d$ level of cobalt in tetrahedral coordination.

The variety of experimental techniques used in this chapter makes it difficult the choice of an order of presentation. After a short comment on the film morphology, for the sake of coherence, we will proceed in the following order:

1. We will present first the transport properties at room temperature (for as-grown and thermally annealed samples) along with FTIR reflectivity measurements (that are in fact high frequency transport measurements), and then the optical properties at the bandgap of the same samples.

2. Then we will present the transport properties as a function of temperature and the optical properties of some of these films as a function of temperature.

3. Finally we will present transport and optical properties as a function of pressure (in the case of resistivity, we will show the effect of both thermodynamic parameters).

5.1 Scanning Electron Microscopy

Although we have not performed a detailed study of electron microscopy for different dopant concentrations, we show an example. Figure 5.1 are SEM images at different scales to a sample of 20% of cobalt and 0.5% of gallium. The image is similar to what we show for pure ZnO (Figure 4.1) and has been shown previously for (Zn,Mn)O thin films[131]. The material has a smooth and homogeneous surface with the presence of some aggregates.

As compared to ZnO[52], the surface appears as smoother and more homogeneous. Nevertheless, in pure ZnO films, the surface did not show the overgrown nanoparticles (around 40 nm in size) here observed. As this work mainly focuses on the optical properties of the material, we have not done any further investigation on the origin of these aggregates, that do not appear to have any critical effect on the transport and optical properties of the films.

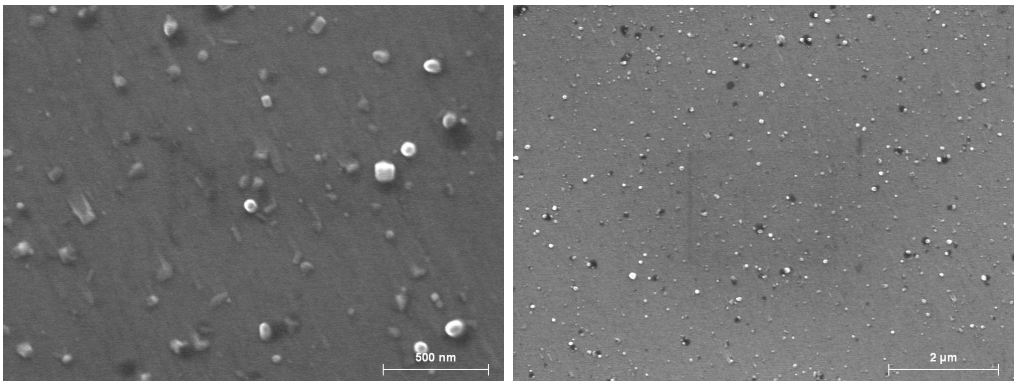

***Figure 5.1**: SEM image of a ZnO doped with 20% of Co and 0.5 of Ga.*

5.2 Correlation between Transport and Optical Properties at Ambient Temperature

5.2.1 Transport Properties at Ambient Pressure and Temperature

Table 5.1 shows the results of transport measurements (transport and Hall effect) at ambient temperature for several samples of the series of Ga doped ZnCoO thin films.

***Table 5.1**: Transport parameters at ambient temperature for a series of Ga-doped ZnCoO samples with 5% of cobalt.*

Nominal Ga content	**sample serie**	$\boldsymbol{\rho}$ **(Ωcm)**	**n (cm^{-3})**	$\boldsymbol{\mu}$ **(cm^2/Vs)**
0.1% Ga	PLD1 sapph. 550 nm	$5.4{\cdot}10^{-2}$	$1.36{\cdot}10^{19}$	8.5
0.1% Ga	PLD1 sapph. 260 nm	$8.6{\cdot}10^{-3}$	$4.6{\cdot}10^{19}$	15
0.1% Ga	PLD2 mica 172 nm	$1.7{\cdot}10^{-3}$	$8.9{\cdot}10^{19}$	40
0.25% Ga	PLD1 600 nm	$8.6{\cdot}10^{-2}$	$7.6{\cdot}10^{18}$	9.6
0.25% Ga	PLD1 600 nm	$2.3{\cdot}10^{-3}$	$9.6{\cdot}10^{19}$	28
0.5% Ga	PLD2 300 nm	$1.5{\cdot}10^{-3}$	$8.9{\cdot}10^{19}$	16
1% Ga	PLD1 140 nm	$1.5{\cdot}10^{-3}$	$2.7{\cdot}10^{20}$	16
1% Ga	PLD2 190 nm	$8.7{\cdot}10^{-4}$	$2.5{\cdot}10^{20}$	37
1% Ga	PLD3 500 nm	$7.5{\cdot}10^{-4}$	$2.3{\cdot}10^{20}$	37
2.5% Ga	PLD1 middle	$6.9{\cdot}10^{-4}$	$2.8{\cdot}10^{20}$	33
2.5% Ga	PLD1 big	$6.5{\cdot}10^{-4}$	$2.9{\cdot}10^{20}$	33
2.5% Ga	PLD1 small	$4.7{\cdot}10^{-4}$	$4.2{\cdot}10^{20}$	32
2.5% Ga	PLD2 mica 260 nm	$6.5{\cdot}10^{-4}$	$2.9{\cdot}10^{20}$	34
2.5% Ga	PLDR2 SCO 260 nm	$5.9{\cdot}10^{-4}$	$3.5{\cdot}10^{20}$	30

Figures 5.2 and 5.3 show the transport parameters: *resistivity*, *free electron concentration* and *electron mobility* as a function of the gallium content and the *resistivity* and *electron mobility* as a function of the *electron concentration*.

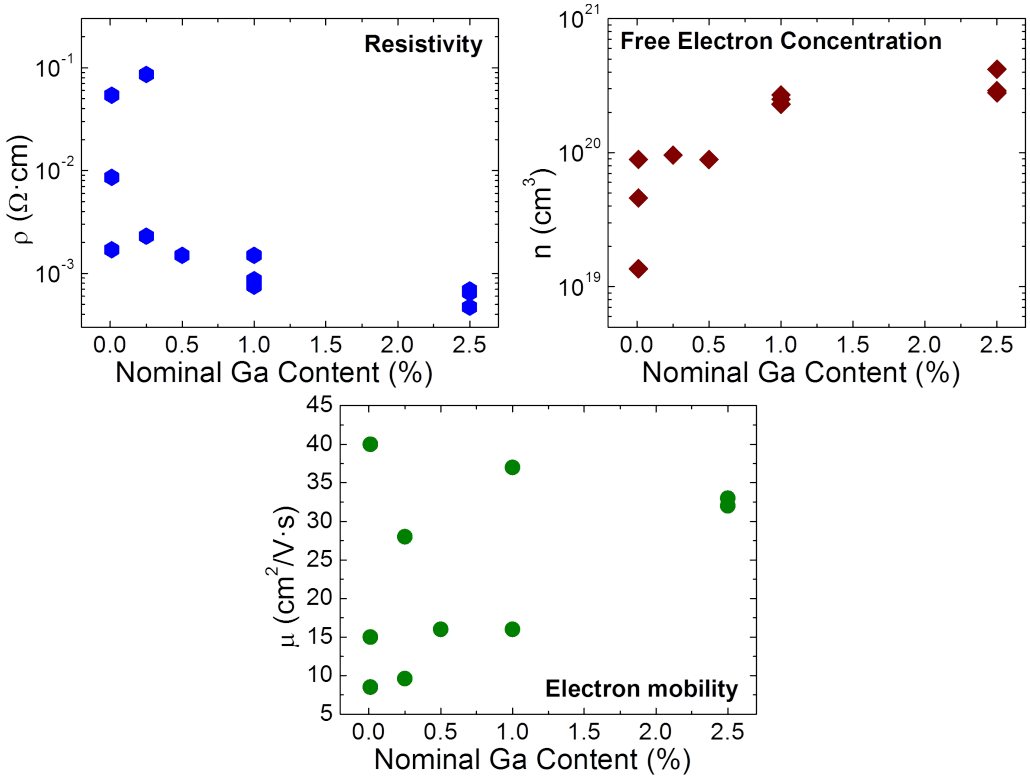

***Figure 5.2**: Resistivity, electron concentration and electron mobility for Ga-doped ZnCoO thin films in function of the content of Ga.*

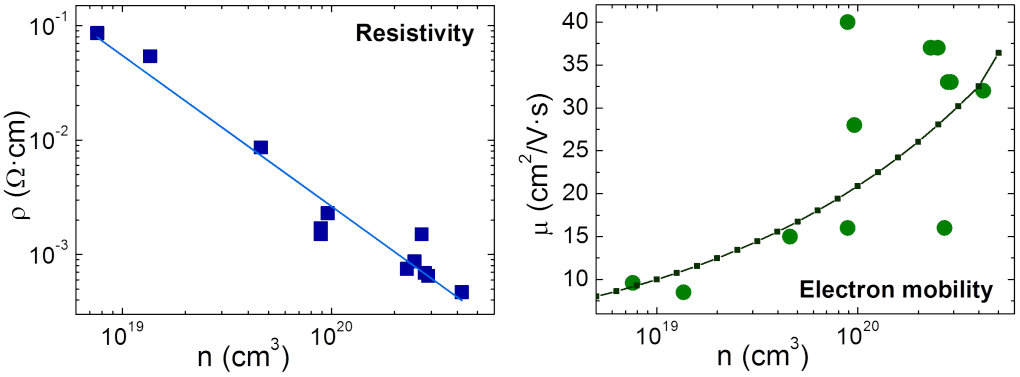

***Figure 5.3**: Resistivity, electron concentration and electron mobility for Ga-doped ZnCoO thin films in function of the electron concentration.*

As observed in Ga-doped ZnO [35][132] the electron concentration does not correspond to the Ga concentration. There are some electrically inactive

Ga atoms (about 40%). For a Ga content of 1%, if all Ga atoms acted as substitutional donors, the electron concentration should be about $4.5{\cdot}10^{20}$ cm^{-3}. This effect has been attributed to the existence of nanocrystallites of spinels like $ZnGa_2O_4$, in which Ga is in octahedral coordination and fully oxidized[124][133].

In spite of some exceptions we can see there is a trend in the electron mobility, that tends to be larger for larger free electron concentrations. This trend is more clearly shown by the fact that in the double logarithmic plot of resistivity versus electron concentration the slope of the straight line fit is not -1, as it should be for a constant electron mobility.

The resistivity depends on n as:

$$\rho = \rho_0 \left(\frac{n}{n_0}\right)^{-1.32} \tag{5.1}$$

This indicates that the electron mobility increases with increasing electron concentration as:

$$\mu = \mu_0 \left(\frac{n}{n_0}\right)^{0.32} \tag{5.2}$$

The line in the mobility plot corresponds to this estimation. This trend reflects the fact that, as the electron concentration increases, the grain boundary potential barriers become smaller. The effect of boundary potential barriers is sometimes incorrectly referred to as *grain boundary controlled mobility*, because the apparent electron mobility is lower for larger grain boundary barriers.

For a given grain size (a fraction of a micron), the electron mean free path should be larger than the grain size for electrons to be scattered mainly by grain boundary barriers. As a matter of fact, even for crystalline ZnO, with an electron mobility as large as 200 cm^2/Vs, the free electron mean free path is shorter than 10 nm, which means that in polycrystalline ZnO grain boundary barriers cannot control the electron mobility because the crystallite size is far larger than the mean free path.

The origin of this behaviour is the fact that only electrons with kinetic energy larger than the potential barrier $\mathbf{E_B}$ take part in macroscopic charge transport across the thin film. Consequently, the effective thin film *conductivity* is given by

$$\sigma = e^2 \mu n_{eff} = e^2 \mu n e^{E_B/kT} \tag{5.3}$$

In standard Hall effect experiments the Hall effect signal reflects the actual electron concentration, and the the Hall coefficient is $R_H = \frac{1}{en}$. Then using standard transport equations yields an *effective mobility*:

$$\mu_{eff} = \sigma R_H = \mu e^{E_B/kT} \tag{5.4}$$

At low electron concentrations this effective electron mobility exhibits an anomalous temperature dependence (due to the Boltzmann factor) and, even if inside the grains mobility is controlled by phonons and should increase as temperature decreases, the Boltzmann factor makes the apparent electron mobility to decrease as temperature decreases.

5.2.2 Infrared Reflectivity of As-grown Samples

Figure 5.4 shows the mid infrared reflectivity spectra of several Ga-doped ZnCoO thin films. The plasma reflection structure is visible, as well as the trend of the plasma reflection minimum shifting to lower wavenumbers as the electron concentration decreases.

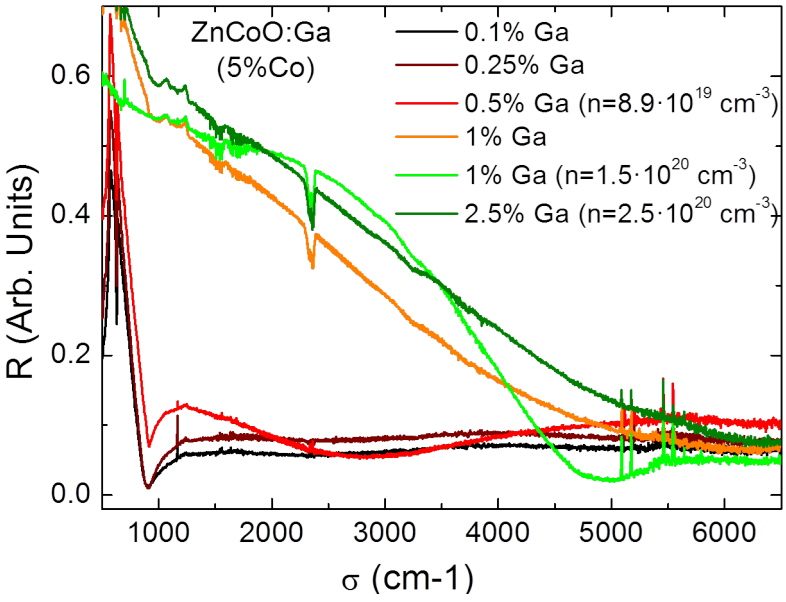

***Figure 5.4**: Infrared reflectivity spectra of Ga-doped ZnCoO thin films.*

The narrow minimum around 900 cm^{-1} correspond to the optical phonon reflectance structure of the sapphire substrate, that is observed for thin films,

especially for the thinnest ones when the plasma frequency becomes smaller and closer to the substrate phonon frequency, or when the plasma reflectance structure becomes very wide.

The plasma reflectivity structure can be accounted for by using a free carrier contribution to the dielectric function described through a Drude model:

$$\varepsilon(\hbar\omega) = \varepsilon_e \left(1 - \frac{\hbar^2\omega_P^2}{\hbar\omega(\hbar\omega + i\gamma)}\right) \tag{5.5}$$

Where $\boldsymbol{\varepsilon_e}$ is the electronic dielectric function, $\boldsymbol{\hbar\omega_P}$ is the carrier plasma energy and $\gamma = \hbar/\tau$ is the free carrier damping energy, related to the carrier relaxation time $\boldsymbol{\tau}$. Figure 5.5 shows two examples of fits, for two thin films with different electron concentrations.

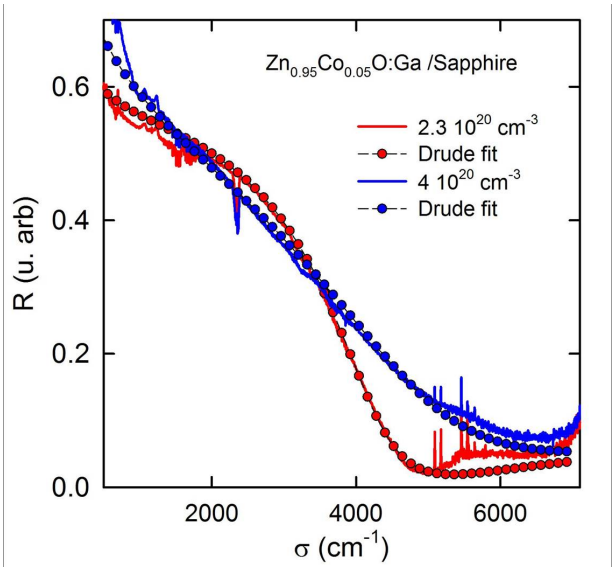

***Figure 5.5**: Drude model fit for two thin films with different electron concentration.*

Table 5.2 shows the fitting parameters:

***Table 5.2**: Parameters of Drude model fitting.*

Nominal Content	**sample serie**	**n (10^{20}cm^{-3})**	$\hbar\omega_P$ **meV**	γ **meV**
5%Co 1%Ga	PLDR3	2.3	546	430
5%Co 2.5% Ga	PLDR3	4	670	75

It is interesting to show that the free carrier damping energies correspond to relaxation times between 2 and 5 fs, which would yield an electron mobility between 10 and 35 cm^2/Vs, exactly in the range of the electron mobility measured by resistivity and Hall effect experiments.

The objective of these FTIR measurements is just to show how ZnCoO Ga-doped thin films basically behave as pure Ga-doped ZnO thin films. Then we will not carry out a systematic fitting of all samples. Instead, we estimate the plasma energy from the reflectivity minimum.

By representing the plasma energy so estimated as a function of the square root of the electron concentration on finds a linear dependence as expected from the plasma frequency equation,

$$\omega_p = \sqrt{\frac{e^2 n}{\varepsilon m}} \tag{5.6}$$

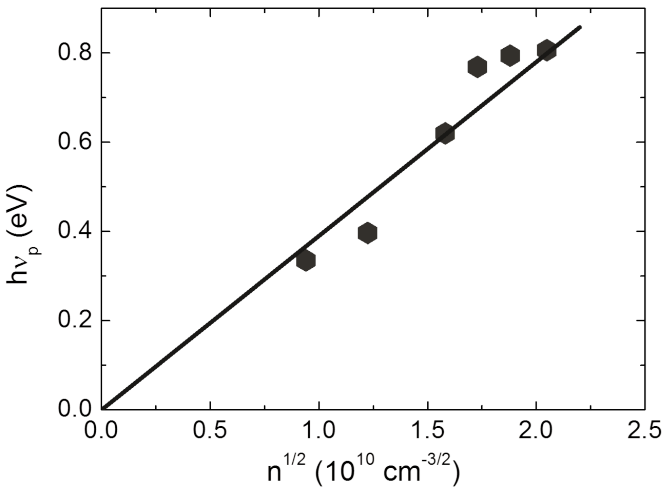

***Figure 5.6**: Plasma frequency as a function of the electron concentration.*

The straight line is a linear fit, imposing a zero ordinate at the origin. From its slope, by assuming a relative electronic dielectric constant close to the one of ZnO ($\varepsilon_e = 4$), we obtain an effective mass $m^*/m_0 = 0.24$, that is slightly below the ZnO value. This is a consequence of the overestimation of the plasma energy by identifying it with the reflectivity minimum. We can conclude that doping ZnCoO with Ga leads to transport and infrared reflectance properties similar to those of ZnO.

5.2.3 Transport and FTIR properties of air annealed samples

It has been unambiguously shown [134] that substitutional Ga^{+3} in tetrahedral coordination, in the ZnO matrix, becomes unstable at high temperature in oxidizing atmosphere. It reacts with oxygen and form a local defect or a small cluster in which the Ga stabilizes as Ga_2O_3 or $ZnGa_2O_4$, in which Ga is in octahedral coordination and is not any loger a donor. Consequently, the carrier concentration can be controlled by thermal annealing and its effect on the absorption edge can be studied in a more systematic way.

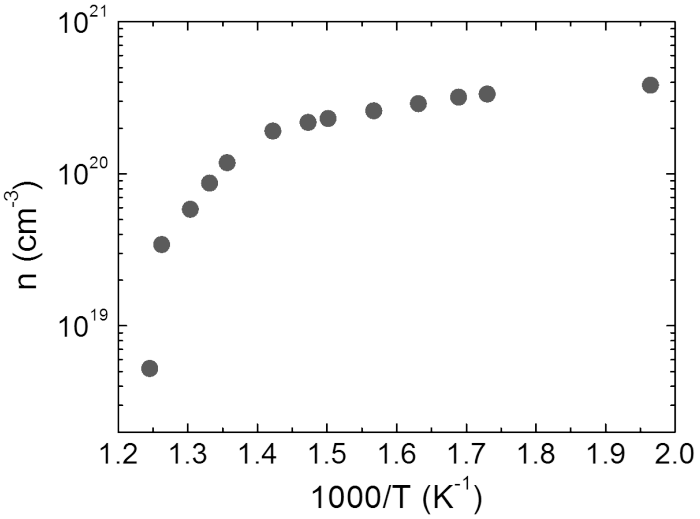

***Figure 5.7**: Arrhenius plot of logarithm of the carrier concentration in function of the inverse of the temperature.*

Figure 5.7 shows the electron concentration at room temperature for a Ga-doped ZnCoO (5% Co, 2.5%Ga) thin film after an annealing at a given temperature. We can see how the carrier concentration at room temperature decreases as the annealing temperature increases. Above 500°C the oxidation process becomes very quick and it is no longer controllable. The activation energy of the process, as calculated from the slope of the Arrhenius plot at high temperature is about 1.3 eV.

When Ga-doped ZnCoO thin films are annealed in air, Ga atoms are gradually oxidized and become electrically inactive as it happens in Ga-doped ZnO. The effect can be studied both by the disappearance of the Burstein-Moss shift and by the shift of the plasma frequency of free electrons in the mid infrared.

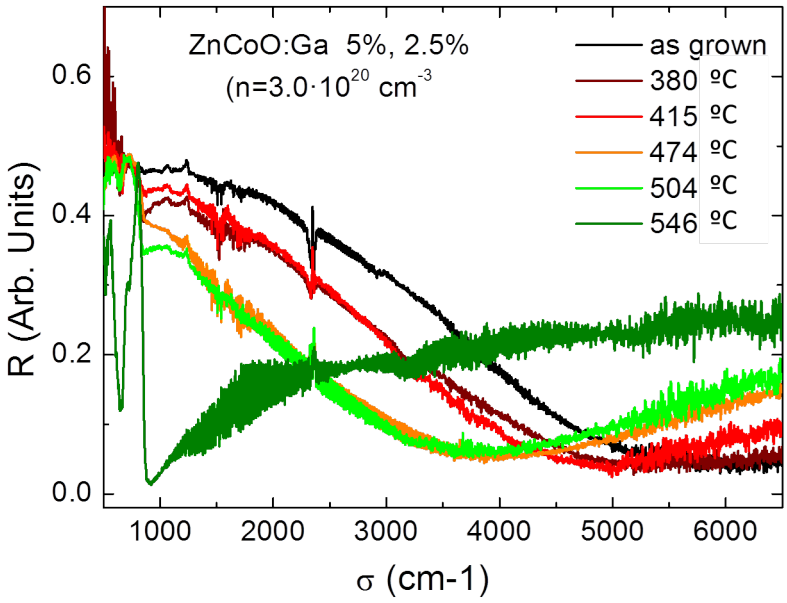

***Figure 5.8**: IR reflectivity spectra of a 2.5% Ga-doped ZnCoO (5%Co) thin film deposited on $ScAlMgO_4$ (SCO) substrate.*

Figure 5.8 shows the mid IR reflectivity spectra of a ZnCoO with 5% of Co and doped with 2.5% of Ga thin film deposited on $ScAlMgO_4$ (SCO) substrate. The as-grown sample has an electron concentration of about $3.0{\cdot}10^{20}$ cm^{-3}, and the plasma reflectivity minimum is at 6000 cm^{-1}.

After annealing at temperatures progressively higher, the plasma minimum appears to shift to lower frequencies. From the previously measured relationship between the plasma reflectivity minimum and the carrier concentration, the free electron concentration after annealing at 504 ºC would be of the order of $1.1x10^{20}$ cm^{-3}. Further annealing at 546ºC leads to a quick inactivation of most Ga donors and the reflectivity spectrum only shows structures related to the SCO LO polar phonon (926 and 656 cm^{-1}) indicating then the plasma frequency of free electrons in the ZnCoO thin films has shifted below the lower spectral limit of the FTIR spectrometer.

5.2.4 Optical Properties at the Absorption Edge

In this section we will focus on the effects of n-doping on the optical properties of ZnCoO thin films at the fundamental absorption edge.

The figure below (Fig. 5.9) compares the spectrum of pure ZnO, ZnCoO with 5% of cobalt and ZnCoO of 5% of Co doped with different concentrations of gallium.

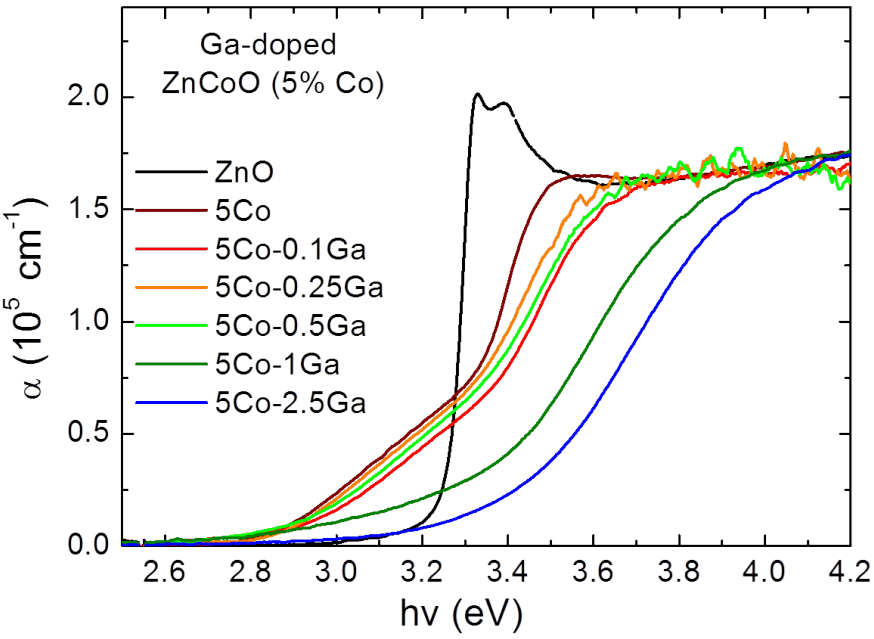

***Figure 5.9**: Optical absorption of Ga-doped ZnCoO thin films of 5% of Co with different Ga content.*

Let us first recall that the presence of substitucional Co induces a relatively large shift of the bandgap, that in this case (5% Co) corresponds to 120 meV, consistently with the previously observed shift of 23 meV/%Co[51]. The ZnCoO thin film also exhibits the pre-gap absorption band associated to the charge transfer transition from the ground state of Co 3*d* in tetrahedral coordination to the alloy conduction band (threshold at about 2.8 eV).

Doping with gallium produces the expected increase of the optical gap (Burstein-Moss shift, due to the filling of the conduction band by free electrons). In addition, there is a clear shift to higher energies of the charge transfer band and, more significantly, a marked decrease in its intensity.

Both effects are consistent with the model proposing that the final state of the CTT is the conduction band. On the one hand, as the band is filled, the final states of the charge transfer transition necessarily are the empty states above the Fermi level, which shifts the band to higher energies. Moreover, as these final states correspond to a larger wave vector values, the absorption intensity should decrease, because for these values of the wave vector, the value of dipole matrix element of the transition is much lower, as we saw in the theory chapter.

Ga-doping experiments have also been carried out with samples with larger cobalt concentrations. Figure 5.10 shows, the spectra of ZnCoO thin

films of 20 and 30% of cobalt, and the same concentrations co-doped with 0.5% of gallium, always taking the spectrum of pure ZnO as a reference. For these samples the carrier concentration is much lower ($6{\cdot}10^{19}$ cm^{-3}) and consequently the effect in the optical spectrum is smaller. We can observe a shift to higher energy of the gap, of some 70 meV, corresponding to a lower carrier concentration ($6{\cdot}10^{19}$ cm^{-3}) but the effect on the intensity of the charge transfer transition is much smaller.

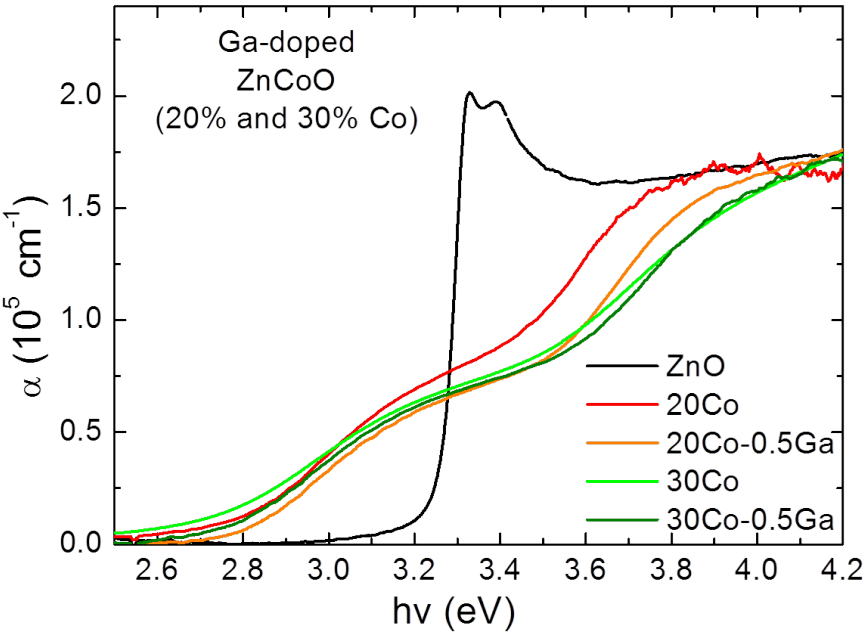

***Figure 5.10**: Optical absorption of ZnCoO thin films of 20 and 30% of Co and doped with 0'5 of Ga.*

Given the lack of a series of samples exhibiting a monotonous variation of the electron concentration, we have not attempted a full interpretation of the results. We will do it for air annealed Ga-doped samples in which it is possible to have a monotonous variation of the carrier concentration.

5.2.5 Optical Properties at the Absorption Edge of Air Annealed Samples

In this section we are going to present and discuss the effect of annealing in air atmosphere on the optical properties of Ga-doped ZnCoO thin films. The application of high temperature to the sample after growth is a process that is widely used to increase crystalline quality. High temperature gives atoms

the kinetic energy needed to relax the crystalline structure, recombine some metastable defects and evolve to most stable configurations.

Figure 5.11 shows the change of the absorption edge of a sample of 5% of Co and doped with gallium (n = $4{\cdot}10^{20}$ cm^{-3}). In the spectrum at higher energy, corresponding to an untreated sample, we can appreciate a Burstein-Moss displacement and the low intensity of the charge transfer transition band. As the treatment temperature is increased, the spectrum (always measured at room temperature) shifts toward lower photon energies (decreasing of the Burstein-Moss shift by decreasing the carrier concentration, while the intensity of the charge transfer transition band increases).

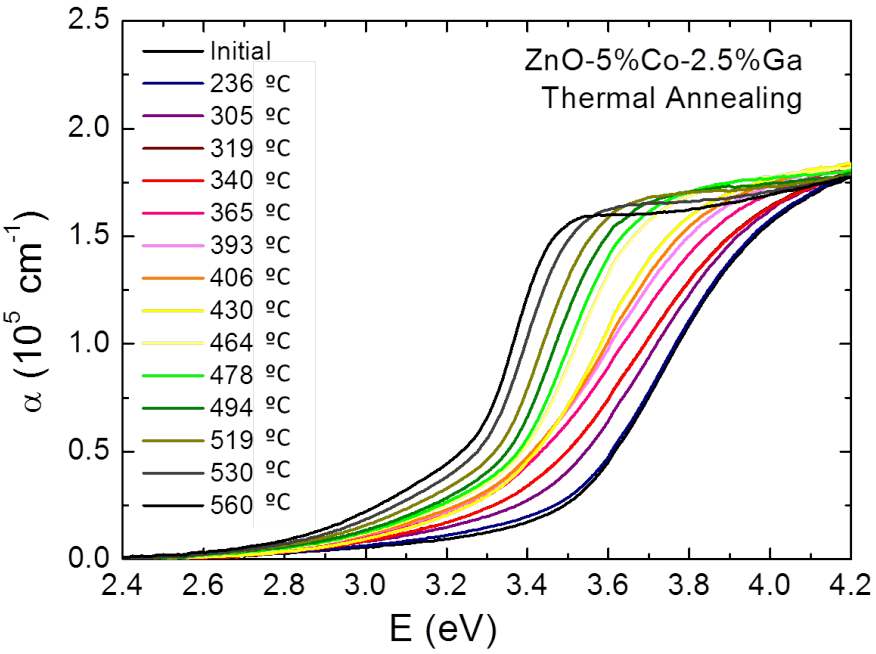

***Figure 5.11**: Evolution of the absorption spectra during the annealing process for a sample of ZnO with 5% of Co and 2.5% of Ga.*

Figures 5.12 show the decomposition of the absorption edge in the different components that contribute to the spectrum, for some of the measured curves. We can see how the width of the fundamental absorption decreases when the annealing temperature increases. This is due to the increase in the crystalline quality. And the decrease in the width allows the excitonic peak to be observed at room temperature[135], which is a good indication of the high quality of the annealed material[134].

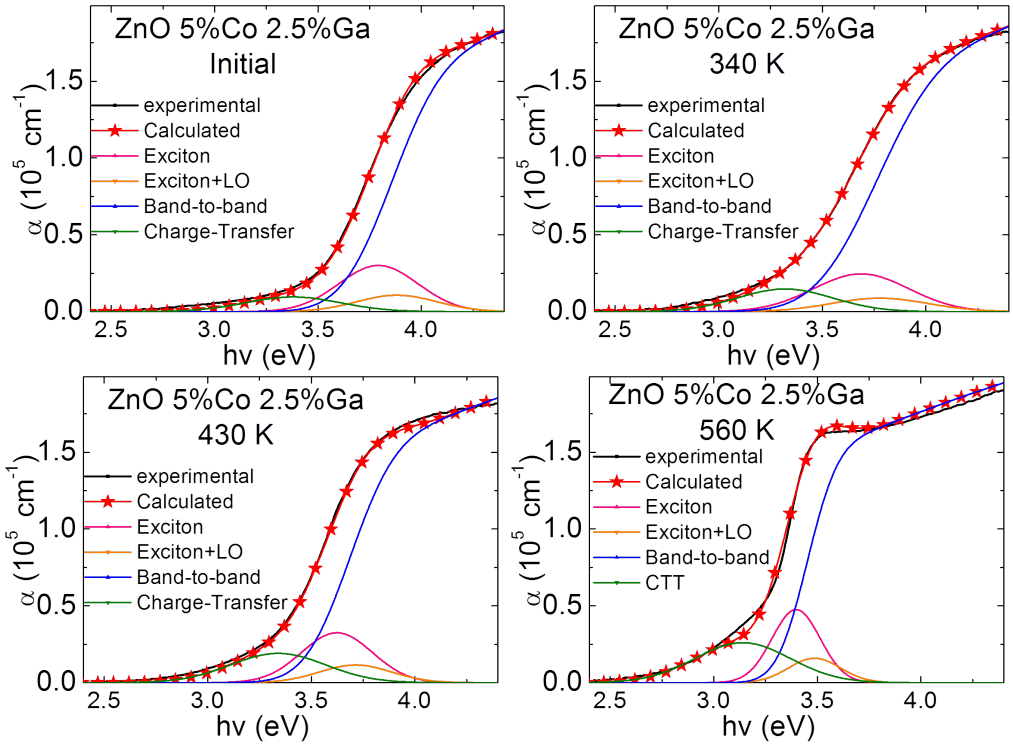

***Figure 5.12**: Decomposition of the some spectra in the different contributions.*

In Figures 5.13 we have plotted the photon energy and intensity of the CTT band maximum as a function of the optical bandgap, as obtained from the fitting procedure.

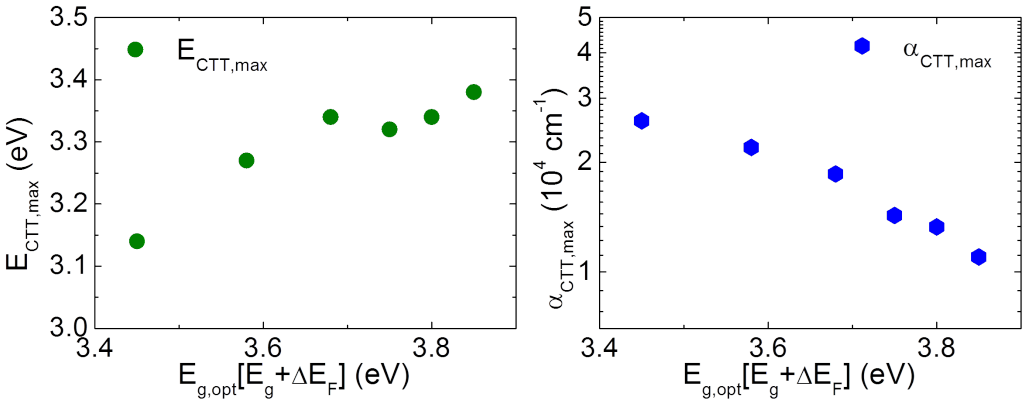

***Figure 5.13**: Decomposition of the some spectra in the different contributions.*

The shift of the optical bandgap can be assimilated to the shift of the Fermi level, as this is exactly what is at the origin of the Burstein-Moss effect.

We can see that, within the dispersion typical of a fitting procedure with correlated parameters, the photon energy at the CTT band maximum follows the Fermi level (with a slightly sub-linear dependence), and the intensity at the maximum exponentially decreases with the Fermi level shift, falling about 40% for 0.2 eV shift of Fermi level, indicating that E_{kin} is of the order of 0.5 eV, as previously found in the interpretation of room temperature spectra of ZnCoO films.

In this way, we have shown, through independent experiments, how the CTT band can be consistently described as a localized-to-extended optical transition, the absorption spectra of which contains information on the localization parameter of the localized state (fundamental state of the Co $3d$ shell in octahedral configuration).

5.3 Correlation between Transport and Optical Properties at Low Temperature

5.3.1 Transport Properties as a Function of Temperature

Resistivity measurements for samples of Ga-doped ZnCoO were carried out at the Centre of Science at Extreme Conditions (CSEC) of the University of Edinburgh. The measurements were conducted in a closed-cycle cryostat, for measurements at ambient pressure and for high pressure. Therefore, for each sample and, the for each pressure, what we really have is a resistivity cycle in temperature. Thus, we do not show discrete points at different pressures (or for different samples) but resistivity as a function of temperature at different starting pressures (and samples). The criteria that we follow in the representations is dark curves for the cooling process and curves of the same color bur lighter for the heating process. But, generally, as we shall see, these curves overlap, and then a single curve (the lighter one) is seen for each sample or start pressure (and sample).

Figures 5.14 and 5.15 show the resistivity as a function of temperature of two sets of samples.

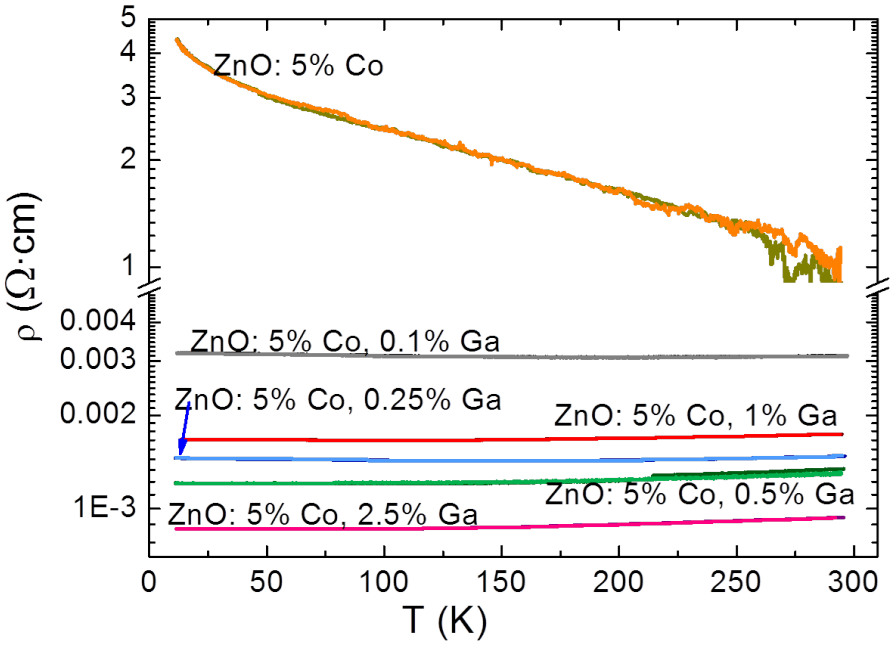

***Figure 5.14**: Resistivity for ZnCoO:Ga with 5% of cobalt and different concentrations of Ga.*

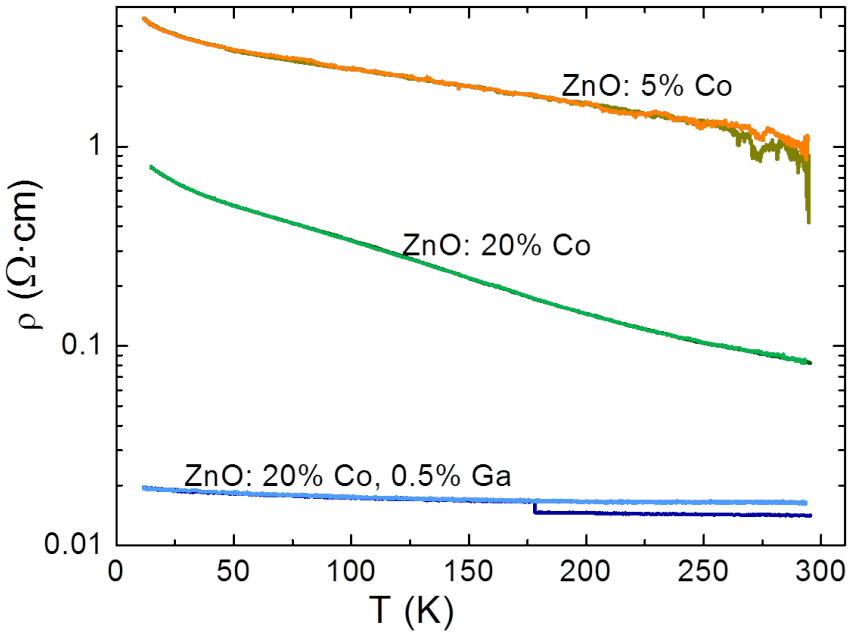

***Figure 5.15**: Resistivity for ZnCoO with 20% of Co, and ZnCoO:Ga with 20% of Co and 0.5% of gallium compared to ZnCoO with 5% of cobalt.*

Figure 5.14 compares the temperature dependence of resistivity for a (Zn,Co)O (5%Co) undoped film and a series of (Zn,Co)O (5%) doped with different amounts of Ga. Fig. 5.15 compares the temperature dependence of resistivity for the same (Zn,Co)O (5%Co) undoped film and two other films: an undoped (Zn,Co)O (20%Co) thin film and a 0.5% Ga-doped (Zn,Co)O (20%Co) thin film.

As previously shown in Table 5.1, Fig. 5.14 clearly shows that in ZnCoO (5% Co) the resistivity decreases with the increase of the Ga content in all the temperature range observed (with the exception of the sample doped with 1% of Ga). This is also the case for (Zn,Co)O (20%Co) (Fig. 5.15). A resistivity decrease is observed in non-Ga-doped samples from 5% to 20% Co films, but this cannot be considered a systematic behaviour.

The derivative ($\mathrm{d}\rho/\mathrm{d}T$) give us a more precise information about the resistivity minimum. As a general trend, we observe that for lower electron mobilities the minimum occurs at a higher temperature.

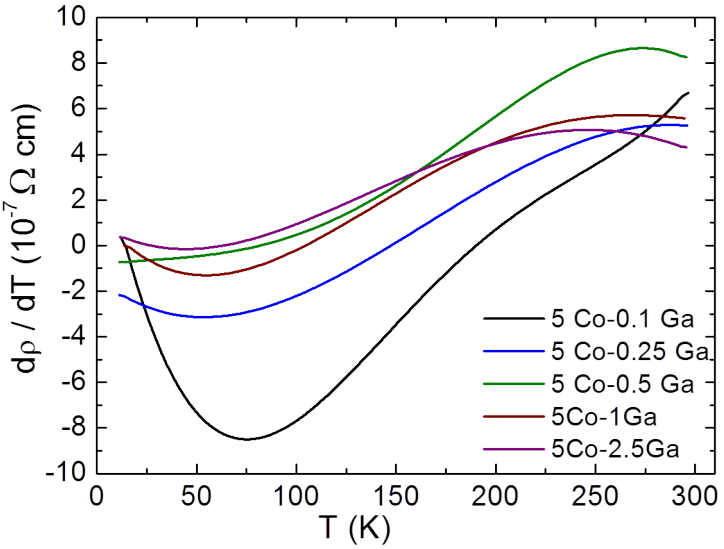

***Figure 5.16**: Derivative $d\rho/dT$.*

The scale of the resistivity in Figure 5.14 is too large to discuss the features of the temperature dependence. A reduced scale is shown below for each sample (Figures 5.17 and 5.18). For degenerate samples, for which the resistivity change is very small across the whole temperature range, a linear scale is chosen. For non-degenerate samples (non-Ga-doped samples) an Arrhenius plot is used, in order to estimate the activation energies of the processes involved in electron transport.

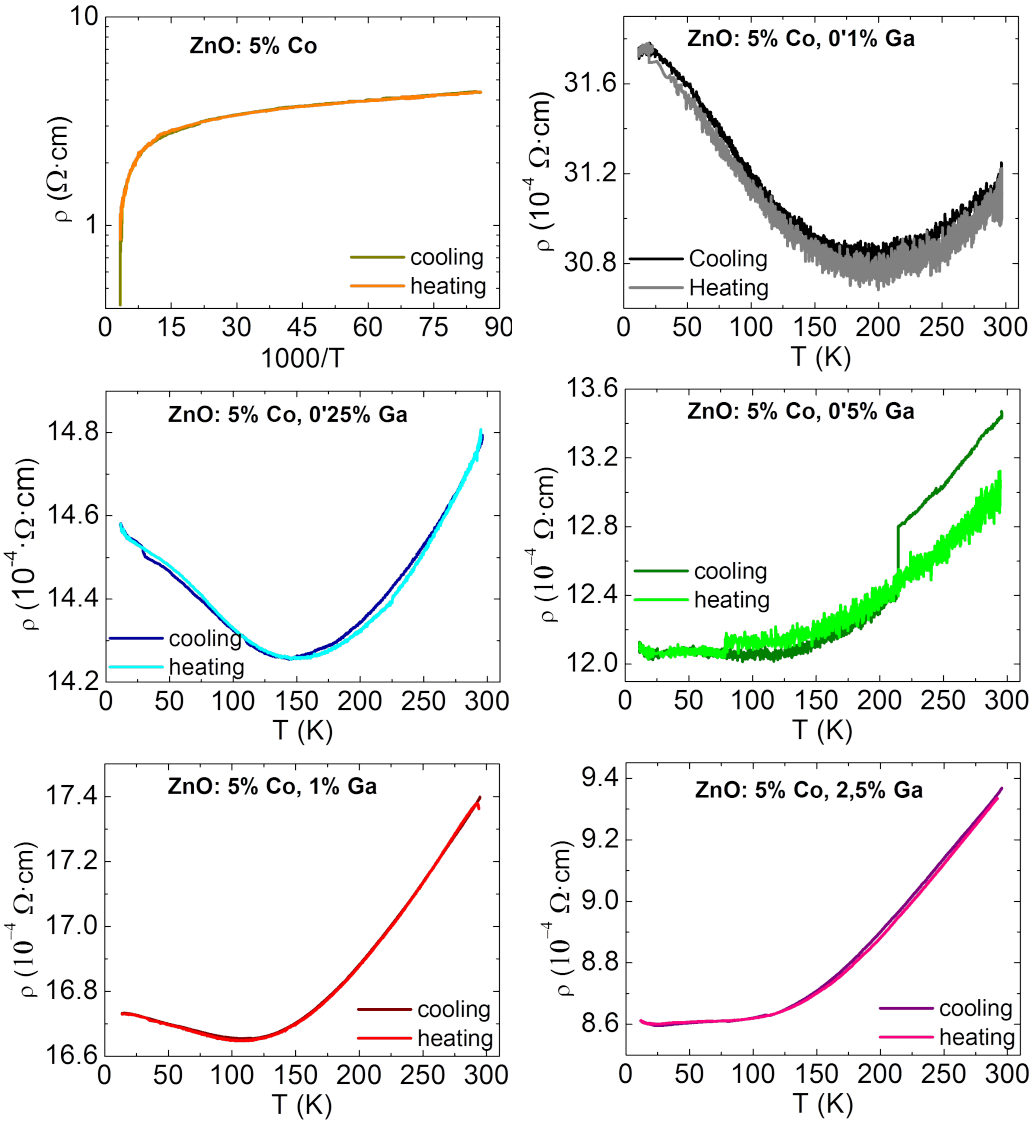

***Figure 5.17**: Resistivity in function of the temperature for each sample of ZnCoO:Ga with 5% of Co.*

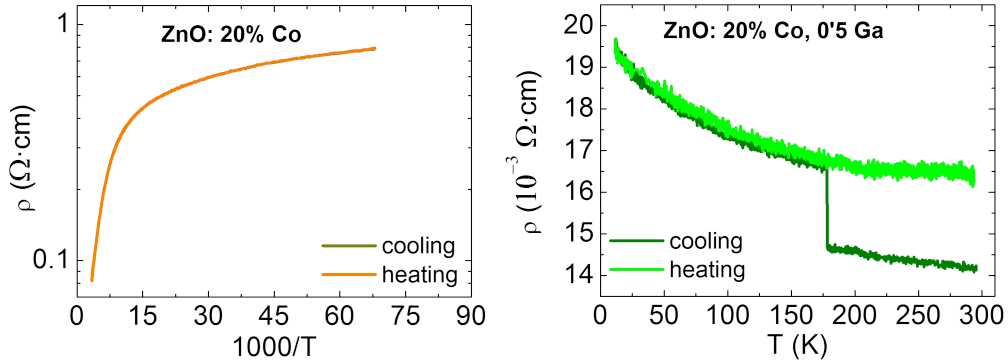

***Figure 5.18**: Resistivity in function of the temperature for each sample of ZnCoO:Ga with 20% of Co.*

There are basically two mechanisms controlling the electron mobility in semiconductors: phonon scattering that dominates at high temperature and ionized impurity scattering that dominates at low temperature.

The observed trend of the temperature dependence of resistivity for all samples can be summarized as follows: resistivity decreases between 300 K and some value of T, that we call $\mathbf{T_m}$ (zero crossing of the derivative). In that range, the mobility slightly increases (in this temperature range phonon dispersion would be slightly dominant). Below $\mathbf{T_m}$, the mobility decreases, indicating that impurity scattering becomes dominant.

An interesting result is that $\mathbf{T_m}$ clearly decreases with increasing the Ga concentration (or the free electron concentration, that is correlated to the Ga concentration), unlike what occurs in non-degenerate semiconductors in which for higher electron concentrations, the ionized impurity concentration would also be higher. Consequently, impurity scattering would become dominant at higher temperature and $\mathbf{T_m}$ would be expected to be higher for higher electron concentrations. This behaviour can have two possible origins. The first one is that as the electron concentrations increases the screening length decreases, which decreases the efficiency of impurity scattering. Also, grain barriers are known to be lower for larger electron concentrations; the effective electron mobility (as described previously) would be larger for larger electron concentrations.

On the basis of these considerations we can understand the temperature dependence of resistivity:

- For the undoped ZnCoO sample, the electron concentration is relatively low (below the Mott concentration and then non-degenerate). Trans-

port is mainly controlled by grain boundary barriers and free electron excitation at high temperature. We then observe a slow decrease of resistivity up to about 80-100 K (increase of the electron effective mobility) and then a larger decrease (most probably due to electron excitation from native donors with ionization energy of the order of 50 meV)

- For the rest of samples the relative change of resistivity from 10 to 100 K is very small (less than 10%) which indicates a degenerate behaviour (the electron concentration for all samples is above the Mott concentration).The electron concentration is constant and the small resistivity changes reflect changes in the electron mobility. For samples with mobilities from 33-37 cm^2/Vs the resistivity decreases for decreasing temperature as a consequence of the electron mobility increase, from 300 K down to about 100 K. For samples with lower mobility, the resistivity has a minimum at higher temperature (150-200 K).

5.3.2 Optical Properties at Low Temperature

In this paragraph we will discuss briefly a result that shows the consistency between transport and optical properties.

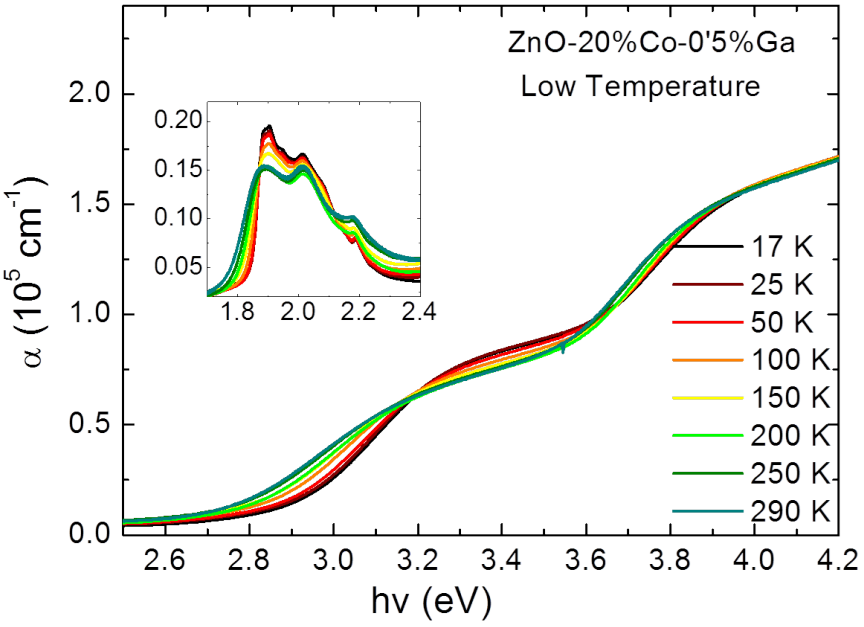

***Figure 5.19**: Evolution with temperature of the optical absorption of ZnCoO:Ga thin film with 15% of Co and 0.5% of Ga.*

Figure 5.19 shows the temperature dependence of the absorption edge of ZnCoO film (20% Co) doped with 0.5% Ga.

As we have discussed in the previous section, the carrier concentration of this sample decreases by nearly an order of magnitude as temperature decreases. Consequently, the Burstein-Moss shift (that would result in a bandgap decrease) partially compensates the increase of the bandgap due to the temperature decrease.

At the same time we observe an increase of the intensity of the charge transfer transition and a decrease of its width, consistently with the fact that the carrier concentration in the conduction band has strongly decreased.

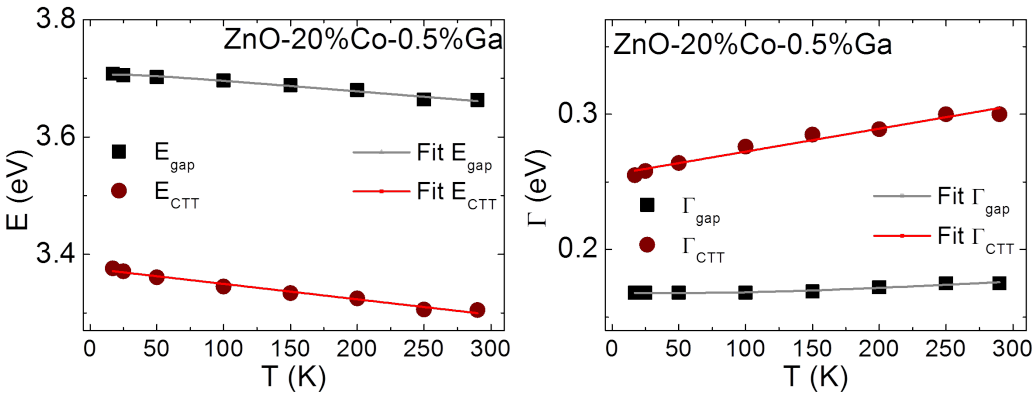

***Figure 5.20**: Temperature dependence of absorption edge and charge transfer transition of a sample of ZnO with 20% of Co and 0.5% of Ga.*

***Table 5.3**: Results of the dependence with temperature fitting.*

$E_{gap}(0)$ (eV)	3.706 ± 0.0002
α_B (meV/K)	0.19 ± 0.02
Θ_B (K)	100 ± 30
$\Gamma_{gap}(0)$ (meV)	167.9 ± 0.4
Γ (meV)	21 ± 14
Θ_B (K)	380 ± 100

5.4 Resistivity and FTIR Measurements Under Pressure

5.4.1 FTIR under Pressure

As we have seen in the previous sections FTIR measurements under pressure in doped samples can provide information about the transport properties, as the thin film optical properties are dominated by the free carrier response to the electromagnetic waves. In particular, free carrier absorption gives rise to an absorption edge proportional to the square of the photon wavelength.

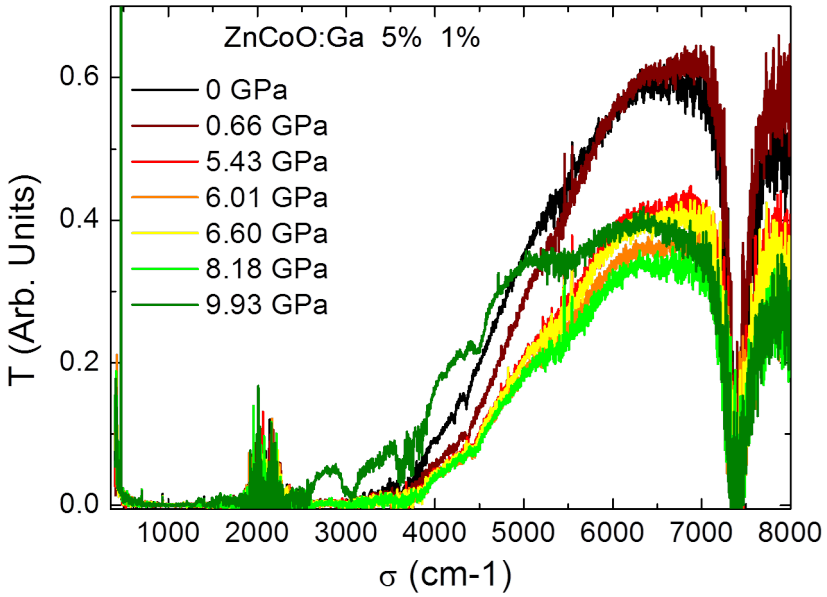

***Figure 5.21**: IR transmission spectra of a 1% Ga-doped ZnCoO (5%Co) under pressure.*

Figure 5.21 shows the transmission spectra of a Ga-doped ZnCoO (5%Co, 1%Ga) thin film on mica at different pressures. At ambient pressure the transmittance decreases as film on mica at different pressures. At ambient pressure the transmittance decreases as the wavenumber decreases and the sample becomes opaque at about 4000 cm^{-1}, which corresponds to the plasma frequency of free electrons at a concentration close to $2{\cdot}10^{20}$ cm^{-3}. Under pressure, up to 8 GPa, no major changes of the spectrum shape are observed. The opacity range does not practically shifts under pressure indicating the plasma frequency remains practically constant.

Changes in the 9 GPa spectrum are due to progressive breaking of the

thin film and mica substrate. Some part of the light passes through the mica and the transmission spectrum shows some of the mica IR active phonon absorption bands.

The observed pressure behaviour of free carrier absorption is consistent with the fact that the transport parameters of degenerate Ga-doped ZnO thin films, at ambient temperature, exhibit very small changes under pressure: the electron concentration remains constant under pressure and the electron mobility slightly decreases (due to the increase of the bandgap and, consequently, of the electron effective mass).

Consequently, no major changes are to be expected in the pressure dependence of the transport parameters, as we will discuss in the next section.

5.4.2 Resistivity under Pressure

In this section, we present the results of resistivity measurements performed under pressure at different temperatures (Figs 5.22, 5.23 and 5.24). Let's first recall that with the kind of cell we used pressure could not be increased beyond 9-10 GPa.

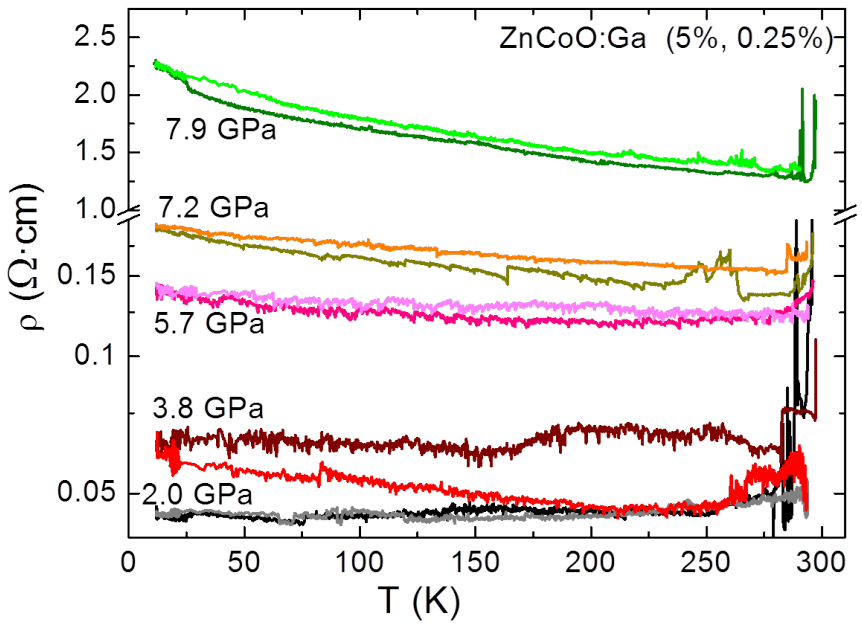

***Figure 5.22**: Resistivity measurements of ZnCoO:Ga with 5% of Co and 0.25% of Ga under pressure.*

Figure 5.22 shows the temperature dependence of resistivity at different

pressures for a thin film of ZnCoO:Ga with 5% of Co and 0.25% of Ga. Let us remind that at ambient pressure the resistivity of this thin film exhibited very little dependence on T as expected in a degenerate sample.

As we pointed out in the previous section, transport parameters of degenerate Ga-doped ZnO thin films, at ambient temperature, exhibit very small changes under pressure. The electron concentration is constant and the electron mobility decreases slightly under pressure. This precise result is in principle consistent with the general trend observed in Figure 5.22 for this sample up to 7.2 GPa: we observe a monotonous increase of the resistivity under pressure together with an increase of the absolute value of the slope of the resistivity versus T. Between 7.2 and 7.9 GPa, a quicker increase is observed in which resistivity increases by a factor 10.

Nevertheless, we must notice that resistivity changes are relatively larger in this experiment (with respect to those at ambient pressure as a function of T). This can be due to the fact that this particular sample has a larger resistivity ($4{\cdot}10^2$ Ωcm) at ambient pressure and temperature, corresponding to an electron concentration between 10^{18} and 10^{19} cm^{-3}, close or below ZnO Mott concentration and then not fully degenerate. In this situation, the increase of the ionization energy of the Ga donors under pressure (due to the increase of the effective mass and the decrease of the dielectric constant) would result in a progressive trapping of electron by Ga donors, which would lead to an increase of the resistivity (as well as an increase of the slope of its temperature dependence) under pressure.

The larger change at the highest pressure is most probably due to changes associated to the phase transition towards the rock-salt phase, as one would not expect such a large change from a progressive change of the electronic structure under pressure.

Figure 5.23 shows the temperature dependence of the resistivity of Ga doped ZnCoO thin film with 5% of Co and 2.5% of Ga at different pressures. From the resistivity values and the slope of the ρ-vs-T plots it turns out that (in spite of the Ga concentration) this sample is even less degenerate than the previous one. All the considerations made for the previous sample are valid for this one, as we observe a clear increase of the resistivity under pressure and its temperature slope (specially at low temperature).

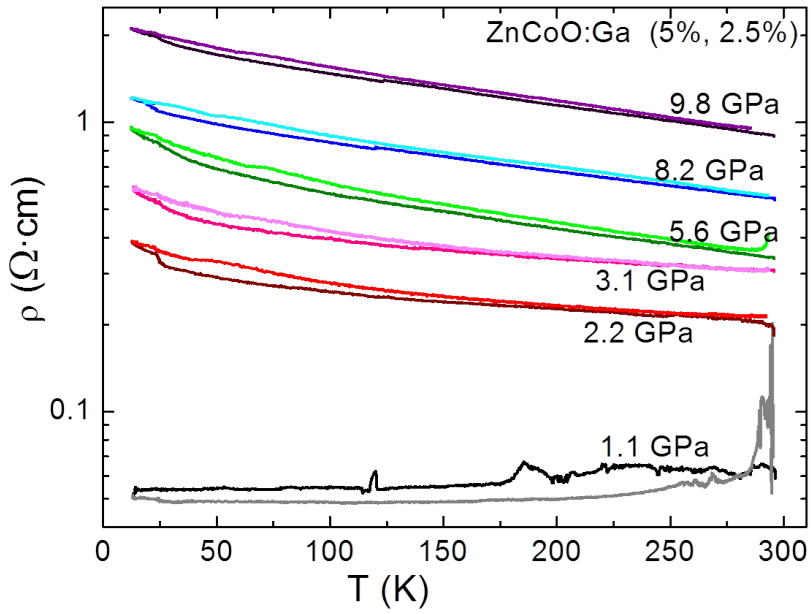

***Figure 5.23**: Resistivity measurements of ZnCoO:Ga with 5% of Co and 2.5% of Ga under pressure.*

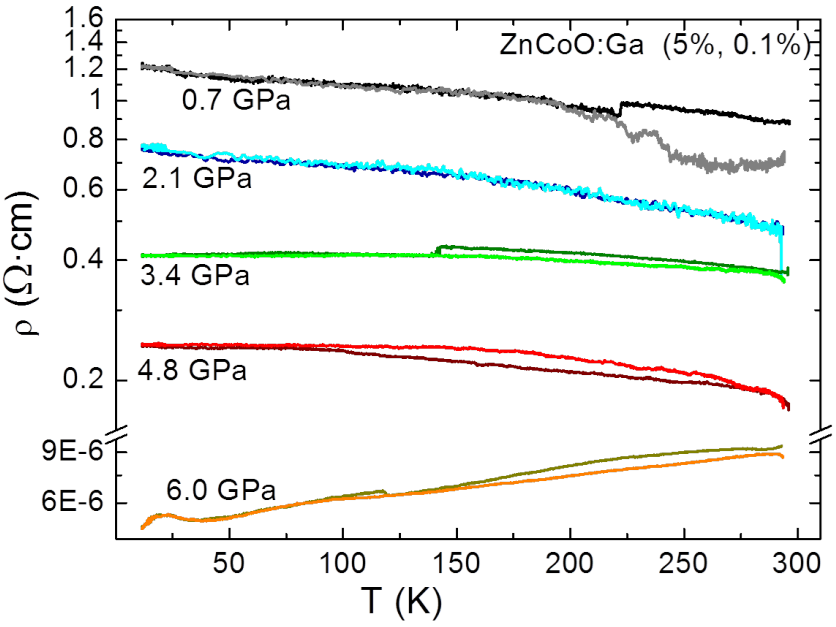

***Figure 5.24**: Resistivity measurements of ZnCoO:Ga with 5% of Co and 0.1% of Ga under pressure.*

Figure 5.24 shows the temperature dependence of resistivity at different pressures for a 5% of Co and 0.1% of Ga sample. In this particular sample the maximum pressure was 6 GPa because, as we noticed when opening the cell, one of the wires had pierced the insulation and was in contact with the gasket. The fact that resistivity decreases under pressure is very anomalous. This might be a result of a small current leak through the gasket that becomes progressively larger under pressure until it becomes a short-circuit when the insulation is pierced.

5.5 Further Characterization of ZnCoO:Ga thin films

5.5.1 Raman Spectroscopy

As we explained in the chapters devoted to experimental methods and those devoted to results on ZnCoO thin films, Raman spectroscopy is a useful tool in the characterization of materials. In this section we will show the results obtained at room conditions for thin films of ZnCoO doped with gallium. All films here studied have been grown on sapphire.

Figures 5.25 and 5.26 show the spectra of several Ga-doped ZnCoO thin films (5% and 20% of cobalt respectively) with different gallium concentrations, compared with undoped samples. Table 5.4 reports the wavenumber of the peaks.

Once we exclude the very fine peaks corresponding to the *c*-oriented sapphire substrate, we can clearly distinguish, as in the un-doped samples, the peaks corresponding to the A_1(TO) and E_2^{high} located at 373.3 cm^{-1} and 432 cm^{-1} respectively.

We can also observe how in the range between 500 and 600 cm^{-1} a combination of peaks appears corresponding to a maximum in the phonon density of states. As discussed in the previous chapter, this is due to the alloy disorder introduced by Co.

Doping with Ga has several effects on the Raman spectrum:

- First, we see that the density of states band (500-600 cm^{-1}) increases in some samples, due to supplementary disorder introduced by doping with Ga. It seems relevant to notice that this band is especially intense in the 0.1% Ga thin film, in which a low electron mobility was measured (also an indication of large disorder).

- The band between 450 and 500 cm^{-1} seems to have the same origin as it also corresponds to a high phonon density of states.

- A new small band is observed around 631 cm^{-1} that is correlated to Ga concentration, and has been previously shown to appear in Ga-doped ZnO and can correspond to local modes associated to Ga centres[136].

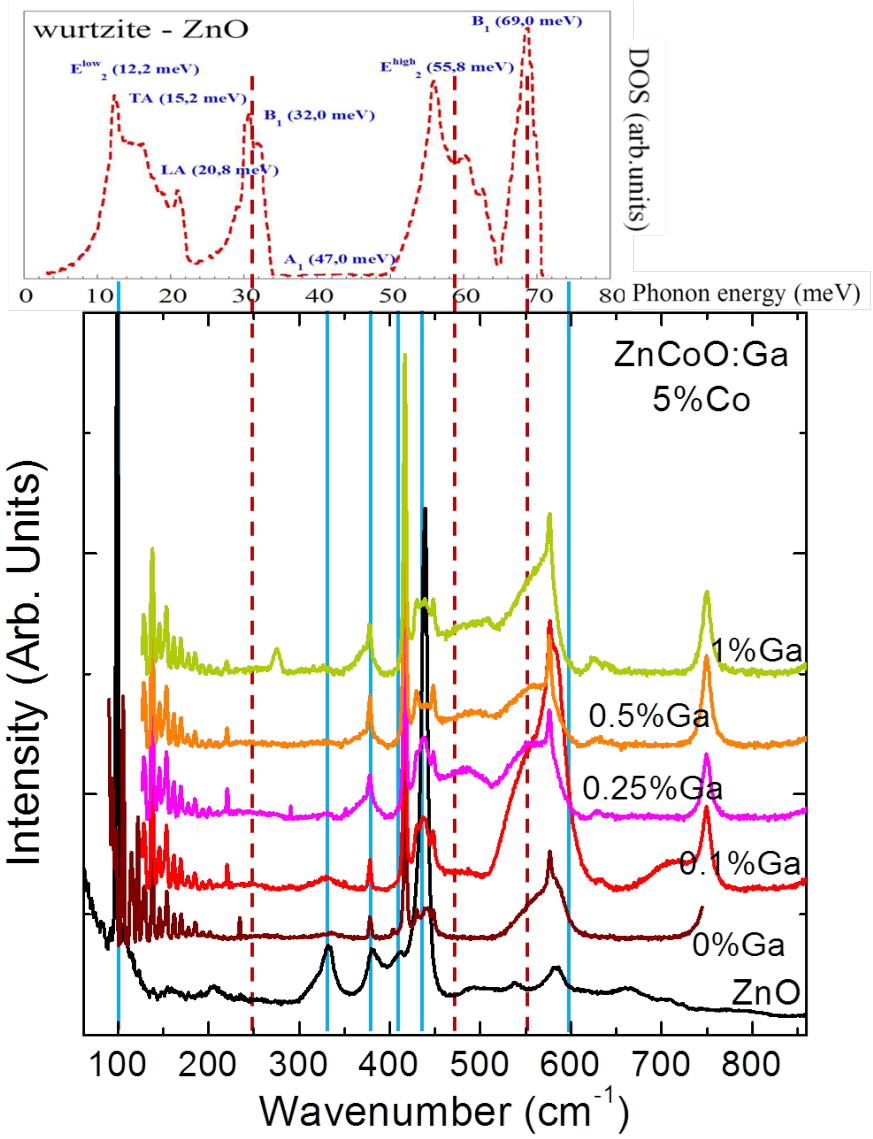

***Figure 5.25**: Raman spectra of ZnCoGaO.*

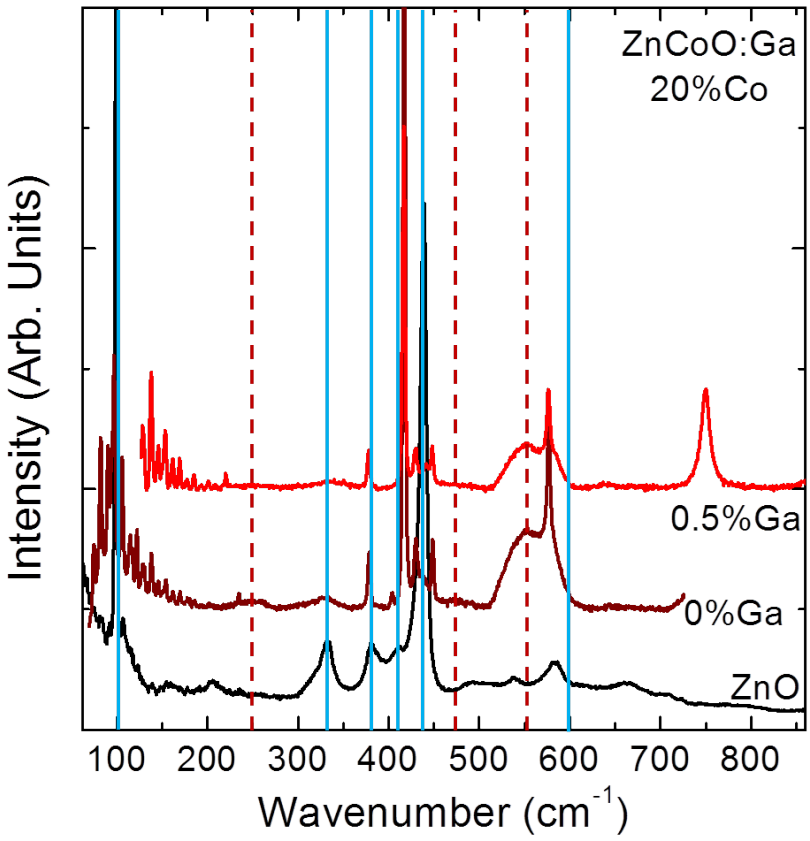

***Figure 5.26**: Raman spectra of ZnCoGaO.*

***Table 5.4**: Experimental Raman phonon frequencies (in cm^{-1}) at room conditions for samples of ZnCoO doped with gallium.*

Mode	**ZnCoO 5%Co 0.1%Ga**	**ZnCoO 5%Co 0.25%Ga**	**ZnCoO 5%Co 0.5%Ga**	**ZnCoO 5%Co 1%Ga**	**ZnCoO 20%Co 0.5%Ga**
	330.1				
	- - -	374.2	372.8	371.0	- - -
A_1(TO)	378.1	378.2	378.3	378.3	378.0
Substrate	416.7	416.7	416.7	416.8	416.7
Substrate	429.4	429.2	429.5	429.3	429.6
E_2^{high}	436.6	436.7	438.0	436.1	441.3
Substrate	448.3	448.2	448.2	448.3	448.2
	559.1	563.6	563.4	558.2	554.7
Substrate	576.6	576.4	576.3	576.5	576.4
E_1(LO)	584.2	582.8	581.5	579.8	580.7
	633.4	631.9	631.0	632.2	- - -

The fact that A_1(LO) and E_1(LO) modes are not observed is to be expected in doped samples, in which there is a strong interaction between the plasmon and the LO polar modes. This interaction leads to the change of both frequencies, especially at doping levels for which the plasmon energy is of the order of the LO phonon energy. The plasmon-LO phonon mixed modes are called L^- and L^+ and its frequencies are given by:

$$\omega_{L\mp} = \frac{1}{\sqrt{2}}\left[\left(\omega_P^2 + \omega_{LO}^2\right) \mp \sqrt{(\omega_P^2 + \omega_{LO}^2)^2 + 4\omega_P^2(\omega_{LO}^2 + \omega_{TO}^2)}\right]^{1/2} \quad (5.7)$$

Figure 5.27 shows a calculation of L^- and L^+ mode frequencies in ZnO as a function of the doping level, for both A_1 and E_1 polar phonon (the values used in the calculation are 0.27 for the relative electron effective mass and 4 for the relative electronic dielectric constant).

This calculation explain why the LO modes are not observed: for most of the Ga-doped thin films here studied, the plasmon frequency is in principle much higher that the phonon modes. At these high doping levels, the L^- mixed mode frequency is the TO frequency and the L^+ mode frequency is the plasmon frequency.

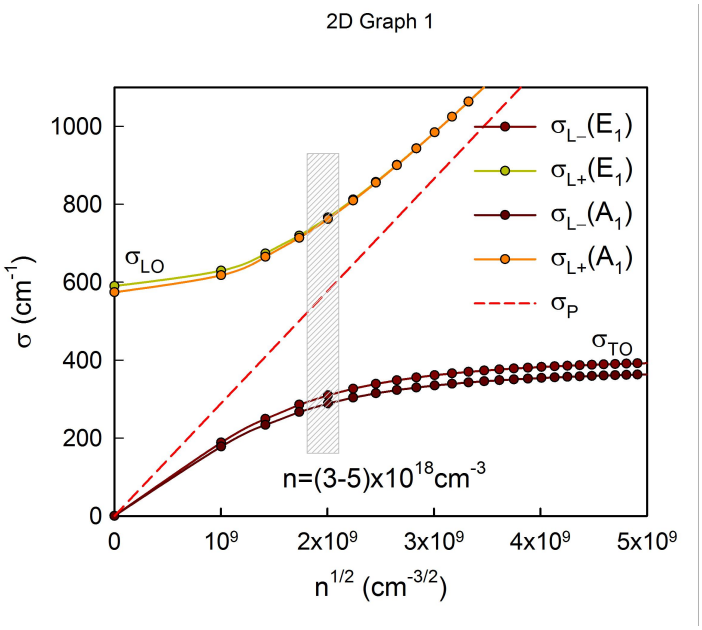

***Figure 5.27**: L^- and L^+ mode frequencies in ZnO as a function of the doping level, for both A_1 and E_1 polar phonon.*

It seems relevant to notice that in the spectrum of the 0.1%Ga doped thin film, two peaks are observed at around 320 and 720 cm^{-1}. In the figure we have outlined the doping level for which the L^- and L^+ mixed mode would have frequencies of the order of the observed peaks. The doping range is below the measured values for this Ga concentration but we must recall that thin films of these series exhibited a large dispersion in the electron concentration and some of the anomalous behaviour observed for them (as in transport measurements under high pressure). According to these results, we could assume that the nominal concentration is higher than the real amount of Ga in the samples.

5.5.2 Magnetic Properties

Finally, we will present the results of some magnetic measurements. Let us keep in mind that the main objective of this thesis is not the investigation of the magnetic properties of ZnCoO thin films. Then we have not attempted to perform a systematic investigation but rather to explore some ideas about the effect of Ga-doping on the magnetic properties, that according to some authors can lead to ferromagnetic behaviour[137]. The magnetic behaviour of such materials depends upon the concentration of the TM ions in the crystal, the carrier density and the crystal quality[14]. It is interesting that the DMS

exhibit ferromagnetic behaviour for spin-based light-emitting diodes, sensors and transistors[138].

Systematically, undoped wurtzite ZnCoO thin films have a paramagnetic behaviour, with a clear evidence of antiferromagnetic coupling between the Co atoms at second neighbouring position (super-exchange mediated through oxygen). This is in agreement with other works[116], where they report that below 20% of cobalt, the Co ion could be successfully substituted at Zn site and showed clear paramagnetism behaviour and an intrinsic ferromagnetic behaviour in the DMS thin film could not be induced by the substituting Co ion themselves. Also, this paper[116] and other works[115][139][14] argue that the structure and magnetic properties in Co-doped ZnO films strongly depends on the samples growth conditions and the post-grow process. However, in recent measurements in thin films of Ga-doped ZnCoO, ferromagnetic behaviour has been observed with a Curie temperature of 150 K (Fig. 5.31).

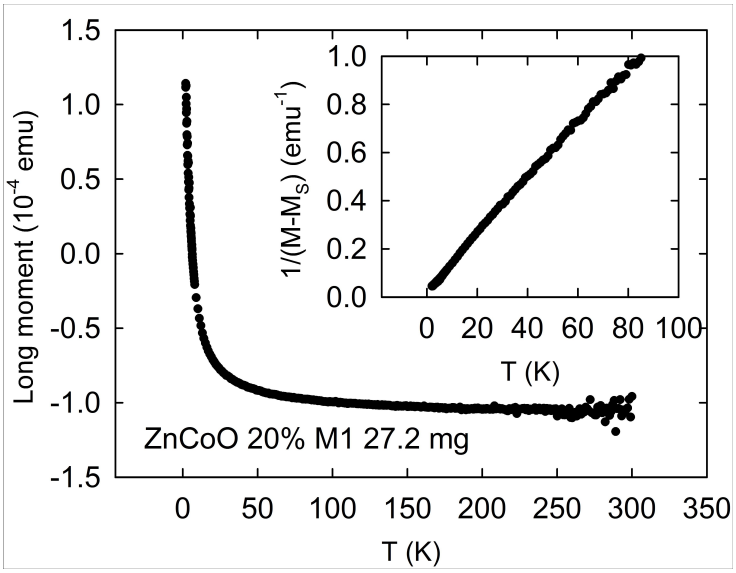

***Figure 5.28**: Temperature dependence of the magnetic moment as a function of T for 20% Co ZnCoO thin film grown on c-sapphire.*

Fig 5.28 shows the temperature dependence of the magnetic moment as a function of temperature for a 20% Co ZnCoO thin film deposited on C-sapphire. The negative value at high temperature is due to the diamagnetic response of the sapphire substrate. The behaviour is clearly paramagnetic as shown in the inset by the almost linear behaviour of the inverse magnetic moment (once the contribution of the substrate is subtracted). Indications of antiferromagnetic behaviour are suggested by the fact the extrapolation

of the straight line in the inset does not cross the temperature axis at T=0 but at T=-2 K.

The previously described behaviour is fully consistent with the literature and also with results on ZnMnO and ZnFeO thin films[35][140].

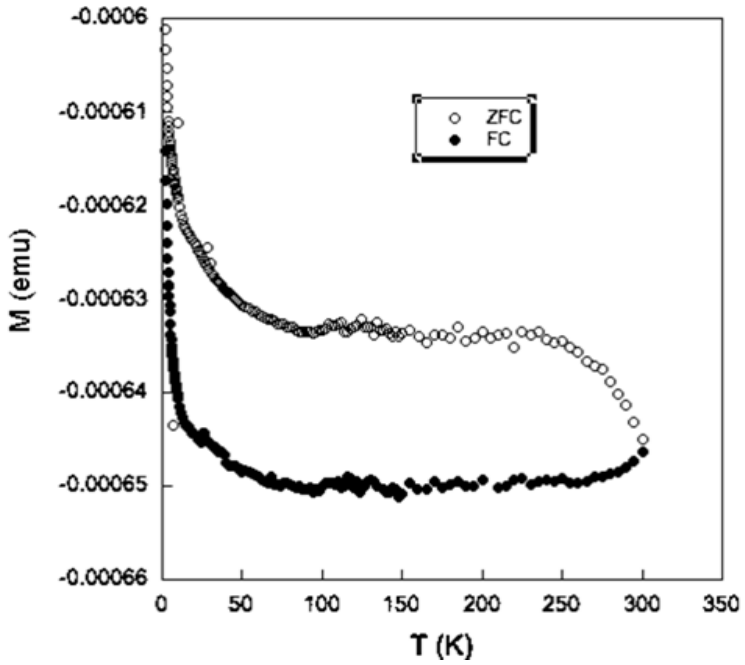

***Figure 5.29**: Temperature dependence of the magnetic moment of 0.5% Ga doped ZnCoO (5%Co) thin film.*

Indication of a more complex behaviour have been found in Ga-doped ZnCoO thin films. Fig. 5.29 shows the temperature dependence of the magnetic moment of a 0.5% Ga-doped ZnCoO (5% Co) thin film. Unfortunately this sample has a magnetic signal at the detection limit of the SQUID, so the substrate contribution could not be corrected. This is the reason why the magnetic moment is negative. However, in spite of the fact the behaviour is mainly paramagnetic, the clear difference between the FC (field cooled) and ZFC (zero field cooled) plots is a clear indication of the presence of a ferromagnetic contribution[137].

The complexity of the magnetic behaviour induced by Ga-doping is further confirmed by measurements on a thicker thin film in which the substrate contribution could be accurately corrected. Figure 5.30 shows the temperature dependence of the magnetic moment of a 0.5% doped ZnCoO (20% Co) thin film.

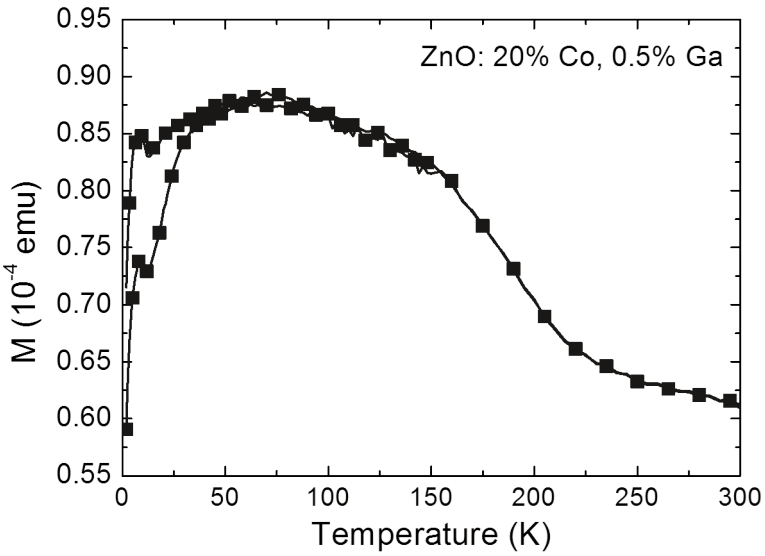

***Figure 5.30**:* Temperature dependence of the magnetic moment of a 0.5% doped ZnCoO (20% Co) thin film.

Apart from the larger value of the magnetic moment, indicating ferromagnetic behaviour, it is clear that there are some other contributions. The slight increase of the magnetic moment as temperature decreases suggests a paramagnetic contribution. The abrupt decrease of the magnetic moment below 40 and 20 K suggests antiferromagnetic behaviour. The presence of a ferromagnetic contribution is further confirmed by the magnetization loops at different temperatures shown in Figure 5.31.

The top shows the magnetization loops at different temperatures in the whole magnetic field range. The loops evolve from a mainly paramagnetic behaviour down to about 25K. Then, along with the decrease of the magnetic moment (probably associated to the antiferromagnetic transition around 20 K), the loops become clearly ferromagnetic, with moment saturation at much lower magnetic field (around 1000 Oe), remanence moment up to 40-50% of the saturation moment and a coercive magnetic field of some 300 Oe.

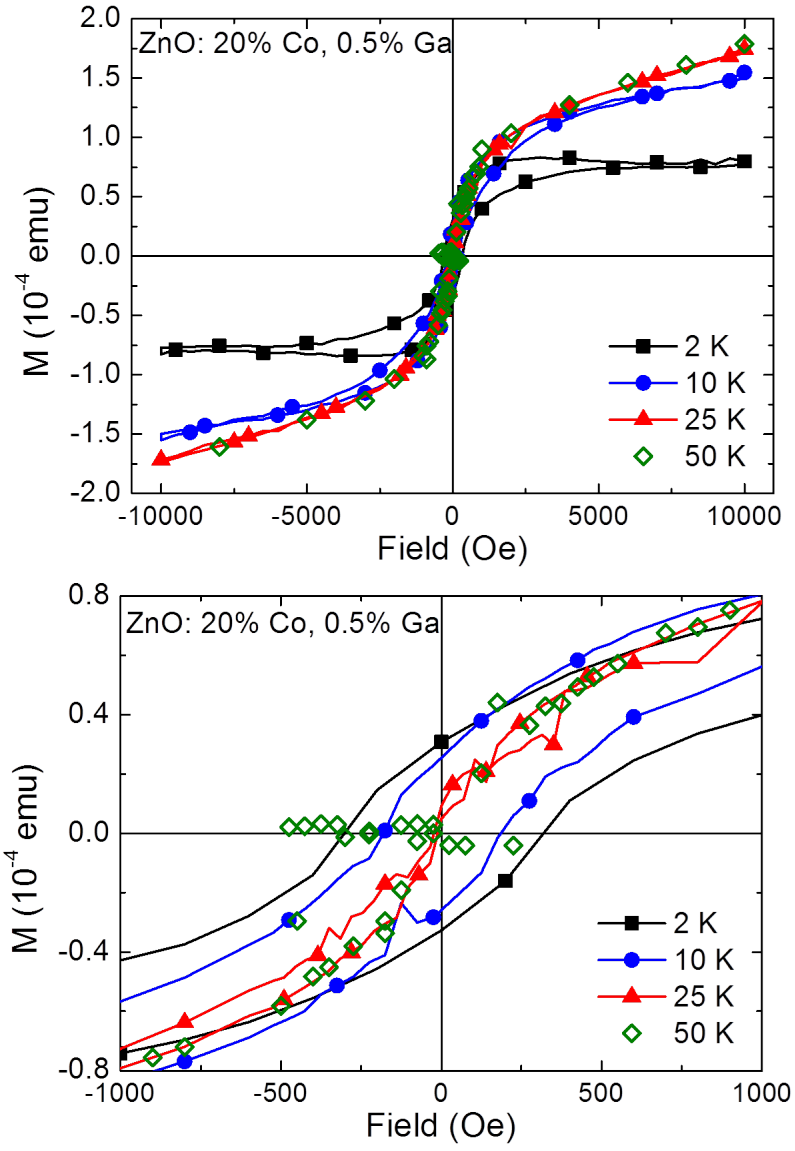

***Figure 5.31**: Magnetisation loops at different temperatures for a sample of ZnO with 20% of Co and 0.5% of Ga.*

5.6 Conclusions

- We have prepared Ga-doped ZnCoO thin films in order to study the effect of free electrons on the Co-related features of the optical properties.
- SEM images of the thin films show that they present a smooth and

homogeneous surface with the presence of some aggregates.

- We have carried out transport measurements at ambient temperature for different concentrations of Ga in a ZnCoGaO thin films with 5% of cobalt. The electron concentration increases with the Ga content indicating Ga also a donor in ZnCoO thin films.

- The electron concentration is smaller than the nominal Ga concentration, as also observed in Ga-doped ZnO. In ZnO, this effect was shown to be related to the presence of fully oxidized Ga in octahedral configuration, probably in nanocrystallites of Ga_2O_3 oxyde or $ZnGa_2O_4$ spinel.

- The electron mobility exhibits a remarkable insensitivity to the alloy disorder. Electron mobilities as high as 35-37 cm^2/Vs have been observed. This could be related to the fact that the interaction between O $2p$ and Co $3d$, the should be the predominant contribution to the alloy disorder potential, mainly affects the valence band.

- There is a trend in the electron mobility, that tends to be larger for larger free electron concentrations. Transport properties seem to be controlled by grain boundary potential barriers whose height becomes smaller as the electron concentration increases.

- The behaviour of transport properties, as a function of temperature and under high pressure can be explained by the same transport mechanisms (grain boundary barriers).

- From the infrared reflectivity of as-grown samples we see that the plasma reflection structure is visible, as well as the trend of the plasma reflection minimum shifting to lower wavenumbers as the electron concentration decreases.

- The passivity of Ga-related donors, associated to full oxidation of Ga-atoms, is observed by air annealing and detected both through transport and FTIR reflectivity spectra. The plasma minimum appears to shift to lower frequencies as the annealing temperature increases. ZnCoO:Ga thin films basically behave as pure ZnO thin films: the carrier concentration can be controlled by thermal annealing. For Ga-doped ZnCoO thin films the carrier concentration at room temperature decreases as the annealing temperature increases. The activation energy of the process is about 1.3 eV.

- The effect of Ga-doping on the optical properties has been studied both in samples with different cobalt (5, 20 and 30% Co) and Ga content (0.1 to 2.5%Ga), and, more especially in air annealed ZnCoO:Ga with 5% Co and 2.5% Ga sample, in which the electron concentration could be controlled in a more continuous way. As the electron density is increased, the fundamental absorption shifts toward high photon energies. The shift of the optical bandgap can be assimilated to the shift of the Fermi level, as it is the origin of the Burstein-Moss effect.

- Increasing the electron concentration in ZnCoO thin films leads to the expected blue shift of the alloy optical bandgap (Burstein-Moss shift). More interestingly, two more effects are observed in the CTT: *1)* There is a clear shift to higher energies of the CTT, practically equal to the shift of the Fermi level, as expected from the shift to higher energies of the empty final states as the conduction band is filled with free electrons and, *2)* There is a pronounced, exponential decrease in its intensity. This has been explained by the k-dependence of the dipole matrix element of the CTT, that has a Gaussian dependence on the k-vector. Higher energies of the final states in the conduction band also correspond to larger k-vector and then lower values of the matrix element and lower absorption intensity. The exponential dependence of the absorption coefficient on the electron kinetic energy explains the exponential decrease of the CTT intensity as the Fermi level energy shifts to higher energies. We have shown how the CTT band can be consistently described as a localized-to-extended states optical transition.

- We have also studied the transport and optical properties of Ga-doped ZnCoO thin films at low temperature. There is a trend in the temperature dependence of resistivity for all samples. Resistivity decreases between 300K and T_m and then increases between T_m and low temperature. By reasonably assuming that most samples are degenerate, and then the electron concentration is constant, the evolution of the resistivity is explained by the temperature dependence of the effective electron mobility. Between 300 K and T_m, the electron mobility slightly increases as the phonon number decreases. Below T_m, the mobility decreases, indicating that the impurity scattering becomes dominant, or that less electron can overcome the grain boundary barriers. The fact that T_m decreases with increasing gallium concentration indicates that the effect of potential barriers becomes less determinant as the electron concentration increases.

- Some samples with lower electron concentration, below the degeneracy limit, exhibit a more pronounced temperature dependence of the resistivity, with an activated behaviour (some 50 meV activation energy) above 100 K. Transport in this case is dominated by the ionization of shallow donors. Its optical properties also reflect this behaviour. At low temperature, as free electrons are trapped by donor levels, along with the expected increase of the bandgap we observe an increase of the intensity of the CTT, with a decrease of its width, consistently with the fact that the carrier concentration in the conduction band has strongly decreased.

- We have carried out resistivity and FTIR measurements under high pressure. From IR transmission spectra of Ga-doped ZnCoO:Ga (5%Co, 1%Ga) up to 8 GPa we see that the opacity range (determined by the plasma frequency) does not practically shift indicating that the plasma frequency remains almost constant.

- Resistivity measurements under pressure have been done or ZnCoO:Ga thin films with 5% Co and different Ga content. For 0.25% and 2.5% of Ga the electron concentration is constant and the electron mobility decreases slightly under pressure. There is a monotonous increase of the resistivity under pressure along with an increase of the absolute value of the slope of the resistivity in function of T.

- To complete the characterization of these samples we have made Raman spectroscopy measurements. There are some effects due to doping with Ga. The density of states band (500-600 cm^{-1}) increases due to supplementary disorder introduced by substitutional and segregated Ga. A new small band is observed around 631 cm^{-1} that is correlated to Ga content and can be associated to some Ga-related local mode. The LO-plasmon coupling is evidenced by the fact that LO modes are not observed for large electron concentrations, at which the L^+ coupled mode has the plasmon frequency, that is in principle much higher than the phonon modes. For one of the samples, with 0.1% Ga and with an electron concentration close to $5{\cdot}10^{18}$ cm^{-3}, two modes are observed that can reasonably correspond to LO-plasmon coupled modes L^- (320 cm^{-1}) and L^+ (720 cm^{-1}).

- Finally, some preliminary evidence of ferromagnetic behaviour associated to Ga doping has been observed in the investigation of the magnetic properties. While ZnCoO thin films systematically exhibit a clear

paramagnetic behaviour, with signs of antiferromagnetic coupling between second neighbour Co atoms, as Ga is added, evidences of ferromagnetic behaviour appear both in the temperature dependence of the magnetic susceptibility as well as in the hysteresis cycles recorded at low temperature.

Chapter 6

Results: ZnMgO and ZnMgCoO Thin Films

As we mentioned in the objectives of this work, one of them was studying the effects of increasing of the material gap on the optical properties associated to the presence of cobalt.

The most studied ZnO-based wide-gap alloy is ZnMgO[141][142][143]. Replacing Zn with Mg has the effect of increasing the alloy bandgap beyond 4 eV while keeping the wurtzite structure up to Mg proportions about 30%[141]. In this chapter we will present and discuss, first the preparation and optical properties of ZnMgO thin films and then the effects of introducing Co in the structure, i.e., (Zn,Mg,Co)O alloys.

Through experiments on ZnMgO and ZnMgCoO thin films we have seen an increase in the gap and thus the transparency range of the semiconductor. This has allowed us to access to the absorption bands of higher energy in the $3d$ shell of cobalt in tetrahedral coordination and thereby confirm the nature of the charge transfer transition, which moves as the absorption edge and becomes narrower, as a consequence of the increase of the density of states effective mass.

6.1 Optical Properties

6.1.1 Optical Properties of (Zn,Mg)O Thin Films at Ambient Temperature

Fig. 6.1 shows the absorption spectra at room temperature of several ZnMgO thin films with different magnesium proportion, deposited on *c*-sapphire, compared with the absorption spectrum of pure ZnO. These absorption edges

have been fitted using the Elliot-Toyozawa's theory as described in previous sections.

The effect of alloying with Mg on the bandgap is similar to the case of ZnCoO. There is a shift to higher energies for the bandgap of the material. As shown in Fig. 6.2 (left) the bandgap increases almost linearly with the Mg nominal proportion, at a rate of about 35 meV/% at. Mg. This rate is higher that the one found in the literature[141] that is around 20 meV/% at. Mg. The reason for this discrepancy is that the actual proportion of Mg in the thin film is higher than the one in the target, owing to the higher vapour pressure of Zn with respect to Mg. At substrate temperature of 600ºC, the Mg proportion in the thin film is nearly twice the proportion in the target[141].

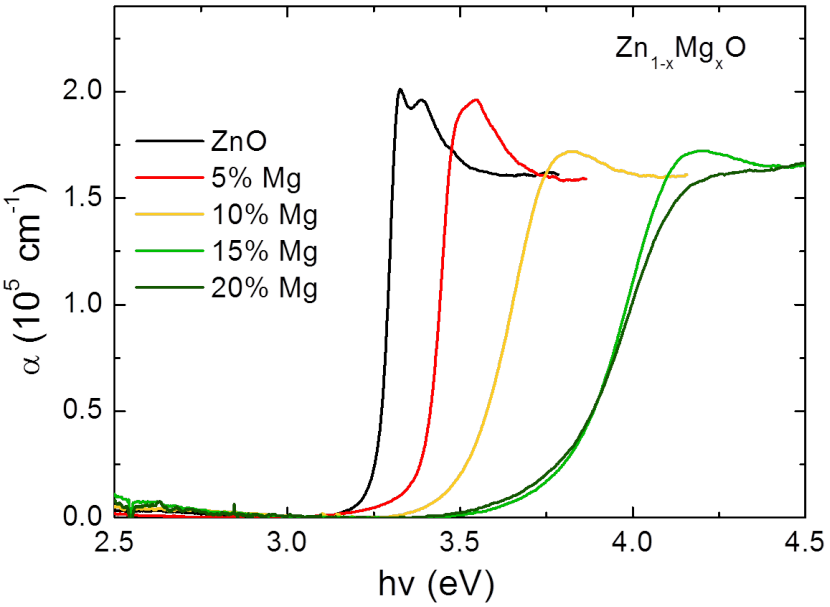

***Figure 6.1**: Optical absorption of ZnMgO thin films with different Mg content.*

Figure 6.2 (right) shows the exciton width as a function of the Mg content. The intensity of the exciton peak, even if it is visible for thin films with nominal 15% Mg (about 30-35% real), decreases with increasing the Mg proportion, due to the increase of alloy disorder. For the 5% Mg sample, ther is a clear indication of the exciton peak and the exciton +LO resonance (that become more clearly resolved at low temperature). For samples with higher Mg proportion only a broad band is observed.

Further increase of the Mg content at the material does not result in a

larger bandgap, but only in a larger transition width. This indicates that the maximum Mg proportion in the thin film (around 33% according to Ohtomo et al.[141]), at the deposition temperature used in this work (600ºC), is reached with 15% Mg targets. Beyond this proportion, segregation occurs and films become mixed-phase, with a growing presence of rock-salt ZnMgO.

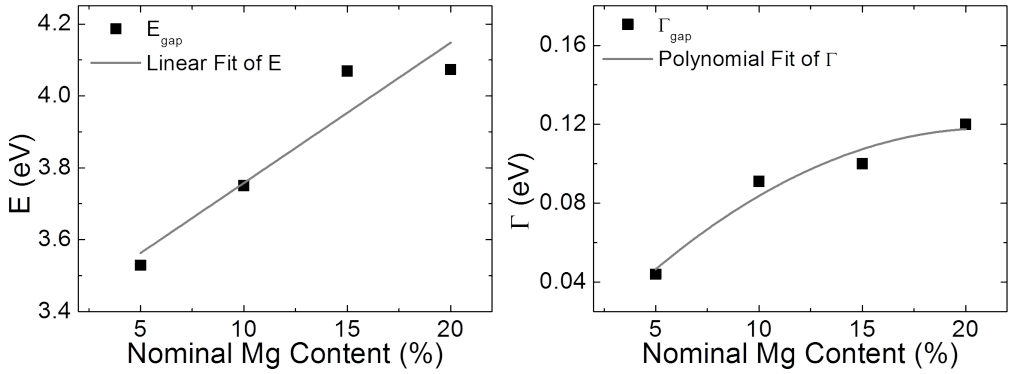

***Figure 6.2**: Dependence of the fitting parameters with the Mg content.*

6.1.2 Optical Properties of (Zn,Mg)O Thin Films at Low Temperature

Figures 6.3, 6.4 and 6.5 show the evolution of the absorption spectra for samples of (Zn,Mg)O thin films with different Mg proportions.

As previously said, for the 5% Mg thin film, as temperature decreases the excitonic peak and the exciton+LO resonance become clearly visible. For films with larger Mg proportion, the broad maximum observed at room temperature increases its intensity but the excitonic peaks are not resolved from the exciton+LO peak[144].

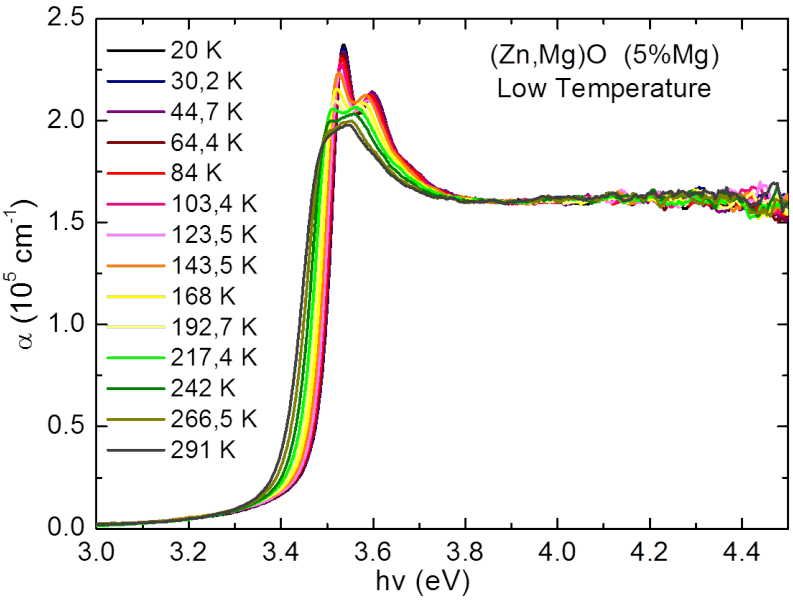

***Figure 6.3**: Evolution with temperature of the optical absorption of ZnMgO thin film with 5% of Mg.*

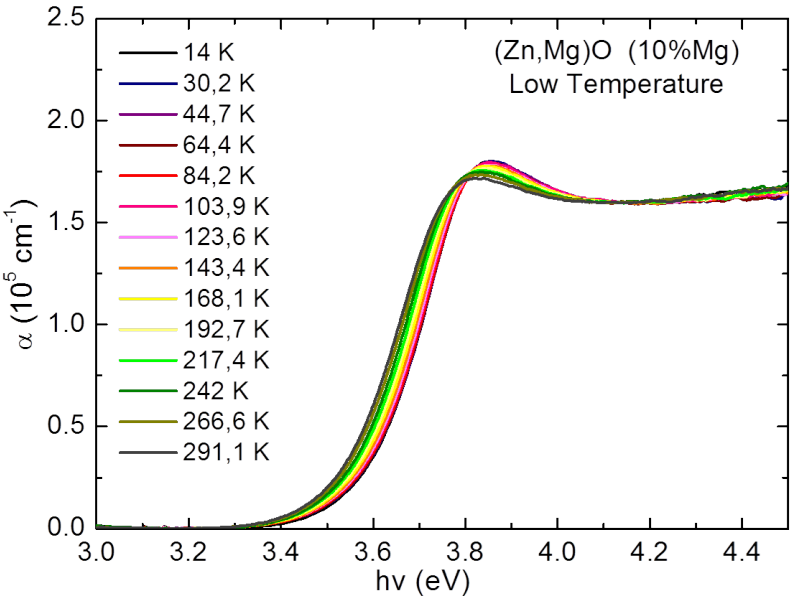

***Figure 6.4**: Evolution with temperature of the optical absorption of ZnMgO thin film with 10% of Mg.*

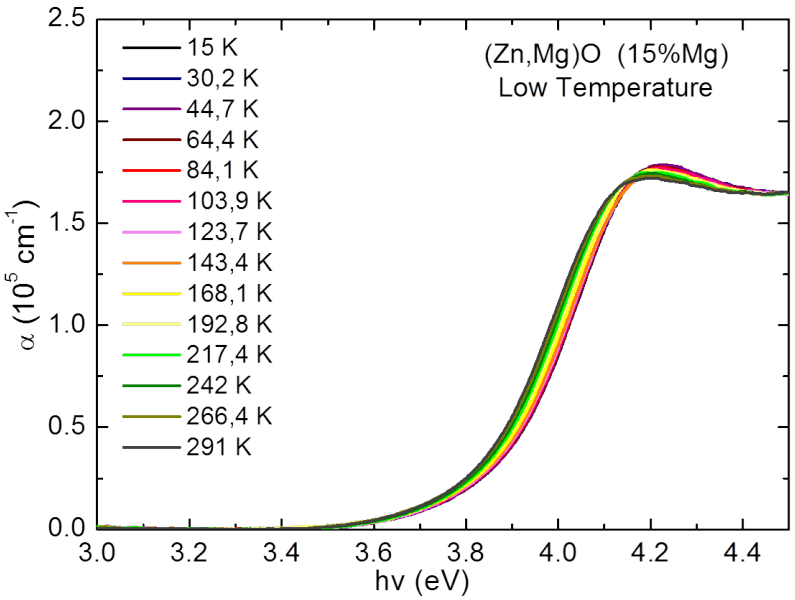

***Figure 6.5**: Evolution with temperature of the optical absorption of ZnMgO thin film with 15% of Mg.*

Spectra at different temperatures have been interpreted with the previously described Elliot-Toyozawa model, from which the bandap and the transition width are obtained. Figures 6.6 show the temperature dependence of those parameters as a function of temperature.

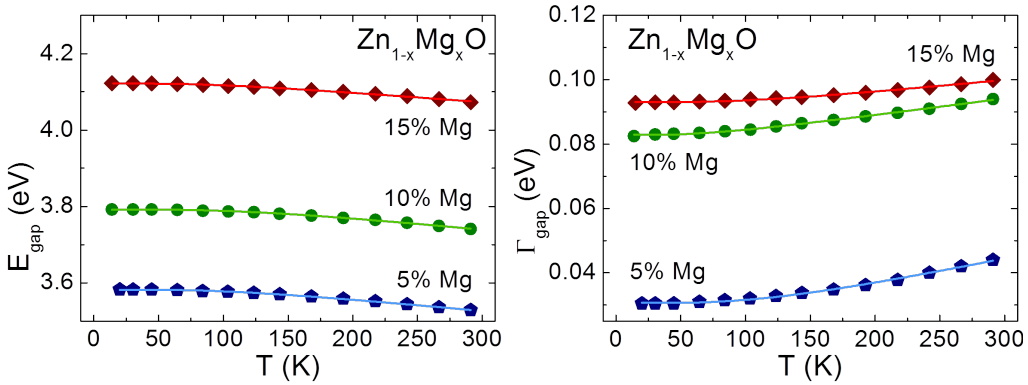

***Figure 6.6**: Dependence of the energy and width of the bandgap with the temperature for ZnMgO thin films with different content of Mg.*

The temperature dependence of the bandgap, for the three samples, exhibits the typical temperature dependence that can be accounted for through a Bose-Einstein model. The results of the Bose-Einstein fit is also shown in

Fig. 6.6 as continuous lines and the fitting parameters are given in the upper part of Table 6.1. The effective temperature (proportional to the phonon energy involved in the bandgap renormalization) is, as expected, close to the one found for ZnO.

***Table 6.1**: Results of the dependence with temperature fitting.*

Nominal Mg Content	**5%**	**10%**	**15%**
$\boldsymbol{E_{gap}(0)}$**(eV)**	3.5820 ± 0.0004	3.7910 ± 0.0004	4.1220 ± 0.0007
$\boldsymbol{\alpha_B}$**(meV/K)**	0.343 ± 0.012	0.354 ± 0.016	0.277 ± 0.018
$\boldsymbol{\Theta_B}$**(K)**	338 ± 15	380 ± 19	290 ± 30
$\boldsymbol{\Gamma_{gap}(0)}$**(meV)**	30.73 ± 0.13	82.90 ± 0.12	93.15 ± 0.12
$\boldsymbol{\Gamma}$**(meV)**	32.7 ± 0.4	11.68 ± 0.14	16 ± 3
$\boldsymbol{\Theta_B}$**(K)**	360 ± 20	210 ± 18	340 ± 40

As regards the temperature dependence of the transition width we can see in Figure 6.6 (right) the evolution from a phonon-controlled mechanism (5% Mg thin films to a defect controlled one). For the 5% Mg film the transition width quickly decreases with temperature and reaches a relatively low value (some 30 meV) at 15 K. It can be interpreted through a Bose-Einstein model with a phonon energy close to the one found for the bandgap, as shown in Table 6.1.

For the other thin films the low temperature width is much larger and its temperature dependence much more reduced, indicating a strong contribution of a localized potential scattering mechanism (most probably the alloy disorder). A localized potential scattering mechanism tends to be more effective for low energy electrons and then leads to a contribution to the transition width that is constant or increases as temperature decreases, so compensating the reduced effect of phonon scattering at low temperature and yielding a more constant and temperature insensitive width, as observed for the 15% Mg thin film.

6.1.3 Optical Properties of (Zn,Mg,Co)O Thin Films at Ambient Temperature

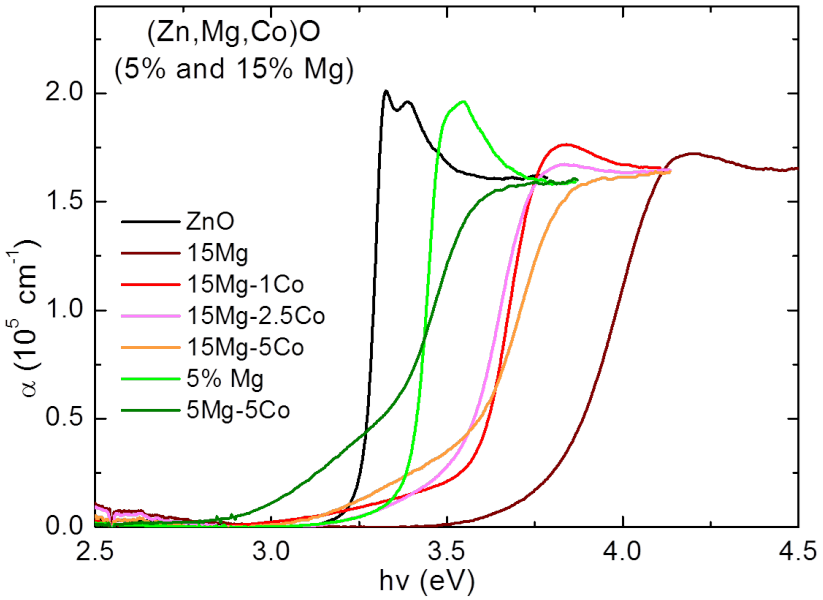

***Figure 6.7**: Optical absorption of ZnMgO thin films of 5 and 15% of Mg and doped with different cobalt content.*

Figure 6.7 shows the absorption spectra for several thin films of the (Zn,Mg,Co)O semiconductor alloy, prepared from single targets with the indicated cation proportions. Spectra have been interpreted with the same previously described modified Elliot-Toyozawa model. The fitting parameters of each spectrum are shown in Table 6.2.

***Table 6.2**: Parameters of the spectra.*

% Mg	% Co	E_{gap} (eV)	Γ_{gap} (eV)	E_{CTT} (eV)	Γ_{CTT} (eV)	I_{CTT} (cm^{-1})
5	**0**	3.534	0.110	—	—	—
5	**5**	3.558	0.110	3.335	0.200	43883.3
15	**0**	4.078	0.100	—	—	—
15	**1**	3.766	0.071	3.554	0.210	20516.8
15	**2.5**	3.755	0.081	3.538	0.150	24733.9
15	**5**	3.817	0.091	3.589	0.200	38497.7

Focusing on the 5% Mg thin films (green lines), we can see that the gap increase is very small and the main effect of the incorporation of Co is the presence of the CTT band.

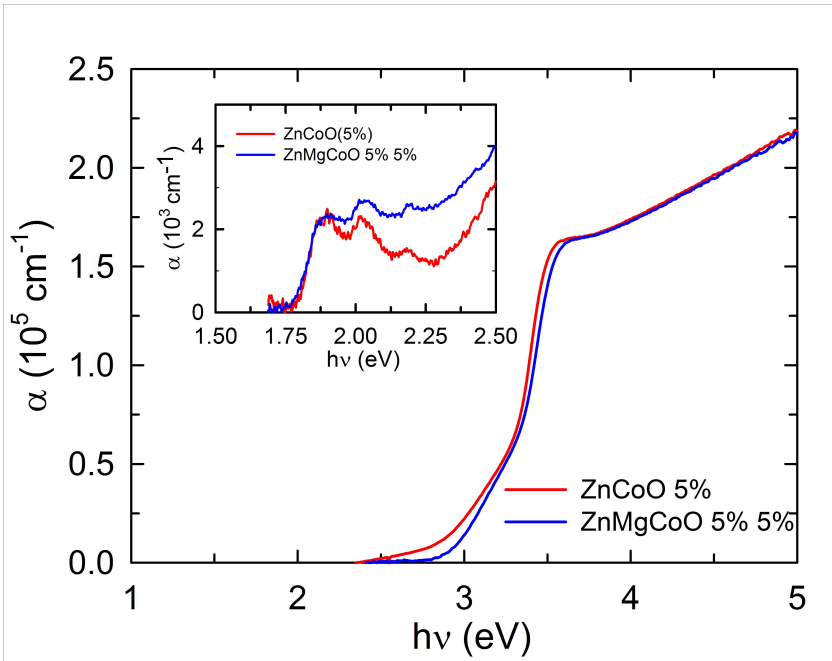

***Figure 6.8**: Optical absorption of ZnMgCoO and ZnCoO thin films in the UV and NIR (inset) range.*

In order to have a more compelling evidence of the Co incorporation, we must test the presence of Co $3d-3d^*$ transitions in the near infrared. Figure 6.8 compares the absorption edges of a ZnMgCoO thin film (5% Mg,5% Co) and a ZnCoO thin film (5% Co) as well as the region of the Co $3d-3d^*$ transitions near 2 eV (inset of Figure 6.8).

The shape and intensity of the Co $3d-3d^*$ (once the absorption tail from the CTT band is taken into account), is the same for both thin films, indicating that Co is indeed incorporated in a tetrahedral substitutional configuration. This result is consistent with fact that the CTT has also very close intensities in both thin films and confirms that the CTT is also a reliable signature of the incorporation of tetrahedral Co in the alloy lattice. The only noticeable effect that can be attributed to the presence of Mg is the 70 meV blue-shift of the fundamental absorption. With the bandgap change rate determined by Othomo et al.[141] (around 20 meV/% at. Mg) this would correspond to some 3.5% Mg in the lattice.

In the case of the 15% Mg/ 5% Co thin films, the bandgap decreases in all cases (with respect to ZnMgO thin films with the same nominal Mg content) and the presence of Co is again shown only by the intensity of the CTT.

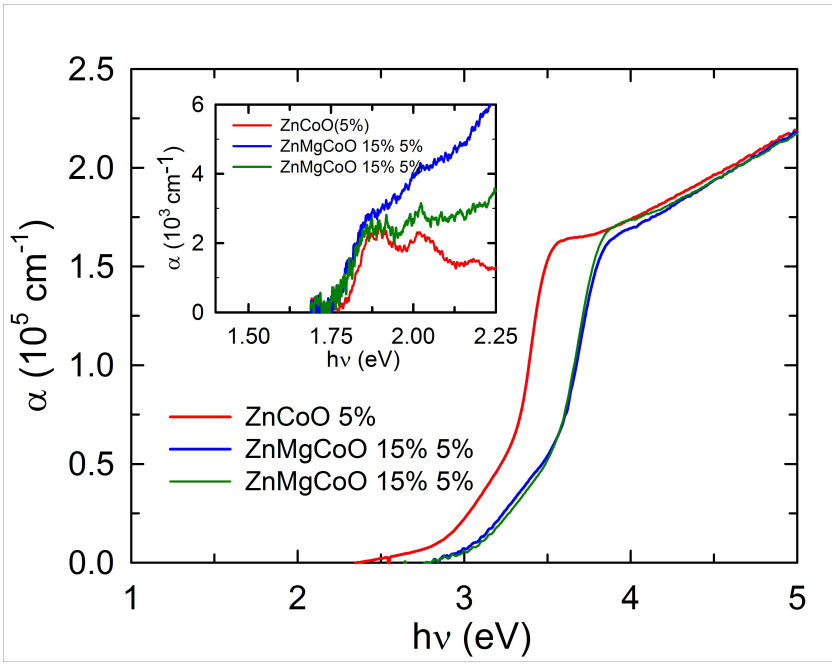

***Figure 6.9**: Optical absorption of ZnMgCoO and ZnCoO thin films in the UV and NIR (inset) range.*

We have also tested the intensity of Co $3d-3d^*$ transitions in the near infrared for this series of thin films. Figure 6.9 compares the absorption edges of two ZnMgCoO thin film (5% Mg,5% Co) and the same ZnCoO thin film (5% Co) as in the previous figure.

The inset of Figure 6.9 confirms that the shape and intensity of the Co $3d-3d^*$ transition is the same for both kind of thin films, indicating that the tetrahedral Co proportion in the thin film is determined by the nominal Co proportion in the target. Interestingly, the onset of the Co $3d-3d^*$ in the ZnMgCoO thin film appears to be red-shifted by some 22 meV with respect to the ZnCoO thin film. This would in principle indicate a smaller intensity of the crystal field acting on the Co $3d$ shell. From a recent determination of the lattice parameters as a function of the Mg proportion by Laumer et al.[145] for a 20% at. Mg in the alloy, the a parameter increases by 0.18% and the c parameter decreases by 0.3%. One could think that this can happen by simple "squeezing" the tetrahedral along the c direction without any change of the Co-O bond-lengths. EXAFS measurements reported by Park et al.

[146] show that there is an actual decrease of the Zn-O bond-length along the c-axis and an increase of the length of the three other Zn-O bonds (forming a small angle with the $a-b$ plane) that should actually result in an overall decrease of the average electrostatic interaction between the Co $3d$ electrons and the first neighbour O atoms.

As regards the CTT band, let us first notice that the intensity of the CTT is of the same order in both ZnMgCoO and ZnCoO thin films (confirming the reliability of this transition as a signature of tetrahedral Co in the lattice). The fundamental absorption edge of the ZnMgCoO films is blue-shifted by 290 meV, which according to Othomo[141] correspond to 15.4% Mg proportion in the film. This is actually about half of the Mg proportion found in ZnMgO thin films deposited from 15% Mg targets.

From results exposed in previous chapters along this thesis, we know that the bandgap of the alloys ZnMgO and ZnCoO increases with the Mg or Co proportion and, from the $p-d$ interaction model and *ab-initio* calculations reported in ref. [51] the effects of the presence of Co and Mg do not compensate each other; they contribute both in the same direction. These results indicate that there seems to be some kind of incompatibility in the simultaneous incorporation of Co and Mg when thin films are prepared from a single target. While the proportion of Co appear to be the one expected from the Co proportion in the target, the Mg proportion is reduced by a factor 2.

In spite of the bandgap being lower than expected, it is relevant to notice that in ZnMgCoO the maximum of the CTT band (and its onset, that is the relevant energy parameter) is blue-shifted by about 0.4 eV with respect to ZnCoO, which is another confirmation of the model proposed in Chapter 4: the final state of the CTT is the alloy conduction band.

6.1.4 Optical Properties of (Zn,Mg,Co)O Thin Films at Low Temperature

Figures 6.10, 6.11 and 6.12 show the evolution of the absorption spectrum with the temperature for (Zn,Mg,Co)O samples with 15% of magnesium doped with 1%, 2.5% and 5% of cobalt respectively.

Spectra have been interpreted with the same previously described modified Elliot-Toyozawa model, including a Gaussian band to give account of the CTT absorption band. The fitting parameters of each spectrum are shown in Table 6.3 (bandgap).

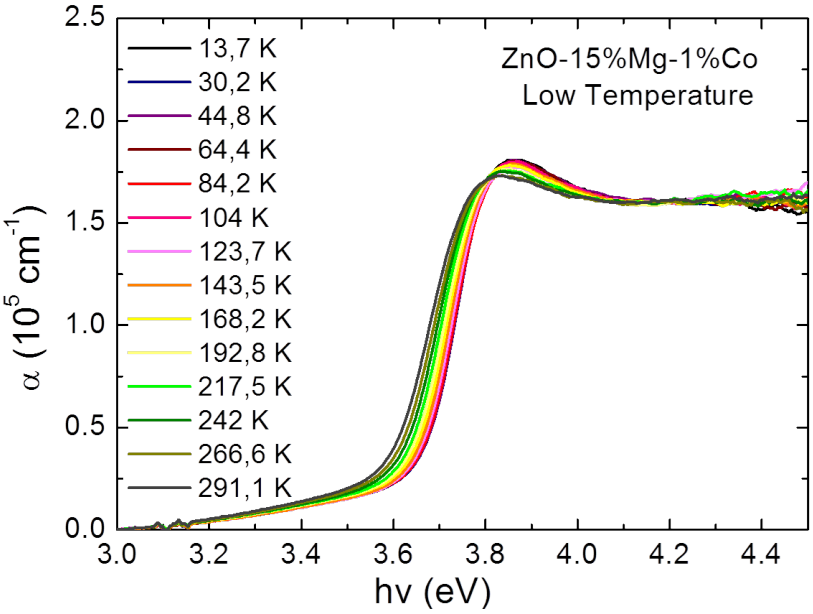

***Figure 6.10**: Evolution with temperature of the optical absorption of ZnMgO:Co thin film with 15% of Mg and 1% of Co.*

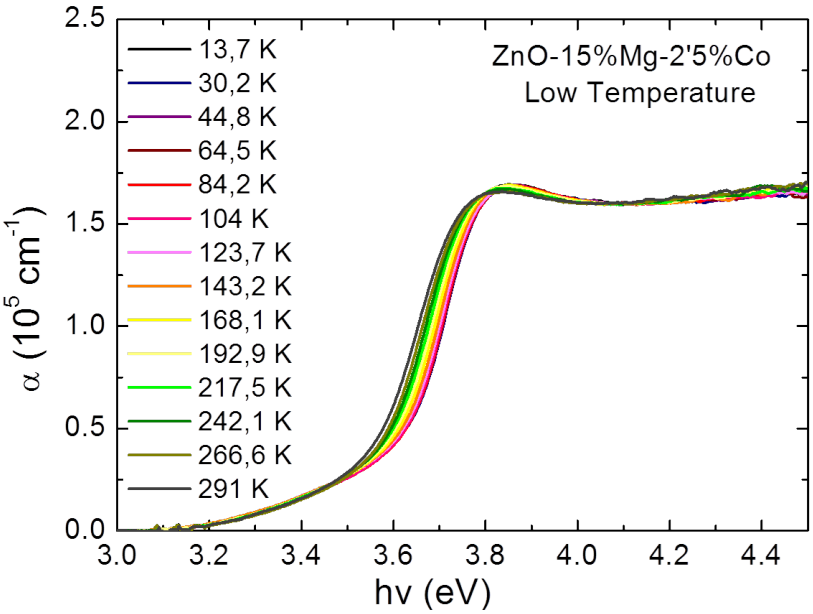

***Figure 6.11**: Evolution with temperature of the optical absorption of ZnMgO:Co thin film with 15% of Mg and 2.5% of Co.*

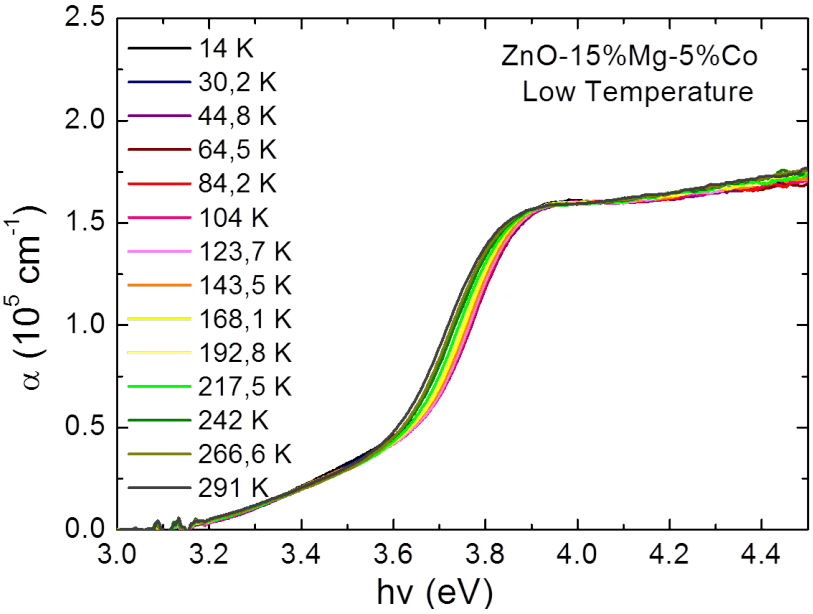

***Figure 6.12**: Evolution with temperature of the optical absorption of ZnMgO:Co thin film with 15% of Mg and 5% of Co.*

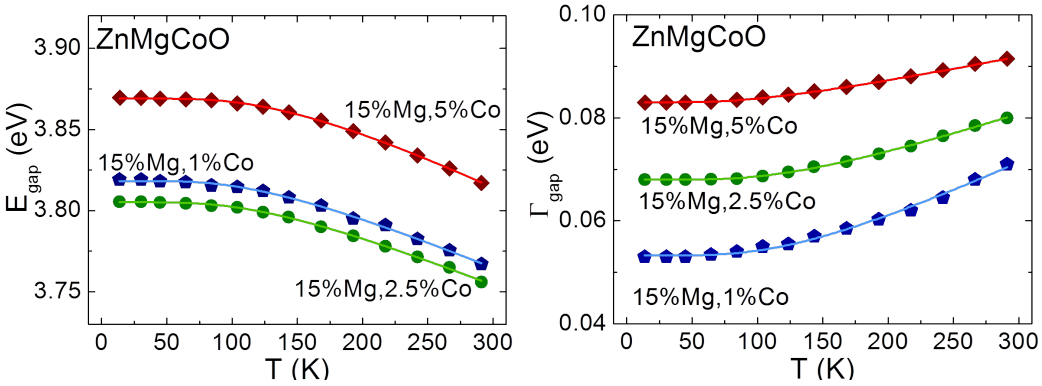

***Figure 6.13**: Dependence of the energy and width of the bandgap with the temperature for ZnMgCoO thin films with 15% of Mg and different concentration of Co.*

Figure 6.13 shows the variation of the bandgap of ZnMgO (15%Mg) and of the transition width as a function of temperature for different proportions of cobalt. It seems relevant to point out that the bandgap for the 1% Co film is larger than the one of the 2.5% Co. This might be due to a larger Mg

proportion in the former film. Table 6.3 shows the results of a Bose-Einstein fit. Only for the 1% Co thin films the results of the fit are closer to those of pure ZnO (with a larger contribution of defects reflected in a larger width at low temperature. As the Co concentration increases the transition width becomes much larger and less temperature dependent as expected from the increase of alloy scattering.

***Table 6.3**: Results of the dependence with temperature fitting.*

Nominal Content	**15%Mg 1%Co**	**15%Mg 2.5%Co**	**15%Mg 5%Co**
$\boldsymbol{E_{gap}(0)}$**(eV)**	3.8180 ± 0.0004	3.8050 ± 0.0002	3.8690 ± 0.0003
$\boldsymbol{\alpha_B}$**(meV/K)**	0.363 ± 0.016	0.353 ± 0.010	0.433 ± 0.010
$\boldsymbol{\Theta_B}$**(K)**	380 ± 19	396 ± 13	460 ± 9
$\boldsymbol{\Gamma_{gap}(0)}$**(meV)**	53.3 ± 0.2	68.03 ± 0.06	83.06 ± 0.05
$\boldsymbol{\Gamma}$ **(meV)**	53 ± 8	37 ± 4	16.8 ± 1.2
$\boldsymbol{\Theta_B}$ **(K)**	410 ± 30	409 ± 14	320 ± 13

Figure 6.14 shows the energy and width parameters of the charge transfer transition band as a function of temperature. We can see that the energy of the CTT has a behaviour similar to the bandgap. It shifts to higher energy as the temperature decreases. The temperature is more pronounced the higher the cobalt concentration.

The CTT width is practically independent of T as it is expected in a transition whose width is mainly determined by the fact that it is a localized to extended state transition. The slight increase of the CTT intensity as temperature decreases was also observed in ZnCoO samples and can be related to carrier trapping, leaving more final states available for the transition.

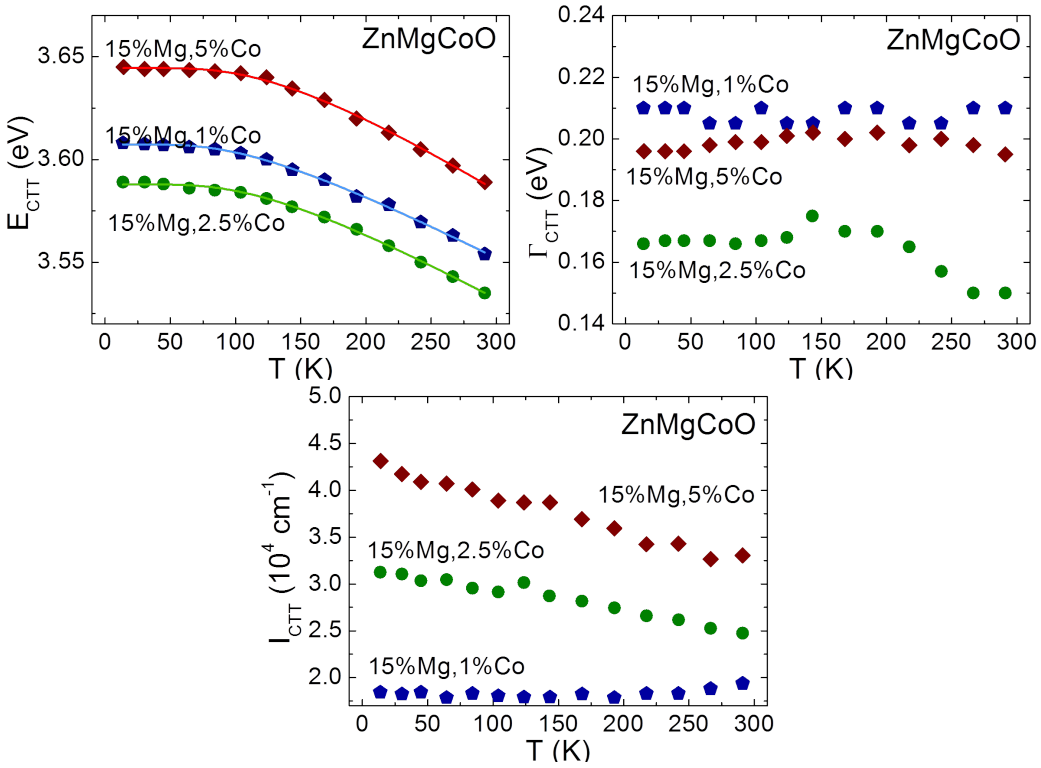

***Figure 6.14**: Dependence of the energy, width and intensity of the CTT band with the temperature for ZnMgCoO thin films with 15% of Mg and different concentration of Co.*

***Table 6.4**: Results of the dependence with temperature fitting.*

Nominal Content	**15%Mg 1%Co**	**15%Mg 2.5%Co**	**15%Mg 5%Co**
$E_{CTT}(0)$(eV)	3.6070 ± 0.0003	3.5880 ± 0.0004	3.6440 ± 0.0004
α_B(meV/K)	0.347 ± 0.013	0.378 ± 0.017	0.439 ± 0.019
Θ_B(K)	350 ± 17	386 ± 19	426 ± 19

6.1.5 Anisotropy

In this section, we present the results of an investigation on thin films deposited on *R*-sapphire as a function of light polarization.

Figure 6.15 shows the evolution of the absorption edge at low temperature as a function of polarization, for a ZnMgO thin film with 5% of Mg

deposited on *R*-sapphire. This results clearly show that there is a large degree of orientation, as reflected by the well-defined maxima at perpendicular orientations.

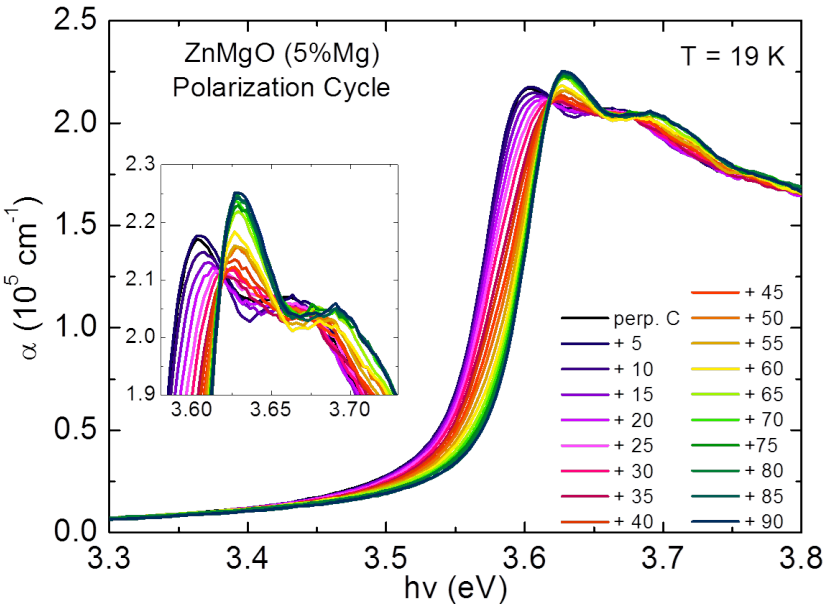

***Figure 6.15**: Evolutios of the spectra of ZnMgO with 5% of Mg corresponding to a cycle of polariser at 19 K.*

Nevertheless, as we observed for ZnCoO thin films, the energy difference between both peaks is only about 27 meV, well below the expected energy difference between the B and C excitons, that should increase as the Mg proportion increases, as a consequence of the increase of the crystal field anisotropy. This is a clear indication of some orientation disorder of the *c*-axis in the thin film plane.

Figure 6.16 shows the temperature dependence of the absorption edge for both polarizations, with the expected blue shift and increase of the exciton peak intensity as temperature decreases.

Figure 6.17 shows the temperature dependence of the absorption edge for both polarizations, for ZnMgO thin film with 10% Mg deposited on *R*-sapphire.

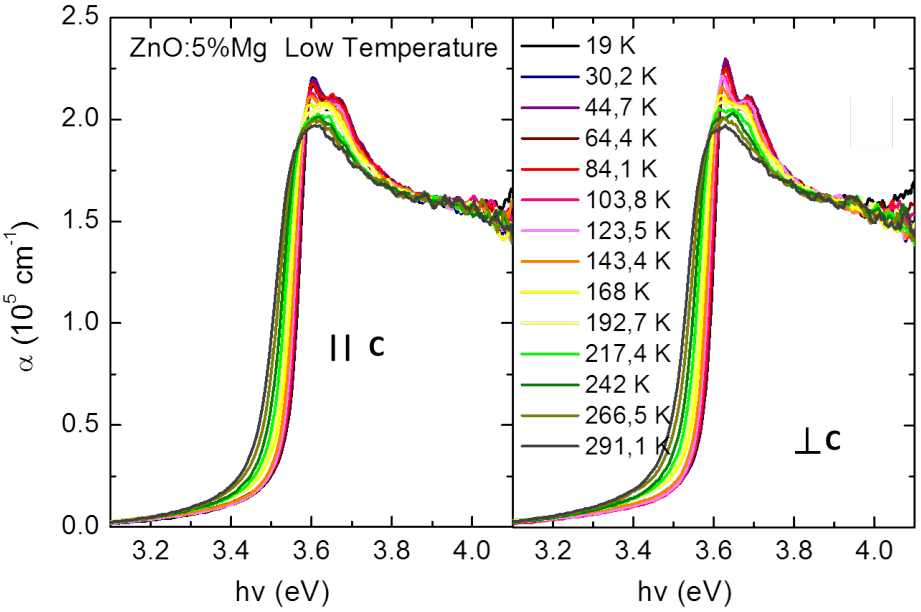

***Figure 6.16**: Evolution in temperature of the absorption spectra of ZnO:5%Mg thin film for both polarizations.*

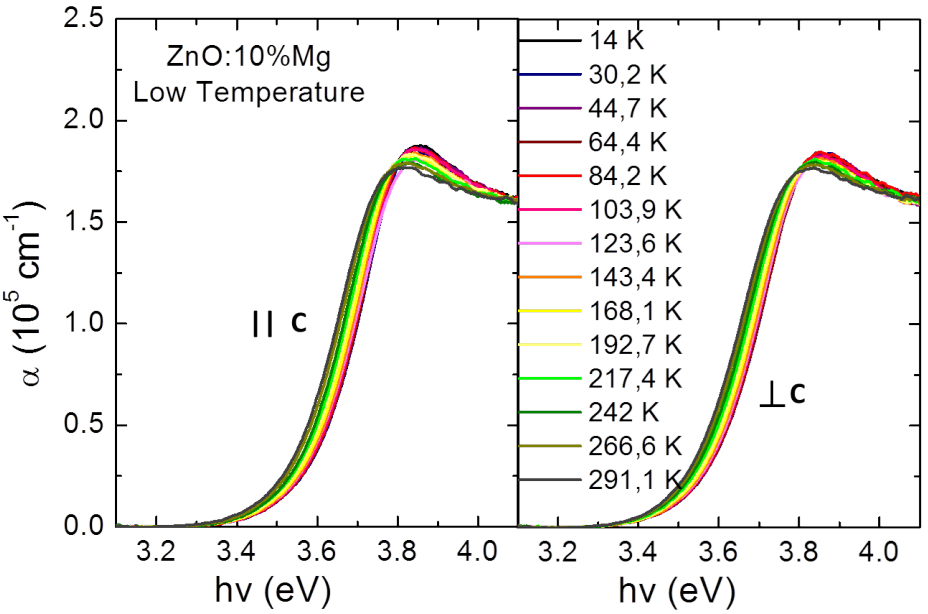

***Figure 6.17**: Evolution in temperature of the absorption spectra of ZnO:10%Mg thin film for both polarizations.*

The energy difference between spectra for perpendicular light polarization

becomes smaller, indicating an increase on the c-axis orientation disorder as the Mg concentration increases.

Figures 6.18, 6.19 and 6.20 show the temperature dependence of the absorption edge for both polarizations, for these ZnMgCoO thin films with 15% Mg and 1, 2.5 and 5% of cobalt respectively, deposited on R-sapphire.

The energy difference between spectra for perpendicular light polarization, even if still observable becomes smaller, reflecting again the increase on the c-axis orientation disorder as the Co concentration increases. In spite of this, some preferential orientation still exist and is clearly reflected on the larger intensity of the CTT transition for light polarization perpendicular to the c-axis.

It is also relevant to notice the previously commented shift of the onset of the CTT band to higher photon energies, with respect to ZnCoO thin films studied in Chapter 4.

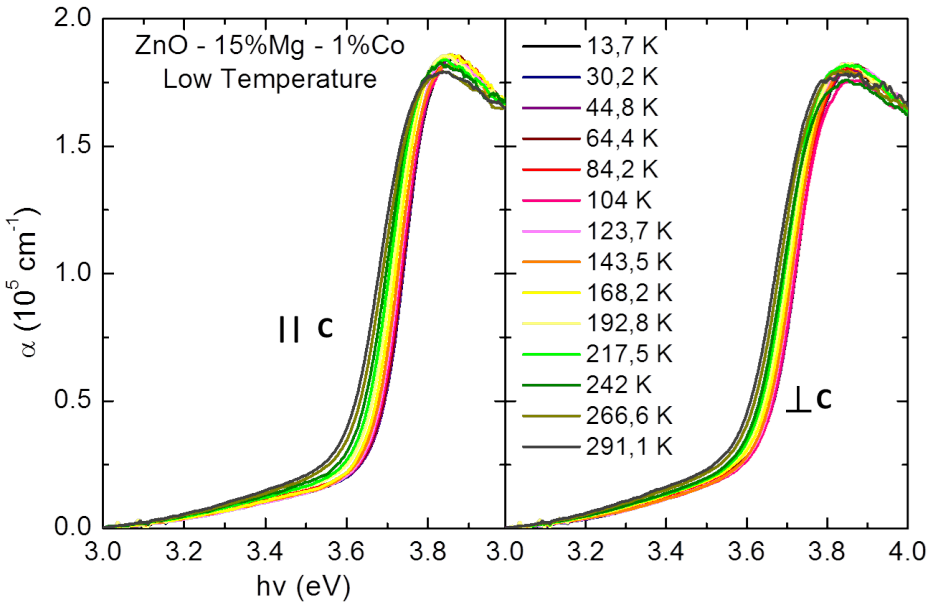

***Figure 6.18**: Evolution in temperature of the absorption spectra of ZnO:15%Mg,1%Co thin film for both polarizations.*

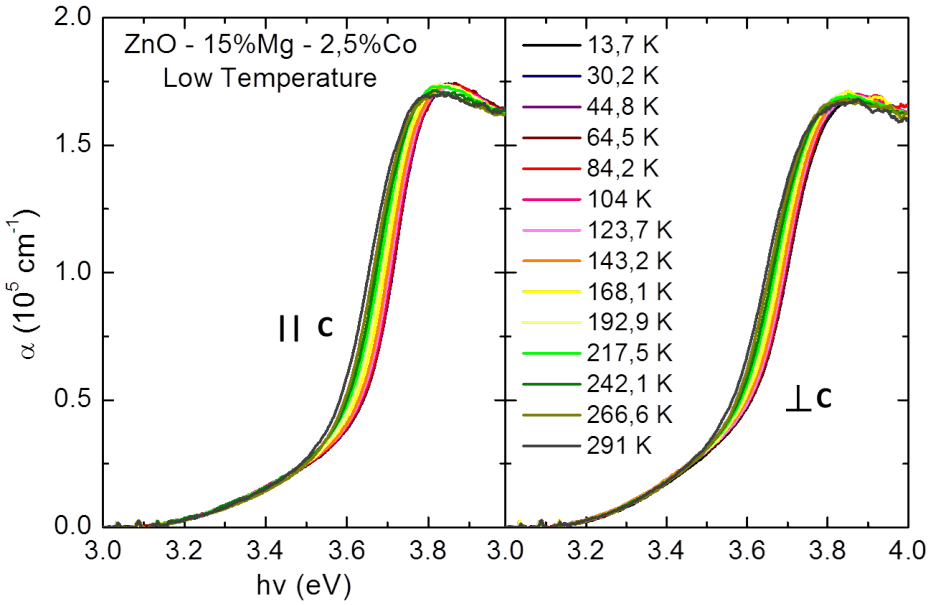

***Figure 6.19**: Evolution in temperature of the absorption spectra of ZnO:15%Mg,2.5%Co thin film for both polarizations.*

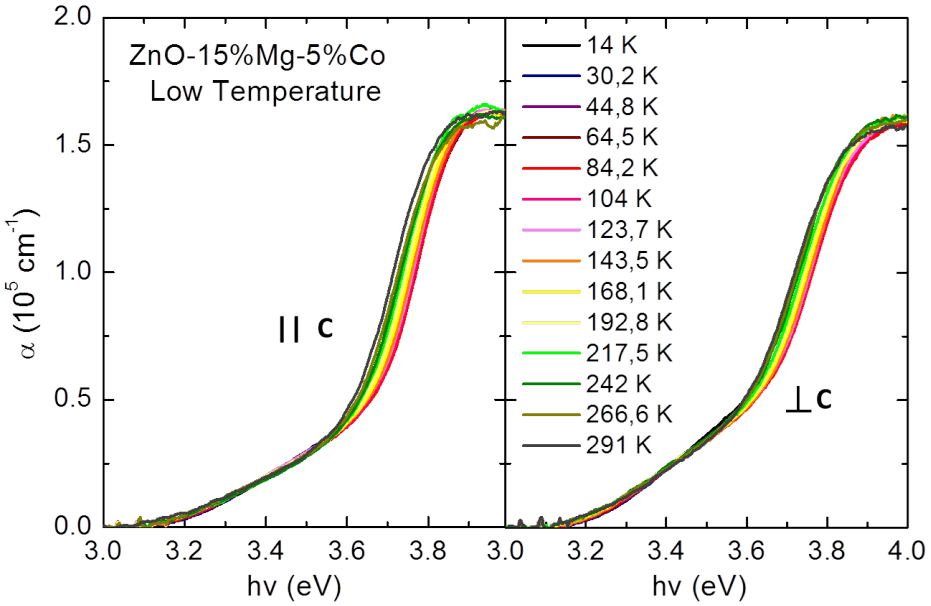

***Figure 6.20**: Evolution in temperature of the absorption spectra of ZnO:15%Mg,5%Co thin film for both polarizations.*

6.2 Optical Properties of (Zn,Mg)O/(Zn,Co)O Multilayer Thin Films at Ambient Temperature: Effects of Quantum Confinement

In previous sections we have seen how, when prepared from a single target containing an oxide mixture, (Zn,Mg,Co)O thin films contain a lower Mg and Co proportion than the one in the target. This is clearly reflected by the fact that the (Zn,Mg,Co)O thin film bandgap is much smaller than expected from the nominal Mg, even if the intensity of the CTT band is close to the corresponding to the Co content in the target (see Figure 6.7).

In order to try to circumvent this apparent incompatibility, we have prepared multilayers by sequential alternate depositions ZnCoO and ZnMgO at high temperature (600 °C) on the assumption that inter-diffusion would be efficient at such temperature[147].

We have carried out two growths, PLDR1 and PLDR2, on different sapphire and SCO substrates. In both cases the growth time of each ZnMgO layer was 30 minutes and 9 layers were deposited. The growth time for each of the ZnCoO layer was 15 minutes in series PLDR1 and 5 minutes series PLDR2. This indicates that the Co proportion is expected to be higher in PLDR1 multilayer. *C* and *R*-oriented sapphire substrates were longer that the homogeneity area of the ablation plume, in order to achieve areas with different single layer thickness and be able to study its effect on the absorption edge. In both cases the SCO substrate was placed in the area of higher intensity of the ablation plume. The structure and thickness of the thin film on SCO is then expected to be closer to the "thick" part of the thin film on *c*-oriented sapphire.

Table 6.5 shows the thickness of the multilayer and the estimated thickness of the single layers deposited on each deposition cycle.

Let us point out that the estimated thickness of the single ZnCoO layers are close or below the thickness for which confinement effects have been reported in ZnO/ZnMgO multiple quantum wells[148][149]. This remark is relevant in case there is no interdifussion and the multilayer thin film is in fact a multiple quantum well (QW) structure with ZnCoO QWs and ZnMgO barriers.

***Table 6.5**: Thickness of the multilayer and estimated thickness of the single layers.*

	PLDR1			**PLDR2**		
textbf(nm)	**Total (nm)**	**Single ZnMgO (nm)**	**Single ZnCoO (nm)**	**Total (nm)**	**Single ZnMgO (nm)**	**Single ZnCoO**
Thick R-sapphire	108	8.4	4	88	8.4	1.6
Thin R-sapphire	64	5	2.4	53	5	1.4
SCO	104	8	3.9	104	10	1.6

Figure 6.21 compares the absorption edge of two different multilayers to the absorption edge of two ZnCoO thin films (with 5 and 30% Co) and a (Zn,Mg,Co)O thin film (5% Mg, 5%Co).

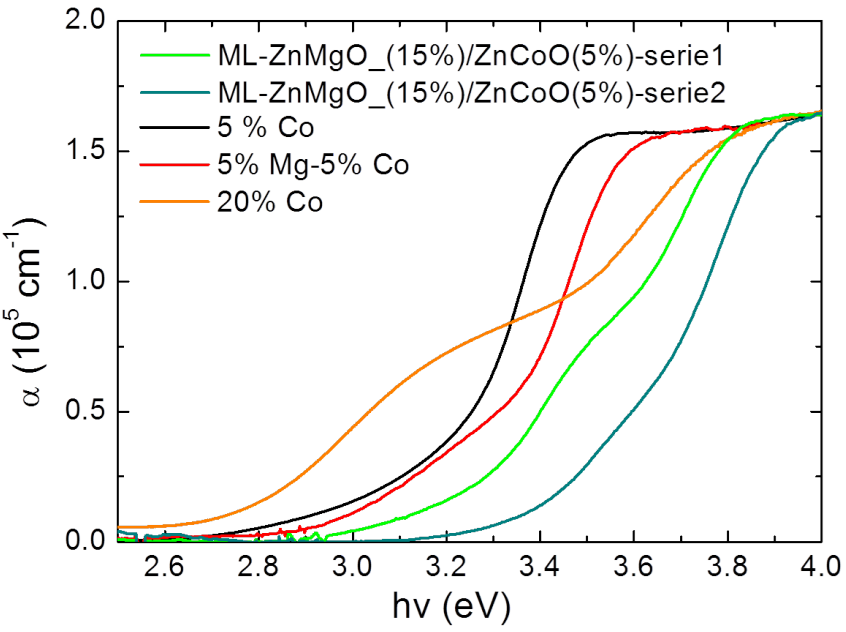

***Figure 6.21**: Absorption spectra of multilayers of ZnMgO(15%)/ZnCoO(5%) comparing with samples of ZnMgO and ZnCoO.*

The comparison clearly shows that those multilayers: *i)* exhibit the largest bandgap of all Co containing thin films here prepared (up to 3.8 eV) and *ii)*

they seem to exhibit a CTT band at the highest photon energy. As a consequence one of them is transparent below 3.2 eV.

Figure 6.22 compares the absorption spectra at room temperature of six multilayer films. For each growth we show the spectra of three thin films: one of them is the one grown on SCO; the two other are the thick and thin parts of the thin films grown on C-oriented sapphire.

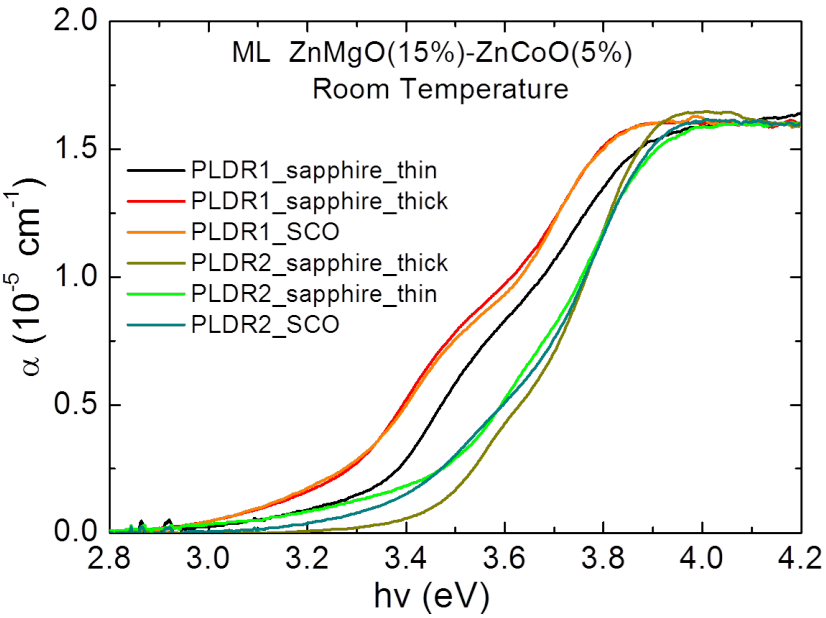

Figure 6.22: *Absorption spectra of multilayers of ZnMgO(15%)/ZnCoO(5%).*

For PLDR1 deposition, absorption spectra for SCO and thick *C*-sapphire are nearly identical, as expected, while the spectrum of the "thin" part of the film on *C*-sapphire is shifted to higher energies.

For PLDR2 thin film the trend is different. The highest photon energy spectrum corresponds to the "thick" part of the *C*-sapphire film and the SCO and "thin" *C*-sapphire films (especially the latter) exhibit a low energy tail.

A closer look at the shape of spectra in Figures 6.21 and 6.22 and the analysis of the $3d{-}d^*$ absorption bands suggests that, even if there is some Mg and Co interdiffusion, these thin films might actually have a inhomogeneous multilayer structure.

Figure 6.23 compares two of the PLDR1 multilayer film spectra with the previously used spectrum of a ZnCoO (5% Co) thin film. It is apparent that

there is a clear correspondence between the low energy part of the multilayer spectra and the spectrum of the ZnCoO thin film.

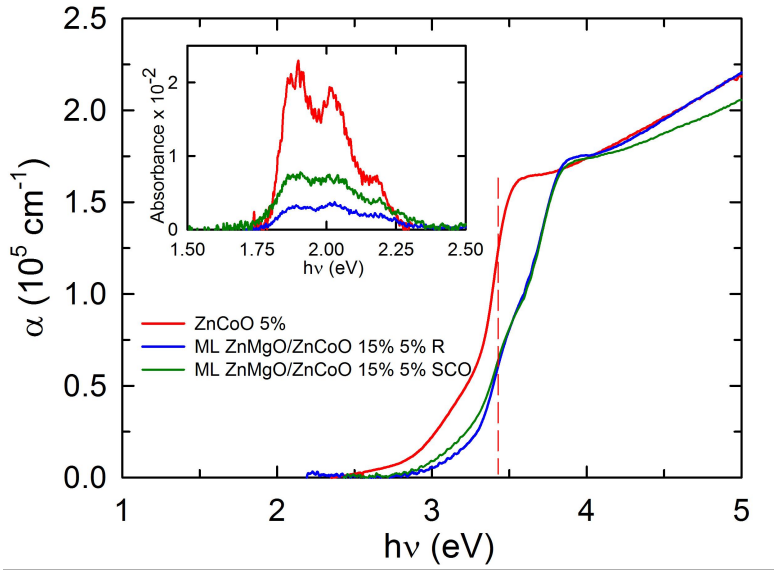

***Figure 6.23**: Spectra of two of the PLDR multilayer compared with ZnCoO (5% Co) thin film.*

This correspondence suggests that the multilayer spectrum is simply the sum of the ZnCoO and ZnMgO multiple sublayers spectra. This interpretation is represented in Figure 6.24. The red dashed spectrum is proportional to the red continuous spectrum (ZnCoO thin film) and represents the contribution of all single ZnCoO layers. When subtracted from the experimental spectrum of the multilayer thin film (continuous blue spectrum) we obtain the dashed blue spectrum, corresponding to the ZnMgO layers contribution.

This interpretation is confirmed by the intensity of the Co 3d-3d* absorption bands, plotted in the inset of Figure 6.23. We have plotted directly the absorbance of each thin film (that is practically proportional to the absorption coefficient as the thin films have very close thickness). If the most intense subgap band was interpreted as the CTT band of the multilayer thin film, then the intensity of the Co 3d-3d* bands in the multilayer should be more intense than in the ZnCoO thin film. This is not the case. We can see that the intensity of the Co 3d-3d* bands follows the trend of the absorption tails between 2.7 and 3.3 eV, that actually correspond to the CTT in each spectrum.

If this interpretation is correct, the absorption spectra of the thinnest parts of the multilayer should exhibit confinement effects.

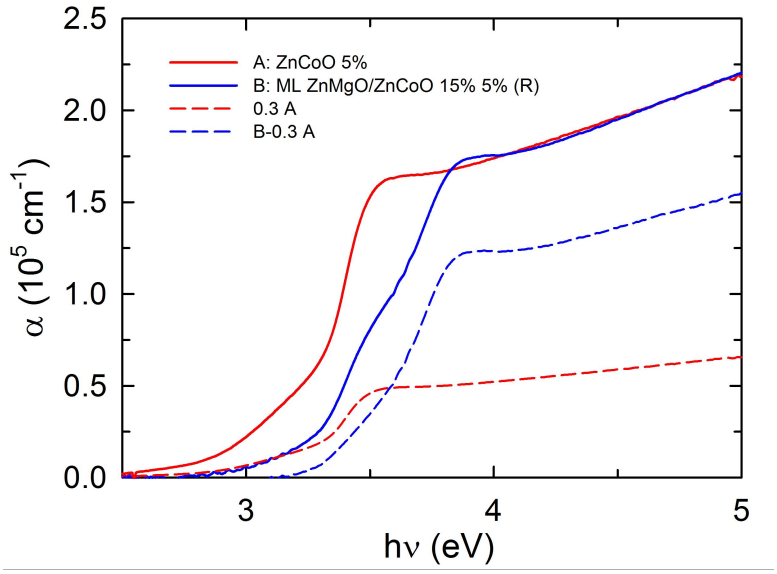

***Figure 6.24**: Spectra of two of the PLDR multilayer compared with ZnCoO (5% Co) thin film.*

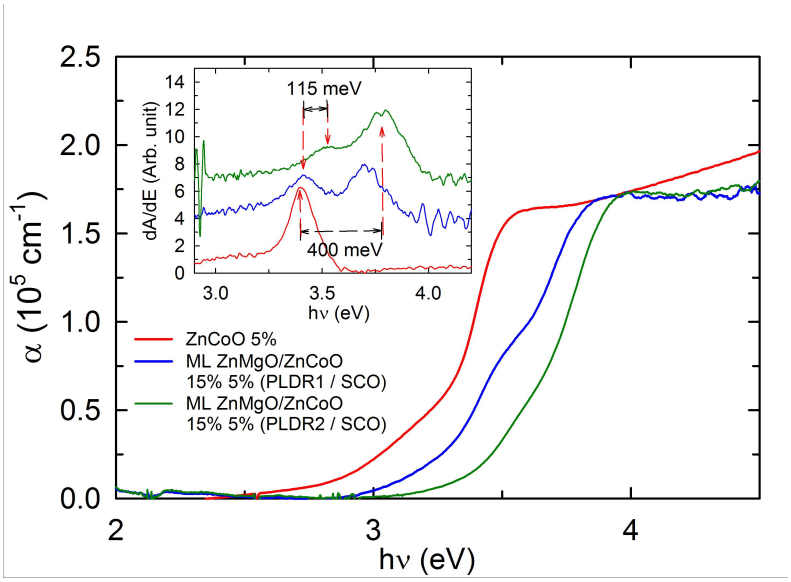

***Figure 6.25**: Spectra of two of the PLDR multilayer compared with ZnCoO (5% Co) thin film.*

Confinement effects are indeed observed in the spectra shown in Fig. 6.25, corresponding to multilayers PLDR1 and PLDR2 deposited on SCO.

While in the spectrum of PLRD1 multilayer thin film (with an estimated ZnCoO layer thickness of 4 nm) the onset of the ZnCoO fundamental absorption is practically at the same energy for the multilayer and the reference thin film, there is a clear shift in the ZnCoO absorption onset of the PLRD2 multilayer thin film (with an estimated ZnCoO layer thickness of 1.6 nm).

The blue-shift associated to confinement effects can be better estimated from the derivative spectrum shown in the inset of Fig 6.27. The first maximum corresponds to the fundamental absorption of the ZnCoO contribution (quantum well in the multilayer film). The second maximum corresponds to the absorption edge of the ZnMgO barriers. The energy shift between the first peak in the ZnCoO thin film derivative spectrum and the second one in the multilayer provides a lowest limit of the total height of the barrier (up to 400 meV in the PLR2 multilayer). The energy shift between the first peak in the ZnCoO thin film derivative spectrum and the first one in the multilayer provides a good estimation of the confinement energy in the quantum well.

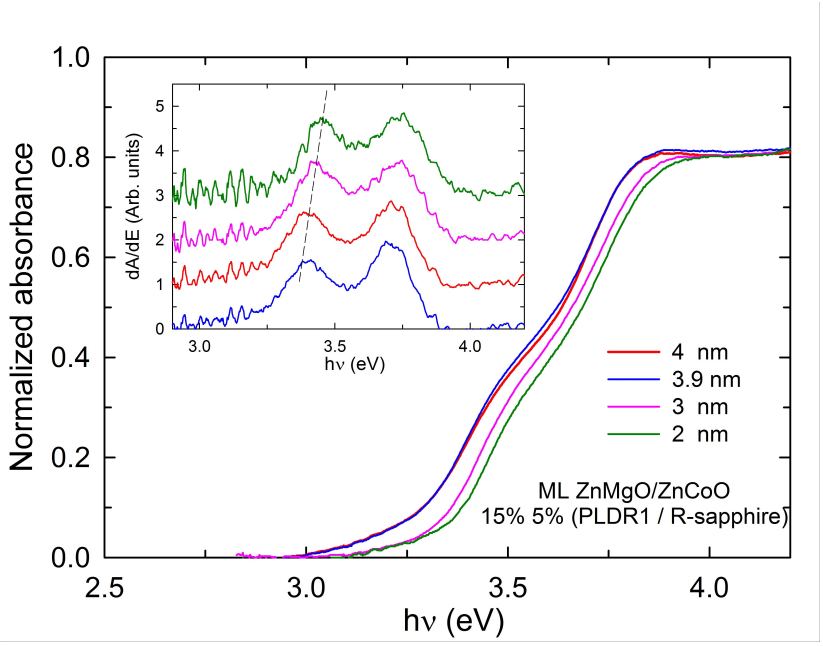

***Figure 6.26**: Spectra of PLDR1 multilayer taken at different areas with decreasing thickness.*

This interpretation is also supported by results in Figure 6.27, that shows the absorbance spectra (normalized at the maximum) of a PLDR1 multilayer

thin film taken at different areas with decreasing thickness. We assume that the thickness of the ZnCoO single layer is proportional to the total thickness. The derivative spectra in the inset clearly show the blue-shit of the ZnCoO layer absorption edge as the thickness decreases (and the ZnMgO barriers height increases).

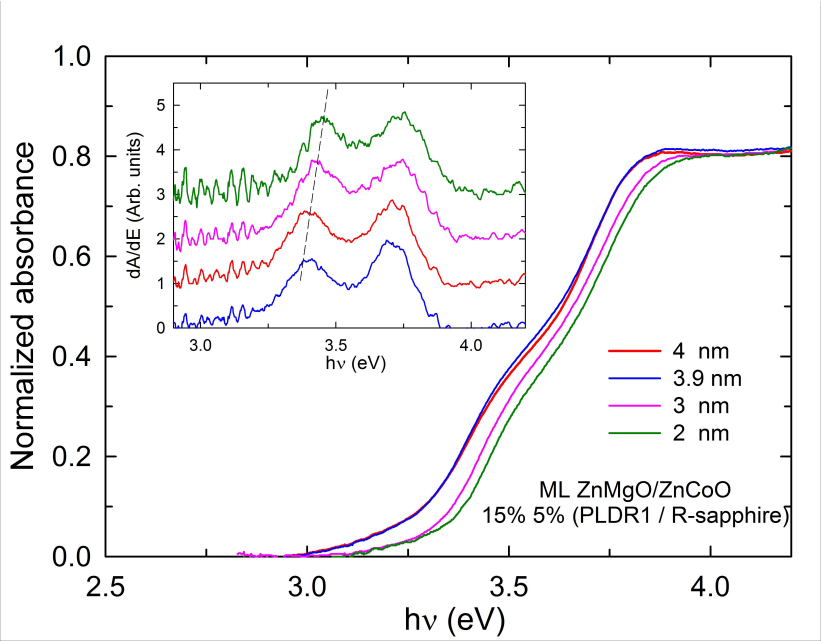

***Figure 6.27**: Spectra of PLDR1 multilayer taken at different areas with decreasing thickness.*

We can then conclude that at the deposition temperature used for both series (600ºC) interdiffusion processes turn out to be slow enough to be negligible. We actually have a multi-quantum-well (MQW) structure .

In order to summarize this interpretation, Figure 6.28 shows the photon energy shift of the first peak in the multilayer derivative spectrum as a function of the QW thickness, compared the energy of the first peak of the reference ZnCoO thin film (red symbols). We have also included data on the exciton absorption peak on ZnO/ZnMgO MQWs from ref [149].

Let us first notice that finding both series of energies in the same energy range is not purely coincidental. In fact ZnCoO QW states should be at higher energies with respect to ZnO QW states. The fact that ZnO/ZnMgO MQW from ref [149] are measured at 77 K (which shifts them to higher energies) while the peaks from this work correspond to the maximum of the

derivative spectrum (which underestimates their energies) makes them to appear in the same energy range.

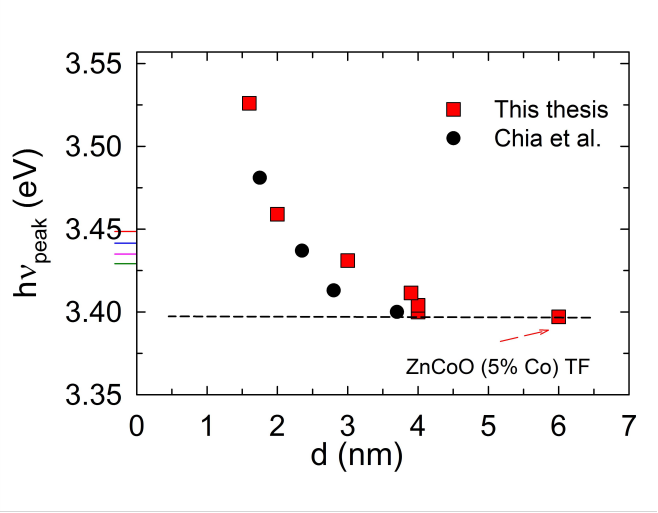

***Figure 6.28**: Photon energy shift in the multilayer derivative spectrum as a function of the QW thickness.*

In spite of the relatively large error in the thickness estimation of our ZnCoO QW, we can see that there is rough quantitative agreement in the thickness dependence of the quantum confinement energy. This is to be expected, given that the value of the reduced effective mass in ZnCoO (5% Co) (the main parameter determining the dependence of quantum confinement energy as a function of the QW thickness) is only about 2-3% larger than the one in ZnO. The reduced mass relative difference is well below the error in the QW thickness and peak energy determination.

Let us now discuss another relevant result on the behaviour of the CTT intensity. Looking at the CTT tail in Fig. 6.27 and 6.28 it is clear that the CTT not only shifts to higher energies (following the final state shift), but also its intensity clearly decreases. This effect, that will be also discussed in connection to the optical properties of ZnCoO nanoparticles is related to the similar effect observed in Ga-doped ZnCoO thin films.

In the case of Ga-doping, empty states are above the Fermi level and at the corresponding k-vector, the dipole matrix element is smaller than it is in the conduction band minimum (k=0). In the case of MQW thin films, final states in the conduction band of ZnCoO QW are discrete and they correspond to specific values of the electron wave-vector, for which the dipole matrix element also becomes progressively smaller as the confinement

energy (and then the associated wave-vector) increases.

Figure 6.29 illustrates this effect. It compares the absorption onset of two MQW thin films with 3.9 and 2 nm thick ZnCoO QWs. The spectra are those in Figure 6.27, but in the spectral range of the ZnCoO QW absorption edge. The broken line is simply the spectrum of the thicker MQW shifted to higher energies by some 80 meV (the confinement energy of the thinner MQWs). In this way, it can be seen that the CTT tail is about 25-40% less intense in the thinner MQW thin film.

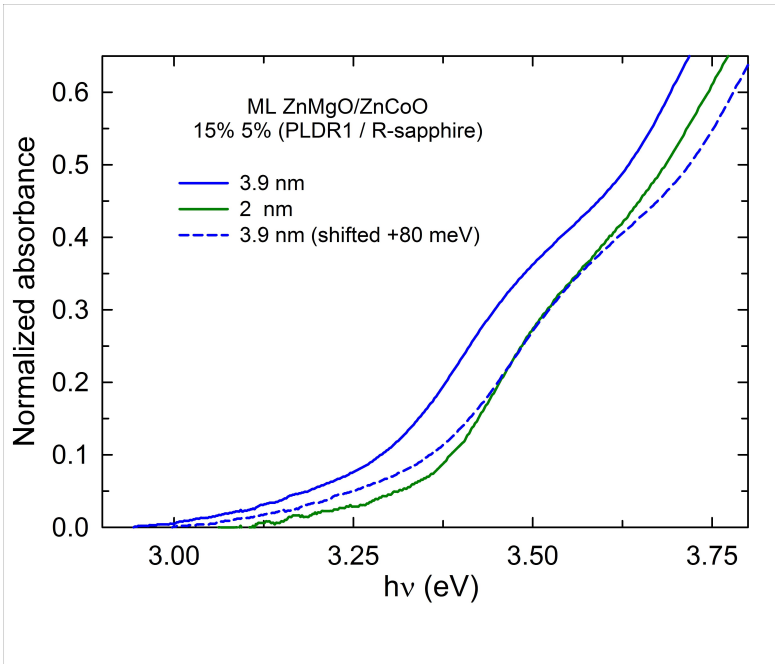

***Figure 6.29**: Comparison of the absorption onset of two MQW thin films with 3.9 and 2 nm thick ZnCoO QWs.*

This effect is described by equation 2.78 in the Theory chapter,

$$\alpha_{CTT,QW}(\hbar\omega) = Cte \times [\hbar\omega\,(E_i + \triangle E_{QW,1})]\, e^{-2\left[\hbar\omega\left(E_i+\triangle E_{QW,1}\right)\right]/E_{kin}} \qquad (6.1)$$

The confinement energy of Co $3d$ fundamental state ($\mathbf{E_{kin}}$ in the equation) was found to be 0.6 eV (Fig. 4.9). With a confinement energy of 80 meV in the 2 nm thick ZnCoO MQW ($\triangle$ $E_{QW,1}$ in the equation) the value of the exponential factor $e^{-2\triangle E_{QW,1}/E_{kin}}$ would be 0.75, which is of the order of magnitude of the observed decrease of the CTT absorption coefficient.

We will further discuss this effect as we present the temperature dependence of the absorption edge for the thinnest QWs.

6.2.1 Optical Properties of (Zn,Mg)O/(Zn,Co)O Multilayer Thin Films at Low Temperature

Finally, in this section we will present and discuss the temperature dependence of the absorption spectrum of all the MQW thin films.

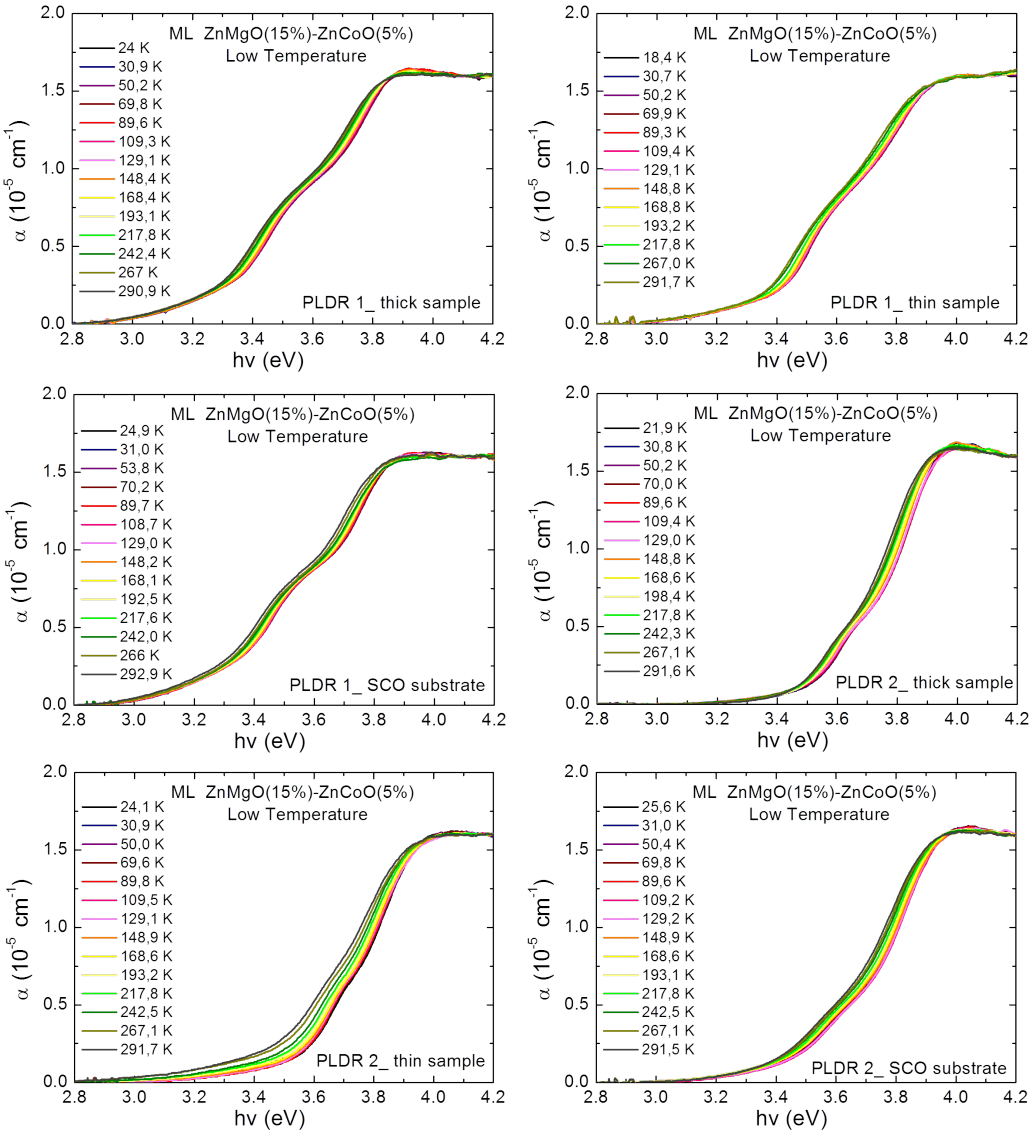

***Figure 6.30**: Evolution with temperature of the optical absorption of the six MQW thin films.*

Figures 6.30 show the temperature dependence of the absorption edge of

the six MQW thin films shown in Fig. 6.22. In five of them, apart from a light decrease in the transitions width for both the QW and barrier absorption onset, we only observe a monotonous shift of the spectra to higher energies. This basically indicates that confinement energies remain practically unchanged as temperature decreases.

If we focus on figure of thin sample of PLDR2 (fifth figure) things become more interesting: not only the temperature blue shift of the ZnCoO QW is larger than the one of the barrier, but also the intensity of the CTT band decreases as temperature decreases. This is more clearly seen in Fig 6.31, that shows a zoom of Fig. 6.30 in the spectral range of the CTT.

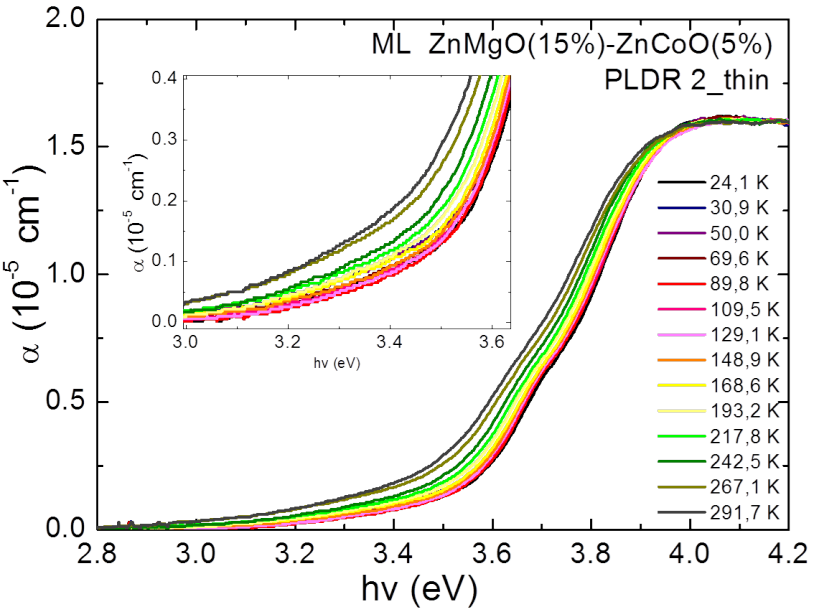

***Figure 6.31**: Evolution with temperature of the optical absorption of the MQW of PLDR2-thin sample.*

Fig. 6.32 shows the derivative spectra for five selected temperatures. The shift of the low energy peak from room temperature to 25 K is about 70 meV, larger than the temperature shift of the bandgap. There is a noticeable increase of the confinement energy.

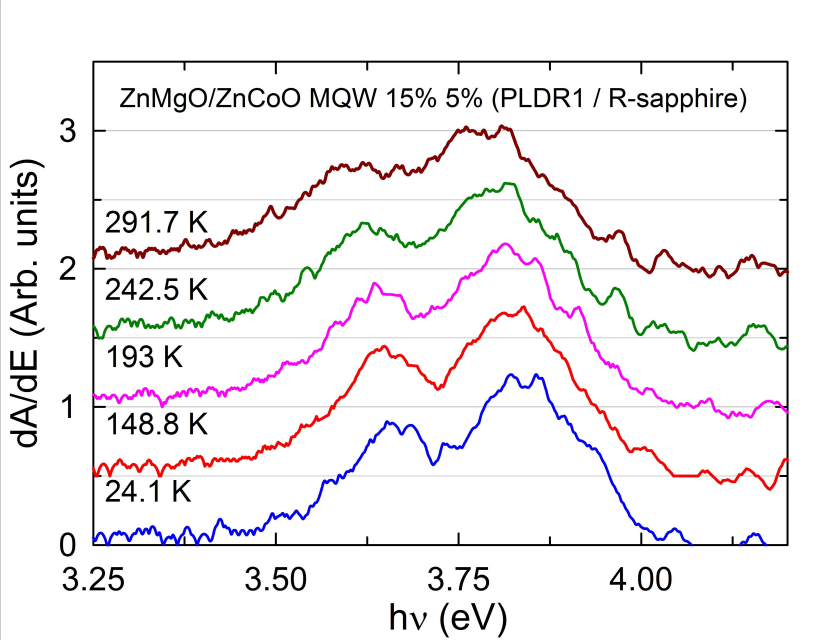

***Figure 6.32**: Derivative spectra for five selected temperatures.*

6.3 Supplementary characterization: High Pressure

In this section we will discuss an experiment on the high pressure behaviour of ZnMgO thin films.

Figures 6.33 and 6.34 show the evolution of the absorption spectra of two ZnMgO thin films, with 5 and 15% Mg proportion respectively, as a function of hydrostatic pressure.

The bandgap in the wurtzite phases shifts to higher pressure with a coefficient of about 25 meV/GPa. At a given pressure, that depends on the Mg concentration, on the Mg concentration (8.5 and 6 GPa for 5 and 15% respectively) the transition to the rock-salt (RS) phase is evidenced by the clear shift of the allowed transition to much higher energies.

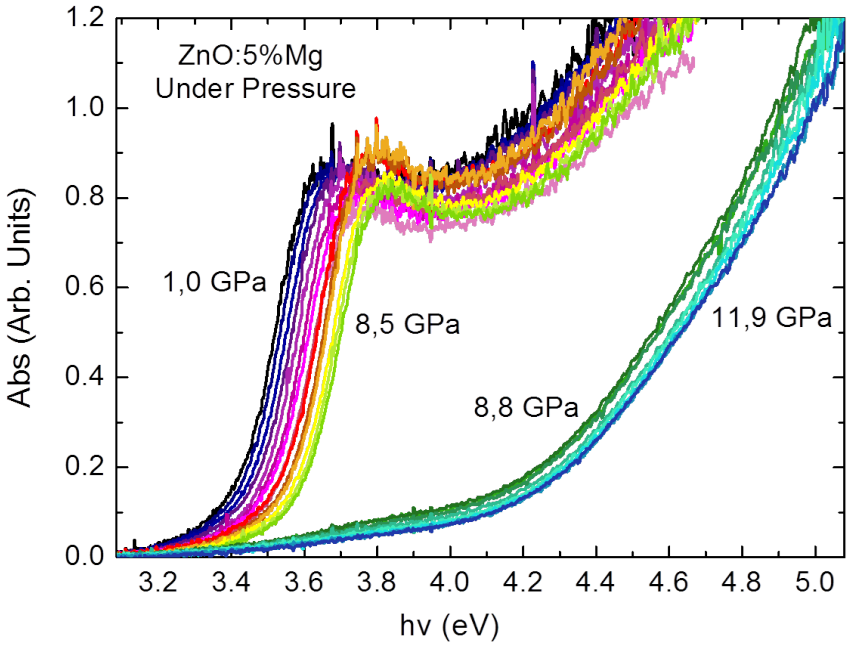

***Figure 6.33**: Evolution with pressure of the absorption spectra of a sample of ZnO doped with 5% of Mg.*

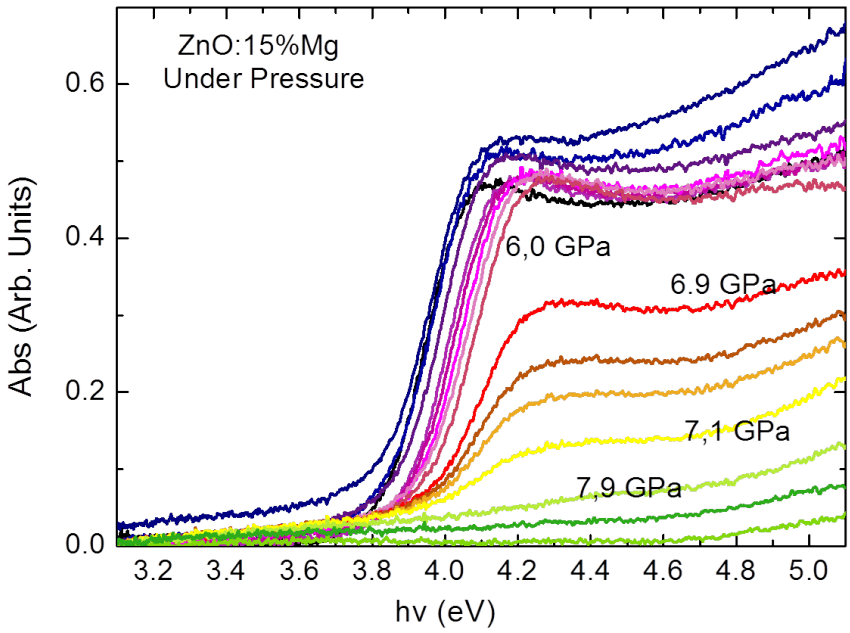

***Figure 6.34**: Evolution with pressure of the absorption spectra of a sample of ZnO doped with 15% of Mg.*

On the pressure down-stroke, while ZnO reverts to the w-phase at 3 GPa, in ZnMgO the rocksalt phase remains metastable at ambient pressure, with a gap about 5 eV, as shown in Figure 6.35.

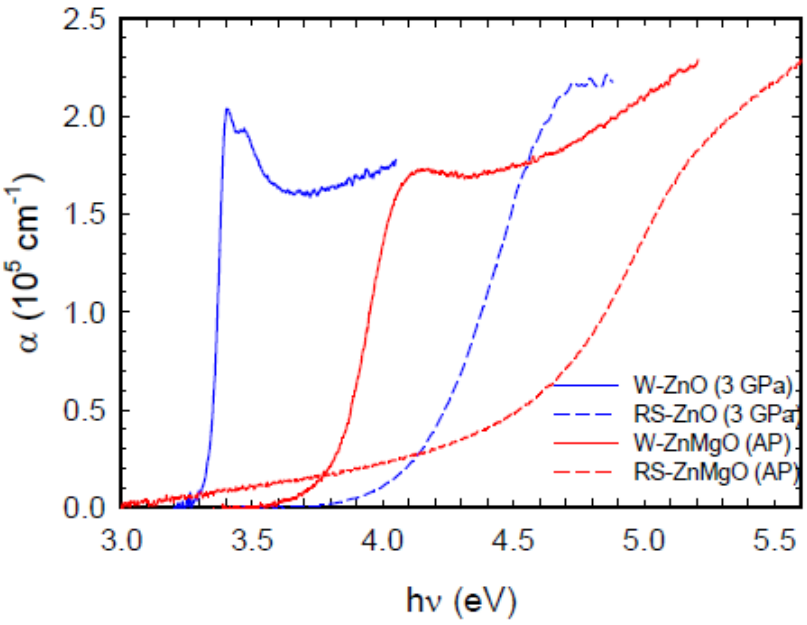

Figure 6.35: .

6.4 Conclusions

- We have studied the optical properties at room conditions of ZnMgO thin films for different Mg concentrations. The effect of alloying with Mg on the bandgap is a shift to higher energies. The bandgap increases almost linearly with the Mg nominal proportion at a rate of about 35 meV/% at. Mg. The rate of the gap increase is higher than the one observed by other authors, indicating that the Mg proportion in the films is higher than the nominal one in the target. The intensity of the exciton peak decreases with increasing the Mg proportion, due to the increase of alloy disorder.

- We have measured the temperature evolution of the absorption spectra for 5, 10 and 15% of Mg. Only for 5% Mg the excitonic peaks and exciton-LO resonance become clearly visible at low temperature. The temperature dependence of the bandgap, for the three samples, can be accounted for by the Bose-Einstein model. The effective temperature

obtained is close to the one found for ZnO. For 10 and 15% Mg thin films the low temperature width and its weak dependence indicate a strong contribution of localized potential scattering (alloy scattering).

- As regards the behaviour of optical anisotropy in ZnMgO films deposited on R-sapphire, the behaviour is similar to the one of ZnCoO thin films. In both cases the anisotropy crystal-field is expected to increase but the energy shift between the C-exciton and the A-B exciton seems to decrease. We attribute this to disorder in the orientation of the c-axis in the crystallites.

- We have also studied thin films of the (Zn,Mg,Co)O semiconductor alloy. The the incorporation of Co is evidenced by the presence of the Co $3d - 3d^*$ absorption bands and the CTT band while the bandgap increase is relatively small with respect to the ZnCoO thin film. This suggest that there is some kind of incompatibility in the simultaneous incorporation of Co and Mg when thin films are prepared from a single target incorporating the three oxides.

- Results of ZnMgCoO(5% Mg, 5% Co) indicate that Co is indeed incorporated in a tetrahedral substitutional configuration as the $3d - 3d^*$ absorption bands are clearly observed with the expected intensity in a ZnCoO thin film with 5% Co. This indicates that the CTT is also a reliable signature of the incorporation of tetrahedral Co in the alloy lattice. The presence of Mg is indicated by the 70 meV blue-shift of the fundamental absorption (with respect to the bandgap of a ZnCoO thin film with 5% Co).

- For ZnMgCoO(15% Mg, 5%Co) the incorporation of Co in tetrahedral sites is again detected by the Co $3d-3d^*$ absorption bands, that appear to be red-shifted by some 22 meV with respect to the ZnCoO thin films. This indicates a smaller intensity of the crystal field acting on the Co $3d$ shell, consistently with the fact that the average bond-length is larger. The presence of Co is also shown by the intensity of the CTT, that is of the same order in both families of thin films. Again, the presence of Mg is shown by the 290 meV shift of the fundamental absorption edge of the alloy (with respect to the bandgap of a ZnCoO thin film with 5% Co).

- We have prepared 2 series of multilayers alternating depositions of (Zn,Mg)O and (Zn,Co)O thin films at high temperature (600°C) on

the assumption that inter-diffusion would be efficient at such temperature. The difference between both series is the time deposition of the ZnCoO layer (15 min in series 1 and 5 min in series 2).

- The presence of a clear absorption edge for the ZnCoO sublayers, whose fundamental absorption shifts to higher energies for lower sublayer thickness indicates that interdiffusion is negligible and that these multilayer thin films are in fact multiple quantum well (MQW) structures with ZnCoO QWs and ZnMgO barriers. The estimated thickness of the single ZnCoO layers are close the thickness for which confinement effects have been reported in ZnO/ZMgO multiple quantum wells. The shift of the ZnCoO QW absorption edge as a function of the QW thickness is in fact very close to the one observed in ZnO/ZnMgO QWs.

- At normalized intensities of the fundamental absorption edge the intensity of the CTT band is lower for thinner QWs, indicating that the intensity of the CTT is affected by QW confinement. This is an important result, consistent with the previously described effect of doping. In QWs, confinement shifts the energy of the localized states to higher energies, corresponding to high values of the quantized k-vector in the confinement direction. For this k-vector values, the dipolar matrix element is lower and the intensity of the CTT decreases exponentially as the confinement energy increases.

Chapter 7

Results: $Zn_{1-x}Co_xO$ Nanoparticles

7.1 Introduction

In this chapter, will present and discuss the results on the characterization of $Zn_{1-x}Co_xO$ nanoparticles, with $0 \leq x \leq 30$ as well as the behaviour of their optical properties under high pressure.

We first describe the growing process of the nanoparticles (NP). After that, we present and discuss the characterization of the nanoparticles using TEM (Transmission Electron Microscopy) and optical absorption measurements. Afterwards, we study the behaviour of NP when they are exposed to high pressures using a diamond anvil cell (DAC). As a consequence of these results we study with more detail the metastability of crystal structure phases and the effects of quantum confinement in the NPs. Finally, we try to stablish a relation between the behaviour of nanoparticles under pressure and the size distribution.

7.2 Synthesis[2]

The nanoparticles used in this study were synthesized in the Department of Chemistry at the University of Washington in Seattle by Rosa Martín Rodríguez[1] during her PhD thesis.

Pure ZnO and $Zn_{1-x}TM_xO$ with $\mathbf{x} < 30\%$ where TM = Co have been prepared using hydrolysis and condensation of acetates($(AC)_2$ in dimethyl

[1]Departamento de Ciencias de la Tierra y Física de la Materia Condensada. Universidad de Cantabria.

sulfoxide (DMSO)[2])[150]. The experimental procedure is detailed below.

The acetates $(Ac)_2$ were dissolved in DMSO[151]. In parallel, a solution of tetramethyl ammonium hydroxide ($N(Me)_4OH$) was prepared and added drop-wise to the above dissolution with constant stirring, starting the reaction. After a fast nucleation, the small crystals become unstable and collapse due to their large surface to volume ratio, while larger particles are stable and grow. The longer reaction times allow the larger nanoparticles obtained. Although the initial nucleation dopants were excluded, they were incorporated into ZnO nanoparticles almost isotropic during the growth of the solution.

***Figure 7.1**: Preparation of ZnO:Co^{2+} colloidal nanocrystals in the department of Chemistry at the University of Washington. The solution change from pink to blue indicates the conversion of octahedral Co^{2+} to tetrahedral Co^{2+}.*

Figure 7.1 shows pictures of a flask during the synthesis reaction of a sample of ZnO doped with Co^{2+}. The first image was taken before the addition, showing the characteristic pink of octahedral Co^{2+} in $(OAc)_2$. The addition of $N(Me)_4OH$ turned the solution from pink to blue, and later to green, indicating the tetrahedral coordination of Co^{2+} in ZnO.

The colloidal nanocrystals were generally stabilized by a surfactant layer added to the surface. The energy with which the surfactant molecules attach to the surfaces of nanocrystals growth is one of the most important parameters that influence the growth of crystals.

Colloidal nanoparticles of wurtzite-CoO were synthesized using the non-aqueous solution method with the reaction system composed of the metal salt of fatty acids and a solvent for hydrocarbons[152].

[2]DMSO = dimethyl sulfoxide

7.3 Characterization

7.3.1 TEM Analysis

Measurements with high resolution analytical transmission electron microscopy (TEM and HRTEM), selected area electron diffraction (SAED), and energy-dispersive X-Ray Spectroscopy (EDX) were conducted at the electronic microscopy facility of the University of Valencia.

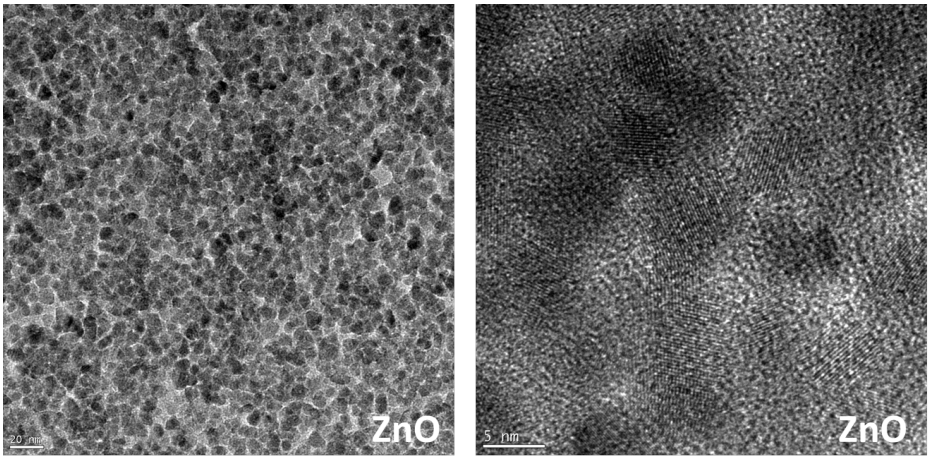

***Figure 7.2**: Low and high resolution images for a NP of pure ZnO.*

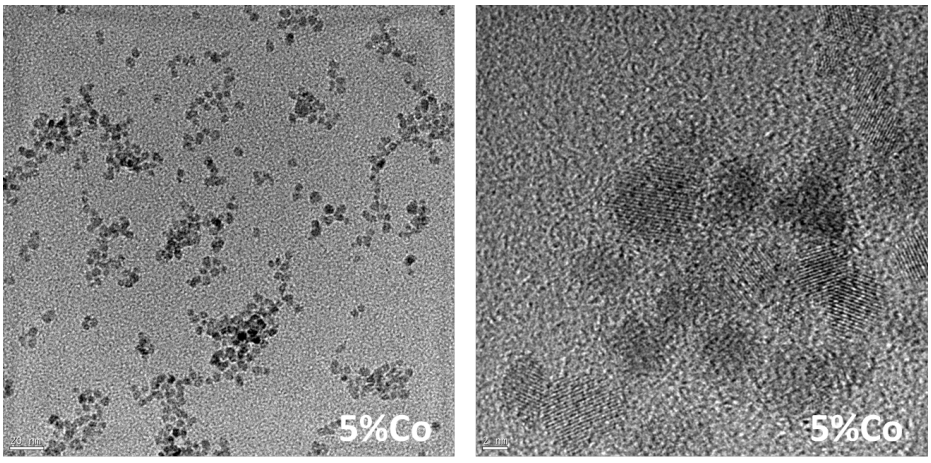

***Figure 7.3**: Low and high resolution images for a NP of Co-doped ZnO with 5% of Co.*

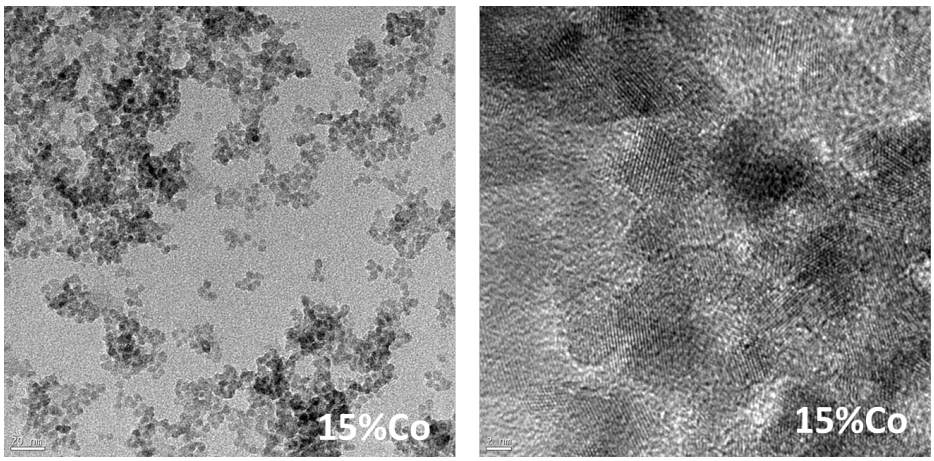

***Figure 7.4**: Low and high resolution images for a NP of Co-doped ZnO with 15% of Co.*

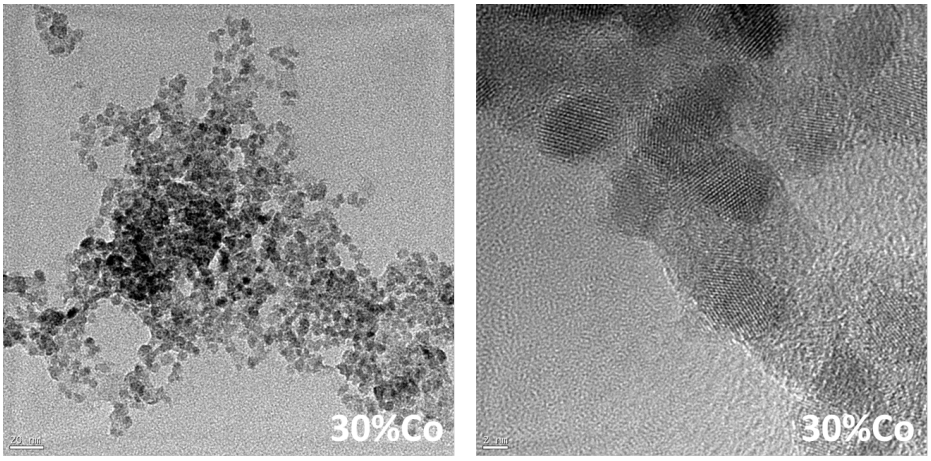

***Figure 7.5**: Low and high resolution images for a NP of Co-doped ZnO with 30% of Co.*

To perform TEM imaging, the samples were prepared by suspending solid samples in ethanol solvent in a small glass vial, followed by a sonication treatment in an ultrasonic water bath[110]. The thickness of a TEM specimen must be very small: usually in the range from 10 nm to 1μm[153].

The Figures 7.2, 7.3, 7.4 and 7.5 show an example of low and high resolution images for several samples with different cobalt concentration.

Several images were made for each of the samples characterized by microscopy. With them, we were able to establish the size distribution of the

nanoparticles of pure ZnO and doped ZnO with 5, 15 and 30% of cobalt, as shown in the histograms at figure 7.6.

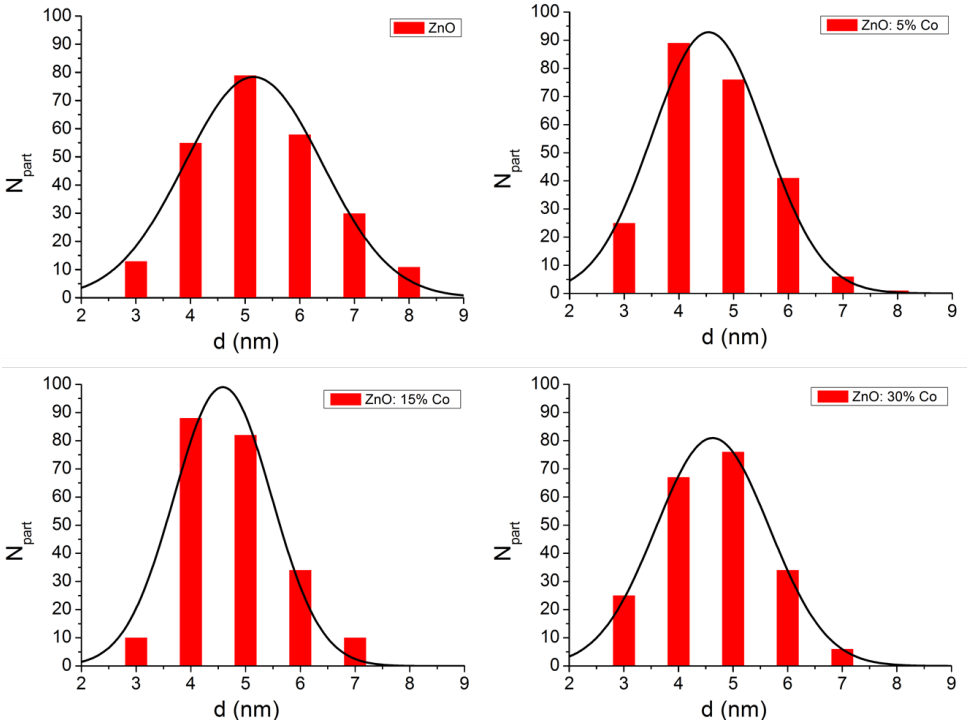

***Figure 7.6**:* Size grain distributions of pure ZnO and doped ZnO with 5, 15, 30% of Co.

The equation 7.1 is used to adjust the experimental size distribution to a Gaussian distribution.

$$N\left(size\right) = \frac{1}{\sqrt{2\pi}} A e^{-\frac{1}{2}\left(\frac{size - size_{\mu}}{size_{\sigma}}\right)^2} \tag{7.1}$$

In that expression, $\mathbf{size_{\mu}}$ and $\mathbf{size_{\sigma}}$ are the centre and the width of the distribution respectively, and **A** is a normalization parameter. Our analysis determine that the size distribution is monomodal and the grain size is independent of the cobalt content for $Zn_{1-x}Co_xO$ and has a value between 4 and 5 nm. This size is around to three times larger than the size of the bulk exciton (1.8 nm) and, therefore, we are in the weak confinement regime[154] for the average size particles, but in the strong confinement regime for NP size below the average. The distribution parameters are shown in table 7.1.

***Table 7.1**: Gaussian parameters for size-grain-nanoparticles distribution.*

Sample	$\mathbf{A\sqrt{2\pi}}$ **(N**$_{part}$**)**	**size**$_\sigma$ **(nm)**	**size**$_\mu$ **(nm)**
ZnO	78.3 ± 0.8	1.26 ± 0.06	5.16 ± 0.06
ZnO:5%Co	92.8 ± 0.6	1.03 ± 0.07	4.54 ± 0.07
ZnO:15%Co	99.1 ± 0.7	0.89 ± 0.08	4.58 ± 0.08
ZnO:30%Co	80.9 ± 0.3	1.04 ± 0.02	4.63 ± 0.02

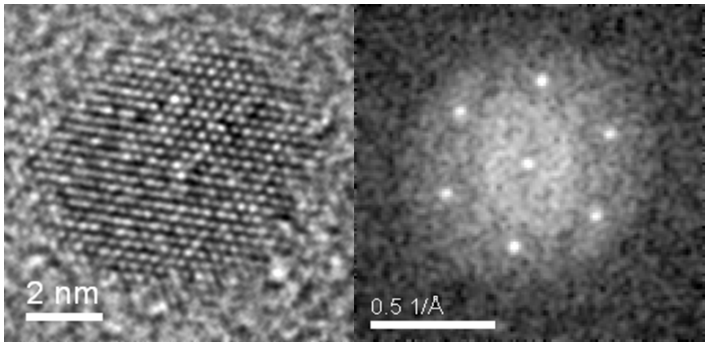

***Figure 7.7**: High resolution and FFT of a sample of 5% doped ZnO.*

The high-resolution images (Fig. 7.7) give directly the size and the shape distributions, they also demonstrate that the nanoparticles internal structure is crystalline. In particular, from the high-resolution image of a given particle, in its Fourier Transformation all the intense reflections correspond to a single crystal (Fig. 7.8).

Since the intensity profiles through the perpendicular to a given crystallographic plane are equidistant, we determine that the nanoparticles are single crystals of good crystalline quality. Using the intensity profile, we also obtained that our nanoparticles have an interplanar distances around 0.283 and 0.284 nm. This corresponds to (100) family in the wurtzite structure, comparing pretty well with the value calculated for the ZnO (0.281nm)[22][25][28]. HRTEM images could be indexed with wurtzite phase of ZnO with space group P63mc.

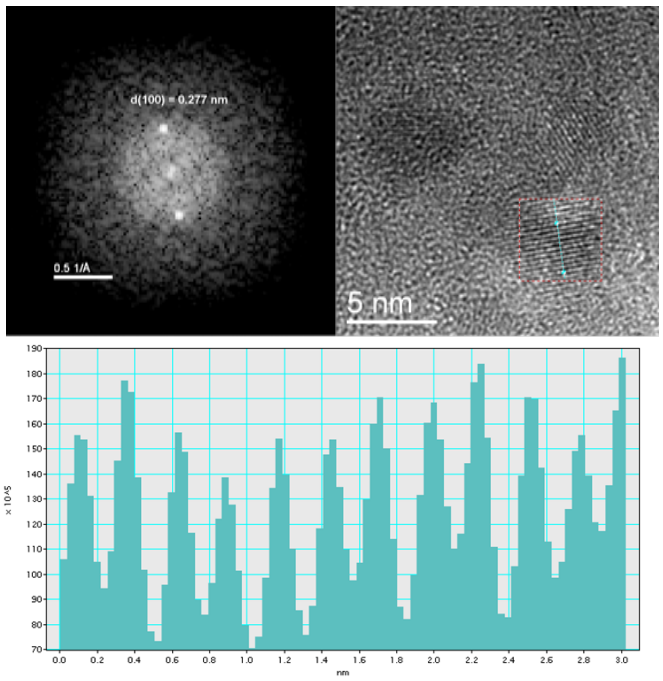

***Figure 7.8**: FFT, HR and intensity profile of a sample of 5% doped ZnO.*

Similarly, the diffraction ring has a correspondence with the interplanar distances (100) and (002). Interplanar distances and lattices parameters are shown in Table 7.2.

***Table 7.2**: Interplanar distances and lattice parameters.*

Sample	**d(100)(Å)**	**a(Å)**	**d(002)(Å)**	**c(Å)**
ZnO	2.843 ± 0.007	3.283 ± 0.013	2.623 ± 0.004	5.246 ± 0.002
ZnO:5%Co	2.883 ± 0.012	3.329 ± 0.014	2.620 ± 0.030	5.230 ± 0.060
ZnO:15%Co	2.900 ± 0.005	3.341 ± 0.008	2.573 ± 0.002	5.146 ± 0.003
ZnO:30%Co	2.870 ± 0.004	3.314 ± 0.004	2.572 ± 0.011	5.140 ± 0.020

We would expect a decrease in both parameters since the ionic radius of cobalt is slightly smaller than the zinc one. However, when increasing the cobalt concentration, **a** tends to increase and **c** tends to decrease. This is consistent with previous thin film measurements published by other authors for low concentration[155] and can be understood as an increase of the ionic character of the alloy as the Co concentration increases (Co $3d$ electrons are less bound and contribute less to covalent bonds with respect to ZnO

3*d*). The decrease of the *c* parameter can then be understood as a result of the electrostatic attraction between cationic (Zn-Co) and anionic (O) planes in the [001] direction as the ionic character of the alloy increases. At high concentrations there is a saturation.

To complete the characterization using microscopy, element mapping has been done by EDX (Energy-Dispersive X-Ray Spectroscopy) for every sample. In Figures 7.9, 7.10 and 7.11 we show examples for several concentration of cobalt. In each one, we can see two images that correspond to Co and Zn maps (green and yellow respectively) and a superposition of all these. In the superposition, Zn is in red and Co in yellow. Our analysis indicate that zinc and cobalt have the same distribution in the material, indicating that the composition of the NPs is very homogeneous. Table 7.3 reports the EDX results.

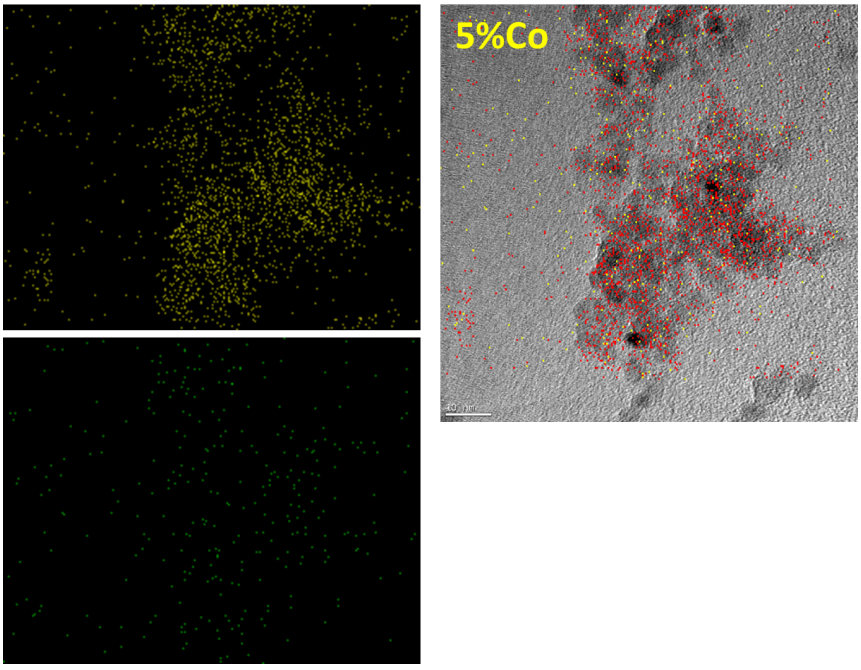

***Figure 7.9**: Element mapping of NP of ZnO doped with 5% of Cobalt.*

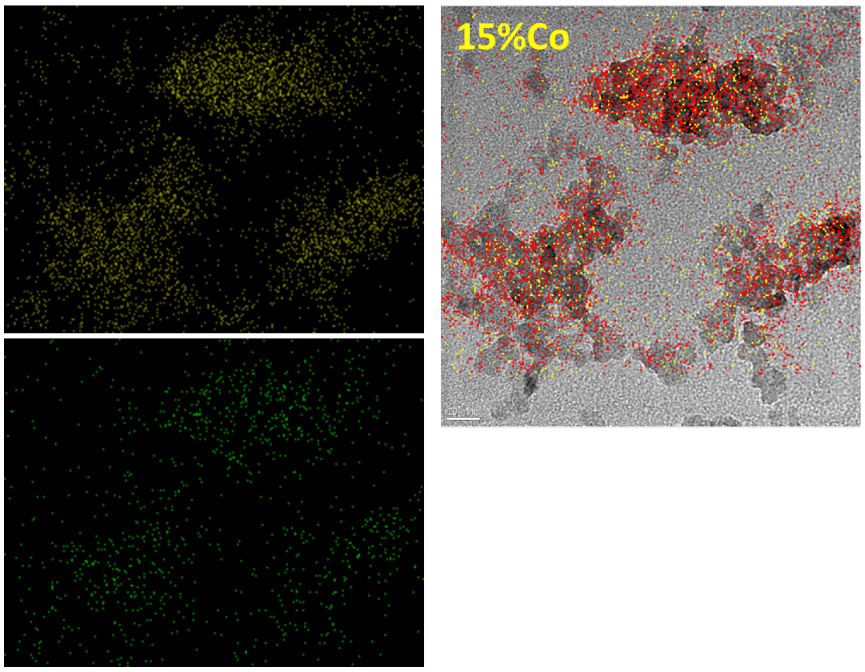

***Figure 7.10**: Element mapping of NP of ZnO doped with 15% of Cobalt.*

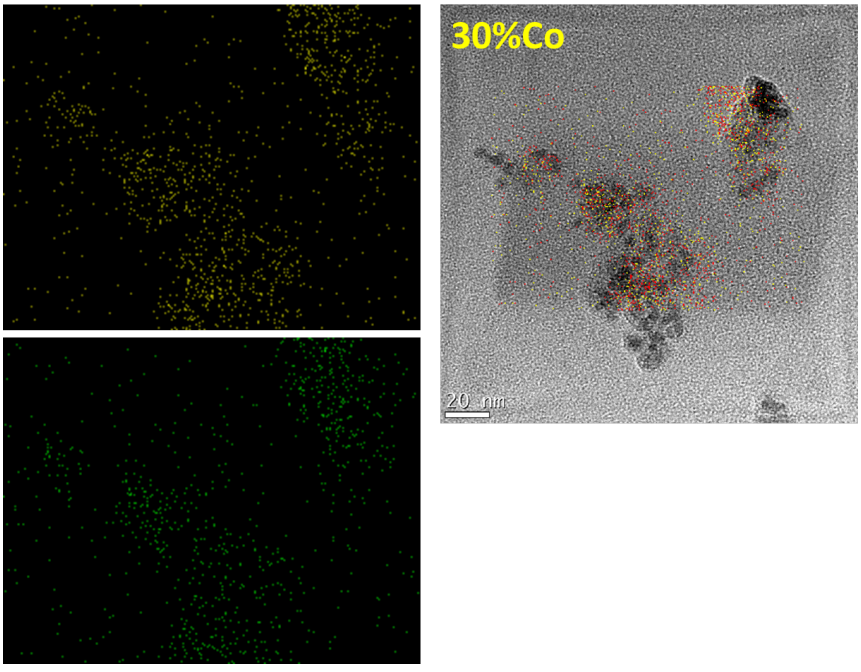

***Figure 7.11**: Element mapping of NP of ZnO doped with 30% of Cobalt.*

***Table 7.3**: EDX Analysis: composition of nanoparticles.*

Sample	EDX Analysis	
Nominal Co content	**Co content measured**	**Zn content measured**
ZnO:5%Co	4.4 - 5.3 %	95.6 - 94.7 %
ZnO:15%Co	8.5 - 13 %	91.5 - 87 %
ZnO:30%Co	21.3 - 32.1 %	78.7 - 67.9 %

7.3.2 Absorption Spectra

For optical absorption measurements in the UV-Vis-NIR range, at ambient and high pressure, a sample was placed together with a ruby into a diamond anvil cell as explained in the section experimental techniques. Samples for optical measurements in diamond cell are obtained from the suspension of nanoparticles in toluene, dropping several drops on a slide. Toluene evaporates and surfactant coated nanoparticles are added forming a "solid" layer. Cracking them, we obtain small rectangular samples with lateral dimensions of a few hundred microns and thickness from a few microns to a few tens of microns.

The absorption spectra at ambient pressure for the $Zn_{1-x}Co_xO$ nanoparticles with different concentrations of cobalt are shown in fig. 7.12. The three characteristics commented in the Introduction and in Chapter 4 can be distinguished in this initial spectra:

1. Absorptions bands around 2 eV, whose intensity increases with increasing concentration of Co. These are due to electronic transitions in the tetrahedral crystal-field split Co 3d levels, from the "d" ground level to the third excited one.

2. Absorption edge which corresponds to band to band transitions: sharp absorption around 3.3 eV, which shifts to higher energies, as increasing the Co concentration. This behaviour is observed from pure ZnO to 1% of cobalt. But for higher concentrations the charge transfer (CT) transition dominates and the fundamental absorption edge is not visible. Excitonic peak is not observed either because the effective thickness of the agglomerate of nanoparticles is high (probably about half a micron) and, therefore, only the lower tail of the band-to-band or CT absorption edge is observed.

3. Charge transfer transitions: they have lower slope and are at lower photon energy than the fundamental absorption edge. Up to 5% of

cobalt content, the CT band and the fundamental absorption can be distinguished (see pictures of evolution under pressure in the following section). For samples of higher concentration only the charge transfer transition absorption band is observed observed, which gradually extends to lower energies and gives rise to even rise to an overlapping with the 3d cobalt bands.

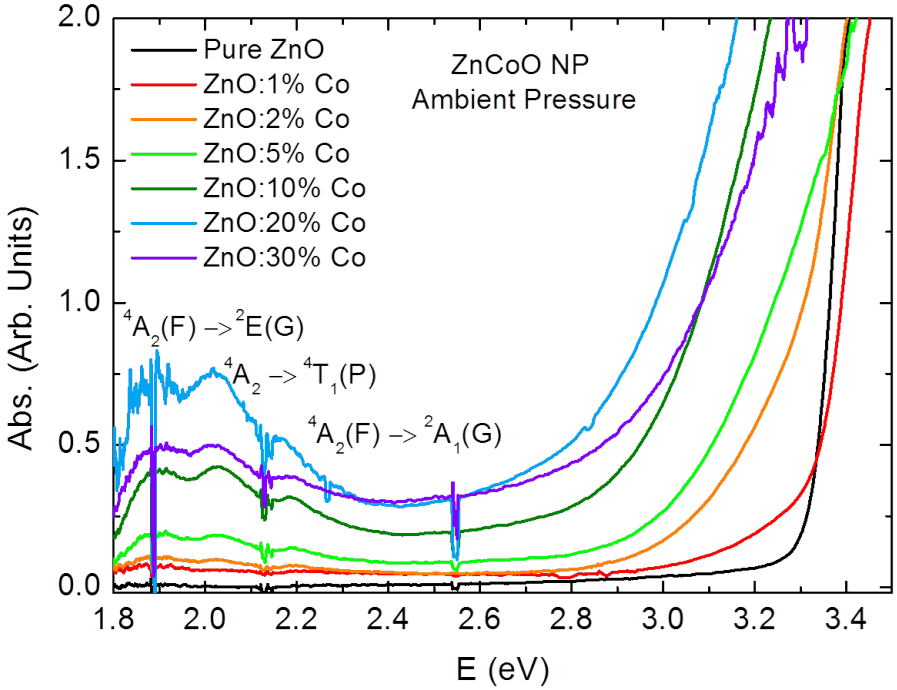

***Figure 7.12**: Initial spectrum of the $Zn_{1-x}Co_xO$ nanoparticles for different values of x. Pressure around 0-0.4 GPa.*

Focusing into the area of $d-d^*$ transitions, we can identify three peaks: T_3 around 2.18 eV, T_2 around 2.02 eV and T_1 around 1.89 eV, corresponding to the $d-d^*$ electronic transitions of the replaced Co^{2+} ions due to the spin-spin interactions in the d-orbitals[116]. They are expressed as: $^4A_2(F) \rightarrow {}^2E(G)$, $^4A_2(F) \rightarrow {}^4T_1(P)$ and $^4A_2(F) \rightarrow {}^4A_1(G)$, respectively. By extrapolating the contribution of the CTT we can substract it and represent only the contribution of $d-d^*$ transition (Fig. 7.13).

There is a clear correlation between the peak absorption intensity and the cobalt concentration as shown in Fig. 7.14. This relationship between absorption intensity and cobalt concentration in the samples is also found when the area under the curve of the spectrum is used[115].

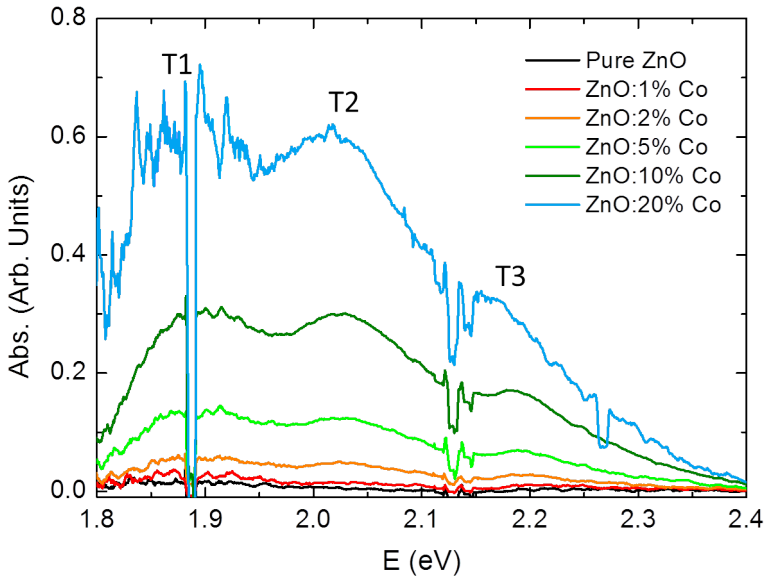

***Figure 7.13**: Absorption spectra in the range of 1.8 to 2.4 eV for different concentrations of cobalt at initial pressure (0-0.4 GPa).*

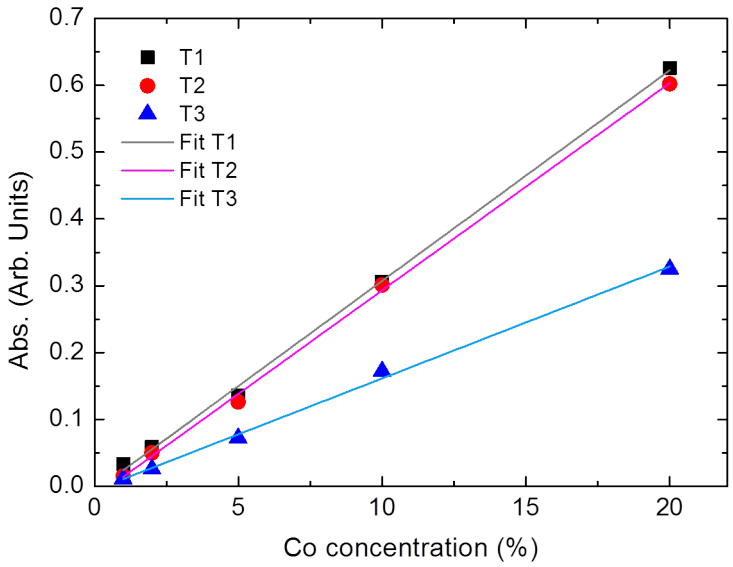

***Figure 7.14**: Absorption Co-peaks intensity in function of the Co content.*

Optical absorption bands produced by the $3d$ internal transitions of cobalt in ZnO have been observed in several papers exploring bulk materials[119][156]. The linearity observed between the absorption peaks and the cobalt concen-

tration is a clear demonstration of the association of these absorption peaks to the presence of tetrahedrally coordinated cobalt.

***Table 7.4**: Fit parameters of the linear fitting (y = a + b*x) between absorption peaks intensity and Co content.*

Peak	a (Arb. Units)	b (Arb.Units/%)	Statistics
T1	-0.008 ± 0.006	0.0315 ± 0.0007	0.998
T2	-0.017 ± 0.006	0.0310 ± 0.0006	0.999
T3	-0.006 ± 0.005	0.0167 ± 0.0004	0.997

7.4 Nanoparticles Under High Pressure

7.4.1 Spectra Evolution Under High Pressure

Once the particles have been characterized at ambient pressure, optical absorption measurements were conducted under pressure, always at room temperature. The following figures (Fig. 7.15, 7.16, 7.17, 7.18, 7.19, 7.20 and 7.21) show the evolution of the absorption spectra of $Zn_{1-x}Co_xO$ nanoparticles under high pressure (up to 23 GPa) for different Cobalt concentrations.

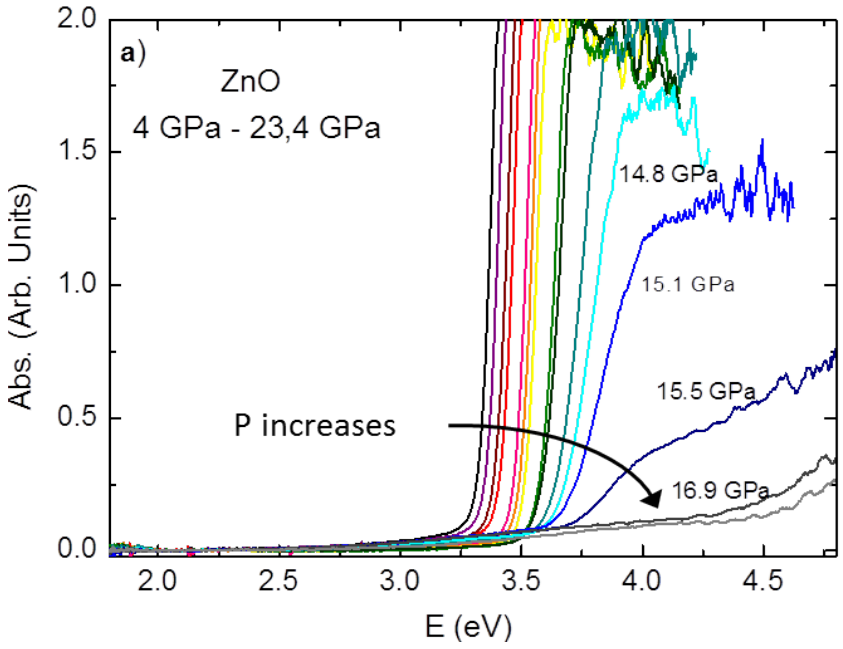

***Figure 7.15**: Evolution of the absorption spectra of nanoparticles: a) pure ZnO*

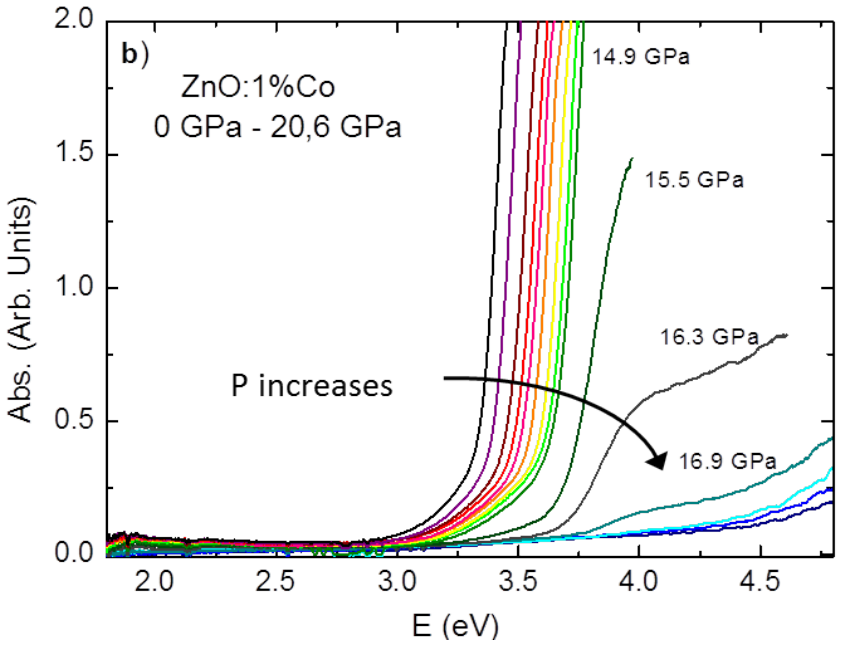

***Figure 7.16**: Evolution of the absorption spectra of the $Zn_{1-x}Co_xO$ nanoparticles: b) ZnO:1%Co*

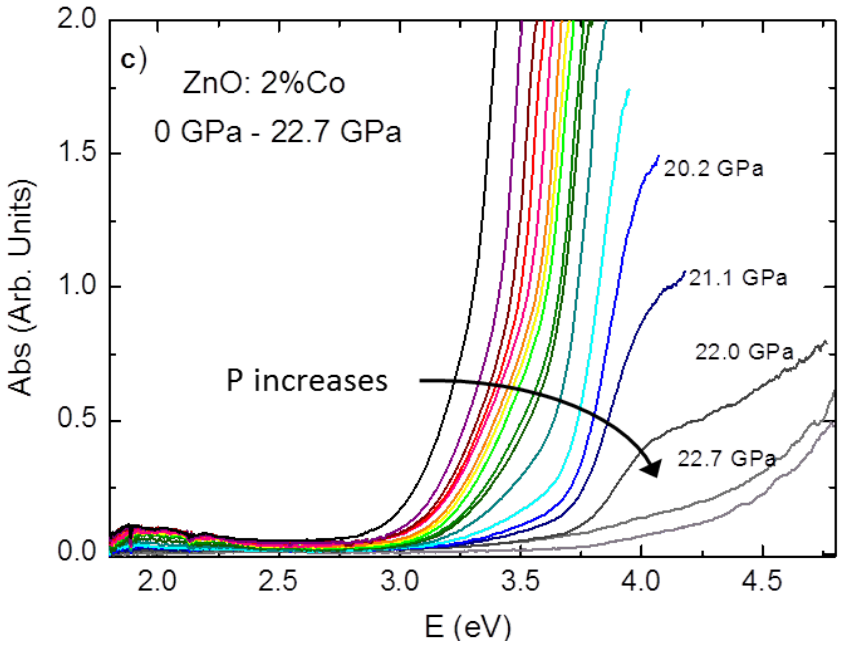

***Figure 7.17**: Evolution of the absorption spectra of the $Zn_{1-x}Co_xO$ nanoparticles: c) ZnO:2%Co*

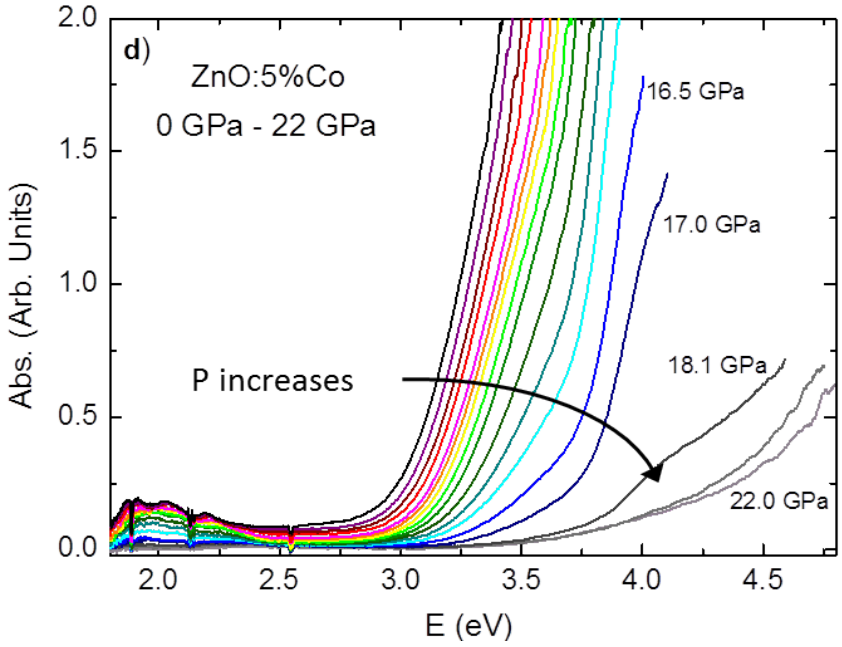

***Figure 7.18**: Evolution of the absorption spectra of the $Zn_{1-x}Co_xO$ nanoparticles: d) ZnO:5%Co*

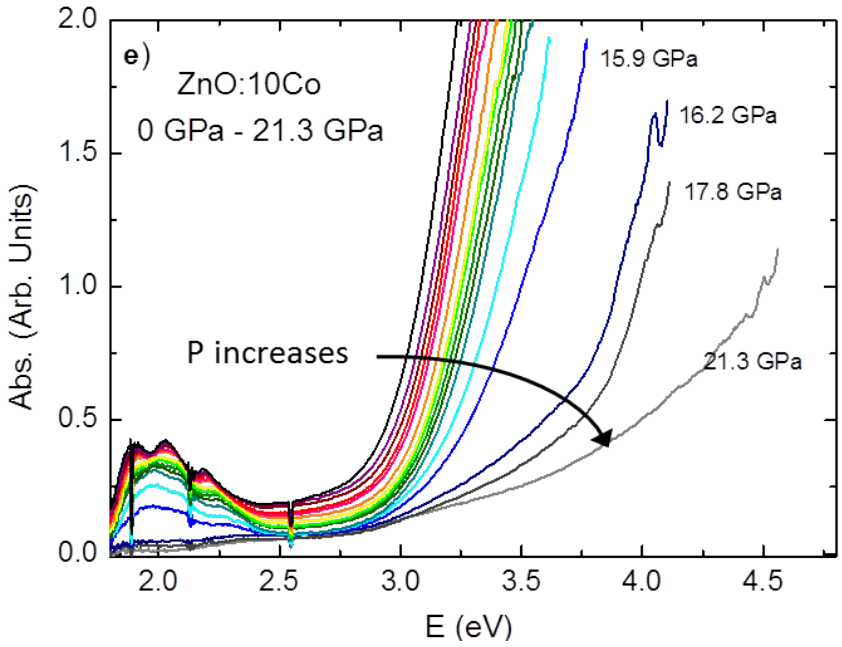

***Figure 7.19**: Evolution of the absorption spectra of the $Zn_{1-x}Co_xO$ nanoparticles: e) ZnO:10% Co*

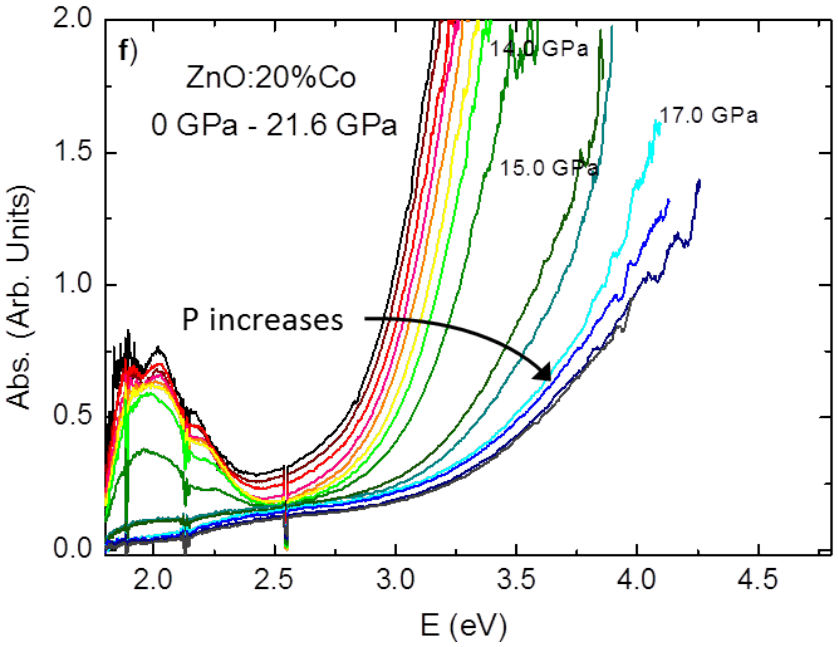

***Figure 7.20**: Evolution of the absorption spectra of the $Zn_{1-x}Co_xO$ nanoparticles: f) ZnO:20%Co*

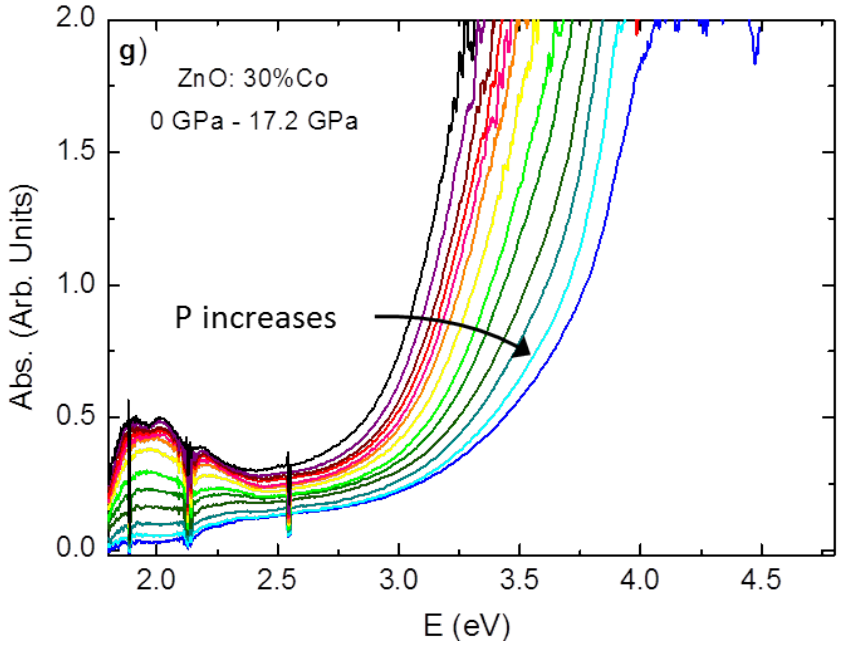

***Figure 7.21**: Evolution of the absorption spectra of the $Zn_{1-x}Co_xO$ nanoparticles: g) ZnO:30%Co*

The following behaviours can be observed in the evolution of the absorption spectra with pressure for different concentrations of Co^{2+} in ZnCoO:

1. The absorption edge moves almost parallel toward higher energies for a first range of pressures (up to $\sim$ 12 GPa).

2. The charge transfer absorption band also shifts toward higher energies with increasing pressure with small changes in intensity.

3. The cobalt $3d - 3d^*$ absorption bands practically do not move with pressure and their intensities decrease slightly.

4. Around 15 GPa some changes happen. We identify this pressure as the transition pressure. These changes are due to the transition of the material from the wurtzite to the rock-salt phase, similar to what happens in thin films[38].

    - The absorption edge undergoes a change in shape, moving at much higher energies and having a smoother dependence on energy.
    - The cobalt bands intensity decreases sharply, disappearing for the samples with low concentrations. Studying more carefully the samples with higher concentration, we observe an absorption band much less intense at energies around 2.5 eV.

5. Although the transition is fast, it is gradual. So, some of the nanoparticles remain in the wurtzite phase up to pressures above 17 GPa.

7.4.2 Bandgap Evolution and Pressure Coefficient

To study in more detail the evolution of the optical spectra of the nanoparticles as a function of the pressure, we represent how the photon energy at constant absorption changes as varying the pressure for each concentration of cobalt. Our results are shown in Figure 7.22.

The behaviour of the gap as a function of pressure (Figure 7.22) has two distinct zones. A first region where the bandgap evolves smoothly with pressure towards higher energies. This behaviour corresponds to the first response to the pressure of the material while it is held in wurtzite structure.

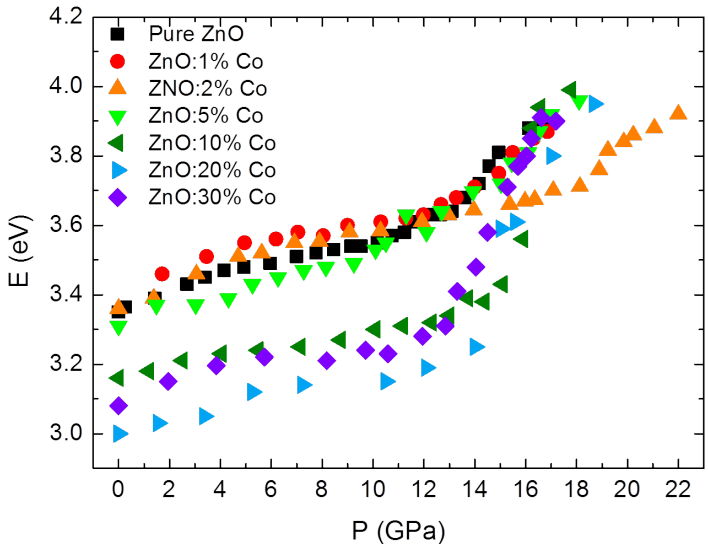

***Figure 7.22**: Representation of the variation of the absorption edge for different Co content in function of the pressure.*

As explained in the theory chapter, on applying hydrostatic pressure to ZnO causes a decrease in the unit cell volume and an increase in Zn-O orbital overlapping. This reduction in the interatomic distance produces an increase in the gap because the energy separation between the bonding and antibonding orbitals increases. After this smooth behaviour, showing a slight tendency to saturation (slope decrease), we observe a second region in which the constant absorption energy increases much more rapidly with pressure. This part corresponds to the transition of the material from the wurtzite (W) phase to the rock-salt (RS) phase. This happens when the material reaches a certain pressure and becomes energetically favorable to assume the more compact rock-salt structure (cubic, $Fm\bar{3}m$ space group).

The change of the slope of the constant absorption energy versus the pressure indicates the beginning of the W-to-RS transition. Consequently, we can establish that the transition of the $Zn_{1-x}Co_xO$ nanoparticles starts between 11 and 13 GPa for all the concentrations of cobalt, except for the 2% of Co for which it begins at 17 GPa in all experiments carried out. We can note the difference with previous works on cobalt doped ZnO, where the wurtzite to rock-salt phase transition in bulk materials and thin films occurs at lower pressures for larger Co proportions. Thus, it moves from 9 GPa in pure ZnO to 6 GPa in the 30% Co doped. For all concentrations, the transition for the thin film and bulk occurs at lower pressure than for nanoparticles. Moreover, for thin film and bulk material the transition is abrupt. However, through the pressure evolution of the photon energy at constant absorption, we can

appreciate that, energy that although the transition of the nanoparticles is fast, it is gradual. This indicates that some of the nanoparticles remain in the wurtzite phase up to pressure above 17 GPa. The fundamental absorption change is due to the fact that RS-ZnO has an indirect gap at lower energy[38], with lower absorption intensity and it is not detected in thin samples. So, the first observable transition is a direct transition that, due to the strong ionic character of bonding in this structure, occurs at much higher energy than the range of the spectrometer (high pressure). Anyway, we will do a more detailed study of the phase transition through the pressure evolution of the cobalt bands at the end of this chapter.

In which follows we focus on the study of the material under pressure while it does not transit to the high-pressure phase. That is, we concentrate on the study of the absorption edge evolution between 0 and 12 GPa (up to 17 GPa for the nanoparticles with 2% of cobalt). We will try to parameterize the dependence of the energy gap with pressure.

It is common use in the literature to assume that the energy of the absorption edge changes linearly with **P** or ***ln*V**. However none of these models are entirely correct because the bulk modulus increases with decreasing volume. For this reason, it is preferable to use a quadratic fitting of the form:

$$E_g(P) = E_g(0) + \alpha P + \beta P^2 \tag{7.2}$$

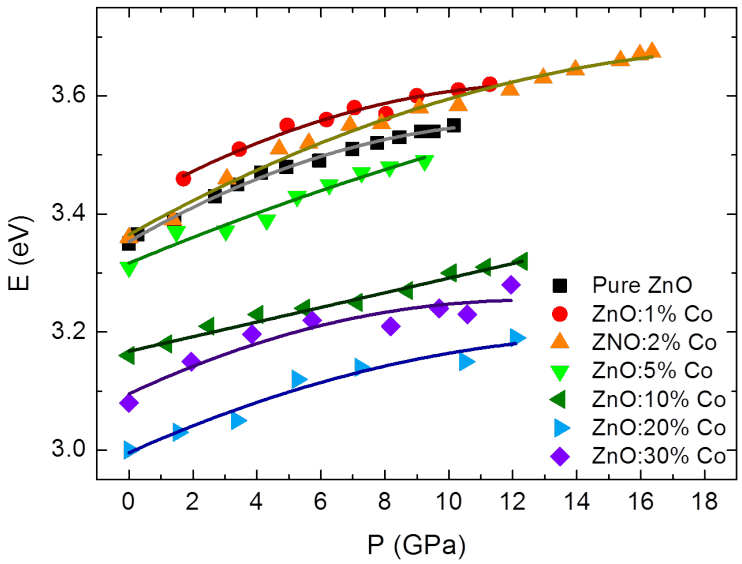

***Figure 7.23**: Pressure dependence of bangap energy for $Zn_{1-x}Co_xO$ nanoparticles.*

On Figure 7.23 we represent the energy of the constant absorption energy as a function of pressure for the range in which the nanoparticles are in W-phase. Overplotted to the experimental data are the fitted dependences using equation 7.2. The results of this fits are shown in the Table 7.5.

***Table 7.5**: Pressure coefficient for $Zn_{1-x}Co_xO$ for x=0, 1, 2, 5, 10 and 20.*

	$\mathbf{E_g(0)(eV)}$	$\boldsymbol{\alpha}$**(meV/GPa)**	$\boldsymbol{\beta}$**(meV/GPa^2)**	$\boldsymbol{\sigma}$
ZnO pure	3.353 ± 0.003	31.3 ± 1.4	-1.2 ± 0.1	0.995
ZnO: 1%Co	3.416 ± 0.014	31 ± 5	-1.1 ± 0.4	0.967
ZnO: 2%Co	3.365 ± 0.008	30 ± 2	-0.72 ± 0.12	0.987
ZnO: 5%Co	3.317 ± 0.011	22 ± 5	-0.4 ± 0.5	0.954
ZnO: 10%Co	3.166 ± 0.007	14 ± 3	-0.2 ± 0.2	0.972
ZnO: 20%Co	2.996 ± 0.014	24 ± 6	-0.7 ± 0.4	0.941
ZnO: 30%Co	3.095 ± 0.019	25 ± 8	-1.0 ± 0.6	0.863

We must first stress that the constant absorption energy whose pressure dependence we study here is not the bandgap of the material, as we only have access to the absorption tail. This, along with the increasing contribution of the CTT for increasing Co content explains the observed trend of lower constant absorption energy for higher Co content.

It is worth noting also that the CTT-band, which is what we are measuring for concentrations of 5% and higher, has a high pressure coefficient, close to the band-to-band transition. This indicates that it is a transition from the ground state of Co $3d$ levels to the conduction band. If it was from the valence band to an excited $3d$ state of Co, the pressure coefficient would be very small or negative[51]. This is because the maximum of the VB in ZnO rises slightly with pressure due to the $p-d$ interaction between ZnO $3d$ levels and oxygen $2d$, while the $3d$ levels are quite insensitive to pressure due to their atomic character. The value of $\boldsymbol{\alpha}$ for pure ZnO nanoparticles is higher than the value ascribed for the same material but in bulk or thin film. For bulk ZnO, Mang et al. [157] reported a values of α = 25.3 ±0.1 meV/GPa and β = -0.28 ± 0.001 meV/GPa^2. For thin films S. Gilliland [52] yields a values of α = 24.4 ±0.3 meV/GPa and β = -0.44 ± 0.05 meV/GPa^2. This higher pressure coefficient is probably due to the fact that, as we will discuss later on, larger size NPs transit at lower pressure and, even with no confinement effects, it would yield an extra shift to higher photon energies. For the rest of compositions of nanoparticles we can compare with the values reported by J.A. Sans et al. [158]. Those values range from 21.3 meV/GPa

for 30% of cobalt to 24.9 meV/GPa for 5% of cobalt, increasing their values the concentration decreases. It seems then clear that the constant absorption energy pressure coefficient for high Co contents corresponds to the CTT pressure coefficient. The phase transition of larger NPs, that will be discussed later on, will clarify this behaviour.

7.4.3 Down Stroke in Pressure. Rock-Salt Phase at Ambient Pressure

We find another difference between the nanoparticles and the thin film or bulk of the same material. For thin film or bulk, the transition is only irreversible for high cobalt concentration[38][158]. Instead, for nanoparticles, by relaxing the pressure, the absorption edge is shifted, as expected, towards lower energies but all the features of the RS phase remains even at ambient pressure. This indicates that the rock-salt phase is metastable at ambient pressure regardless of the concentration of cobalt showing its metastability even for pure ZnO, as already observed by Decremps *et al*[159]. In following figures (from 7.24 to 7.30), we show the spectra evolution for the $Zn_{1-x}Co_xO$ nanoparticles, with different cobalt content, during relaxation of the pressure.

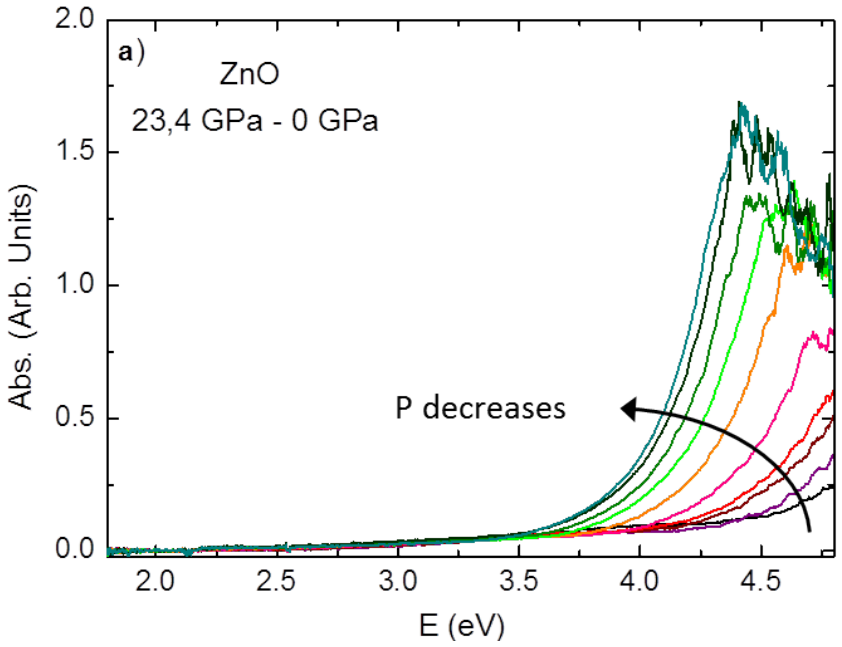

***Figure 7.24**: Spectra evolution during the pressure release in nanoparticles: a) pure ZnO*

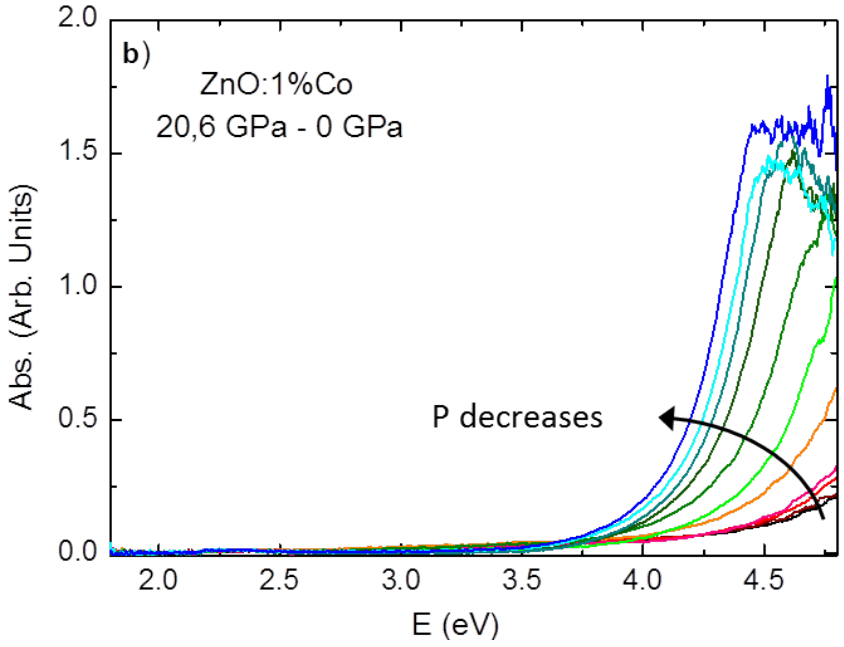

***Figure 7.25**: Spectra evolution during the pressure decrease of the $Zn_{1-x}Co_xO$ nanoparticles: b) ZnO:1%Co*

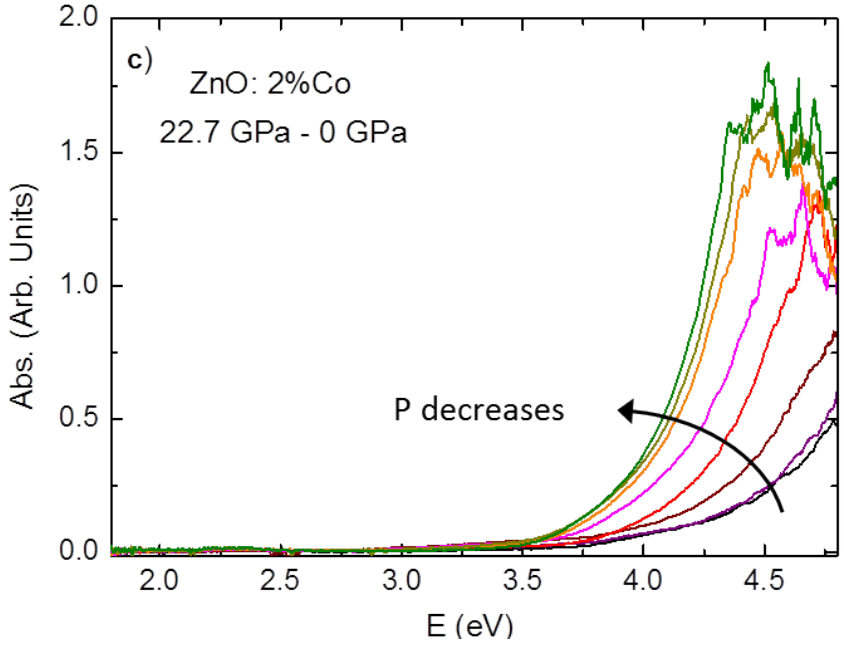

***Figure 7.26**: Spectra evolution during the pressure decrease of the $Zn_{1-x}Co_xO$ nanoparticles: c) ZnO:2%Co*

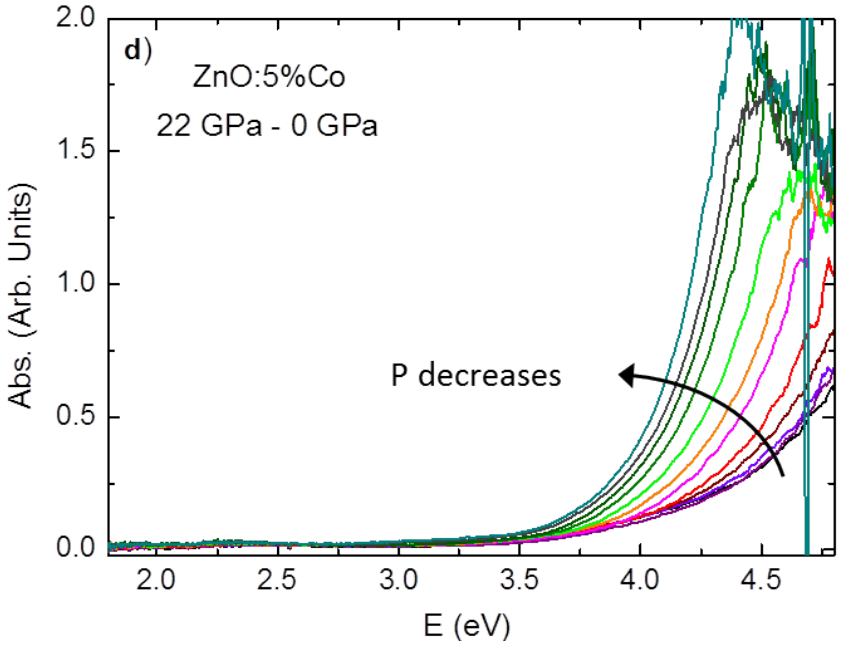

***Figure 7.27**: Spectra evolution during the pressure decrease of the $Zn_{1-x}Co_xO$ nanoparticles: d) ZnO:5%Co*

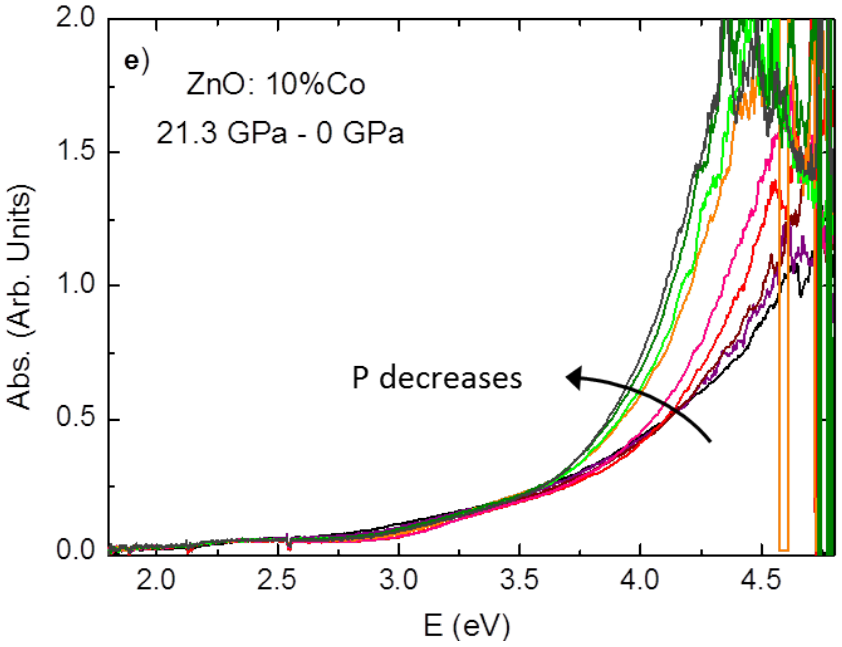

***Figure 7.28**: Spectra evolution during the pressure decrease of the $Zn_{1-x}Co_xO$ nanoparticles: e) ZnO:10% Co*

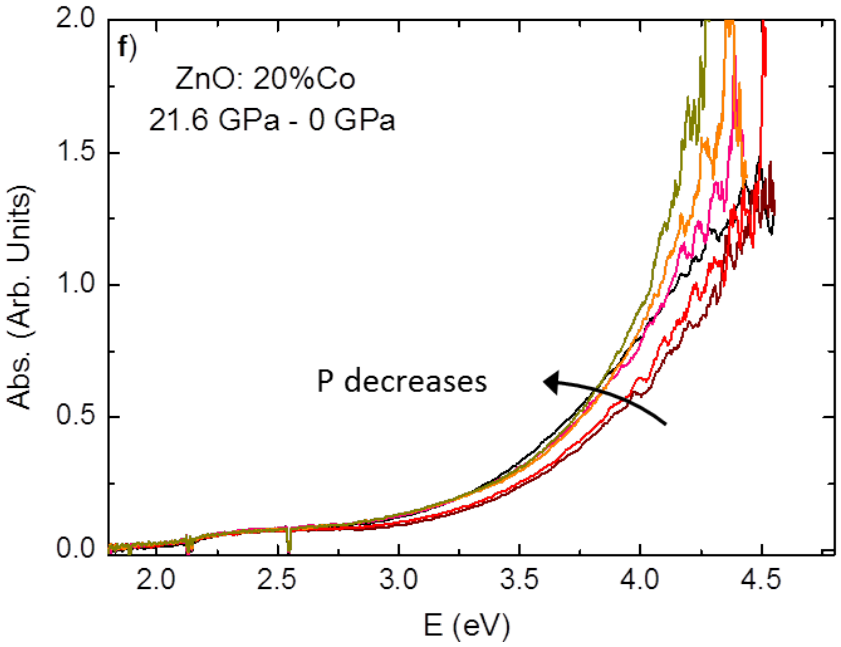

***Figure 7.29**: Spectra evolution during the pressure decrease of the $Zn_{1-x}Co_xO$ nanoparticles: f) ZnO:20%Co*

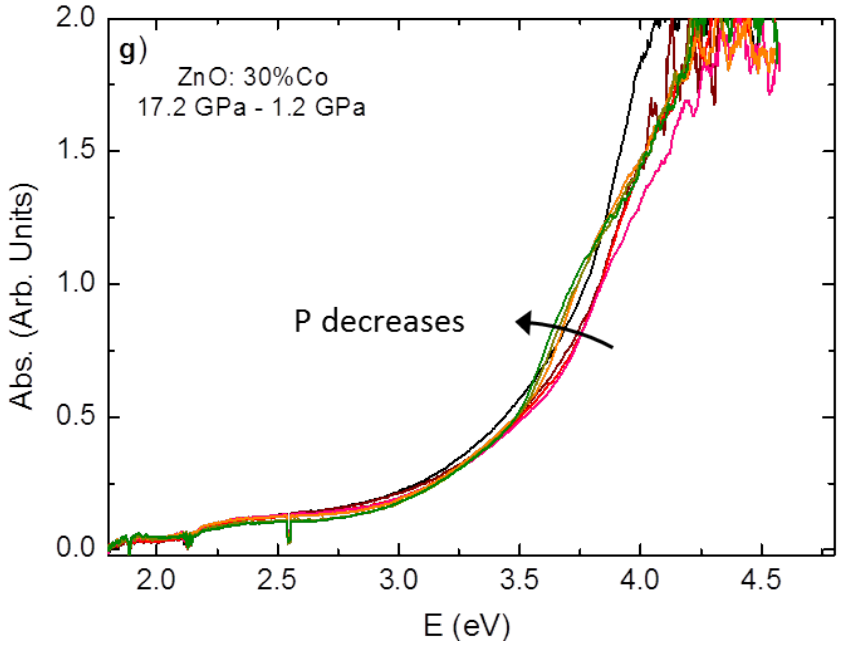

***Figure 7.30**: Spectra evolution during the pressure decrease of the $Zn_{1-x}Co_xO$ nanoparticles: g) ZnO:30%Co*

For pure ZnO or for samples with low concentrations of cobalt, the absorption edge is fairly abrupt. And, at ambient pressure, there is no absorption below 3.75 eV, so that we can attribute the threshold to the direct Gamma-Gamma transition in the rock-salt phase[38]. However, for the highest concentration of Co, the absorption edge is smoother and extends to almost 2 eV, indicating that in the rock-salt phase there are also internal cobalt and charge transfer transitions.

Focusing on $d - d^*$ transitions, it should be noted that in the RS-phase, although they exist, are less intense. If we look to the tail of low energy absorption of the sample with 20% of Co, we see that there are traces of an absorption band:

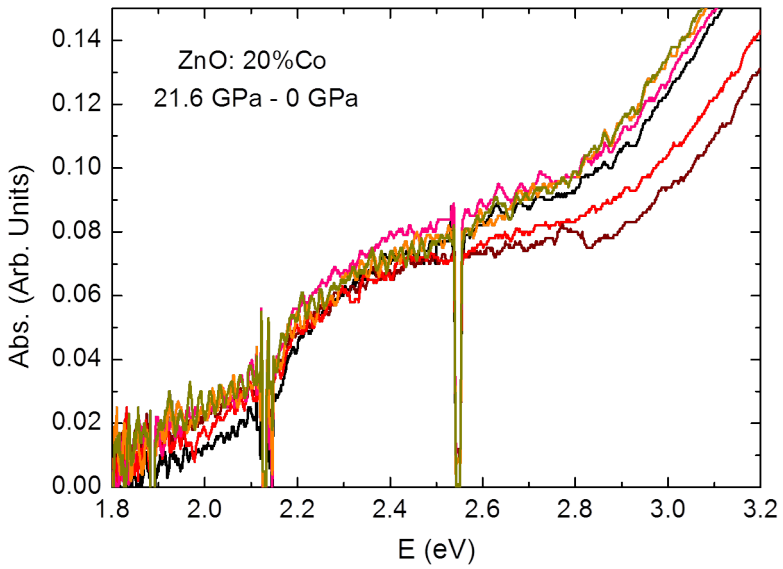

***Figure 7.31**: Down-stroke in pressure for nanoparticles of $Zn_{1-x}Co_xO$ with 20% of Co between 1.8 and 3.2 eV.*

To determine the energy of this absorption, we subtract the absorption edge as a quadratic function, thus being able to identify a band centred around 2.4 eV, which basically corresponds to the energy of the main $3d-2d^*$ transition observed in RS CoO as reported by Pratt and Coelho[160].

The shift to higher energies for the $d - d^*$ transitions in the RS-phase is due to electrostatic repulsion between the $3d$ electrons and the O^{2+} ions. The ionic character if the NaCl phase and the increase in the number of neighbours when goings from tetrahedral to octahedral coordination contribute both the shift towards higher energies of the Co $3d - 3d^*$ transitions.

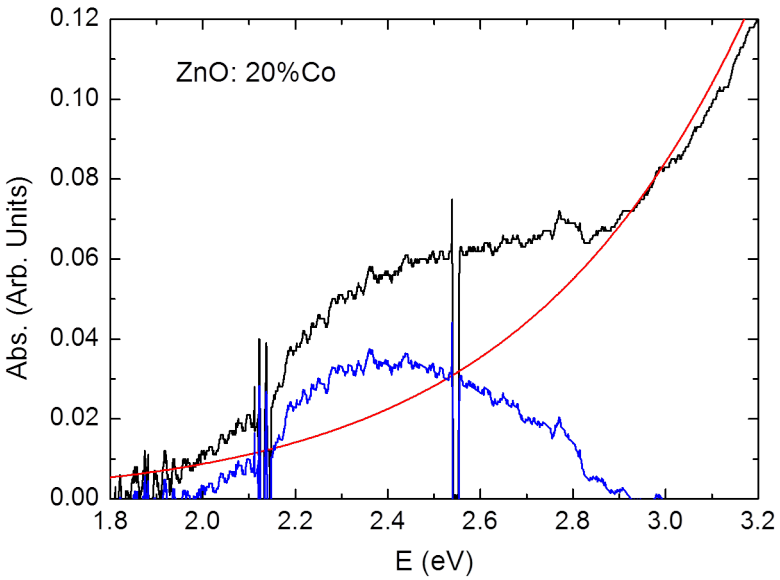

***Figure 7.32**: Absorption at low energies.*

The reason why the transitions are less intense in the rock-salt phase is the presence of inversion symmetry. In a system with a centre of inversion, the transitions between states of the same parity would be prohibited. The wurtzite phase has no center of inversion, and the crystal field modifies *d*-levels so that the transitions between them are not strictly forbidden and are intensified by the influence of the vibrations of the oxygens located around Co atoms. In RS-phase, the inversion symmetry would ban the $d-d^*$ transitions. These are only possible by breaking the symmetry due to the local distortion of such symmetry by vibration of the oxygen atoms in the first shell of the Co coordination.

7.5 Non-completed Cycle and Metastability

To study the origin of the rock-salt phase metastability and the gradual transition, optical absorption measurements have been done under pressure without reaching the pressure at which all nanoparticles have transited to the rock-salt phase. The Figures 7.33, 7.34, 7.35, 7.36 and 7.37 show the evolution of the nanoparticles spectra for different cobalt concentration, both in the up- and the down-stroke in pressure. In these conditions, as the optical bandgap of the cobalt-doped-ZnO in rock-salt phase is at higher energies, transited particles do not contribute to the absorption spectrum and it is dominated by wurtzite nanoparticles.

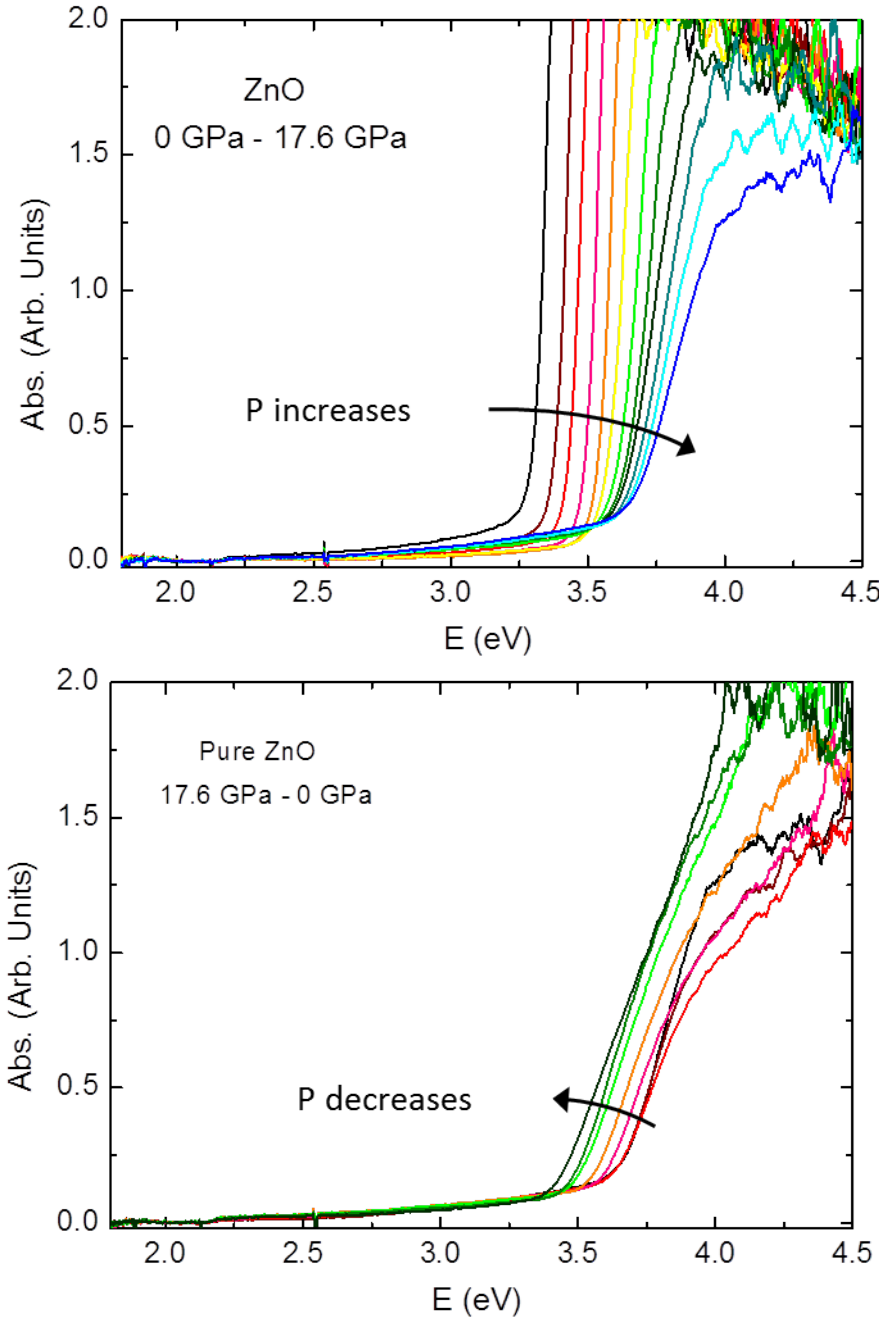

***Figure 7.33**: Up and down-stroke in pressure of the absorption spectra in a non-completed transition for pure ZnO NP.*

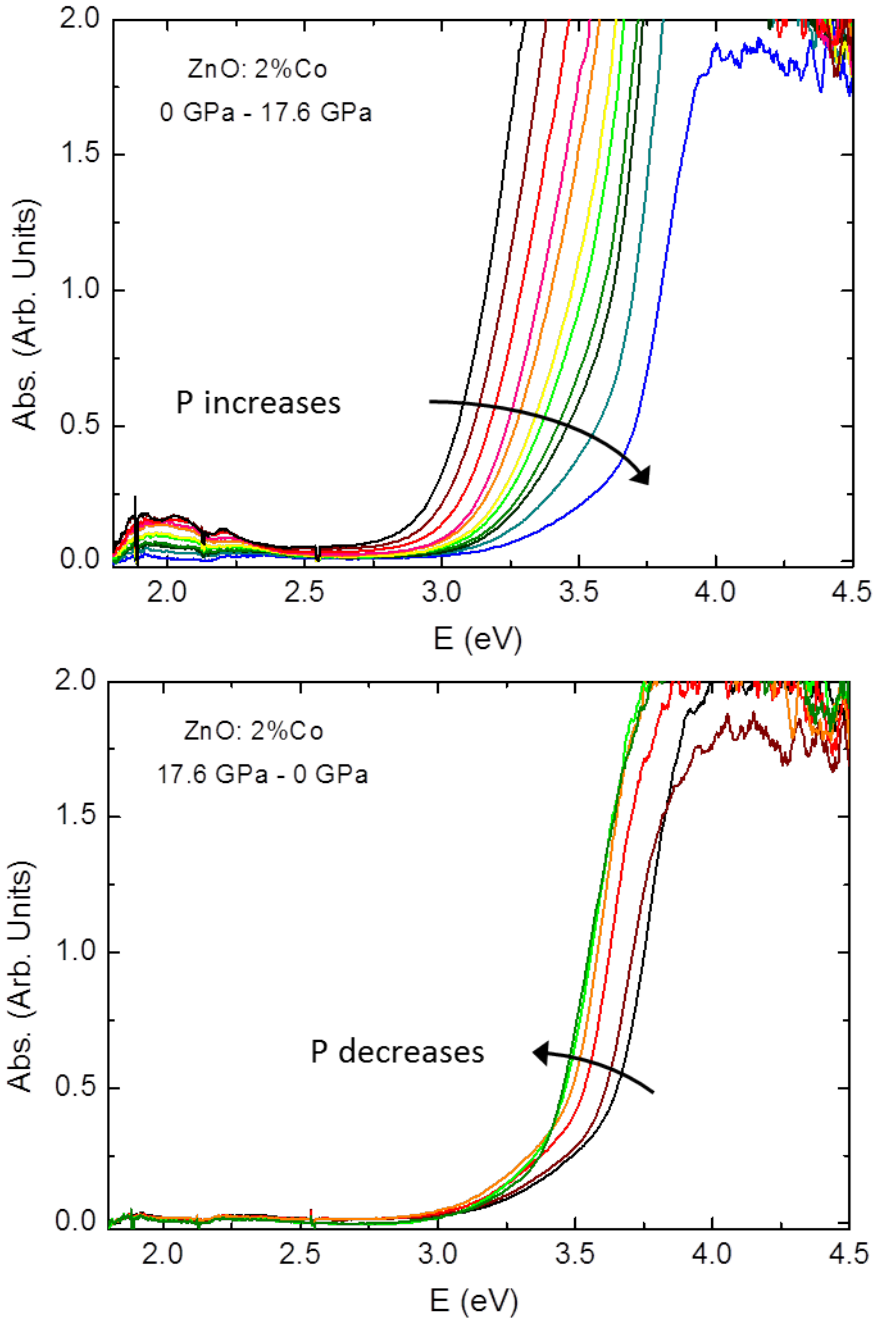

***Figure 7.34**: Up and down-stroke in pressure of the absorption spectra in a non-completed transition for ZnO:2%Co NP.*

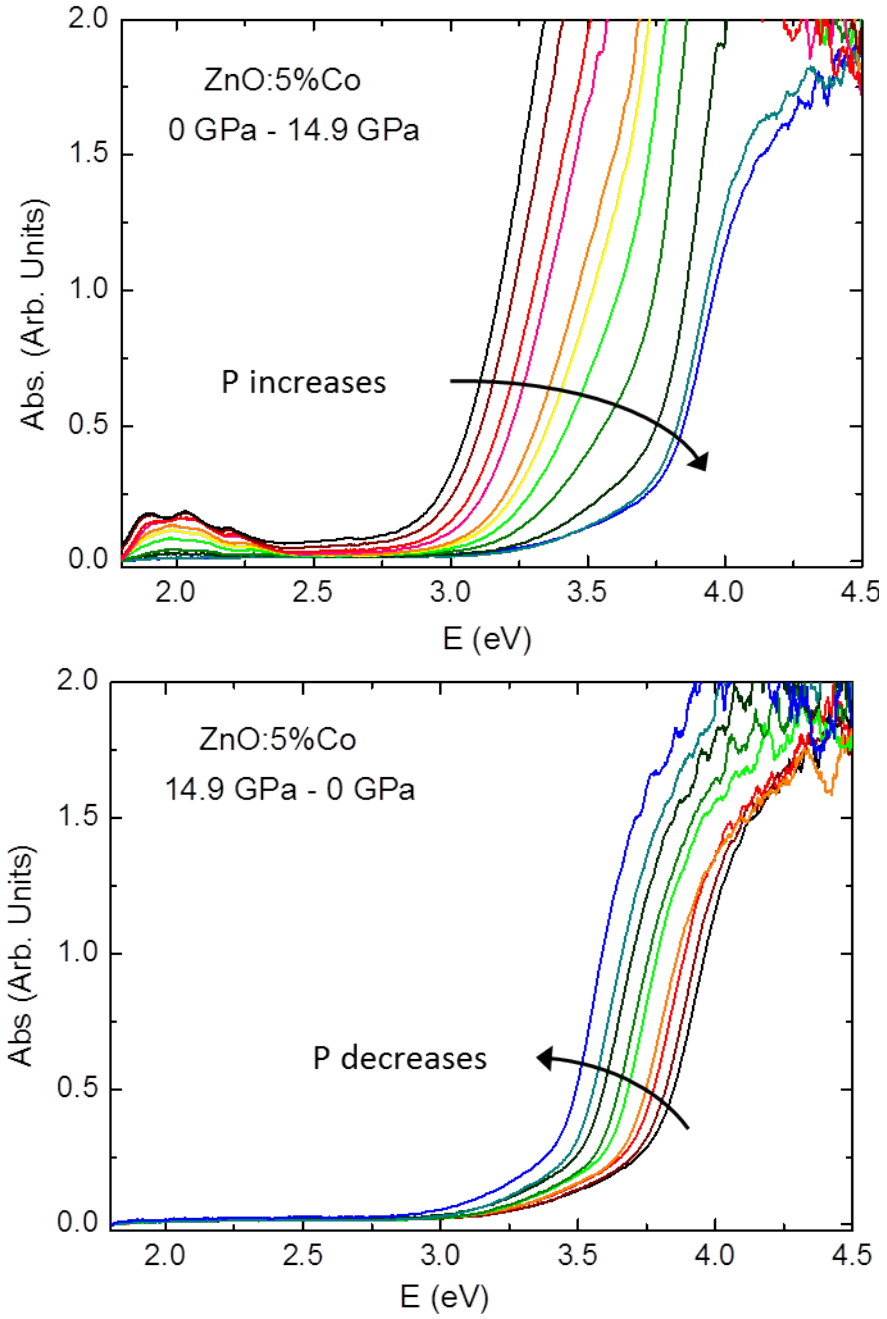

***Figure 7.35**: Up and down-stroke in pressure of the absorption spectra in a non-completed transition for ZnO:5%Co NP.*

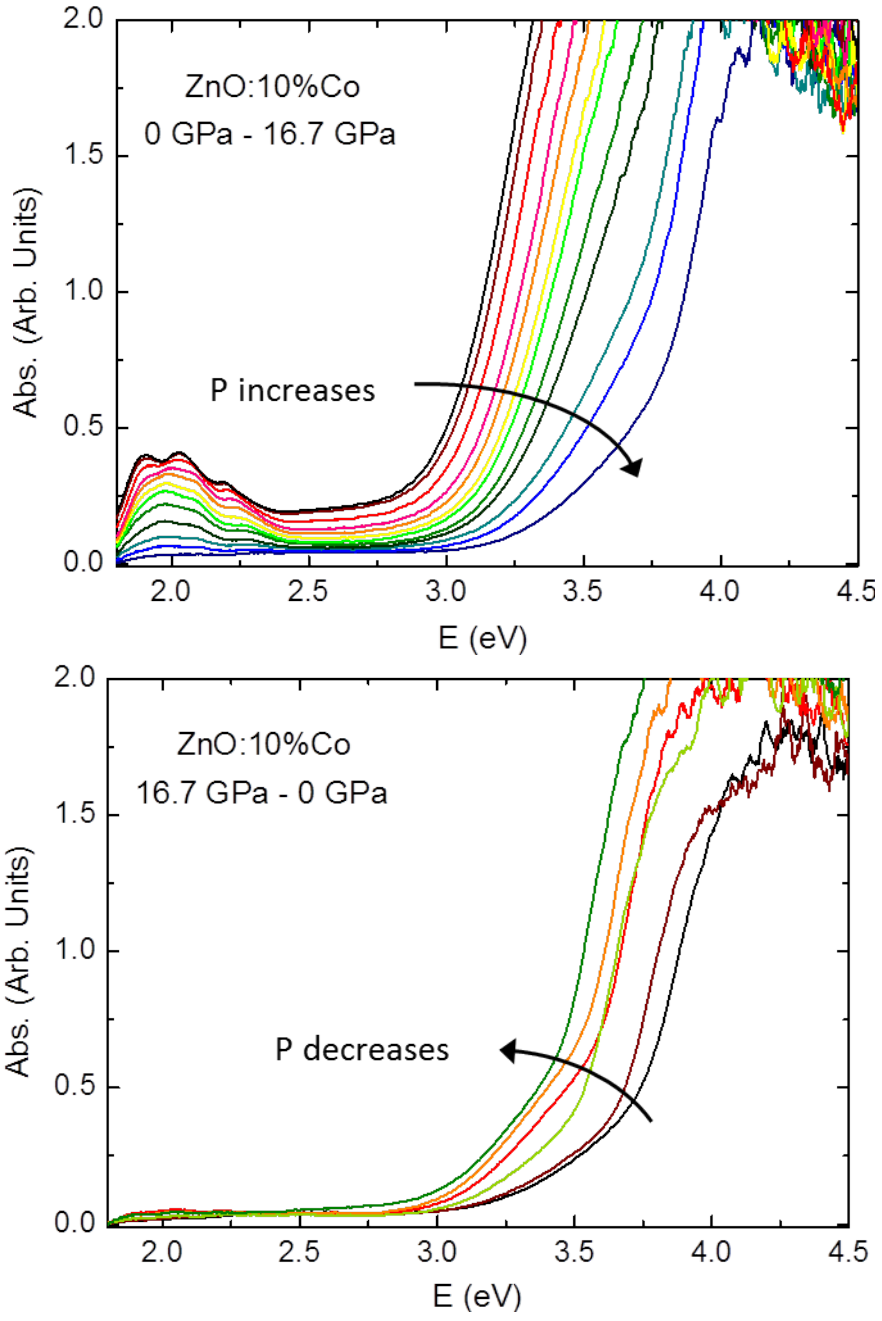

***Figure 7.36**: Up and down-stroke in pressure of the absorption spectra in a non-completed transition for ZnO:10%Co NP.*

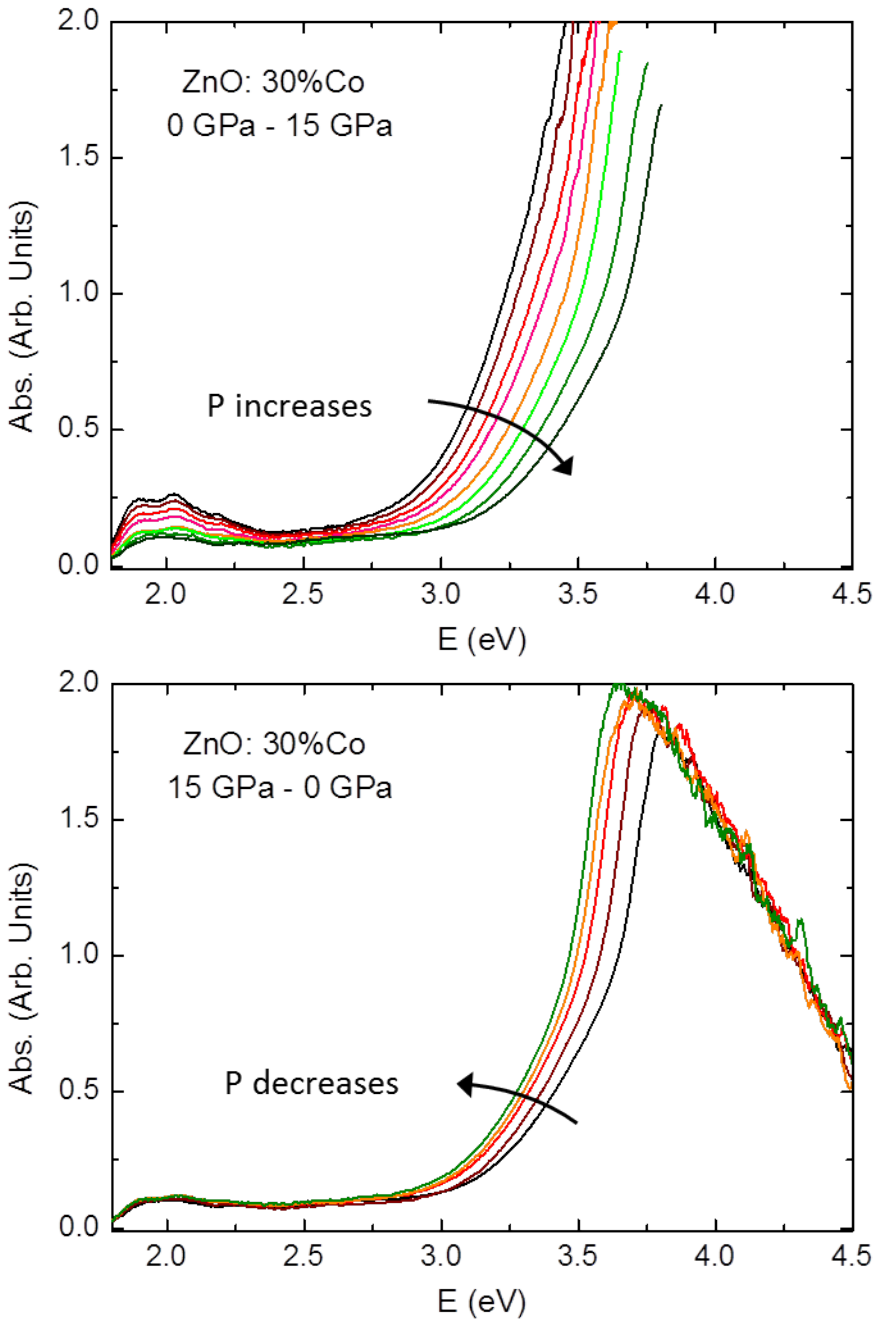

***Figure 7.37**: Up and down-stroke in pressure of the absorption spectra in a non-completed transition for ZnO:30%Co NP.*

By relaxing the pressure, as expected, the absorption onset of the nanoparticles is shifted to lower energies, but without reaching the initial position

at which it started. We can see how the final spectrum at ambient pressure is better defined compared to the original spectrum of the material. In the tail, we can clearly distinguish two parts. The first, between 3 and 3.4 eV, corresponding to the charge transfer transition, where the slope is smoother. And the second part, starting at 3.4 eV with steeper slope, corresponding to the bandgap of the material (band-to-band transition). We can also observe now how the charge transfer is much more pronounced for those samples with the highest concentration of cobalt and smoother for those with lower cobalt content.

According to the theory, when a material is synthesized as a nanoparticle, due to the confinement effect, electronic states become discrete and their energies are shifted to higher energies as the NPs size decreases. The corresponding wave vector values are also discrete and larger for smaller sizes, similarly to what occurs with band filling effects (Burstein-Moss shift) when a material is doped. Figure 7.38 shows a scheme of both effects. In them, the charge transfer absorption decreases its intensity due to the lower value of the k-wave function of localized 3d cobalt states for larger wavevectors. At the low wavevectors for which the k-wavefunction has a maximum the optical transition is not possible due to the confinement shift (nanoparticles) or the occupancy of final states (Ga-doping).

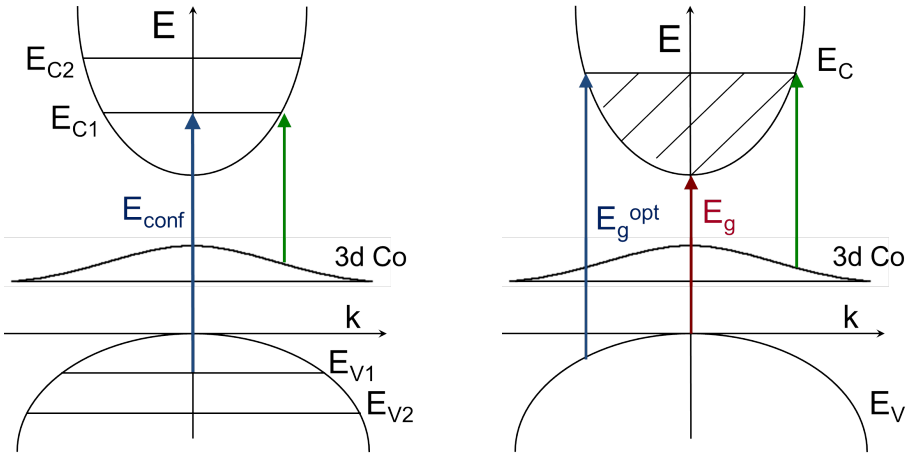

***Figure 7.38**: Schematic diagram of the quantum confinement (left) and the Burstein-Moss shift (right).*

Figure 7.39 compares the absorption spectrum of a ZnCoO (5% Co) thin film with the one of ZnCoO (5% Co). The comparison shows both non-transited nanoparticles (Figure 7.39) shows both a blue-shift of more than 200 meV as well as a significant large decrease of intensity of the charge

transfer absorption band as we had previously observed in Chapters 5 and 6. This behaviour is identical to that previously observed in this thesis for gallium doped ZnCoO thin films (Chapter 5) and ZnCoO/ZnMgO MQWs (chapter 7). The fact that for nanoparticles confinement occurs in the three directions makes its effect to be larger both in energy shift and in overall reduction of the CTT intensity. While for 3.9 nm wide QWs the energy shift is 80 meV and the CTT intensity is reduced by 25-30%, for 4.7 nm NPs (see the next paragraph) the energy shift is 220 meV and the CTT intensity is reduced by 75%.

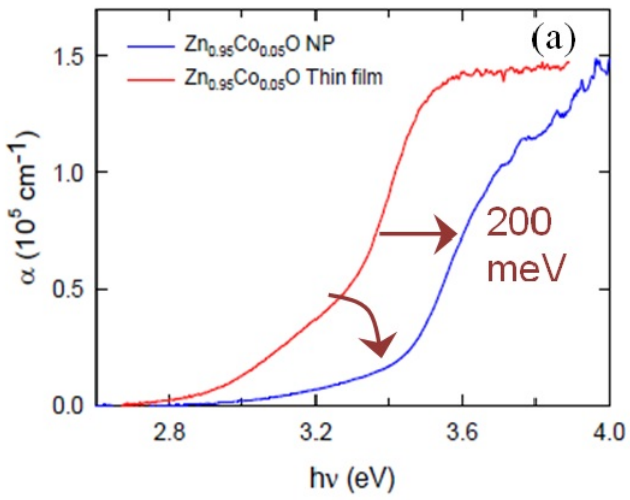

***Figure 7.39**: Absorption spectra at ambient pressure for ZnCoO thin films compared with ZnCoO nanoparticles, both materials with 5% of Co.*

We can compare with other experimental and theoretical works in the size-dependent development of bulk electronic properties in semiconductor crystallites[68]. Following the theory explained in the Chapter 2, and the fact that the structure is the same in the nanoparticles as in the thin film material, it follows that the particles molecular orbitals (MOs) evolve into Bloch MOs as size increases. Finally, we arrive to the following analytical approximation for the confinement effect:

$$E_n = \frac{\hbar^2 \mathbf{k}^2}{2m*} = \frac{\hbar^2}{2m*}\left(\frac{n\pi}{2R}\right)^2 \quad \text{with} \quad n = 1, 2, 3... \tag{7.3}$$

whose representation is:

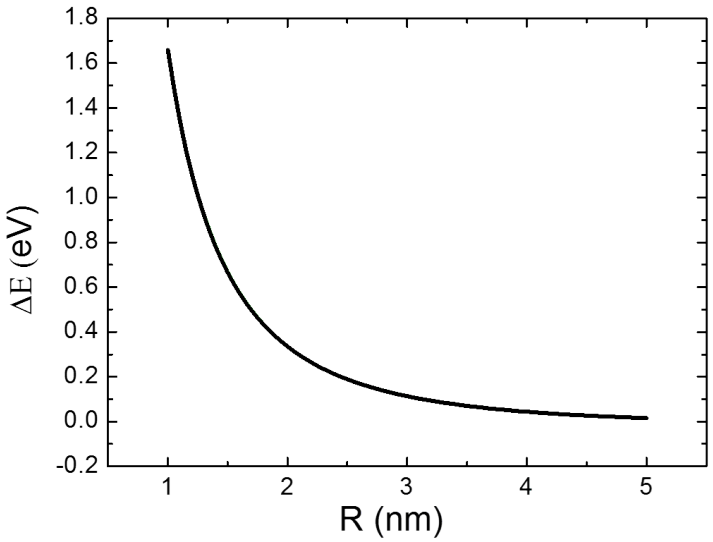

***Figure 7.40**: Confinement effect as a function of the size of the nanoparticles.*

Therefore, using the blue-shift of 220 meV of our nanoparticles into the Equation 7.3, we have a correspondence to the quantum confinement energy for nanoparticles of the order of 4.71 nm, showing that the smaller particles are those which are contributing to the spectrum and the larger are the first to have passed to the rock-salt phase.

7.5.1 TEM Analysis of recovered NP

To complete the characterization of the recovered NPs after a pressure cycle, we have tried doing electronic microscopy experiments on them. However, for carrying out this type of measurements a very thin sample is needed. We were unable to dissolve enough our nanoparticles, due to they were very compacted after measurements under pressure. Anyway, we took some images at the edges of the samples. Figures 7.41 and 7.42 are high resolution images for recovered nanoparticles of pure ZnO and ZnCoO with 5% of cobalt.

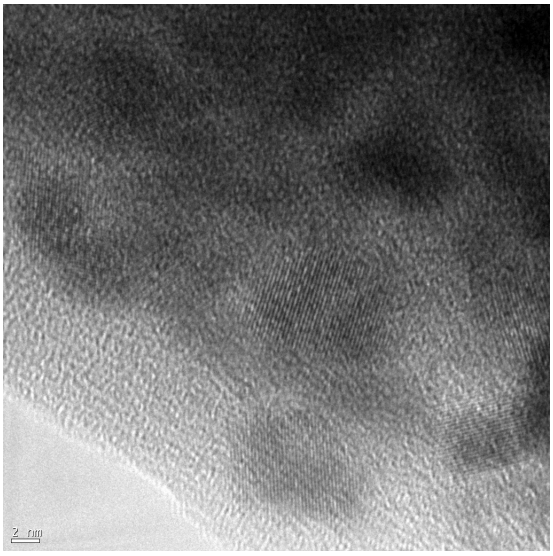

***Figure 7.41**: High resolution image for recovered nanoparticles of pure ZnO.*

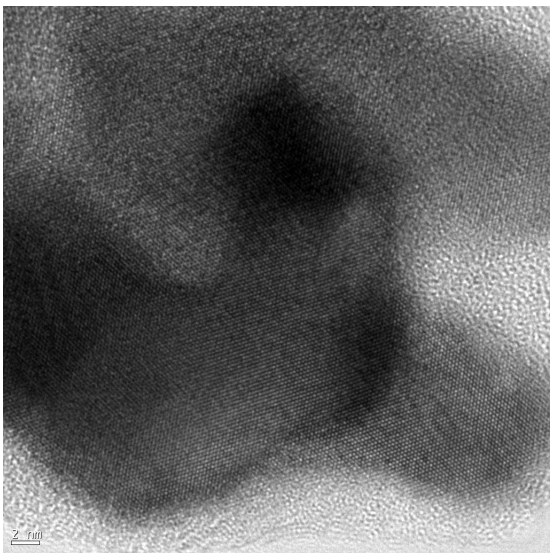

***Figure 7.42**: High resolution image for recovered ZnCoO nanoparticles with 5% of Co.*

The TEM images show how nanoparticles form aggregates overcoming even the 10 nm size (see Fig. 7.42). The analysis by FFT and EDX show that nanoparticles are indeed in the rock-salt phase. We obtain an interplanar

distance of 2.50 $\AA$ for the (111) direction of rock-salt structure, consistent with the value of 2.47 $\AA$ calculated for RS-ZnO.

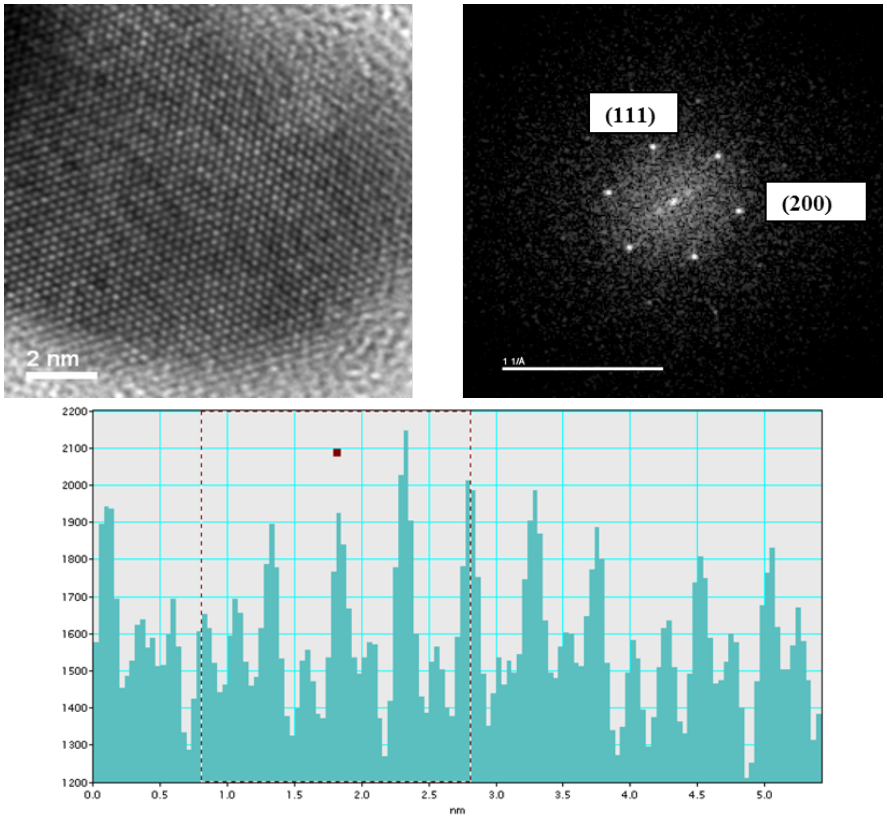

***Figure 7.43**: HR, FFT and intensity profile for non-transited ZnCoO nanoparticles with 5% of Co.*

7.5.2 Cobalt Bands and Completed Phase Transition

In this section, we will focus again on the pressure evolution of the absorption spectrum, until the pressure at which all nanoparticles have passed to the rock-salt phase. We will concentrate in the range between 1.8 to 2.4 eV, where we find the bands due to the electronic transitions at cobalt 3*d* levels. In Figure 7.44 we can see in more detail the evolution of this cobalt bands with pressure for $Zn_{1-x}Co_xO$ nanoparticles with 2, 5, 10, 20 and 30% of cobalt.

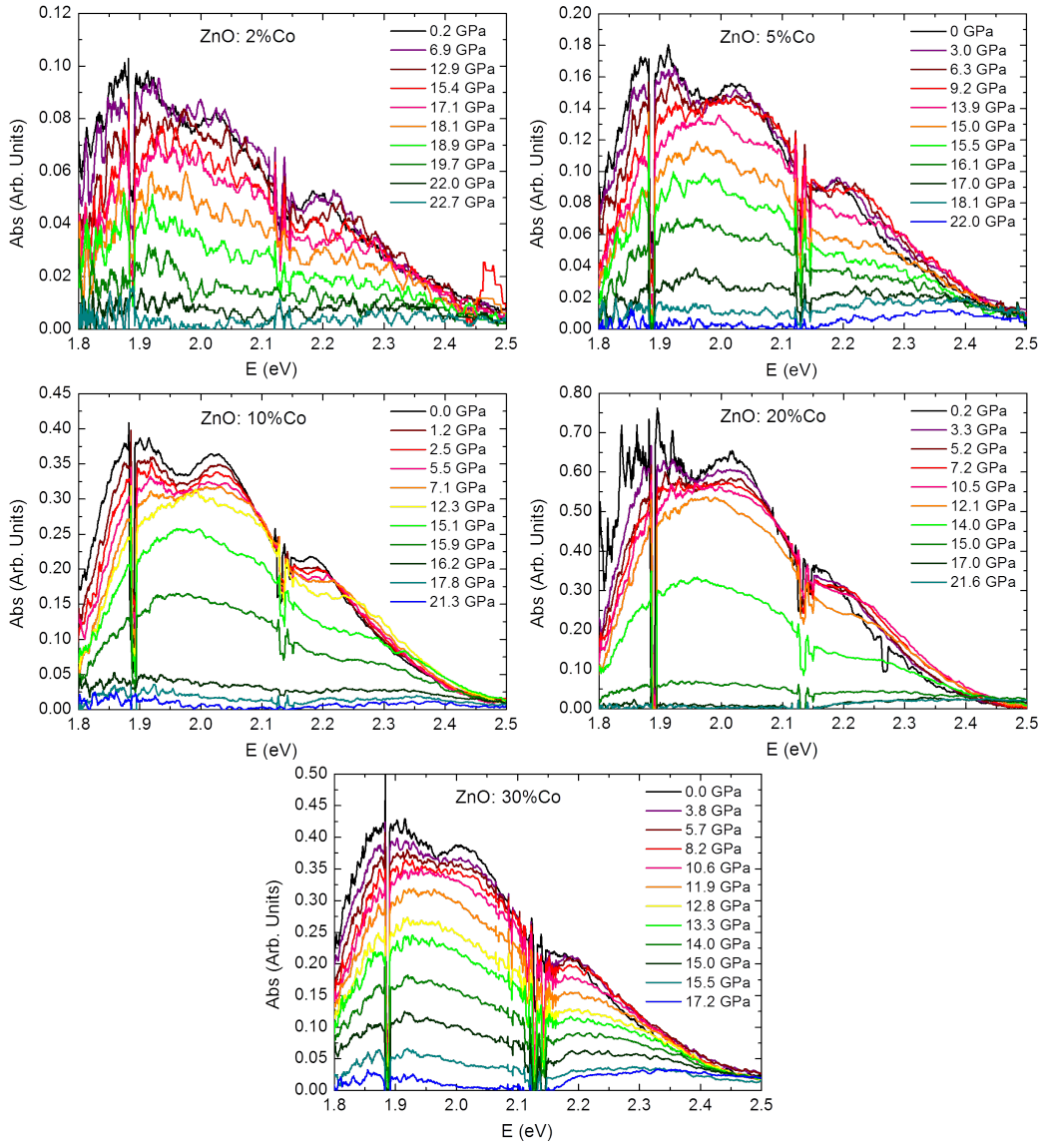

***Figure 7.44**: Spectra evolution for the Co-bands range for nanoparticles of 2, 5, 10, 20 and 30% of cobalt.*

The first effect that we can see is a small decrease in the intensity of the spectrum at low pressure ($\leq$5GPa). This is most probably due to the transition of some particles with higher cobalt content which have a lower transition pressure. As we know from the analysis of the gap of the material, the transition does not start until approximately 11 GPa (higher for the 2%Co nanoparticles). From 8 GPa until the transition begins with the decrease of the intensity of cobalt bands, a change occurs in the spectrum shape. This

is due to the fact that pressure does not affect in the same way each of the 3 peaks which compose this part of the optical spectrum. Using one of the concentrations, we can exemplify in more detail the evolution of the peaks with pressure. Figure 7.45 shows the spectrum evolution for the ZnCoO nanoparticles with 20% of Co.

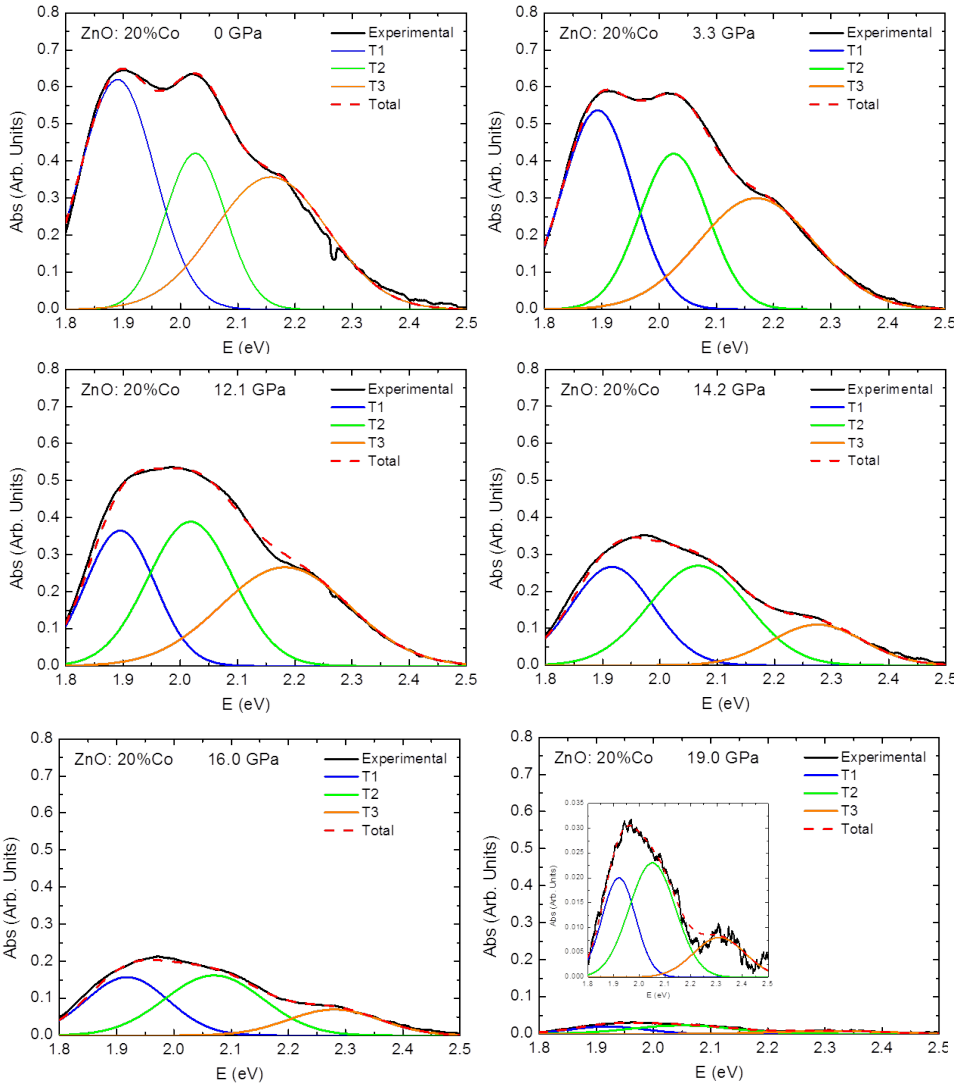

***Figure 7.45**: Detailed spectra evolution for the Co-bands range for nanoparticles of 20% of cobalt.*

A visual inspection of Figures 7.44 and 7.45 suggests that when the transition begins, the cobalt bands decrease in intensity until almost disappear. Note, however, that this evolution does not take place at the same speed

throughout the process. To see this more clearly, we represent the area enclosed by the spectrum in the range that we are working against the pressure (Figure 7.46).

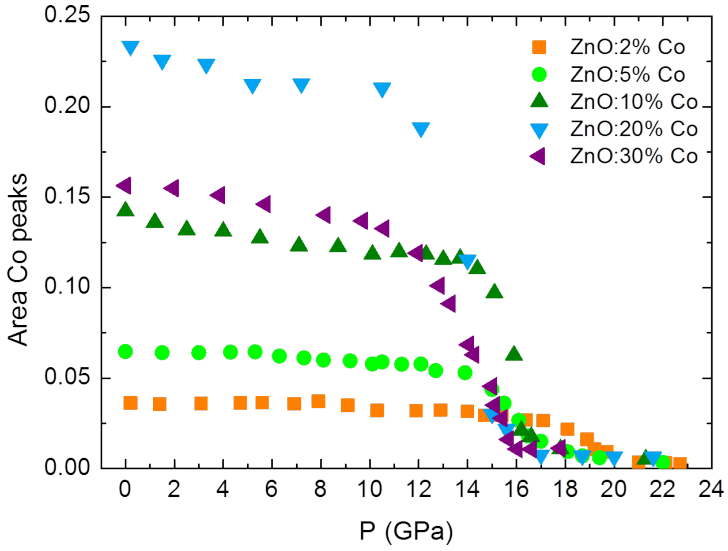

***Figure 7.46**: Area of cobalt bands in function of the pressure.*

The first difference between the materials used in this study is the intensity at ambient pressure, which depends on the content of cobalt in the sample and was already was already studied in Section 4.3.2. So, now we want to focus on the transition. We can observe that the transition has a *complementary Gauss error function* shape, i.e. the profile of the graph can be describe mathematically by the following function:

$$A = A_{max}\left\{1 - \frac{1}{P_\sigma\sqrt{2\pi}}\int_0^\infty e^{-\frac{1}{2}\left(\frac{P-P_\mu}{P_\sigma}\right)^2} dP\right\} \tag{7.4}$$

where $\mathbf{P_\mu}$ is the central pressure at which the transition occurs, $\mathbf{P_\sigma}$ is the width of the transition and $\mathbf{A_{max}}$ is the value of the cobalt bands area when the transition begins.

To facilitate the comparison of the samples, we rescale the vertical axis. Thus, we obtain the Figure 7.47, where we also show the fits of the data to the above Equation 7.4. The resulting parameters for each of the samples are shown in Table 7.6.

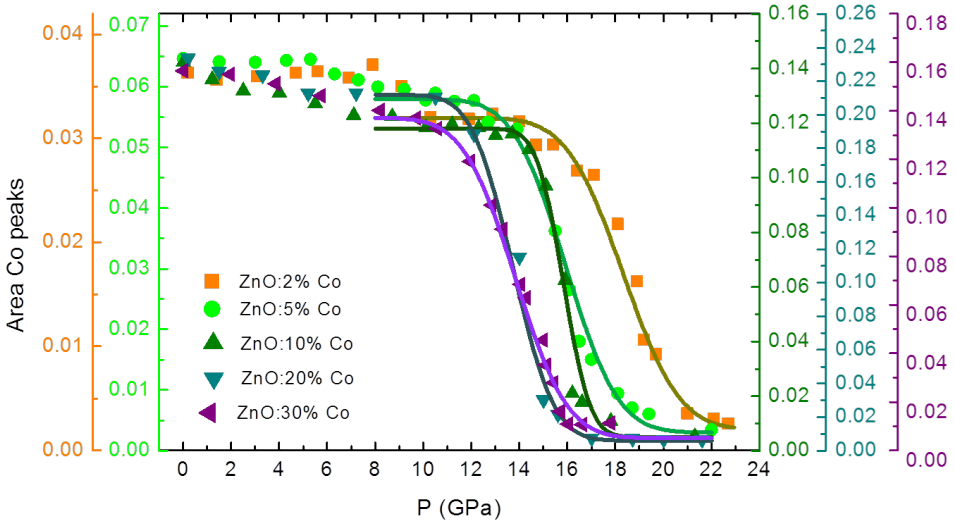

***Figure 7.47**: Area of cobalt bands as a function of the pressure. Overplotted to the data are the fitting according to the error function.*

***Table 7.6**: Parameters obtained at fitting equation 7.4 to the data.*

	P_μ(GPa)	P_σ(GPa)	A_{max}
ZnO: 2%Co	18.3	1.85	0.030
ZnO: 5%Co	15.9	1.72	0.055
ZnO: 10%Co	15.8	0.88	0.113
ZnO: 20%Co	13.7	1.35	0.206
ZnO: 30%Co	13.8	1.70	0.130

Let's summarize what we have obtained so far. On the one hand, using the incomplete transition experiments under pressure and the resulting confinement effects, we have concluded that the larger particles are the first to transit to the rock-salt phase. On the other hand, from the microscopic analysis, we established that the $Zn_{1-x}Co_xO$ nanoparticles have a Gaussian distribution with respect to their size.

Mathematically, there is a direct link between the Gaussian function (which describes the size distribution of the nanoparticles) and the error function that we have used to describe the transition of the nanoparticles. It is straight forward then, following the Equation 7.5 connect the parameters that define the two functions.

Using:

$$P_\sigma = \alpha_\sigma size_\sigma \tag{7.5}$$
$$P_\mu = \alpha_\mu size_\mu \tag{7.6}$$

introduced in equation 7.4 and develop:

$$A = A_{max}\left\{1 - \frac{1}{\alpha_\sigma size_\sigma\sqrt{2\pi}}\int_0^\infty e^{-\frac{1}{2}\left(\frac{\alpha_\mu^2}{\alpha_\sigma^2}\frac{size-size_\mu}{size_\sigma}\right)^2}\alpha_\mu dsize\right\} \tag{7.7}$$

Finally, we get:

$$A = A_{max}\left\{1 - \frac{1}{\alpha}e^{-(\alpha)^2}\int_0^\infty N(size)d(size)\right\} \tag{7.8}$$

where $\alpha = \alpha_\mu/\alpha_\sigma$.

The Equation 7.8 shows that effectively there is a direct relation between the intensity of the cobalt band and the size of the nanoparticles during the wurtzite-to-rocksalt transition. Again, this supports the hypothesis that the $Zn_{1-x}Co_xO$ nanoparticles gradually transit from the largest to the smallest size. To establish a numerical relation (i.e. to calculate the parameters α, α_σ and α_μ) more experiments should be conducted. Moreover, there should be a more comprehensive study of microscopy to improve the size distributions and complete all cobalt concentrations that are available. This would be a good future work to complete the characterization of this material.

7.6 XANES

Figure 7.48 compares the XANES (X-ray Absorption Near-Edge Structure) spectra of ZnCoO and CoO nanoparticles to the one of a pure wurtzite $Zn_{0.7}Co_{0.3}O$ thin film. The main features of pure wurtzite structure (Co in tetrahedral coordination) are: *i)* A well defined pre-edge peak (A), *ii)* A white line (B) whose intensity is about 50% larger than the absorption step at the K-edge, iii) Three well defined structures (C, D, E) above the Co K-edge. Most NP spectra shown in Fig. 7.48 reveal the presence of a large content of octahedrally coordinated Co (as expected in *RS*-ZnCoO), as indicated by the low intensity of the pre-edge peak, the larger intensity of the white line (close to the double of the absorption step in the edge) and a

smearing of peaks C, D and E. It is important to notice, as we will discuss below, that all the other characterization techniques are far less sensitive to octahedrally coordinated Co, due to the inversion symmetry that strongly reduce the intensity of optical transitions and Raman effect. The fact that it was neither observed in STEM and X-ray diffraction suggest that most octahedrally coordinated Co must be in the form of very small nanoparticles.

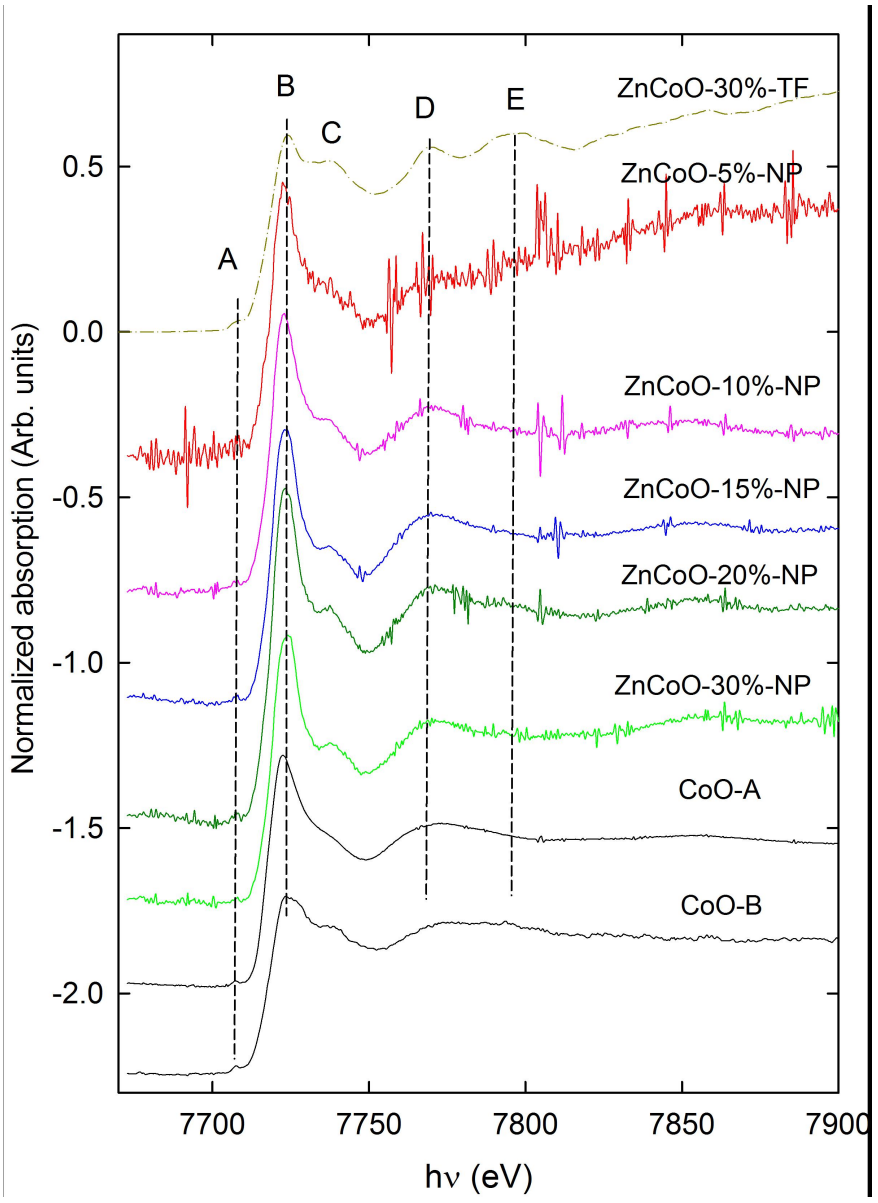

***Figure 7.48**: XAS results on ZnCoO nanoparticles.*

7.7 Conclusions

In this part of the work measurements of optical absorption have been made under pressure for nanoparticles of ZnO:Co with proportions of 0%, 1%, 2%, 5%, 10%, 20% and 30% of cobalt. These measurements have allowed us to establish the evolution of several phenomena by changing the pressure and the differences between the samples due to the varying cobalt concentration.

- We have found that the absorption bands that appear around 2 eV, due to electronic transitions in the tetrahedral crystal-field split Co 3d levels, increase linearly with increasing cobalt content.
- During the process of increasing the pressure, a first range of pressures is identified in which there are a monotonic evolution of the absorption spectra of the samples. In this range, the absorption edge moves almost parallel toward higher energies and the intensity of the d-d* absorptions bands decreases slightly. The charge transfer absorption band also shifts toward higher energies with increasing pressure with small changes in intensity.
- At higher pressure, a material transition occurs from the wurtzite phase to the rock-salt one causing drastic changes in the absorption spectrum. The absorption edge undergoes a change in shape, moving at much higher energies and having a smoother dependence with the photon energy. The cobalt band intensity decreases abruptly, disappearing for the samples with low concentration. We observe an absorption band much less intense at energies around 2.5 eV. Although the transition is fast, it is gradual. So, some of nanoparticles remain in the wurtzite phase up to pressures above 17 GPa.
- After rising to the high pressure and induce the phase transition, the system remains metastable relaxing the pressure. We know by RX-diffraction measurements that this phase has the NaCl structure. For this reason, the displacement of the absorption edge was studied over the entire range of pressures. Therefore, in this chapter, the optical absorption edge has been studied in two different crystalline phases, in a very wide range of pressure (ambient pressure up to 15 GPa).
- It is worth noting the different behaviour of the nanoparticles respect to the thin layers. In the thin films, the phase transition is reversible until Co concentrations reach between 15 and 20%, while in the nanoparticles, the RS-phase remains metastable even even for pure ZnO.

- Measurements have also been done under pressure without reaching the pressure at which all nanoparticles have transited to the RS-phase. With these results, and comparing with another configuration of the same material, we have concluded that for the non-transited nanoparticles there is a clear effect of quantum confinement. Therefore, the smaller particles are those which are contributing to the spectrum and the larger are the first to have passed to rock-salt phase. It has also been seen that the behaviour due to confinement of the nanoparticles is similar to that previously observed in the gallium doped layers.

- The confinement effect shown by the nanoparticles, along with the relation between the evolution of the spectra during the transition and the size distribution of the nanoparticles, provides that, by subjecting the nanoparticles under pressure, they pass from wurtzite phase to rock-salt structure by size, from largest to smaller.

Chapter 8

Resumen en español

8.1 Introducción

8.1.1 Motivación

Hay muchas razones para justificar una tesis sobre semiconductores. Es importante conocer estos materiales para mejorar su fabricación como para ampliar el conocimiento de su estructura y propiedades físicas. El interés por los semiconductores no es puramente teórico, de hecho, estos materiales son conocidos por sus aplicaciones, principalmente tecnológicas. En esta introducción, voy a comenzar por lo básico, definiendo qué es un semiconductor y viendo como se ha ido introduciendo el uso de estos materiales y porqué son de tanta utilidad. En el siguiente apartado, además, veremos aplicaciones inmediatas ya estudiadas o puestas en marcha para el caso concreto del ZnO y sus derivados. Y, por último, haremos una explicación más técnica del material en sí mismo.

Por definición[3], un *semiconductor* es una sustancia aislante que se transforma en conductor por la adición de determinadas impurezas. También se describe como un elemento o compuesto que se comporta como un conductor o como un aislante dependiendo de varios factores como, por ejemplo, el campo eléctrico o magnético, la presión, la radiación que le incide o la temperatura a la que se encuentre.

Partiendo de la teoría de bandas, que es la base para el estudio la estructura electrónica de los sólidos, definimos la banda prohibida o gap como la diferencia de energía entre el mínimo de la banda de conducción y el máximo de la banda de valencia. Un semiconductor se define como un material con una banda prohibida o gap no nula, con valor comprendido entre unas pocas decenas de meV y unos pocos eV. Desde el punto de vista de sus propiedades

eléctricas, y como consecuencia de esa estructura electrónica, un semiconductor se puede definir como un material con una resistividad eléctrica situada en el intervalo entre 10^{-2} y 10^{9} ohm·cm.

Aunque algunos autores consideran a los materiales con un gap mayor a 3 eV como aislantes, el límite superior del gap en la definición de semiconductor depende de la posibilidad de que un determinado material pueda doparse o pueda usarse como base para fabricar dispositivos electrónicos semiconductores. La familia de los semiconductores forma una de las más versátiles clases de materiales conocidos. De hecho, éstos se pueden encontrar con muchas composiciones químicas diferentes y con una gran variedad de estructuras cristalinas.

Leyendo los estudios sobre semiconductores es fácil percatarse de que todos coinciden en que los grandes avances de la electrónica del estado sólido han sido posibles a la evolución en la obtención de cristales semiconductores en distintas configuraciones (monocristales, láminas delgadas, nanopartículas...), basados en variedad de elementos y compuestos.

Actualmente, por ejemplo, se ha generalizado el comercio de diodos emisores de luz con longitudes de onda larga basados en la tecnología del arseniuro de galio (GaAs). Pero el desarrollo de semiconductores de gap ancho abriría las puertas al progreso de dispositivos optoelectrónicos emisores en todo el rango de longitudes de onda.

Para los dispositivos ópticos de onda corta, se considera a los nitruros, especialmente el GaN, como los materiales más prometedores. Pero la obtención de capas de GaN de buena calidad está limitada por la escasa disponibilidad de sustratos[4]. Esto llevó al renacimiento del interés en el estudio del óxido de zinc (ZnO), un semiconductor de gap ancho y de sus aleaciones con otros óxidos de metales divalentes que dan lugar a gran familia de materiales con estructura wurtzita. De hecho, las nanoestructuras de óxido de zinc son materiales tecnológicos de gran importancia debido a las aplicaciones que ofrecen para células solares, sensores de gas, varistores, pinturas, cerámica, cosméticos[5], diodos láser[6] y sensores[7].

El ZnO también presenta una gran compatibilidad a la hora de formar compuestos ternarios. De esta manera, llegamos a los *semiconductores magnéticos diluidos* o *DMS* (Diluted Magnetic Semiconductor). Éstos se caracterizan por la sustitución de cierta proporción del catión del semiconductor por iones magnéticos variando así las propiedades del material base.

Resumiendo, las características físicas del ZnO junto a un proceso de crecimiento sencillo, rápido y económico, que no requiere de grandes y complicadas infraestructuras, propician la obtención de un material semiconductor de buena calidad con un coste bajo. Además, la compatibilidad con otros

elementos para el crecimiento de compuestos ternarios y de dopaje, ofrecen una gran variedad en las posibilidades de este material. Es decir, la incorporación controlada de iones en la red del ZnO permite el control de los parámetros físicos, electrónicos y las propiedades ópticas de los compuestos, lo que beneficia la fabricación de dispositivos específicos.

Al sustituir una parte del Zn por otros iones divalentes (aleaciones) o trivalentes (dopado), se obtienen nuevos materiales de los cuales se requiere un estudio de su estructura y de sus propiedades ópticas, magnéticas, electrónicas... De esta forma se puede determinar la calidad del material y sus características físicas en función de las concentraciones de los iones incorporados y, en última instancia, sus aplicaciones.

Cambiando de configuración morfológica a escala nanométrica, los efectos de confinamiento cuántico en nanopartículas semiconductoras son conocidos debido a que sus propiedades ópticas y eléctricas son significativamente diferentes a las de los materiales masivos, o estructurados a escala micrométrica. Además aparecen fases metaestables únicamente observadas en los configuraciones nanométricas[8]. Las nanopartículas semiconductoras son interesantes debido a sus aspectos básicos, así como sus aplicaciones en dispositivos. También prometen tener una enorme y versátil utilidad como marcadores biológicos[9], aplicaciones en ciencias de la salud y en energías renovables[10][11].

Por lo tanto, esta tesis se orienta al estudio de algunos DMSs basados en el ZnO para así aportar un mayor entendimiento y variedad de propiedades a este amplio campo con tanta utilidad en la actualidad. Particularmente, en este trabajo estudiaremos láminas delgadas de ZnCoO, ZnCoGaO, ZnMgO y ZnMgCoO con distintas concentraciones de los iones, así como nanopartículas de ZnCoO (para distintas concentraciones de cobalto) y, comenzaremos la caracterización de multicapas de ZnMgO/ZnCoO. Para ello se han realizado medidas con gran variedad de técnicas como microscopia electrónica de barrido (SEM), espectroscopia RAMAN e infrarroja, absorción óptica, medidas de transporte y resistividad y medidas magnéticas. Varias de estas experiencias, además, se han realizado a baja y/o a alta temperatura o a alta presión, con las técnicas que se describen en el capítulo de métodos experimentales.

8.1.2 Aplicaciones

Como ya hemos comentado, la principal aplicación de los semiconductores basados en el ZnO es la optoelectrónica debido a su ancho gap de 3.3 eV a temperatura ambiente y a sus extraordinarias propiedades ópticas. Por estas razones podría ser una alternativa al GaN, que se utiliza para la producción

de emisores de luz blanca, verde o UV, dada la mejor calidad de los cristales de ZnO y por ser mucho más simple y, por tanto, mucho más económica la técnica de preparación del material y de fabricación de dispositivos basados en el ZnO.

Como semiconductor de gap ancho, se han producido avances prometedores en la ingeniería del ZnO. El gap de energía es ajustable desde 2.8 a 3.3 eV introduciendo cadmio o desde 3.3 a 4 eV introduciendo magnesio en el material. Lo cual mejora aun más la gama de detectores de UV para el control de la calidad del aire, la detección de gas, aplicaciones militares... La respuesta de estos materiales depende de varios factores como el grosor, el tamaño de grano, la orientación, el dopado, etc. Controlando principalmente el crecimiento, como puede ser de los nanohilos, se controlan otras propiedades, lo que facilita la fabricación de micro y nano dispositivos con un importante papel químico en los sensores. En el trabajo de Kar et al.[12], describen en detenimiento el control en el crecimiento de estos nanohilos y la fabricación de fotodetectores de UV basados en éstos.

La energía de ionización del excitón 60 meV permite la generación de excitones tanto a temperatura ambiente como a altas temperaturas, lo que implica la utilización del ZnO en láseres en un gran rango de temperaturas.

Dopando el ZnO y controlando el nivel de dopaje, las propiedades eléctricas pueden ser cambiadas de forma que se puede pasar de un semiconductor tipo n a un metal, manteniendo invariable la transparencia óptica lo cuál es muy útil para la fabricación de electrodos transparentes para paneles y células solares[10].

Según Dietl et al[13] también es un candidato prometedor para las aplicaciones espintrónicas. Estos autores predicen una temperatura de Curie < 300 K para el ZnO dopado con Mn. También se ha predicho un comportamiento ferromagnético con estabilidad a alta temperatura de Curie en ZnO dopado con hierro, cobalto y níquel. Aunque hay publicaciones que confirman estas predicciones, existe cierta controversia[7][14].

También se están realizando investigaciones acerca de las heteroestructuras de ZnCdO y ZnMgO para la fabricación de células fotoelectroquímicas[15] en el campo de las energías limpias. El ZnMgO se usa en estructuras de pozo cuántico en forma de multicapas de ZnMgO/ZnO/ZnMgO asegurando un confinamiento de cargas en el ZnO. Siendo que la fabricación de estos materiales es fácil y asequible, es lógico incorporarlos a la nueva generación de dispositivos para la obtención de energías limpias.

Rout et al[16] han demostrado que las nanopartículas de ZnO impregnadas con Pt y/o dopadas con Co muestran una muy buena sensibilidad para el H_2 a relativa baja temperatura. Los sensores de nanopartículas de ZnO

son estables durante varios ciclos de largos periodos de tiempo, demostrando así su utilidad práctica como sensores de H_2. Finalmente, Y.-z. Lv et al[17] comprobaron que las nanobarras de ZnO bien cristalizadas tienen una mayor sensibilidad y selectividad para detectar bajas concentraciones de gases de etanol, benzeno, tolueno y acetona a temperaturas de 150ºC.

8.2 Conclusiones

8.2.1 Láminas delgadas de ZnO y ZnCoO

En el primer capítulo de resultados nos centramos en el estudio de láminas delgadas de ZnO puro y $Zn_{1-x}Co_xO$ con diferentes concentraciones de cobalto, crecidas sobre distintos tipos de sustrato.

En primer lugar mostramos algunas imágenes de microscopía, en las que se observan que las muestras tienen superficies homogéneas y compactas, aunque con pequeños cristales (agregados granulares en el caso del 20% de Co y cristales incrustrados para el 30% de Co). Estos resultados son similares a trabajos anteriores que emplearon la misma técnica para la preparación de las láminas delgadas.

En segundo lugar, se han estudiado las propiedades ópticas del material, tanto a temperatura ambiente para diferentes concentraciones de Co (entre 0% y 30%) como a baja temperatura para dos muestras, una con baja concentración y otra con alto contenido de Co.

Hemos podido confirmar los tres efectos principales que se producen al introducir cobalto en el ZnO:

1. La banda de absorción fundamental (transición de banda a banda) se desplaza hacia energías más altas. El correspondiente desplazamiento del pico del excitón viene acompañado de un rápido aumento en su anchura, debido al desorden en la aleación, de tal manera que el excitón y sus réplicas no son observables para concentraciones de cobalto mayores al 5%.

2. Aparece una banda de absorción intensa por debajo del umbral de absorción fundamental, cuya intensidad aumenta conforme se incrementa el contenido de cobalto. Esta banda corresponde a la transición de transferencia de carga (CTT) desde el estado fundamental de la capa $3d$ del cobalto a la banda de conducción. El máximo de la CTT se desplaza a mayores energía para mayores concentraciones de Co, y su anchura también aumenta.

3. Se observa una estructura más compleja entre 1.7 y 2.3 eV cuya intensidad es proporcional al contenido de Co. Estas bandas están asociadas a las transiciones desde el estado fundamental a estados excitados de la capa Co^{+2} $3d^7$ desdoblada por el campo cristalino tetraédrico.

Este trabajo se ha centrado en un estudio detallado de la CTT, mediante el estudio de su energía de inicio, intensidad y anchura como una función del contenido de Co, la temperatura y la polarización. Este estudio ha proporcionado las siguientes conclusiones:

- La CTT es una transición de un estado localizado a uno extendido. El estado inicial es el estado fundamental de la capa Co $3d$ en el campo cristalino tetraédrico. El estado final es la banda de conducción de la aleación ZnCoO.

- La forma y la anchura de la banda CTT corresponde mejor a un estado inicial con una función de ondas de tipo gaussiano que con una de tipo hidrogenoide.

- El umbral de absorción de la banda CTT muestra una dependencia en $(\hbar\omega\text{-}\mathrm{E}_i)^{3/2}$ respecto a la energía de los fotones, a partir de la cual es posible determinar el umbral de energía E_i. Por extrapolación de la gráfica $\alpha^{2/3}$ obtenemos $\mathrm{E}_i = 2.8$ eV para bajas concentraciones de Co (alrededor del 2.5%).

- A partir de las energías del umbral E_i y del máximo de la CTT es posible obtener la energía de localización del estado fundamental. Se define como la energía cinética correspondiente a un vector de ondas igual a la inversa del parámetro de localización gausiano. La energía de localización es del orden de 0.6 eV, que corresponde a un parámetro de localización de unos 0.5 nm.

- Para mayores concentraciones de cobalto, aunque el máximo de la CTT se desplaza a energías más altas, como ocurre con el frente de absorción fundamental de la aleación, se observa un comportamiento no lineal, tanto para su anchura como para su intensidad. Esto indica que debe haber efectos asociados a la interacción entre los átomos de Co en posición de segundos vecinos. Esto es de esperar porque la distancia de localización del estado fundamental de la capa $3d$ del Co es ligeramente mayor que el parámetro a (distancia típica entre segundos vecinos). Esta interacción entre segundos vecinos, en pares aislados o grupos más grandes, debe afectar a la energía y a la función de ondas de

localización, respecto al 3d Co aislado, dando lugar a una distribución de umbrales de energía y de anchuras.

- Los experimentos a baja temperatura indican una disminución de la energía y un aumento de la anchura tanto para el gap como para la CTT al aumentar la temperatura.

- Hemos discutido y explicado la aparente contradicción entre nuestros resultados y los resultados de fotoconductividad, que sitúan el estado excitado del nivel Co $3d$ en resonancia con el mínimo de la banda de conducción a bajas concentraciones de Co. Esto colocaría el estado fundamental de los niveles $3d$ del Co 1.8 eV por debajo del mínimo de la banda de conducción, lo que indicaría que el umbral de la CTT debe estar a 1.8 eV, casi 1 eV por debajo del valor de E_i=2.8 eV. La discrepancia aparente se resuelve teniendo en cuenta que el CTT implica una ionización interna de la capa $3d$ Co, desde el estado de la configuración estequiométrica doblemente ionizada (Co $3d^7)^{+2}$ a la configuración triplemente ionizada (Co $3d^6)^{+3}$. La diferencia de 1 eV correspondería a la diferencia de energía de configuración entre los dos estados de ionización.

- Las láminas delgadas crecidas sobre zafiro-R han permitido una investigación de la anisotropía de la CTT. No se ha detectado desplazamiento de energía entre la polarización paralela y la perpendicualar al eje c de la wurtzita. Sin embargo, se observa sistemáticamente y con independencia de la concentración de Co una intensidad de absorción mayor para la polarización perpendicular al eje c.

- En cuanto a los picos de absorción excitónicos en el umbral de absorción, se observa una disminución de la diferencia de energía entre el excitón-C (polarización paralela al eje c) y el excitón A-B (polarización perpendicular al eje c), conforme aumenta la concentración de Co. Dado que se espera que el campo de anisotropía cristalina aumente a medida que aumente el contenido de cobalto, la disminución observada es muy probablemente debida a algún desorden en la orientación del eje c en los cristalitos que forman la lámina delgada.

- Finalmente, se han llevado a cabo medidas de dispersión Raman en láminas delgadas de ZnCoO crecidas sobre sustratos de mica y de zafiro. Aunque los fonones más característico del ZnO (E_2 "alto" y "bajo") se observan en la aleación, el desorden de aleación rompe parcialmente la simetría de la wurtzita y da lugar a la aparición de picos Raman asociados a los máximos de la densidad total de estados de fonones.

8.2.2 Láminas delgadas de ZnCoGaO

- Hemos preparado láminas delgadas de ZnCoO dopadas con Ga con el fin de estudiar el efecto de los electrones libres en los propiedades ópticas relacionadas con el cobalto.
- Las imágenes SEM de las láminas delgadas muestras una superficie lisa y homogénea con la presencia de algunos agregados.
- Hemos llevado a cabo medidas de transporte a temperatura ambiente para distintas concentraciones de Ga en láminas delgadas de ZnCoGaO con 5% de cobalto. La concentración de electrones aumenta con el contenido de Ga indicando así que el Ga también es un dador en las láminas delgadas de ZnCoO.
- La concentración de electrones es menor que la concentración nominal de Ga, como también se observaba en el ZnO dopado con Ga. En el ZnO, este efecto se demostró que está relacionado con la presencia de Ga totalmente oxidado en configuración octaédrica, probablemente en nanocristales de óxido Ga_2O_3 o espinelas como $ZnGa_2O_4$.
- La movilidad de los electrones muestra una notable falta de sensibilidad al desorden de la aleación. Se han observado movilidades de electrones de hasta 35-37 cm^2/Vs, comparables, e incluso superiores, a las medidas en ZnO dopado con Ga. Esto podría estar relacionado con el hecho de que la interacción entre O $2p$ y Co $3d$, que debería ser la contribución predominante del desorden de la aleación, afecta principalmente a la banda de valencia.
- Existe un patrón de comportamiento en la movilidad de los electrones. Ésta tiende a ser mayor para mayores concentraciones de electrones libres. Las propiedades de transporte parecen estar controladas por el por las barreras de potencial de las juntas de grano cuya altura se hace menor cuando la concentración de electrones aumenta.
- El comportamiento de las propiedades de transporte, en función de la temperatura y bajo alta presión, puede ser explicada por los mismos mecanismos de transporte mencionados (barreras de junta de grano).
- A partir de las medidas de reflectividad infrarroja de las muestras recién crecidas se observa que la estructura de reflexión de plasma es visible, así como una tendencia del mínimo de reflexión que se desplaza a menores números de onda conforme la concentración de electrones disminuye.

- La pasivación de los dadores de Ga, asociada a la oxidación completa de los átomos de galio, se observa en el recocido en aire y se detecta tanto en las medidas de transporte como en los espectros de reflectividad FTIR. El mínimo de la reflexión de plasma se desplaza a frecuencias más bajas conforme la temperatura de recocido aumenta. Las láminas delgadas de ZnCoO:Ga básicamente se comportan como láminas delgadas de ZnO puro: la concentración de portadores puede ser controlada mediante el tratamiento térmico. Para las láminas delgadas de ZnCoO dopadas con Ga la concentración de portadores a temperatura ambiente disminuye a medida que aumenta la temperatura de recocido. La energía de activación del proceso es de aproximadamente 1.3 eV.

- El efecto de dopado con Ga en las propiedades ópticas se ha estudiado tanto en las muestras con diferente concentración de cobalto (5, 20 y 30% de Co) como con distinto contenido de Ga (de 0.1 a 2.5% de Ga) y, más específicamente las muestras de ZnCoO:Ga con 5% de Co y 2.5% de Ga recocidas en aire, en la que la concentración de electrones puede ser controlada de una manera más continua. A medida que aumenta la densidad de electrones, la absorción fundamental se desplaza hacia altas energías. El desplazamiento del gap es debido al desplazamiento del nivel de Fermi, ya que es el origen del efecto Burstein-Moss.

- El aumento de la concentración de electrones en las láminas delgadas de ZnCoO conduce al esperado corrimiento al azul del gap óptico de la aleación (desplazamiento Burstein-Moss). Lo más interesante son los dos efectos que se observan en la CTT: *1)* hay un claro desplazamiento hacia mayores energías de la CTT, prácticamente igual al desplazamiento del nivel de Fermi, como se espera del desplazamiento a altas energías de los estados finales vacíos como el llenado de la banda de conducción con eletrones libres y, *2)* hay una pronunciada disminución en la intensidad de la banda. Esto puede ser explicado por la dependencia en k del elemento de matriz dipolar de la CTT, que tiene una dependencia gausiana con el vector k. Las energías más altas de los estados finales en la banda de conducción también corresponden a un mayor vector de ondas y, por tanto, a valores más bajos del elemento de matriz y una menor intensidad de absorción. La dependencia exponencial del coeficiente de absorción de la energía cinética del electrón explica la disminución exponencial de la intensidad de la CTT así como los cambios de energía del nivel de Fermi a energías más altas.

- En resumen, hemos demostrado cómo la banda CTT puede ser descrita consistentemente como una transición óptica de estados localizados a

estados extendidos.

- También hemos estudiado las propiedades ópticas y de transporte de las láminas delgadas de ZnCoO dopadas con Ga a baja temperatura. Hay una tendencia en la temperatura de la resistividad para todas las muestras. La resistividad disminuye entre 300 K y T_m y luego aumenta entre T_m y baja temperatura. Tomando por razonable el supuesto de que la mayoría de las muestras son degeneradas y entonces la concentración de electrones es constante, la evolución de la resistividad se explica por la dependencia con la temperatura de la movilidad efectiva de los electrones. Entre 300 K y T_m, la movilidad de los electrones aumenta ligeramente a medida que el número de fonones disminuye. Por debajo de T_m, la movilidad disminuye, lo que indica que la dispersión de impurezas pasa a ser dominante o que menos electrones pueden superar las barreras de potencial. El hecho de que T_m disminuya conforme aumenta la concentración de Ga indica que el efecto de barrera se vuelve menos determinante a medida que la concentración de electrones aumenta.

- Algunas muestras con menos concentración de electrones, por debajo del límite de degeneración, muestran una mayore dependencia con la temperatura de la resistividad, con un comportamiento activado (unos 50 meV de energía de activación) por encima de 100 K. El transporte en este caso está dominado por la ionización de los dadores. Sus propiedades ópticas también reflejan este comportamiento. A baja temperatura, a medida que los portadores libres pasan a ocupar los los niveles dadores localizados por los niveles dadores, junto con el aumento esperado del gap, se observa un aumento de la intensidad de la CTT, con una disminución de su anchura, consistentemente con la fuerte reducción de concentración de portadores libres en la banda de conducción.

- Hemos realizado medidas de resistividad y FTIR bajo presión. En los espectros de transmisión IR de las láminas de ZnCoO:Ga (5%Co, 1%Ga) hasta 8 GPa vemos que el rango de opacidad (determinado por la frecuencia de plasma) no cambia prácticamente indicando que la frecuencia de plasma permanece casi constante.

- Las medidas de resistividad bajo presión se han hecho para láminas delgadas ce ZnCoO:Ga con 5% de Co y distintas concentraciones de Ga. Para el 0.25% y el 2.5% de Ga la concentración de electrones es constante y la movilidad de los electrones disminuye ligeramente bajo

presión. Hay un aumento monótono de la resistividad bajo presión además de un aumento del valor absoluto de la pendiente de la resistividad en función de T.

- Para completar la caracterización de estas muestras, hemos realizado medidas de espectroscopía Raman. Hay algunos defectos debido al dopado con Ga. La banda de densidad de estados (500-600 cm^{-1}) se incrementa debido al desorden suplementario introducido por el galio sustitucional y el galio segregado. Se observa una nueva banda pequeña alrededor de 631 cm^{-1} que se correlaciona con el contenido de Ga y puede asociarse a algún modo local relacionado con el Ga. El acoplamiento plasmón-LO se evidencia por el hecho de que los modos LO no son observados para grandes concentraciones de electrones, para los cuales el modo acoplado L^+ tiene la frecuencia de plasmón que es en principio mucho mayor que la de los modos fonónicos. Para una de las muestras, con 0.1% de Ga y con una concentración de electronces cercana a los $5{\cdot}10^{18}$ cm^{-3}, se observan dos modos que se corresponden razonablemente a los modos acoplados plasmón-LO L^- (320 cm^{-1}) y L^+ (720 cm^{-1}).

- Por último, se ha observado alguna evidencia preliminar de comportamiento ferromagnético asociado al dopado con Ga en la investigación de las propiedades magnéticas. Mientras que las láminas delgadas de ZnCoO presentan sistemáticamente un comportamiento paramagnético claro, con signos de acoplamiento antiferromagnético entre átomos de Co en posiciones de segundos vecinos, al dopar con Ga, aparecen evidencias de comportamiento ferromagnético tanto en la dependencia en temperatura de la susceptibilidad magnética, así como en los ciclos de histéresis medidos a baja temperatura.

8.2.3 Láminas delgadas de ZnMgO y ZnMgCoO

- Hemos estudiado las propiedades ópticas en condiciones ambientales de láminas delgadas de ZnMgO para diferentes concentraciones de Mg. El efecto de la aleación con Mg en el gap es un desplazamiento a energías más altas. El gap aumenta casi linealmente con la proporción nominal de Mg con una tasa de aproximadamente 35 meV/% Mg. La tasa de incremento del gap es mayor que lo observado por otros autores, indicando que la proporción de Mg en las láminas es mayor que la proporción nominal en el blanco con que se crecieron. La intensidad del pico excitónico disminuye con el aumento de contenido en Mg debido al aumento del desorden en la aleación.

- Hemos estudiado la evolución con la temperatura de los espectros de absorción de láminas delgadas de ZnMgO con 5, 10 y 15% de Mg. Sólo en la muestra del 5% se hacen claramente visibles los picos excitónicos y su resonancias ex-LO a bajas temperaturas. La dependencia del gap con la temperatura, para las tres muestras, puede ser explicada por el modelo de Bose-Einstein. La temperatura efectiva obtenida se aproxima a la hallada para el ZnO. En las láminas delgadas del 10 y el 15% de Mg el aumento de la anchura de la transición y su escasa sensibilidad a la temperatura indican una fuerte contribución de la dispersión por potencial localizado (dispersión por potencial de aleación).

- En lo que respecta al comportamiento de la anisotropía óptica en láminas delgadas de ZnMgO depositadas sobre zafiro-R, éste es similar al de las láminas de ZnCoO. En ambos casos se espera que la anisotropía del campo cristalino aumente, pero la diferencia de energía entre el excitón-C y el excitón A-B parece disminuir. Atribuimos este efecto a un desorden en la orientación del eje c en los cristalitos de la capa delgada.

- También hemos estudiado láminas delgadas de la aleación semiconductora (Zn,Mg,Co)O. La incorporación de cobalto se evidencia por la presencia de las bandas de absorción de los niveles $3d-3d^*$ del Co y la banda CTT mientras que el aumento del gap es relativamente pequeño con respecto a las láminas delgadas de ZnCoO. Esto sugiere que existe algún tipo de incompatibilidad en la incorporación simultánea de Co y Mg cuando las láminas delgadas se preparan a partir de la incorporación de los tres óxidos en un único objetivo.

- Los resultados del ZnMgCoO (5% Mg, 5% Co) indican que el Co está incorporado en una configuración tetraédrica sustitucional pues las bandas de absorción $3d-3d^*$ se observan claramente con la misma intensidad que las láminas delgadas de ZnCoO con un 5% de Co. Esto indica que la CTT también es una firma fiable de la incorporación del Co en posición tetraédrica en la red cristalina de la aleación. La presencia de Mg se constata por el desplazamiento al azul de 70 meV en la absorción fundamental del espectro (con respecto al borde de absorción de una lámina delgada de ZnCoO con 5% de Co).

- Para el ZnMgCoO (15% Mg, 5% Co) la incorporación de cobalto en posiciones tetraédricas se detecta de nuevo por las bandas de absorción $3d-3d^*$ del Co, que parecen desplazarse hacia el rojo unos 22 meV

con respecto a las láminas delgadas de ZnCoO. Esto indica una intensidad menor del campo cristalino que actúa sobre la capa $3d$ del Co, consistente con el hecho de que en promedio la longitud de enlace es mayor. La presencia de Co también se muestra por la intensidad de la CTT que es del mismo orden en ambas familias de láminas delgadas. Una vez más, la presencia de Mg queda evidenciada por 290 meV de desplazamiento en el borde de absorción fundamental de la aleación (con respecto al gap de una lámina delgada de ZnCoO con 5% de Co).

- Hemos preparado 2 series de crecimientos de multicapas alternando láminas delgadas de (Zn,Mg)O y (Zn,Co)O, depositados a alta temperatura (600ºC), con el supuesto de que la interdifusión sería eficiente a dicha temperatura. La diferencia entre ambas series es el tiempo de deposición de la capa de ZnCoO (15 minutos en la serie 1 y 5 minutos en la serie 2).

- La presencia de un claro umbral de absorción para las subcapas de ZnCoO, cuya absorción fundamental se desplaza a mayores energias para menor espesor de la subcapa indica que la interdifusión es poco relevante y que estas láminas delgadas de múltiples capas son, de hecho, estructuras de múltiples pozos cuánticos (MQW)con pozos cuánticos de ZnCoO y barreras de ZnMgO. El espesor estimado de las capas individuales de ZnCoO está cerca del espesor para el que se han observado efectos de confinamiento en MQW de ZnO/ZnMgO. El desplazamiento del umbral de absorción de las QW de ZnCoO en función del espesor es, de hecho, muy cercano al observado en los QW de ZnO/ZnMgO.

- En las intensidades normalizadas del umbral de absorción fundamental de los pozos cuánticos de ZnCoO, la intensidad de la banda CTT es menor para los QW más delgados, lo que indica que la intensidad de la CTT se ve afectada por el confinamiento de los QW. Éste es un resultado importante, consistente con el efecto de dopado descrito anteriormente. En los QWs, el confinamiento desplaza la energía de los estados localizados hacia mayores energías, correspondiendo a valores más altos del vector k cuantizado en la dirección de confinamiento. Para estos valores del vector k, el elemento de matriz dipolar es menor y la intensidad de la CTT disminuye exponencialmente conforme la energía de confinamiento aumenta.

8.2.4 Nanopartículas

- En esta parte del trabajo, se han realizado medidas de absorción óptica bajo presión para nanopartículas de ZnO:Co con concentraciones del 0%, 1%, 2%, 5%, 10%, 20% y 30% de cobalto. Estas medidas nos han permitido establecer la evolución de varios fenómenos al cambiar la presión y las diferencias entre muestras debido a la composición.

- Hemos observado que las bandas de absorción que aparecen entorno a los 2 eV, debidas a las transiciones electrónicas $d - d^*$ de la capa $3d$ del cobalto, aumentan linealmente en intensidad con el aumento en concentración de Co.

- En el proceso de aumento de la presión podemos distinguir un primer rango de presiones en el que se dan evoluciones monótonas de los espectros de absorción de las muestras. En éste, el frente de absorción se desplaza casi paralelamente hacia energías mayores y la intensidad de las bandas de absorción $d - d^*$ disminuye ligeramente.

- A presiones más elevadas se produce una transición del material provocando asi cambios drásticos en el espectro de absorción. El frente de absorción experimenta un cambio en su forma, desplazandose a energías mucho más altas y pasando de ser abrupto a tener una dependencia más suave con la energía del fotón. La intensidad de la banda de transiciones $d - d^*$ disminuye bruscamente llegano, incluso, a desaparecer.

- Después de subir a la presión máxima e inducir la transición de fase, la fase de alta presión, que sabemos por medidas de difracción de RX que tiene la estructura NaCl, permanece metaestable al relajar la presión, de manera que ha sido posible estudiar, en todo el rango de presiones, el desplazamiento de su frente de absorción. Por tanto, en este trabajo, hemos podido estudiar el frente de absorción óptica en dos fases cristalinas diferentes, en un rango de presiones muy amplio (de presión ambiente hasta 15GPa). Cabe destacar el diferente comportamiento de las nanopartículas respecto a las capas delgadas. En éstas la transición de fase es reversible hasta concentraciones de Co de entre 15 y 20%, mientras que en las nanopartículas la fase NaCl permanece metaestable incluso en ausencia de Co.

- El efecto de confinamiento mostrado por las nanopartículas, junto con la evolución de los espectros durante la transición y la distribución de tamaños de las nanopartículas, nos indica que sometiendo las nanopartículas

a presión, éstas transitan de estructura wurzita a fase NaCl por tamaños, desde las más grandes a las más pequeñas.

- También hemos realizado medidas bajo presión pero sin alcanzar la presión a la cuál todas las nanopartículas han transitado a la fase RS. Con estos resultados, y comparando con otra configuración del mismo material, podemos concluir que para las nanopartículas no-transitadas existe un claro efecto de confinamiento cuántico reflejado tanto en el desplazamiento del umbral de absorción como en el desplazamiento y disminución de la intensidad de la CTT. De manera que, las partículas más pequeñas son las que están contribuyendo al espectro y las más grandes han sido las primeras en transitar a la fase NaCl. Este comportamiento debido al confinamiento de las nanopartículas es similar a lo que anteriormente se había visto al dopar láminas de ZnCoO con galio.

List of publications

1. S.G. Gilliland, J.A. Sans, J.F. Sánchez-Royo, **G. Almonacid**, A. Segura. Charge-transfer absorption band in Zn(1-x)M(x)O (M: Co, Mn) investigated by means of photoconductivity, Ga doping, and optical measurements under pressure. *Appl. Phys. Lett.*, **96**, p. 241902. (2010)

2. A. Segura, J.F. Sánchez-Royo, B. García-Domene, **G. Almonacid**. Current underestimation of the optical gap and Burstein-Moss shift in CdO thin films: A consequence of extended misuse of $\alpha 2$-versus-hν plots. *Appl. Phys. Lett.*, **99**, 151907 (2011)

3. S.G. Gilliland, J.A. Sans, J.F. Sánchez-Royo, **G. Almonacid**, B. García-Domene, A. Segura, G. Tobias and E. Canadell. Role of p-d and s-d interactions in the electronic structure an band gap of $Zn_{1-x}M_xO$ (M = Cr, Mn, Fe, Co, Ni, and Cu): Photoelectron and optical spectroscopy and first principles band structure calculations. *Physical Review B*, **86**, 155203 (2012).

4. C. Renero-Lecuna, R. Martín-Rodríguez, J. González, F. Rodriguez, **G. Almonacid**, A. Segura, V. Munoz-Sanjose, D. Gamelin, R. Valiente. Photoluminescence in ZnO:Co^{2+} (0.01% - 5%) nanocrystals, nanorods, thin-films and single crystals as a function of pressure and temperature: exploring electron-phonon interactions. *Chemistry of Materials*, **26** (2), 1100-1107 (2013).

5. **G. Almonacid**, A. Segura, R. Martín-Rodríguez..... Origin of the metastability of the $Zn_{1-x}M_xO$ nanoparticles under pressure. *In preparation.*

Bibliography

[1] A. Jayaraman. Diamond anvil cell and high pressure physical investigations. *Reviews of Modern Physics*, 55(1):65–108, 1983.

[2] Rosa Martín-Rodríguez. *Synthesis, structural characterization and spectroscopic study of nanocrystalline and microcrystalline materials.* PhD thesis, Universidad de Cantabria, 2011.

[3] RAE. Semiconductor. http://lema.rae.es/drae/?val=semiconductor.

[4] M.Dolores Tortosa Jorques. *Preparació y caracterización de capas finas de semiconductores ternarios de ZnO mediante electrodeposición.* PhD thesis, Universidad Politécnica de Valencia, 2011.

[5] M.A. Majeed Khan, M. Wasi Khan, M. Alhosan, M.S. AlSalhi, and A.S. Aldwayyan. Influences of co doping on the structural and optical properties zno nanostructured. *Applied Physics A*, 100:45–51, 2010.

[6] M.H. Huang, S. Mao, H. Feick, H.Q. Yan, Y.Y. Wu, H. Kind, R. Weber, E. ans Russo, and Yang P.D. Room-temperature ultraviolet nanowire nanolaser. *Science*, 292:1897–1899, 2001.

[7] S.J. Pearton, D.P. Norton, K. Ip, Y.W. Heo, and T. Steiner. Recent progress in processing and properties of zno. *Progress in Material Science*, 50:293–340, 2005.

[8] C. Ricolleau, L. Audinet, M. Gandais, and Gacoin T. Structural transformations in II-VI semiconductornanocrystals. *Eur.Phys. J. D*, 9(1-4 SI):565–570, 1999.

[9] Patricia Rodríguez Fragoso. *Síntesis de nanopartículas semiconductoras recubiertas con almidón.* PhD thesis, Instituto Politécnico Nacional. México, 2008.

[10] Edward L. Wolf. *Nanophysics and Nanotechnology. An Introduction to Modern Concepts in Nanoscience.* Wiley-VCH, Weinheim, Germany, 2006.

[11] G.L. Hornyak, J. Dutta, H.F. Tibbals, and A.K. Rao. *Introduction to Nanoscience.* CRC Press, Taylor and Francis group, Florida, 2008.

[12] J.P. Kar, S.N. Das, J.H. Choi, Y.A. Lee, T.Y. Lee, and J.M. Myoung. Fabrication of uv detectors based on zno nanowires using silicon microchannel. *Journal of Crystal Growth*, 311:3305–3309, 2009.

[13] T. Dietl, H. Ohno, F. Matsukura, J. Cibert, and D. Ferrand. Zener model description of ferromagnetism in zinc-blende magnetic semiconductors. *Science*, 287(5455):1019–1022, 2000.

[14] S.J. Pearton, D.P. Norton, M.P. Ivill, A.F. Herbard, J.M Zavada, , W.M Chen, and I.A. Buyanova. Zno doped with transition metal ions. *IEEE Transactions on Electron Devices*, 54(5):1040–1048, 2007.

[15] Mareike Trunk. *Novel Ternary Oxides for Optoelectronic Applications.* PhD thesis, University of Oslo, 2012.

[16] Ch.S. Rout, A.R. Raju, A. Govindaraj, and C.N.R. Rao. Hydrogen sensors based on zno nanoparticles. *Solid State Communications*, 138:136–138, 2006.

[17] Y.z. Lv, C.-r. Li, L. Guo, F.-c. Wang, Y. Xu, and X.-f. Chu. Triethylamine gas sensor based on zno nanorods prepared by a simple solution route. *Sensors and Actuators B: Chemical*, 141:85–88, 2009.

[18] A. Hernández Battez, R González, J.L. Viesca, J.L. Fernández, J.M. Díaz Fernández, A. Machado, R. Chou, and J. Riba. Cuo, zro_2 and zno nanoparticles as antiwear additive in oil lubricants. *Wear*, 265:422–428, 2008.

[19] Zinc oxide. http://en.wikipedia.org/wiki/Zinc_oxide.

[20] A. Filippetti, V. Fiorentini, G. Cappellini, and A. Bosin. Anomalous relaxations and chemical trends at iii-v semiconductor nitride nonpolar surfaces. *Physical Review B*, 59(12):8026–8031, 1999.

[21] E. Kaldis. *Current topics in material science.* 1981.

[22] Ü. Özgür, Ya.I. Alivov, C. Liu, A. Teke, M.A. Reshchikov, S. Doğan, V. Avrutin, S.-J. Cho, and H. Mokoç. A comprehensive review of zno materials and devices. *Journal of Applied Physics*, 98(041301), 2005.

[23] Akira Onodera and Masaki Takesada. *Advances in Ferroelectrics*, chapter 11. InTech, 2012.

[24] F. Decremps, F. Datchi, A.M. Saitta, and A. Polian. Local structure of condensed zinc oxide. *Physical Review B*, 68:104101, 2003.

[25] J.M. Recio, M.A. Blanco, V. Luaña, R. Pandey, L. Gerward, and J.S. Olsen. Compressibility of the high-pressure rock-salt phase of zno. *Physical Review B*, 58(14):8949–8954, 1998.

[26] Serge Desgreniers. High-density phases of zno: Structural and compressive parameters. *Physical Review B*, 58(21):14102–14105, 1998.

[27] Ch. Bates, R. Roy, and Wb. White. New high-pressure polymorph of zinc oxide. *Science*, 137:993, 1962.

[28] H. Karzel, W. Potzel, M. Köfferlein, W. Schiessl, M. Steiner, U. Hiller, G.M. Kalvius, D.W. Mitchell, T.P. Das, P. Blaha, K. Schwarz, and M.P. Pasternak. Lattice dynamics and hyperfine interaction in zno and znse at high external pressures. *Physical Review B*, 53(17):11425(14), 1996.

[29] F.J. Manjon, K. Syasses, and R. Lauck. Effect of pressure on phonon modes in wurtzite zinc oxide. *High Pressure Research*, 22:299–304, 2002.

[30] U. Rossler. Energy bands of hexagonal 2-6-semiconductors. *Physical Review*, 184:733, 1969.

[31] S.M. Sze. *Physics of semiconductor devices*. 1981.

[32] J.J. Hopfield. Fine structure in the optical absorption edge of anisotropic crystals. *Journal of Physics and Chemistry of Solids*, 15:97–107, 1960.

[33] D.G. Thomas. The exciton spectrum of zinc oxide. 15(1-2):86–96, 1960.

[34] W.R.L. Lambrecht, A.V. Rodina, S. Limpijumnong, B. Segall, and B.K. Meyer. Valence-band ordering and magneto-optic exciton fine structure in zno. *Physical Review B*, 65:075207, 2002.

[35] Juan Ángel Sans Tresserras. *Electronic structure of ZnO-based wide band gap semiconductors: Growth and characterization of the transparent conducting oxide ZnO:Ga and the semimagnetic alloy $Zn_{1-x}Co_xO$ and their high pressure phases.* PhD thesis, Universitat de València, 2007.

[36] Peter Y. Yu and Manuel Cardona. *Fundamentals of Semiconductors. Physics and Materials Properties.* •, 2010.

[37] D. Vogel, P. Kruger, and J. Pollmann. Ab-initio electronic-structure calculations for ii-vi semiconductors using self-interaction-corrected pseudopotentials. *Physical Review B*, 52:14316–14319, 1995.

[38] A. Segura, J.A. Sans, F.J. Manjón, A. Muñoz, and M.J. Herrera-Cabrera. Optical properties and electronic structure of rock-salt ZnO under pressure. *Applied Physics Letters*, 83(2):278–280, 2003.

[39] Mark Fox. *Optical Properties of Solids*. Oxford University Press, 2001.

[40] Robert Seiple Knox. *Theory of Excitons*. Academic P, 1964.

[41] R.J. Elliott. Intensity of optical absorption by excitons. *Physical Review*, 108(6):1384–1389, 1957.

[42] Y. Toyozawa. Theory of line-shapes of the exciton absorption bands. *Progress of Theoretical Physics*, 20(1):53–81, 1958.

[43] A.R. Goni, A. Cantarero, and K. Syassen. Effect of pressure on the low-temperature exciton absorption in gaas. *Physical Review B*, 41(14):10111–10119, 1990.

[44] S.H. Wei and A. Zunger. Role of metal d-states in ii-vi semiconductors. *Physical Review B*, 37(15):8958–8981, 1988.

[45] S.H. Wei and A. Zunger. Predicted band-gap pressure coefficients of all diamond and zinc-blende semiconductors: Chemical trends. *Physical Review B*, 60(8):5404–5411, 1999.

[46] S.H. Wei, X.L. Nie, I.G. Batyrev, and S.B. Zhang. Breakdown of the band-gap-common-cation rule: The origin of the small band gap of inn. *Physical Review B*, 67(16):165209, 2003.

[47] J. Wu and W. Walukiewicz. Band gaps of inn and group iii nitride alloys. *Superlattices and microstructures*, 34(1-2):63–75, 2004.

[48] G.G. Hall. The electronic structure of diamond. *Philosophical magazine*, 43(338):338–343, 1952.

[49] W.A. Harrison. Bond-orbital model and properties of tetrahedrally coordinated solids. *Physical Review B*, 8(10):4487–4498, 1973.

[50] S.H. Wei and A. Zunger. Calculated natural band offsets of all ii-vi and iii-v semiconductors: Chemical trends and the role of cation d orbitals. *Applied Physics Letters*, 72(16):2011–2013, 1998.

[51] S.J. Gilliland, J.A. Sans, J.F. Sánchez-Royo, G. Almonacid, B. García-Domene, A. Segura, G. Tobias, and E. Canadell. Role of p-d and s-d interactions in the electronic structure and bandgap of zn1-xmxo (m= cr, mn, fe, co, ni, cu): an investigation by means of photoelectron and optical spectroscopy and first-principles band structure calculations. *Physical Review B*, 86:155203, 2012.

[52] Samuel John Gilliland. *Structural and Optical Characterisation of Pulsed Laser Deposited Thin Films of Zn1-xMxO (M = Mn, Fe, Ni, Cu) Transparent Magnetic Alloys.* PhD thesis, Universitat de València, 2008.

[53] N. Ichieda, M. Kasuno, K. Banu, S. Kihara, and H. Nakamatsu. Evaluation of hydration enthalpies of monatomic cations by considering both long-range and short-range interactions. *Journal of Physical Chemistry A*, 107(38):7597–7603, 2003.

[54] L. Soderholm, CK. Loong, GL. Goodman, and BD. Dabrowski. Crystal-field splittings and magnetic-properties of pr3+ and nd3+ in rba2cu3o7. *Physical Review B*, 43(10):7923–7935, 1991.

[55] D. Reinen, W. Rauw, U. Kesper, M. Atanasov, H.U. Gudel, M. Hazenkamp, and U. Oetliker. Colour, luminescence and bonding properties of tetrahedrally coordinated chromium(iv), mandanese (v) and iron(vi) in various oxide ceramics. *Journal of Alloys and Compounds*, 246(1-2):193–208, 1997.

[56] J.M. Garcia-Lastra, M.T. Barriuso, J.A. Aramburu, and M. Moreno. Origin of the differen color of ruby and emerald. *Physical Review B*, 72(113104), 2005.

[57] Hans L. Schlafer and Gunter Gliemann. *Basic Principles of Ligand Field Theory.* John Wiley and Sons Ltd, 1969.

[58] M. Orchin, R.S. Macomber, A.R. Pinhas, and R.M. Wilson. *The Vocabulary and Concepts of Organic Chemistry.* 2 edition, 2005.

[59] L.E. Brus. Electron-electron and electron-hole interactions in small semiconductor crystallites: the size dependence of the lowest excited electronic state. *J. Chem. Phys.*, 80:4403–4409, 1984.

[60] P.F. Trwoga, A.J. Kenyon, and C.W. Pitt. Modeling the contribution of quantum confinement to luminescence from silicon nanoclusters. *J. Appl. Phys.*, (80):3789–3794, 1998.

[61] G. Schmid and D. Fenske. Metal clusters and nanoparticles. *Phil. Trans. R. Soc. A*, 368:1207–1210, 2010.

[62] M.G. Bawendi, A.R. Kortan, M.L. Steigerwald, and L.E. Brus. X-ray structural characterization of larger cdse semiconductor clusters. *J. Chem. Phys.*, 91:7282, 1989.

[63] C.Q. Sun, T.P. Chen, B.K. Tay, S. Li, H. Huang, H.B. Zhang, L.K. Pan, S.P. Lau, and X.W. Sun. An extended quantum confinement theory: surface-coordination imperfection modifies the entire band structure of a nanosolid. *J. Phys. D: Appl. Phys.*, 34:3470–3479, 2001.

[64] A.P. Alivisatos. Perspectives on the physical chemistry of semiconductor nanocrystals. *J. Phys. Chem.*, 100(31):13226–13239, 1996.

[65] R. Rossetti, S. Nakahara, and L.E. Brus. Quantum size effects in the redox potentials, resonance raman spectra, and electronic spectra of cds crystallites in aqueous solutions. *J. Chem. Phys.*, 79:1086, 1983.

[66] D.L. Klein, P.L. McEuen, R. Bowen Katari, J.E. andRoth, and A.P. Alivisatos. A new approach to electrical studies of single nanocrystals. *Appl. Phys. Lett.*, 68:2574, 1996.

[67] Al.L. Efros and A.L. Efros. Interband absorption of light in a semiconductor sphere. *Sov. Phys. Semicond.*, 16:772–775, 1982.

[68] L. Brus. Electronic wave functions in semiconductor cluster: experiment and theory. *J. Phys. Chem.*, 90:2555–2560, 1986.

[69] L.E. Brus. On the development of bulk optical properties in small semiconductor crystallites. *J. Lumin.*, 31-32:381–384, 1984.

[70] Tadeusz Suski and William Paul. *Semiconductors and Semimetals.* Academic Press, San Diego, 1998.

[71] *Electronic Structure and the Properties of Solids: The Physics of the Chemical Bond*. Dover Publications, 1989.

[72] F.D. Murnaghan. The compressibility of media under extreme pressures. *Proceedings of the National Academy of Sciences of the USA*, 30:244–247, 194.

[73] X.Y. Zhang, Z.W. Chen, Y.P. Qi, Y. Feng, L. Zhao, L. Qi, M.Z Ma, R.P. Liu, and W.K. Wang. Ab initio comparative study of zincblende and wurtzite zno. *Chinese Physics Letters*, 24(4):1032–1034, 2007.

[74] *Basic Inorganic Chemistry*. 1995.

[75] Y. Yu Peter and Manuel Cardona. *Fundamentals of Semiconductors: Physics and Materials Properties.* 2010.

[76] John G. Webster, editor. *Electrical measurement, signal processing, and displays.* CRC Press, USA, 2004.

[77] Paul L. Rossitier. *The electrical resistivity of metals and alloys.* Cambridge University Press. Oakleigh, Australia, 1987.

[78] L.J. van der Pauw. A method of measuring specific resistivity and Hall effect of discs of arbitrary shape. *Pjilips Research Reports*, 13(1):1–9, 1958.

[79] H.M. Smith and A.F Turner. Vacuum deposited thin films using a ruby laser. *Applied Optics*, 4(1):147, 1965.

[80] P.A. Miles and H.E. Edgerton. Optically efficient ruby laser pump. *Journal of Applied Physics*, 32(4):740, 1961.

[81] A. Bakin, A. El-Shaer, A. Che Mofor, M. Kreye, A. Waag, F. Bertram, J. Christen, M. Heuken, and J. Stoimenos. Mbe growth of zno layers on sapphire employing hydrogen peroxide as an oxidant. *Journal of Crystal Growth*, 287:7–11, 2006.

[82] K. Nakahara, H. Takasu, P. Fons, K. Iwata, A. Yamada, K. Matsubara, R. Hunger, and S. Niki. Growth and characterization of undoped zno films for single crystal based device use by radical source molecular beam epitaxy (rs-mbe). *Journal of Crystal Growth*, 227-228:923–928, 2001.

[83] S. Tripatchi, R.J. Choudhary, A. Tripathi, V. Baranwal, A.C. Pandey, J.W Gerlach, C. Dar, and D. Kanjilal. Studies of effect of deposition parameters on the zno films prepared by pld. *Nuclear Instruments and Methods in Physics Research B*, 266:1533–1536, 2008.

[84] X.Q. Wei, Z. Zhang, Y.X. Yu, and B.Y. Man. Comparative study on structural an optical properties of zno thin films prepared by pld using zno powder target and ceramic target. *Optics and Laser Technology*, 41:530–534, 2009.

[85] P.F. Zhang, H.Y. Wei, G.W. Cong, W.G. Hu, H.B. Fan, J.J. Wu, Q.S. Zhu, and X.L. Liu. Effects of disk rotation rate on the growth of zno films by low-pressure metal-organic chemical vapor deposition. *Thin Solid Films*, 516:925–928, 2008.

[86] S. Agouram, M.C. Martínez-Tomás, and V. Muñoz-Sanjosé. Zno films grown by mocvd on gaas substrates: Effects of a zn buffer deposition on interface, structural and morphological properties. *Journal of Crystal Growth*, 311:2564–2571, 2009.

[87] T. Fujii, N. Yoshii, Y. Kumagai, and A. Koukitu. Halide vapor phase epitaxy of zno studied by thermodynamic analysis and growth experiments. *Journal of Crystal Growth*, 314:108–112, 2011.

[88] N. Yoshii, T. Fujii, R. Masuda, S. Hosaka, A. Kamisawa, and A. Kumagai, Y. Koukitu. Growth of zno crystal on sapphire and nitridated sapphire substrates at 1000 °c by halide vapor phase epitaxy. *Materials Letters*, 64:25–27, 2010.

[89] M.S. Al-Busaidy, O.E. Kusmartseva, and M.D. Crapper. Pulsed laser deposition of metallic multilayers: the influence of laser power on microstructure. *Applied Physics A*, 79:1453–1456, 2004.

[90] R. Kelly and A. Miotello. *Pulsed Laser Deposition of Thin Films.* John Wiley and Sons, New York, 1994.

[91] M. N.R. Ashfold, F. Claeyssens, G.M. Fuge, and Henley S.J. Pulsed laser ablation and deposition of thin films. *Chem. Soc. Rev.*, 33:23–31, 2003.

[92] F. Claeyssens, R.J. Lade, K.N. Rosser, and N.R. Ashfold. Investigations of the plume accompanying pulsed ultraviolet laser ablation of graphite in vacuum. *Journal of Applied Physics*, 89(1):697–709, 2001.

[93] K.L. Bray. *High pressure probes of electronic structure and luminescence properties of transition metal and lanthanides systems.*, volume 213 of *Topic in Current Chemistry*. Spring-Verlag. Berlin, 2001.

[94] M. Ruiz-Castillo, A Segura, J.A. Sans, J. Martínez-Pastor, D. Fuster, Y. González, and González L. Pressure dependence of photoluminescence of inas/inp self-assembled quantum wires. *Phys. Stat. Sol (b)*, 244(1):59–64, 2007.

[95] I.V. Aleksandrov, A.F. Goncharov, A.N. Zisman, and S.M. Stishov. Diamond at high pressures: Raman scattering of light, equation of state, and high pressure scale. *Zhurnal Eksperimentalnoi i Teoreticheskoi Fiziki*, 93(2):680–691, 1987.

[96] C.E. Weir, E.R. Lippincott, A. Van Valkenburg, and A.N. Bunting. Infrared studies in the 1- to 15-micron region to 30.000 atmospheres. *Journal of Research of the National Bureau of Standards Section A.-Physics and Chemistry*, 63A(1):55, 1959.

[97] Raúl E. Lacomba Perales. Estudio de las propiedades ópticas bajo presión de las scheelitas de $PbWO_4$ y $BaWO_4$ y la wolframita de $ZnWO_4$. Master's thesis, Universitat de València, 2007.

[98] Francisco Javier Manjón Herrera. *Estudio de la estructura de bandas del seleniuro de indio mediante medidas ópticas bajo presión hidrostática.* PhD thesis, Universitat de València, 1999.

[99] Somchai Tancharakorn. *Instrumentation development for studies of magnetic and structural properties of molecular magnets.* PhD thesis, School of Engineering an Electronics, University of Edinburgh, 2008.

[100] H.K. Mao. Specific volumen measurements of Cu, Mo, Pd, and Ag and calibration of the ruby R_1 fluorescence pressure gauge from 0.06 to 1 Mbar. *Journal Applied Physics*, 49(6):3276–3283, 1978.

[101] G.L. Piermarini, S. Block, J.D. Barnett, and R.A. Forman. Calibration of the pressure dependence of the R1 ruby fluorescence line to 195 kbar. *Journal of Applied Physics*, 46(6):2774–2780, 1975.

[102] J. García Solé, L.E. Bausá, and D. Jaque. *An Introduction to the Optical Spectroscopy of Inorganic Solids.* John Wiley and Sons Ltd, England, 2005.

[103] B. Henderson and G.F. Imbusch. *Optical Spectroscopy of Inorganic Solids.* Clarendon Press, Oxford, 1989.

[104] E.I. Solomon and A.B.P. Lever. *Inorganic Electronic Structure and Spectroscopy: Methodology.* John Wiley and Sons, New York, 1999.

[105] K. Samanta, P. Bhattacharya, R.S. Katiyar, W. Iwamoto, P.G. Pagliuso, and C. Rettori. Raman scattering studies in dilute magnetic semiconductor zn1-xcoxo. *Physical Review B*, 73(24):245213, 2006.

[106] Fredéric Decremps, Julio Pellicer-Porres, A. Marco Saitta, Jean-Claude Chervin, and Alain Polian. High-pressure raman spectroscopy study of wurtzite zno. *Phys. Rev. B*, 65:092101, Feb 2002.

[107] R. Cuscó, E. Alarcón-Lladó, J. Ibáñez, L. Artús, J. Jiménez, B. Wang, and M.J. Callahan. Temperature dependence of raman scattering in zno. *Physical Review B*, 75:165202, 2007.

[108] J. Pellicer-Porres, A. Segura, V. Muñoz, and J.C. Chervin. Refractive index of gate under high pressure. *Semiconductor Science Technology*, 15:902–907, 2000.

[109] V. Panchal, A. Segura, and J. Pellicer-Porres. Low-cost set-up for fourier-transform infrared spectroscopy in diamond anvil cell from 4000 to 400 cm^{-1}. *High Pressure Research*, 31(3):445–453, 2011.

[110] K.X. Yao and H.C. Zeng. Architectural processes and physicochemical properties of CoO/ZnO and $Zn_{1-x}Co_xO/Co_{1-x}Zn_xO$ nanocomposites. *The Journal of Physical Chemistry C*, 113(4):1373–1385, 2009.

[111] *Physical Principles of Electron Microscopy: An Introduction to TEM, SEM and AEM.* Inc. Edmonton, Alberta, Canada, 2005.

[112] John G. Webster, editor. *Electrical measurement, signal processing, and displays.* CRC Press, 2004.

[113] Diego Alba. *Comportamiento de super vidrio de espin en peliculas delgadas nanogranulares diluidas de Fe-Au, Ag y Cu.* PhD thesis, Universidad de Cantabria, 2011.

[114] Cristina Echevarría. *Influencia de la reducción del tamaño en las propiedades electrónicas y magnéticas de aleaciones binarias de Tierras Raras.* PhD thesis, Universidad de Cantabria, 2014.

[115] M. Ivill, S.J. Pearton, S. Rawal, L. Leu, P. Sadik, R. Das, A.F. Hebard, M. Chisholm, J.D. Budai, and D.P. Norton. Structure and magnetism of cobalt-doped ZnO thin films. *New Journal of Physics*, 10(065002), 2008.

[116] S.-J. Kim, Y.C. Cho, S.J. Kim, S. Lee, W.-K. Kim, S.-Y. Jeong, C.R. Cho, J.-S. Bae, S. Park, and I.K. Jeong. Comparison of the structural, magnetic, electronic, and optical properties for ZnCoO and Co-precipitation samples. *Journal of the Korean Physical Society*, 56(4):1374–1377, 2010.

[117] A.C. Tuan, J.D. Bryan, A.B. Pakhomov, V. Shutthanandan, S. Thevuthasan, D.E. McCready, D. Gaspar, M.H. Engelhard, J.W. Rogers, K. Krishnan, D.R. Gamelin, and S.A. Chambers. Epitaxial growth and properties of cobalt-doped ZnO on alpha-Al2O3 single-crystal substrates. *Physical Review B*, 70(5-054424), 2004.

[118] Shivaraman Ramachandran. *Zinc Oxide based Diluted Magnetic Semiconductors*. PhD thesis, North Carolina State University, 2006.

[119] N. Hasuike, K. Nishio, T. Isshiki, K. Kisoda, and H. Harima. Structural and electronic properties of Co-doped ZnO nanocrystals synthesized by co-precipitation method. *Physica status solidi C*, 6(1):213–216, 2009.

[120] P. Koidl. Optical absorption of Co2+ in ZnO. *Physical Review B*, 15(5):2493–2499, 1977.

[121] K.J. Button, B. Lax, D.R. Cohn, M.V. Ortenber, E. Mollwo, and R. Helbig. Zeeman splitting of anomalous shallow bound-states in zno. *Physical Review Letters*, 28(25):1637, 1972.

[122] William K. Liu, G. Mackay Salley, and Daniel R. Gamelin. Spectroscopy of photovoltaic and photovoltaic and photoconductive nanocrystalline co-doped zno electrodes. *Physical Chemistry B*, 109(30):14486–14495, 2005.

[123] Claire A. Johnson, Alicia Cohn, Tiffany Kaspar, Scott A. Chambers, G. Mackay Salley, and Daniel R. Gamelin. Visible-light photoconductivity of $zn_{1-x}co_xo$ and its dependence on co^{2+} concentration. *Physical Review B*, 84(12):125203, 2011.

[124] J.A. Sans, G. Martínez-Criado, J. Pellicer-Porres, J.F. Sánchez-Royo, and A. Segura. Thermal instability of electrically active centers in

heavily ga-doped zno thin films: X-ray absorption study of the ga-site configuration. *Applied Physics Letters*, 97(221904), 2007.

[125] O. Vennéguès, J.M. Chauveau, M. Korytov, C. Deparis, J. Zuniga-Perez, and C. Morhain. Interfacial structure and defect analysis of nonpolar zno films grown on r-plane sapphire by molecular beam epitaxy. *Journal of Applied Physics*, 103(8):083525, 2008.

[126] C.R. Gorla, N.W. Emanetoglu, S. Liang, W.E. Mayo, Y. Lu, M. Wraback, and H. Shen. Structural, optical, and surface acoustic wave properties of epitaxial zno films grown on (01(1)over-bar2) sapphire by metalorganic chemical vapor deposition. *Journal of Applied Physics*, 85(5):2595–2602, 1999.

[127] W.Y. Liang and A.D. Yoffe. Transmission spectra of zno single crystals. *Physical Review Letters*, 20(2):59–62, 1968.

[128] T. Makino, C.H. Chia, N.T. Tuan, Y. Segawa, M. Kawasaki, A. Ohtomo, K. Tamura, and H. Koinuma. Exciton spectra of zno epitaxial layers on lattice-matched substrates grown with laser-molecular-beam epitaxy. *Applied Physics Letters*, 76(24):3549 – 3551, 2000.

[129] W. Pacuski, D. Ferrand, J. Cibert, C. Deparis, P. Kossacki, and C. Morhain. Magneto-optical spectroscopy of (zn,co)o epilayers. *Physica Status Solidi (b)*, 243(4):863–867, 2006.

[130] M. Millot, J. Gonzalez, I. Molina, B. Salas, Z. Golacki, J.M. Broto, H. Rakoto, and M. Goiran. Raman spectroscopy and magnetic properties of bulk zno:co single crystal. *Journal of Alloys and Compounds*, 423:224–227, 2006.

[131] J.A. Sans, A. Segura, M. Mollar, and B. Mari. Optical properties of thin films of zno prepared by pulsed laser deposition. *Thin Solid Films*, 251:453–454, 2004.

[132] J.A. Sans, J.F. Sánchez-Royo, A. Segura, G. Tobias, and E. Canadell. Chemical effects on the optical band-gap of heavily doped zno:m_{III}(m=al,ga,in): An investigation by means of photoelectron spectroscopy, optical measurements under pressure, and band structure calculations. *Physical Review B*, 79(195105), 2009.

[133] J.A. Sans, A. Segura, J.F. Sánchez-Royo, V. Barber, M.A. Hernández-Fenollosa, and B. Marí. Correlation between optical and transport

properties of ga-doped zno thin films prepared by pulsed laser deposition. *Superlattices and Microstructures*, 39:282–290, 2006.

[134] A. Segura, J.A. Sans, D. Errandonea, D. Martinez-García, and V. Fages. High conductivity of ga-doped rock-salt zno under pressure. hint on deep-ultraviolet transparent conducting oxides. *Applied Physics Letters*, 88:11910, 2006.

[135] J.F. Muth, R.M. Kolbas, A.K. Sharma, S. Oktyabrsky, and J. Narayan. Exitonic structure and absorption coefficient measurements of ZnO single crystal epitaxial films deposited by pulsed laser deposition. *Journal of Applied Physics*, 85(11):7884–7887, 1999.

[136] C. Bundesmann, N. Ashkenov, M. Schubert, D. Spemann, T. Butz, E.M. Kaidashev, M. Lorenz, and M. Grundmann. Raman scattering in zno thin films doped with fe, sb, al, ga and li. *Applied Physics Letters*, 83(10):1974–1976, 2003.

[137] Y. He, P. Sharma, K. Biswas, E.Z. Liu, Naofumi Ohtsu, A. Inoue, Y. Inada, M. Nomura, J.S. Tse, S. Yin, and J.Z. Jiang. Origin of ferromagnetism in zno codoped with ga and co: Experiment and theory. *Physical Review B*, 78(15):155202, 2008.

[138] S.A. Wolf, D.D. Awschalom, R.A. Buhrman, J.M. Daughton, S. von Molnár, M.L. Roukes, A.Y. Chtchelkanova, and D.M. Treger. Spintronics: A spin-based electronics vision for the future. *Science*, 294(5546):1488–1495, 2001.

[139] N.H. Hong, J. Sakai, N.T. Huong, N. Poirot, and A. Ruyter. Role of defects in tunning ferromagnetism in diluted magnetic oxide thin fims. *Physical Review B*, 72(4):045336, 2005.

[140] S.G. Gilliland, A. Segura, J.F. Sánchez-Royo, L.M. García, F. Bartolomé, J.A. Sans, G. Martínez-Criado, and F. Jimenez-Villacorta. Absence of ferromagnetism in single-phase wurtzite zn1−xmnxo polycrystalline thin films. *Journal of Applied Physics*, 108:073922, 2010.

[141] A. Ohtomo, M. Kawasaki, T. Koida, K. Masubuchi, and H. Koinuma. Mgxzn1-xo as a ii-vi widgap semiconductor alloy. *Applied Physics Letters*, 72(19):2466–2468, 1998.

[142] W.I. Park, G.C. Yi, and H.M. Jang. Metalorganic vapor-phase epitaxial growth and photoluminescent properties of zn1-xmgxo(0 ¡= x ¡= 0.49) thin films. *Applied Physics Letters*, 79(13):2022–2024, 2001.

[143] A.K. Sharma, J. Narayan, J.F. Muth, C.W. Teng, and C. Jin. Optical and structural properties of epitaxial mgxzn1-xo alloys. *Applied Physics Letters*, 75(21):3327–3329, 1999.

[144] T.A. Wassner, B. Laumer, S. Maier, A. Laufer, B.K. Meyer, M. Stutzmann, and M. Eickhoff. Optical properties and structural characteristics of znmgo grown by plasma assisted molecular beam epitaxy. *Journal of Applied Physics*, 105:023505, 2009.

[145] B. Laumer, F. Schuster, M. Stutzmann, A. Bergmaier, G. Dollinger, and M. Eickhoff. Accurate determination of optical bandgap and lattice parameters of zn1-xmgxo epitaxial films (0 ¡= x ¡= 0.3) grown by plasma-assisted molecular beam epitaxy on a-plane sapphire. *Journal of Applied Physics*, 113(23):233512–233512, 2013.

[146] S.H. Park, K.B. Kim, S.Y. Seo, S.H. Kim, and S.W. Han. Structural and optical properties of zn1-xmgxo thin films synthesized with metal organic chemical vapor deposition. *Journal of Electronic Materials*, 35(8):1680–1684, 2006.

[147] J.-M. Chauveau, J. Vives, J. Zuniga-Perez, M. Laügt, M. Teisseire, C. Deparis, C. Morhain, and B. Vinter. Residual strain in nonpolar a -plane zn 1 x mg x o (0 x 0.55) and its effect on the band structure of (zn,mg)o/zno quantum wells. *Applied Physics Letters*, 93:231911, 2008.

[148] H.D. Sun, T. Makino, Y. Segawa, M. Kawasaki, A. Ohtomo, K. Tamura, and H. Koinuma. Biexciton emission from zno/zn0.74mg0.26o multiquantum wells. *Applied Physics Letters*, 78(22):3385–3387, 2001.

[149] C.H. Chia, T. Makino, K. Tamura, Y. Segawa, M. Kawasaki, A. Ohtomo, and H. Koinuma. Confinement-enhanced biexciton binding energy in zno/znmgo multiple quantum wells. *Applied Physics Letters*, 82(12):1848–1850, 2003.

[150] D.A. Schwartz, N.S. Norberg, Q.P. Ngyen, J.M. Parker, and D.R. Gamelin. Magnetic quantum dots: Synthesis, spectroscopy, and magnetism of CO2+ and Ni2+ doped ZnO nanocrystals. *Journal of the American Chemical Society*, 125(43):13205–13218, 2003.

[151] M.A. White, S.T. Ochsenbein, and D.R. Gamelin. Colloidal nanocrystals of wurtzite Zn1-xCoxO (0 ¡= x ¡= 1): Models of spinodal decom-

position in an oxide diluted magnetic semiconductor. *Chemistry of Materials*, 20(22):7107–7116, 2008.

[152] N.R. Jana, Y. Chen, and X. Peng. Size-and shape- controlled magnetic (cr, mn, fe, co, ni) oxide nanocrystals via a simple and general approach. *Chem. Mater.*, 16:3931–3935, 2004.

[153] Ray F. Egerton. *Physical Principles of Electron Microscopy: An Introduction to TEM, SEM, and AEM.* Springer Science+Business Media, Inc.Edmonton, Alberta, Canada, 2005.

[154] V.A. Fonoberov and A.A. Balandin. Radiative lifetime of excitons in zno nanocrystals: The dead-layer effect. *Physical Review B*, 70(195410), 2004.

[155] A.S. Risbud, N.A. Spaldin, Z.Q. Chen, S. Stemmer, and Ram. Seshadri. Magnetism in polycrystalline cobalt-substituted zinc oxide. *Physical Review B*, 68:205202, 2003.

[156] M. Venkatesan, C.B. Fitsgerald, J.G. Lunney, and J.M.D. Coey. Anisotropic ferromagnetism in substituted zinc oxide. *Physical Review Letters*, 93(17, 177206), 2004.

[157] A. Mang, K. Reimann, and St. Rübenache. Band gaps, crystal-field splitting, spin-orbit coupling, and exciton binding energies in zno under hydrostatic pressure. *Solid State Communications*, 94:251, 1995.

[158] J.A. Sans, A. Segura, J.F. Sánchez-Royo, Ch. Ferrer-Roca, and E. Guillotel. Pressure dependence of the optical properties of wurtzita and rock-salt Zn1-xCoxO thin film. *Physica Status Solidi B*, 244(1):407–412, 2007.

[159] F. Decremps, J. Pellicer-Porres, F. Datchi, J.P. Itie, A. Polian, and F. Baudelet. Trapping of cubic zno nanocrystallites at ambient conditions. *Applied Physics Letters*, 81:4820–4822, 2002.

[160] G.W. Pratt and R. Coelho. Optical absorption of coo and mno above and below the neel temperature. *Physical Review*, 116:281–286, 1959.